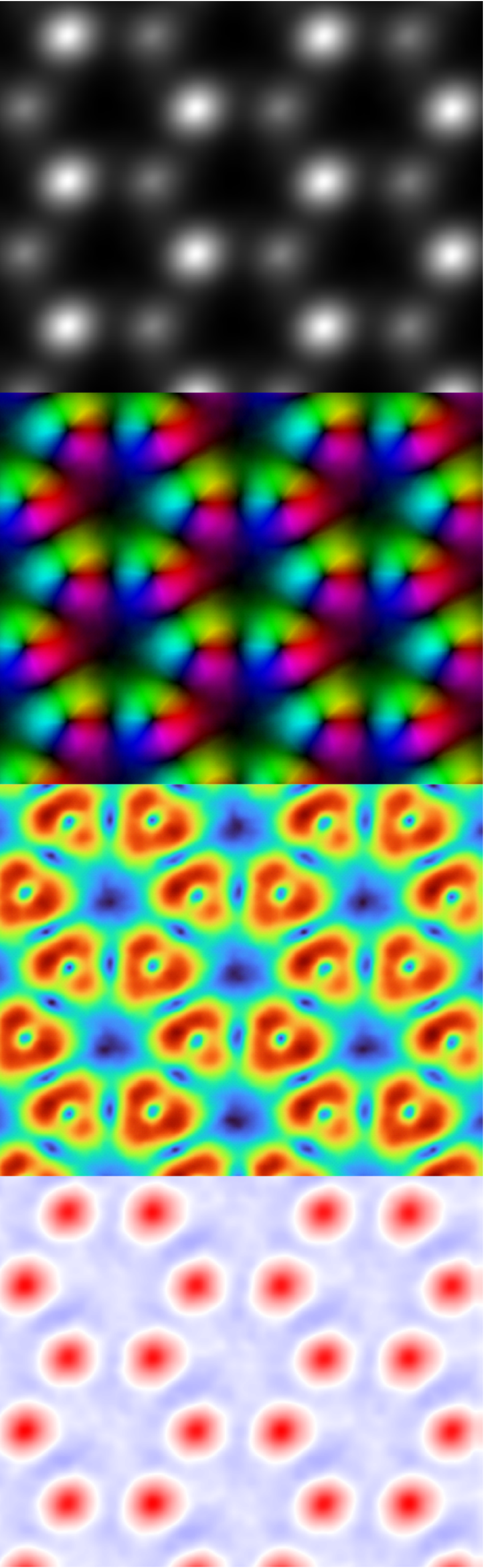

Differential Phase Contrast Imaging on 2D Materials

von

Maja Groll

– Dissertation –

Zur Erlangung des Doktorgrades
der Naturwissenschaften
von der Fakultät für Naturwissenschaften
der Universität Paderborn

vorgelegt am 3. Dezember 2025

1. Gutachter: Prof. Dr. Jörg K. N. Lindner

2. Gutachter: Prof. Dr. Uwe Gerstmann

Contents

Acknowledgements

The PhD is a challenging task and this endeavour would not have been possible without the support of supervisors, colleagues, family and friends. I would therefore like to take this opportunity to express my gratitude to all those who have encouraged this work:

- I would like to thank Prof. Dr. Jörg Lindner, Nanopatterning–Nanoanalysis–Photonic Materials, for the great opportunity to work on such an emerging new STEM technique and being part of a highly dynamic and evolving research field. Thanks for the scientific support, reviewing the thesis, and the many opportunities to participate in different conferences covering microscopy and material research communities.
- Special thanks to Prof. Dr. Uwe Gerstmann, Quantum Materials Modelling, for reviewing this rather extensive work so readily and for his understanding regarding the tight schedule. I would also like to thank him for his contribution and support with DFT calculations of defects in WSe_2.
- Many thanks to the Committee for Research and Junior Academics from Paderborn University for the funding over almost three years of my PhD, which gave me the opportunity to start my research here.
- I would also like to express my gratitude to Dr. Julius Bürger for the continuos software support and, above all, for the fruitful and inspiring scientific discussions as well as for the motivational speeches whenever I felt frustrated.
- I would like to thank the research team of Prof. Dr. Klaus Jöns, Hybrid Quantum Photonic Devices, for the collaboration in sample preparation of 2D materials. Special thanks to Ioannis Caltzidis with whom I started the challenging journey of transferring 2D materials to TEM grids. Thanks for the time and effort! Many thanks also to Bastian Thomßen, Maranatha Andalis and Henri Hübschmann for the joint efforts on the sample preparation, transfer of 2D materials and the optical investigations as well as for the dip into the fascinating project of the ion bombardment of 2D materials.
- Many thanks to my colleagues in the NNP group which supported me during this time by interdisciplinary discussions and extended coffee breaks. Many thanks to Felix Lohmeyer and Hari Venugopal for the culinary exchange, the encouraging chats and the joint efforts to get through the PhD phase. Thanks also to Philipp Hodges for motivating me to keep going and for highlighting the good things about finishing.

In addition, I would like to emphasise the great support from my flat mate and friend Philip Held who listened to every drama. Thanks for the enjoyable evenings.

Finally, I would like to express my gratitude to my family for their continuous and unwavering support, understanding and distraction. In particular, huge thanks to Markus Groll and Marie-Christin Lakemeyer for letting me get things off my chest whenever I needed to, and for always being there to listen. Your support means a lot to me!

Abstract

Differential phase contrast (DPC) imaging is a technique in scanning transmission electron microscopy which enables parallel investigations of the structural properties and the electric field distribution in solids at sub-atomic resolution. Aim of this thesis is the correct quantitative investigation of the atomic electric field and charge density distributions in 2D materials. With focus on DPC imaging using a segmented detector, influences of microscope and specimen-related parameters, such as lens aberrations, detector anisotropy as well as the stacking of atoms and their atomic number are investigated by measurements and multislice image simulations. It is demonstrated that the way the detector segments capture the post-specimen intensity distribution introduces pronounced artefacts in the atomic electric field. The interaction of the electron beam with the atomic potentials is intensively studied, indicating a refocussing of the electron beam during the propagation along atomic columns in thin specimens and a non-linear behaviour of the DPC signal with the atomic number. The different effects are superimposed in the obtained atomic electric field distributions making a correct quantitative analysis difficult. For WSe_2 and MoS_2 mono- and bilayers, the atomic electric field distributions are quantitatively analysed considering the different influences. Furthermore, changes in the electric field distribution due to point defects in a WSe_2 monolayer are evaluated.

Kurzzusammenfassung

Differentieller Phasenkontrast ist eine Technik in der Rastertransmissionselektronenmikroskopie, welche die Untersuchung der atomaren Struktur und elektrischen Feldverteilung in Festkörpern mit subatomarer Auflösung ermöglicht. Ziel dieser Arbeit ist die quantitative Untersuchung von atomaren elektrischen Feld- und Ladungsdichteverteilungen in 2D-Materialien. Mit Fokus auf DPC-Messungen mittels eines segmentierten Detektors werden die unterschiedlichen Einflüsse von Mikroskop- und Proben-Parametern wie Linsenfehlern, Detektoranisotropie sowie die Stapelung von Atomen und deren Ordnungszahl mithilfe von Messungen und Simulationen untersucht. Es wird gezeigt, dass die Art und Weise, wie die Detektorsegmente die Intensitätsverteilung nach Durchgang durch die Probe erfassen, zu ausgeprägten Artefakten in den gemessenen atomaren Feldern führt. Zudem wird die Wechselwirkung des Elektronenstrahls mit den atomaren Potentialen untersucht, was eine Refokussierung des Strahls während der Propagation entlang einer Atomsäule und einem nichtlinearen Verhalten des DPC-Signals mit der Ordnungszahl führt. Die verschiedenen Effekte überlagern sich, was eine quantitative Analyse der gemessenen Feldverteilungen erschwert. Für WSe_2 und MoS_2 Mono- und Doppellagen werden die atomaren Feldverteilungen unter Berücksichtigung der verschiedenen Einflüsse quantitativ analysiert. Zudem werden Änderungen in der elektrischen Feldverteilung aufgrund punktförmiger Defekte in einer WSe_2 Monolage untersucht.

Chapter 1

Introduction

A scanning transmission electron microscope (STEM) is one of the most powerful analytical characterization tools which combines a high spatial resolution down to the sub-angström level with a multitude of different analytical techniques to investigate material properties including the atomic structure, chemical composition, band structure and other electro-optical properties. Among the variety of different analytical imaging techniques is differential phase contrast (DPC) imaging which is a technique to measure electric and magnetic fields inside the specimen [1–3].

In STEM-DPC, a convergent electron probe is scanned across the specimen. At each scan position, the incident electrons interact with the electromagnetic fields inside the specimen and are deflected by the Lorentz force. This leads to an intensity redistribution in the post-specimen electron wave [4, 5]. Using a position-sensitive detector, such as a segmented or pixelated detector, the deflection can be measured as a shift of the centre-of-mass (CoM) of the post-specimen intensity distribution. For a segmented detector, the CoM is obtained by calculating difference signals of opposing segments. As the shift of the CoM is related to the deflection of the electrons and therefore proportional to the present field inside the specimen, the causing (atomic) electric or magnetic field can be accessed [4–8]. Furthermore, even the charge distribution can be spatially visualized and analysed using the electric field distribution measured by STEM-DPC and Gauss' law.

In the past 15 years, significant theoretical and experimental efforts have been made to improve the accuracy of STEM-DPC to quantitatively measure atomic electric fields and potential charge redistributions due to bonding. Among the different achievements is the introduction of fast pixelated direct electron detectors with a high number of detector segments (pixels). In contrast to segmented detectors, which only consist of few segments and therefore only approximate the shift of the CoM in DPC, the pixelated detectors capture the full post-specimen intensity distribution and are, thus, quantitatively more accurate.

Although pixelated detectors offer a great accuracy in the quantitative measurement of atomic fields, they currently exhibit a slower acquisition speed compared to segmented detectors. At the time of writing, the image acquisition with segmented detectors is at least two times faster for pixelated detectors [9–11]. Therefore, segmented detectors still outperform pixelated detectors in terms of acquisition time and are therefore of great interest for in-situ DPC investigations and beam-sensitive materials, e. g. 2D materials.

The application of STEM-DPC for the quantitative measurement of mesoscopic fields was successfully shown for built-in electric fields at pn-junctions [12–15] and quantum wells [16, 17] in semiconductors, and also for magnetic domains [18, 19] and skyrmions [20, 21], highlighting its value for analytical investigation.

With the introduction of state-of-the-art lens aberration correctors and the resulting increase in spatial resolution below 0.5 Å in STEM imaging, the space between the atomic nuclei and the electron clouds can nowadays be readily probed [22, 23]. In combination with DPC, this enables the exploration of atomic electric fields e. g. in $BaTiO_3$ [24], $SrTiO_3$ [4, 8], GaN [4, 25] and Si [26]. However, the quantitative investigation of atomic electric fields remains challenging as the post-specimen intensity distribution is strongly influenced by dynamical diffraction effects, which are pronounced for thick specimens. Thus, quantitative DPC measurements of atomic electric fields are only possible for specimen thickness in the single digit nanometre regime where dynamical diffraction effects are reduced [27, 28]. Therefore, 2D materials came into focus for the quantitative investigation of atomic electric fields by STEM-DPC as their layered structure facilitates a preparation of specimens with a thickness of only a few atomic layers. Under this condition, the DPC signal is described to be linearly related to the projected potential, which scales with the atomic number and the number of atoms in the specific atomic column [6, 29, 30]. Hence, STEM-DPC offers the possibility to quantify internal fields on the atomic scale and relate it to the material structure and chemical composition. Especially, changes in the atomic electric field distribution introduced by individual defects, such as (single atom) vacancies, can now be visualized and quantitatively measured with sub-atomic resolution.

2D materials exhibit interesting layer-number dependent optoelectronic and electrical properties, which make these materials of great interest for future application in optoelectronic devices [31–33]. Due to their low-dimensionality, the internal atomic electric field distribution strongly determines the materials properties. Therefore, the quantitative measurement of the atomic fields in 2D materials by STEM-DPC can give insight into the relation between the atomic structure, the atomic field distribution and the material properties. Investigation of atomic electric fields in pristine and defective 2D materials, such as graphene [34], hexagonal BN [35, 36] as well as transition metal dichalcogenides (TMDs), e. g. MoS_2 [27, 37, 38], WS_2 [37, 39] and WSe_2 [40, 41], show a great qualitative agreement between the electric field derived by STEM-DPC and corresponding multislice image simulations. Quantitatively, the atomic electric field distributions in 2D TMDs obtained by STEM-DPC, especially the ones of MoS_2 and WSe_2, show an unexpected behaviour. For the different atomic columns in these materials, the DPC signal close to the atomic column with a lower projected atomic number shows a higher electric field magnitude compared to the electric field at the atomic column with the higher projected atomic number. This contrasts the expected linear relationship of DPC with the projected atomic number and the number of atoms.

This behaviour can be observed for different TMD monolayers investigated by DPC. The origin is partially assigned to the presence of lens aberrations [40, 42], however, no overall agreement on this problem is currently found in literature. Therefore, this thesis aims to exploit the origin of this unexpected electric field in TMD monolayers obtained by DPC imaging. Since DPC imaging is sensitive to various microscope and specimen-related parameters, the unexpected behaviour can be an artefact arising from measurement conditions or due to the specific specimen structure and potential of TMDs. This thesis addresses the investigation of these different parameters and therefore contributes to the fundamental understanding of DPC imaging with a special focus on the correct quantitative interpretation of atomic electric field and charge density distributions in 2D materials.

In this work, DPC measurements of WSe_2 and MoS_2 monolayers are compared with corresponding multislice image simulations and detailed analyses of their atomic electric field distributions are done. The influence of microscope-related parameters such as lens aberrations and the detector settings on the DPC signal and the resulting atomic electric fields are investigated. Furthermore, the influence of dynamical diffraction effects and the impact of the arrangement of atoms on the beam propagation in the specimen as well as the resulting DPC image is analysed by multislice image simulations of individual atoms. The influence of the atomic number, the distance between the atoms along the beam propagation direction, and the number of atoms stacked on top of each other is evaluated in a detailed study.

Quantitative investigations of the atomic electric field and charge density distribution by DPC are conducted for WSe_2 bilayers in different high-symmetry stacking configurations. Changes of features in the atomic electric field distribution due to the stacking are discussed in reference to an analogous measurement of a WSe_2 monolayer. In addition, a twisted WSe_2 bilayer is investigated and the influence of the local change in stacking configuration and long-range fields possibly introduced by the Moiré superlattice is evaluated.

Since defects in these low-dimensional materials drastically influence the material properties and are expected to lead to interesting optoelectronic properties such as excitons and single photon emission, local changes in the electric field distribution in the vicinity of these defects are important [43, 44]. Thus, the influence of point defects on the electric field distribution in a WSe_2 monolayer is studied. The local change in the electric field distribution is visualized and related to DFT calculations.

The thesis is structured in the following way. In Chapter 2, the fundamental concepts of STEM and DPC are given including the basic concepts for the multislice image simulation of STEM images and the calculation of the atomic potentials by DFT. In addition, a description of 2D transition metal dichalcogenides including their stacking configurations and different point defects as well as their behaviour under electron irradiation are given. In Chapter 3, the experimental details are elaborated with focus on the microscope and detector used. Furthermore, the signal- and post-processing steps of the experimental data are described. Moreover, the sample preparation including a mechanical exfoliation of TMDs and a polymer-based transfer process of TMD mono- and multilayers to TEM grids are explained. In Chapter 4, the atomic electric field and charge density distributions of a WSe_2 monolayer are quantitatively analysed and compared to analogous multislice image simulations. Qualitative and quantitative similarities as well as differences are highlighted and their possible origins are discussed. The influences of lens aberrations, the detector layout and specimen contaminations on the DPC signal and the resulting electric field and charge density distributions are analysed by measurements and simulations. Using multislice image simulations of single and multiple individual atoms, the dependency of the DPC signal on the atomic number, the number of atoms as well as the vertical stacking distance of atoms in beam propagation direction is investigated.

In Chapter 5, the electric field and charge density distributions in a monolayer of MoS_2 are analysed and compared with the DPC measurement of a WSe_2 monolayer.

In Chapter 6, the electric field distributions of WSe_2 bilayers in different high-symmetry and Moiré stacking configurations are investigated and the influence of the stacking of atoms is analysed.

Chapter 7 reveals the local change in the electric field distribution due to the presence of point defects by quantitative analysis and comparison with multislice image simulations. The findings are compared to the defect-induced electron density distribution obtained by DFT calculations. Finally, Chapter 8 summarizes the thesis. Additional information and simulations related to the shown work are compiled in the Appendix.

Chapter 2

Fundamentals

2.1 Transmission Electron Microscopy

Transmission electron microscopy (TEM) is an analytical high-resolution imaging technique which enables the investigation of a material's atomic structure by using highly energetic electrons. Using accelerated electrons offers the possibility to overcome the resolution limit of conventional visible light (VIS) microscopes set by the diffraction limit. Therefore, a much higher spatial resolution can be achieved with TEMs than with VIS microscopes. Based on the wave-particle dualism of electrons, the wavelength is related to the electrons kinetic energy E_0 and described by the de-Broglie wavelength λ

$$\lambda = \frac{h}{\sqrt{2m_0E_0(1+\frac{E_0}{2m_0c^2})}} \tag{2.1}$$

where h corresponds to the Planck's constant, m_0 to the rest mass of the electron, and c to the speed of light [45]. The kinetic energy E_0 of the electrons, given by the acceleration voltage V times the electron charge e, is typically between 30 keV and 300 keV. For an acceleration voltage of 80 keV this results in a wavelength of about 4.2 pm, much smaller than the wavelength of visible light and even the typical interatomic distance of a few angstroms in solids. In TEM, diffraction and lens aberrations reduce the possible resolution. However, with today's aberration correctors a spatial resolution in the order of only a few ten picometres is readily achieved [23].

The capabilities of state-of-the-art transmission electron microscopes are not limited to structural investigations, as a variety of spectroscopic and analytical techniques are available to analyse specimen properties such as chemical composition, band structure, bonding information and others [46–48]. TEM is therefore a versatile tool which combines high spatial resolution with analytical imaging techniques facilitating the exploration of structural, chemical and electronic properties of a material.

In transmission electron microscopy, an electron transparent specimen is illuminated by a beam of accelerated electrons which interact with the specimen. The electron beam is generated in the electron gun which consists of the electron emitter itself, two anodes to extract and converge the electrons into a minimum beam cross-section called crossover and an acceleration tube [48]. The acceleration tube enables the acceleration of the extracted electrons to an arbitrary energy and thus determines the wavelength λ of the electrons (Equation 2.1). The image formation is then done by detecting the electrons transmitted through the material. In general, transmission electron microscopy is divided into two operation modes. One operation mode is based on a stationary parallel illumination of the specimen and is called (conventional) transmission electron microscopy ((c)TEM). The other operation mode uses a convergent electron beam which is scanned across the specimen and is called scanning transmission electron microscopy (STEM). Both modes enable atomic resolution but differ in the illumination and detection concepts. As this thesis mostly focusses on STEM imaging, the following fundamentals will describe the STEM imaging mode. The working principles of cTEM imaging can be reviewed elsewhere [48].

2.2 Scanning Transmission Electron Microscopy

In scanning transmission electron microscopy a convergent electron beam is focused onto the specimen and scanned across the specimen in x- and y-direction by the lens system above the specimen. Figure 2.1 a) depicts a sketch of the lens system forming the sharp electron probe in the STEM mode of the microscope. This probe-forming lens system de-magnifies the gun crossover into an atomically sharp electron probe. The first and second condenser lens are used to focus the electron beam. The subsequent condenser lens aperture defines the convergence semi-angle of the electron beam and limits the contribution of lens aberrations due to the cut-off of off-axial rays. In probe-side corrected (S)TEMs the electron beam then enters an aberration corrector which consists of multiple transfer lenses and multipoles to minimize aberrations introduced by the previous lenses. In high-resolution (S)TEM imaging, the spherical aberration, expressed by the spherical aberration coefficient C_s, is typically the resolution limiting factor [49–51]. Hence, these correctors are designed to correct for this higher-order lens aberration and are referred to as C_s-correctors. With modern aberration correction a probe size of only a few picometres is possible, enabling the investigation of the materials atomic structure [52].

A pair of scan coils is then used to scan the electron probe parallel to the optical axis across the specimen in the x- and y-direction. Finally, the aberration corrected electron probe is focused on the specimen using a third condenser lens.

The STEM image formation is obtained in a serial manner by detecting the transmitted electrons which were scattered either in forward direction or to angles (far) off the optical axis.

Since the incident high-energy electrons can interact in different ways with the specimen, a variety of signals is generated. These signals not only enable the investigation of the atomic structure, but also provide information about the chemical composition, bonding states and optoelectronic properties.

Figure 2.1 b) depicts an illustration of the variety of signals generated by electron-matter interaction. It is to mention that in (S)TEM imaging most of the incident electrons pass through the specimen without any interaction with the specimen. These electrons are termed as the direct beam. Only a part of the incident beam electrons interact with the atoms in the specimen, generate different kinds of signals and get scattered. The scattering process results in a change of the electrons travelling direction either with or without energy loss. Therefore, the scattering of an electron in the TEM can be divided into elastic and inelastic scattering.

Elastic scattering arises from the Coulomb interaction of the beam electrons with the positively charged nuclei and the negatively charged electron clouds screening the atomic nuclei. Both interactions with the electrostatic field lead to a scattering of the beam electron without energy transfer but different scattering angles. If the incident electron travels close to an atomic nucleus, the attractive Coulomb force leads to a change in travelling direction of the electron which typically results in high scattering angles. In contrast, if the incident beam electron is elastically scattered under small angles it mostly interacts with the electron cloud of an atom in the specimen. The interaction of the high-energetic

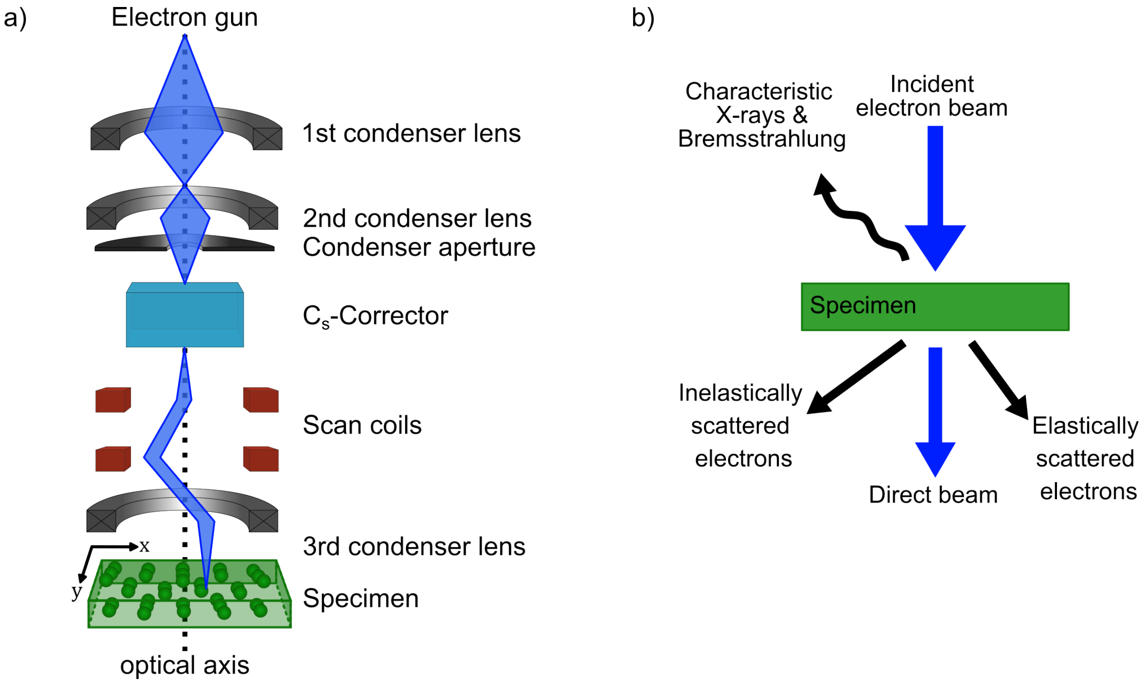

Figure 2.1: a) Sketch of the probe-forming lens system in STEM imaging. b) Illustration of the different signals generated by the interaction of highly energetic electrons of the incident electron beam with the specimen (adapted from Ref. [48]).

beam electrons and the atomic core, screened by its atomic electrons, is typically a complex many-body problem. However, the scattering process can be approximately described using atomic scattering factors [53–56]. The atomic scattering factors describe the strength of the interaction between an electron and an isolated atom and give a measure of the scattering power as a function of the scattering angle [53, 57]. The atomic scattering factor is basically the Fourier transform of the Coulomb potential of the atoms which is related to its spatial charge distribution of the atom and therefore depends on the atomic number Z of the scattering atom. With increasing atomic number the scattering power of an atom increases [58, 59]. In addition, atoms with a high atomic number exhibit a higher scattering power at large scattering angles. Therefore, high-Z atoms scatter more electrons to high scattering angles than atoms with a low atomic number. As the description of the scattering process using atomic scattering factors includes scattering processes with the nuclei and the surrounding electron clouds it can even account for thermal induced lattice vibrations as well as ionization of atoms. These scattering factors are commonly used for STEM image simulations [56]. The atomic scattering factors are therefore important for the explanation of image contrast of different atoms in STEM images.

Scattering processes with both, the nuclei and shell electrons, are elastic but contain different information, which can be explained by the wave nature of the incident electrons. The scattering with the (screened) atomic nucleus is mostly incoherent at high scattering angles. Incoherent scattering means that the scattered electrons do not exhibit a fixed phase relation to the incident electron beam. Contrary to this, scattering at small scattering angles is mainly coherent, and the scattered electrons retain a fixed phase relation.

In contrast to the elastic interaction, the interaction of a beam electron with an inner-shell electron of an atom leads to an energy exchange, which is referred to as inelastic scattering. The high energetic beam electron loses some of its initial energy which is transferred to an inner- or outer-shell electron of the atom, knocking it off and thereby ionizing the atom. As the energy transfer to shell electrons is quantized and thus characteristic for the element, inelastic scattering is the origin of many different signals which are important for analytical investigations. Among these is X-ray emission, for which an atom is ionized by the ejection of an inner-shell electron from the atom due to the interaction with a high energetic beam electron. As a result, the atom is in an excited state. The relaxation to the energetic ground state occurs when an electron of an outer shell fills up the empty state of the inner shell, releasing its excess energy by the emission of an X-ray. The energy of the emitted X-ray is characteristic for the specific shells involved in the process [48, 60].

Complementary to the energy of the characteristic X-ray, the amount of energy the incident beam electron loses due to the ionization of the atom is characteristic to the atomic species involved in this inelastic scattering process. Besides the ionization of atoms, a variety of different inelastic scattering processes can result in an energy loss of the incident electrons which depend on the chemical composition and bonding, the electronic and plasmonic properties as well as the structure of the material [48, 61, 62].

2.3 Wave-optical Picture in STEM

The description of the different scattering processes in the particle picture allows to understand the image formation and the contrast mechanism of STEM measurements using atomic scattering factors. However, the wave properties of the electrons can not be neglected for quantitative STEM analysis. While both, the particle and wave-optical picture, are equally valid, the wave-optical picture provides a more accessible way to explain the phase contrast in STEM imaging. Here, the electron deflection due to scattering with an atom is described by a phase shift of the wave [29]. Thus, the description of the probe and image formation in wave optics are given in the following.

Figure 2.2 depicts a schematic illustration of the probe formation and image formation in STEM imaging. In accordance with Chapter 2.2, the probe-forming lens systems demagnifies the gun crossover and focuses a spherical electron wave onto the specimen. The electron wave Ψ_0 incident on the specimen is affected by the lenses and apertures of the probe-forming lens system which alter the amplitude and phase of the incident wave front as a function of the wave vector $\vec{k}$ with the components k_x and k_y perpendicular to the optical axis (see Chapter 2.2) [63]. Therefore, the resulting transmission function $L(\vec{k})$, representing the probe-forming lens system, includes the aperture function $A(\vec{k})$ and a lens aberration function $\chi(\vec{k})$. The aperture function $A(\vec{k})$ cuts off wave vectors $\vec{k}$ higher than the radius of the condenser lens aperture used and determines the angular distribution of electrons contributing to the electron beam formation. As a result, the aperture function defines the convergence semi-angle α of the incident electron beam, i. e. the maximum polar angle that the electrons in the incident beam travel to with respect to the optical axis (see Figure 2.2) [48]. In total, the incident electron wave $\Psi_0(\vec{k})$ at the real space scan position

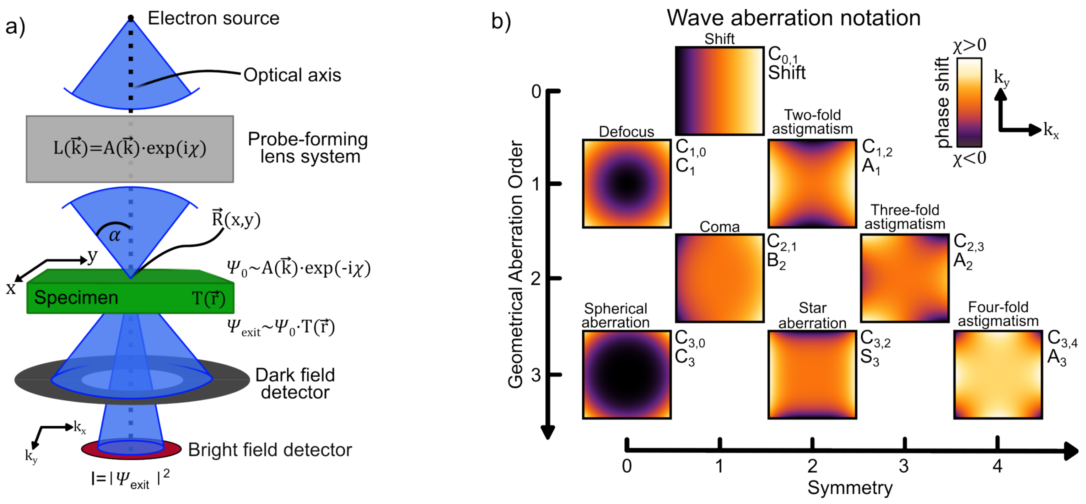

Figure 2.2: a) Schematic description of the STEM image formation in the wave-optical picture (adapted from Ref. [22]). b) Phase plate representation of different lens aberrations up to the third geometrical order. For each lens aberration the aberration coefficients $C_{m,n}$ based on Ref. [22] and [65], and the notation from Ref. [52] are used in this work.

$\vec{R}$ is described by

$$\Psi_0(\vec{k},\vec{R}) = A(\vec{k}) \cdot e^{-i\chi(\vec{k})} \cdot e^{-2\pi i \vec{r}\cdot\vec{k}}, \tag{2.2}$$

where $A(\vec{k})$ is the aperture function and $\chi(\vec{k})$ the lens aberration function [22, 63, 64]. The lens aberration function $\chi(\vec{k})$ describes phase changes which alter the spherical wave front of the electron wave. This function is described by a polynomial of the form

$$\chi(\vec{k}) = \frac{\pi}{\lambda}\Big[\sum_{m,n} \frac{1}{m+n} C_{mn}\bar{\omega}^m \omega^n + \text{c.c.}\Big] \tag{2.3}$$

which includes the aberration coefficients $C_{m,n}$ of the lens aberrations and c.c. indicates the corresponding complex conjugated term [22]. The term ω denotes the complex-valued angle between the incident electron trajectory and the optical axis accounting for the polar and azimuthal direction. It is defined as $\omega = \lambda(k_x + ik_{ky})$ with k_x and k_y being perpendicular to the optical axis. $\bar{\omega}$ is the complex-conjugated angle and the wavelength is given by λ. The lens aberration coefficients $C_{m,n}$ are assigned to a certain symmetry by m and n. The sum of m and n denotes the geometrical order of the lens aberration. Figure 2.2 b) depicts an illustration of the lens aberration for different geometrical order and symmetry given by the aberration coefficients C_{mn} and an equivalent notation introduced by Ref. [52], which are used throughout this thesis. The impact of individual lens aberrations on the incident electron wave is represented in Figure 2.2 b) by phase plates illustrating the phase shift. Depending on the symmetry of the lens aberration present, the ideal point-shaped electron probe is modified by the probe-forming lens system. For example, it receives a non-round shaped intensity distribution for non-rotational symmetric lens aberrations which significantly impact the obtainable STEM image intensity distribution. The correction of lens aberrations is therefore of great importance for the resolution in STEM imaging.

The incident electron wave Ψ_0 interacts with the local specimen potential at each scan position $\vec{R}$. This interaction is described by using a specimen transmission function $T(\vec{r}) \propto e^{i\Delta\varphi}$ which accounts for modifications of the incoming electron wave by phase shifts and amplitude changes $\Delta\varphi$ due to the (inelastic) interaction with the specimen potential [48, 66]. As a result, the post-specimen electron wave Ψ_{exit} is calculated by the multiplication of the incident electron wave Ψ_0 with the specimen transmission function. Usually the interaction of electron wave and specimen is more complex and thus different approximations need to be taken into account for an analytical description and calculation of the exit wave. These approximations are described in more detail in Chapter 2.4.

To obtain a STEM image experimentally and also by simulations, the intensity of the exit wave at each scan position $\vec{R}$ is detected by different kinds of circular or ring-shaped detectors, which differ in their angular collection semi-angles. Theoretically this is described in three steps. First, the intensity distribution $I(\vec{k})$ is calculated by the squared modulus of the exit wave function. Second, the integration of the detector into the wave-optical description of STEM imaging is done by introducing a detector function $D(\vec{k})$. This function describes the extension of the detector defined by inner and outer polar collection angles of the detector. Third, the STEM intensity on the detector is calculated as $\int_{\vec{k}} I(\vec{k})D(\vec{k})d\vec{k}$, i.e. the integration of intensity $I(\vec{k})$ across the detector $D(\vec{k})$ [63, 67]. Depending on the detector collection angles, different contrasts are obtained and thus different information can be extracted (see Chapter 2.2). For conventional STEM imaging two detector types are commonly used, namely bright field and (high-angle) annular dark-field detectors. Both types of detectors are schematically depicted in Figure 2.2 a) and differ in their detector geometry. The bright-field (BF) detector is a disk-shaped detector centred around the optical axis. With a typical collection semi-angle β_{outer} in the range of the convergence semi-angle, these detectors collect the direct electron beam and the electrons coherently scattered under low scattering angles. As BF detectors are located on the optical axis and collect only electrons scattered under low angles, these detectors are often used for imaging of light atoms as the scattering power for these elements is low and results in a small scattering angles of the electrons. The resulting images retain phase-information of the object imaged and are thus of importance for phase-retrieval methods. Conventional high-resolution BF STEM images show the atomic columns as dark spots on a bright background as most of the intensity on the detector comes from the direct beam. Close to

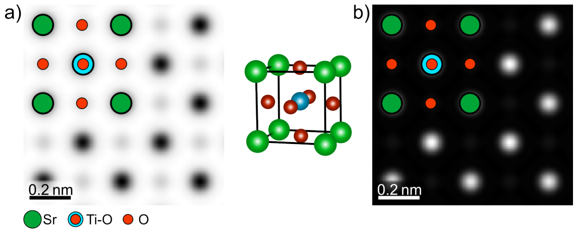

Figure 2.3: High-resolution a) BF- and b) HAADF-STEM image of $SrTiO_3$ with a thickness of one unit cell (t=3.91 Å) in [001] zone-axis orientation. The atomic column position and type are marked by coloured dots in reference to the legend on the bottom. An illustration of a $SrTiO_3$ unit cell is depicted with the same colour code. Information on the simulation are given in Table 9.2.

the atomic columns a small fraction of electrons is scattered out of the detection range by the atoms in the specimen and a reduced intensity is registered by the detector resulting in a darker spot in the corresponding BF image. Figure 2.3 a) shows a simulated BF image of $SrTiO_3$ in [001] zone-axis orientation using the multislice approach and the software Dr. Probe [63, 67]. The atomic column positions and types are exemplarily marked by the coloured dots where red indicates pure oxygen atomic columns, green marked the strontium atomic column and the mixed titanium-oxygen atomic column is indicated by the blue and red dots. The influence of the scattering power of the different atomic columns is visible by the different shades of the different types of atomic columns in Figure 2.3 a): at the positions of the high-Z strontium atomic columns (green dots) a darker spot is visible in the BF image compared to the position of the low-Z oxygen atomic columns (by red dots). High-angle annular dark-field (HAADF) detectors are ring-shaped detectors, which are centred around the optical axis and only collect electrons scattered at high angles. The inner and outer collection semi-angles of this detector type are typically $\beta_{\text{inner}} = 50\,\text{mrad}$ and to $\beta_{\text{outer}} = 200\,\text{mrad}$ [48]. These electrons are mostly incoherently scattered in this range of angles and do therefore not exhibit a fixed phase relation [60, 68]. The resulting HAADF image intensity is thus not determined by interference and therefore is directly related to the atomic column positions and is roughly proportional to the atomic number Z^{x} with x being between 1.2 and 1.8 depending on the detector collection angles but is commonly approximated with x=2 [68–72]. Based on this relation to the atomic number of the scattering atom this imaging technique is called Z-contrast imaging. Due to the increasing atomic scattering factors of high-Z atoms, heavier atoms scatter electrons more effectively under higher angles compared to lower Z atoms and, therefore, the image contrast is related to the projected atomic number of the atomic column [68]. Figure 2.3 b) depicts an HAADF image of $SrTiO_3$ in [001] zone-axis orientation. In contrast to the BF image in a), the atomic columns appear as bright spots on dark background in the HAADF image. However, the general assumed Z^2-dependency is only an approximation. The exact dependency of the image intensity on the atomic number of the atomic column depends on the detection angles as the atomic scattering factors are a function of the scattering angle [60]. Thus, HAADF imaging can contain chemical composition information. However, the differentiation between types of atomic columns is only possible with prior knowledge of the elements within the specimen and specimen thickness and needs to be done with caution as other effects such as electron channelling and the gain and brightness settings of the detector might alter the HAADF image intensity. Instead of the Z^2-dependency, the image intensity typically scales with $\text{Z}^{1.2\text{-}1.7}$ for 3D specimens depending on the material and detector collection angles. This relation is proposed to deviate even more in case of the investigation of 2D materials, where only a few layers or single atoms are imaged [68, 72].

2.4 Phase Object Approximation in STEM

The interaction of the electron beam with the specimen is dominated by the electrostatic potential and is described by the specimen transmission function $T(\vec{r})$. The transmission function introduces the modulation of the incident electron wave by phase shifts resulting from the interaction with the three-dimensional potential. In order to access the resulting electron wave modulation and thereby the resulting STEM image, approximations are needed. In STEM imaging two approximations are commonly used for the interpretation and simulation of image contrast. These two approximations, namely the phase object approximation and the weak phase object approximation, are discussed in the following. In general, the specimen transmission function $T(x, y, z)$ is described by a phase term given by

$$T(x, y, z) = \exp(-i\sigma V(x, y, z) - \mu(x, y, z)) \tag{2.4}$$

where $\mu(x, y, z)$ is the absorption function and σ is the interaction constant defined by $\sigma = m\lambda/2\pi\hbar$. Here, $\hbar$ is the reduced Planck constant, λ is the wavelength and m is the relativistic mass of the electrons [48]. $V(x, y, z)$ is the three-dimensional potential of the specimen. The term $\sigma V(x, y, z)$ therefore describes the phase shift of the incident electron wave induced by the specimen potential [48, 67].

To simplify the specimen transmission function the first approximation assumes a thin specimen that only alters the phase of the electron wave but not its amplitude. Therefore, this approximation is called phase object approximation (POA). Under this assumption the absorption $\mu(x, y, z)$ is neglected, and the three-dimensional potential can be projected into a two-dimensional potential. As the electron passes through the specimen in a certain orientation the image is always a projection along the beam propagation direction (usually defined as the z-direction). The projected potential $V_{\mathrm{P}}(x, y)$ is thus given by the integration of the potential along the z-direction $V_{\mathrm{P}}(x, y) = \int_0^t V(x, y, z)dz$ [67, 73]. In this approximation the specimen transfer function is reduced to

$$T(x, y) \underset{POA}{=} \exp(-i\sigma V_{\mathrm{P}}(x, y)). \tag{2.5}$$

The interaction of the electron wave with the specimen can further be simplified assuming that the thin specimen only consists of weakly scattering atoms. This assumption is then called weak phase object approximation (WPOA) and allows to expand the exponential function into a Taylor series. For a thin, weakly scattering specimen multiple scattering can be neglected and the higher-order terms of the series expansion can be omitted. By this, the modification of the electron wave is linearized to the projected specimen potential [6, 66, 74].

$$T(x, y) \underset{WPOA}{=} 1 - i\sigma V_{\mathrm{P}}(x, y). \tag{2.6}$$

The consequence of the WPOA is a linear relation of the projected potential V_{P} with the phase change of the exit wave $\Psi_{\mathrm{exit}} = \Psi_0 e^{-i\sigma V_{\mathrm{P}}}$ after interaction with the specimen. Therefore, these two approximations simplify the description of the electron-specimen interaction and promote a quantitative modelling of STEM images [73].

However, the WPO approximation is only valid if the sample under investigation meets the necessary requirements of low thickness and weak scattering. As the interaction of the electron wave with the specimen is determined by the scattering power of the atoms, the critical thickness for which the WPOA is still valid depends on the material composition [67].

As atoms with a higher atomic number exhibit a higher scattering power, the maximum thickness for which the approximation is still valid decreases with increasing atomic number. Typically, specimens with a thickness up to about 2 nm fulfil the requirements [4, 7, 36].

2.5 Differential Phase Contrast

Besides the structural analysis using dark-field detectors and the chemical and electronic analysis using electron energy-loss spectroscopy, STEM imaging even enables the measurement of electric and magnetic fields inside the specimen. This advanced STEM imaging technique is called differential phase contrast (DPC) imaging and is based on the information of the sample encoded in the phase change of the electron exit wave [75]. STEM-DPC utilizes differential signals stemming from variations in the phase of the electron wave across the probe to quantitatively measure the electromagnetic fields inside the specimen [4, 12]. DPC has been successfully employed to visualise and measure mesoscopic fields of pn-junctions [12–15], quantum wells [16, 17] as well as magnetic domains [18, 19] and magnetic skyrmions [20]. In combination with today's lens aberration correctors and the resulting increase in resolution in STEM imaging [19, 52], DPC measurements can be performed with sub-atomic resolution which enables to measure atomic electric field distributions [4, 8]. Thus, STEM-DPC is a powerful technique to investigate fundamental electronic properties of a material, giving insights into the correlation between atomic electric field distributions and macroscopic structural and electric properties.

In STEM-DPC, the deflection of the transmitted electrons due to the Lorentz force with the specimen's electromagnetic potential is exploited by evaluating the resulting intensity redistribution using dedicated position-sensitive detectors. This is usually achieved with a segmented or a pixelated detector located on the optical axis mostly recording the coherent bright-field intensity distribution. This accounts for the fact that the deflection of the electrons typically leads to polar angles of only a few microradiants [76–80].

Although there are different types of detectors suitable for DPC imaging the following description is restricted to STEM-DPC with a four-fold segmented detector (Figure 2.4 a) as it is the simplest configuration and among the first by which DPC imaging was achieved. The evaluation of the DPC signal might change slightly depending on the detector and its geometry, however, the physics and basic concept of the signal evaluation remain the same. By calculating difference signals of opposing detector segments (Figure 2.4 a,b), a shift of the BF intensity due to the deflection of the beam caused by the interaction with an electromagnetic field in the specimen can be detected. With an appropriate calibration, the causing fields can be measured quantitatively using STEM-DPC. In general, the DPC signal generation and the corresponding description of the electron deflection arising from the Lorentz force with an electrostatic and/or magnetic field in the specimen have to be divided into two situations, with either a homogeneous or inhomogeneous field distribution across the beam diameter. In the following, both situations are discussed. However, the description here is limited to only electric fields, while the description for magnetic fields is analogous and can be reviewed in Ref. [77]. Thus, the Lorentz force is reduced to its electric component described by the Coulomb force.

In the case of homogeneous electric fields across the electron beam diameter, the interaction of the convergent electron beam with the electrostatic potential can be described by a plate capacitor approximation. Figure 2.4 a) and b) schematically depict the STEM illumination of the specimen and the segmented DPC detector, without and with a mesoscopic electric

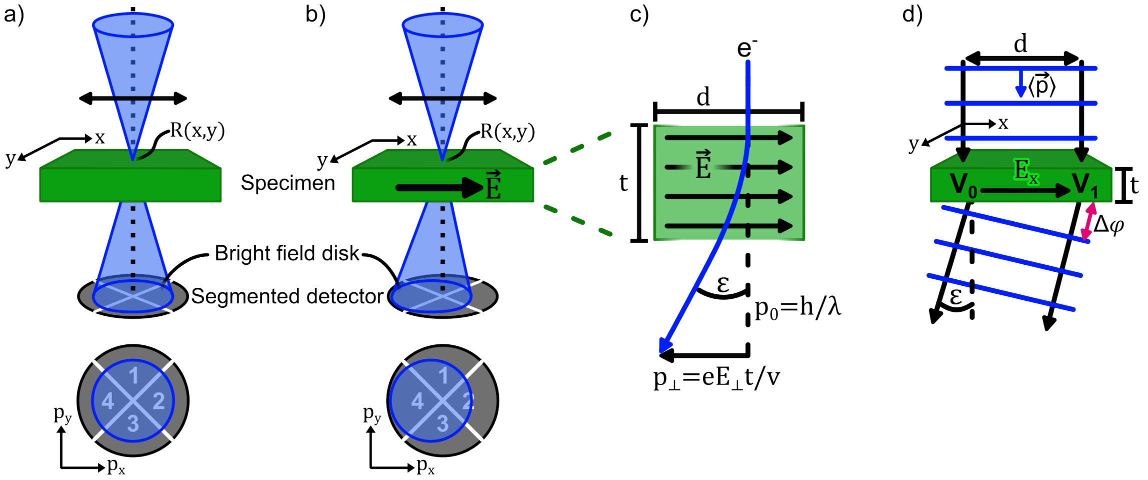

Figure 2.4: Illustration of STEM-DPC imaging of homogeneous electric fields. a) and b) depict the illumination of the specimen and a segmented detector without and in presence of a mesoscopic electric field $\vec{E}$ within the specimen, respectively. The electric field at the scan position $R(x, y)$ leads to a rigid shift of the BF disk on the segmented detector. The directions on the detector are defined by $p_{x,y}$ in the momentum space. The sketch is adapted from Ref. [4, 5, 24] c) Schematic illustration of the plate capacitor approximation of a scan pixel at the scan position $R(x, x)$ in the classical picture of an electron as a particle. The lateral extension of the plate capacitor is given by d and the height of the capacitor corresponds to the specimen thickness t. The incident electron of the electron probe has an initial momentum of $p_0 = \frac{h}{\lambda}$ with h the Planck constant and λ the (relativistic) wavelength of the electron. The Coulomb interaction results in a transfer of momentum $\vec{p}_\perp = \frac{e\vec{E}_\perp t}{v}$ and the electron is deflected at an angle ε. The elementary charge is given by e and the relativistic velocity of the incident electron is denoted by v. The electric field components perpendicular to the electron propagation direction is indicated by $\vec{E}_\perp$. d) Schematic illustration of the transferred momentum $\vec{p}$ in the wave optical description. Here, V_0 and V_1 indicate different potentials in the specimen which causes a phase shift $\Delta\varphi$ of the electron exit wave. This sketch is adapted from Ref. [77].

field $\vec{E}$. The convergent electron beam interacts with the specimen potential at the scan position $R(x, y)$ and is then projected onto the segmented detector. Without a homogeneous electric field, the BF disk of the electron probe is centred on the detector and all detector segments are equally illuminated (Figure 2.4 a). For this situation, a calculation of a signal difference between opposing detector segments results in zero and, thus, no deflection is measured. However, if a homogeneous electric field is present in the specimen, the electrons of the convergent electron probe are deflected by an angle ε due to the Lorentz force. Since the acting force is the same for all electrons in an electron beam with a negligible energy width, the homogeneous field leads to a rigid displacement of the bright field disc in the detector plane which is related to the magnitude of the present electric field (Figure 2.4 b) [4]. This displacement of the BF disk on the detector can be determined by calculating difference signals of opposing detector segments. In the plate capacitor approximation, the deflection angle of the electrons then depends on the specimen thickness t and the electric field magnitude and direction.

Figure 2.4 c) illustrates the plate capacitor approximation. For each scan position $R(x, y)$ of the scanning convergent electron beam the deflection angle can be calculated assuming a homogeneous electric field of a plate capacitor of the height t which corresponds to the specimen thickness. The lateral extension d of the capacitor is equal to the pixel size. The incident electron has an initial momentum $p_0 = \frac{h}{\lambda}$ with h denoting the Planck constant and λ the relativistic wavelength of the electrons. Due to the Coulomb interaction with the electrostatic field a momentum $\vec{p}_\perp = \frac{e\vec{E}_\perp t}{v}$ is transferred and the electron is deflected by an angle ε. $\vec{E}_\perp$ denotes the projected electric field components perpendicular to the incident propagation direction of the electron as only these lateral components contribute to the deflection. The deflection angle ε can then be calculated using the transferred momentum $\vec{p}_\perp$ [78, 81]:

$$\varepsilon = \frac{|\vec{p}_\perp|}{|\vec{p}_0|} = \frac{e \cdot t}{m_0 \cdot v_{\mathrm{rel}}^2} \cdot |\vec{E}_\perp| \quad . \tag{2.7}$$

Here, m_0 and v_{rel} are the rest mass and relativistic velocity of the electron and e is the elementary charge.

To further explain the rigid shift of the BF disk in the detector plane the wave-optical description is used as it readily reveals the relation between the deflection angle and the introduced phase shift of the electron wave. Figure 2.4 d) depicts the wave-optical description of the interaction of the convergent electron beam with the electrostatic field inside the specimen. For the sake of simplicity the description of the interaction of the incoming electron wave with the local specimen potential is limited to an electric field in x-direction, however, it can be generalized to all dimensions using the two-dimensional Nabla operator ∇ for a derivative in x- and y-direction. The incident electron wave is described by a plane wave with the wave front indicated by blue lines in Figure 2.4 d) which extend perpendicular to the propagation direction (indicated by black arrows in Figure 2.4 d). The phase of the electron wave is altered by the electric field inside the specimen caused by a potential difference $\Delta V = V_1 - V_0$ between two points which are separated by a distance d within the specimen. The phase gradient induced by the potential difference inside the specimen can therefore be described by

$$\frac{d\varphi}{dx} = \xi \frac{dV(x)}{dx} \cdot t = \xi E_x \cdot t \tag{2.8}$$

where ξ is an interaction constant given by $\xi = 2\pi \frac{e}{hv}$, $V(x)$ is the potential and E_x the electric field induced by the potential difference [77]. The phase difference between incident and exit electron wave over the distance d is then given by

$$\Delta\varphi = \xi E_x \cdot t \cdot d \quad . \tag{2.9}$$

Notably, STEM-DPC can not measure the phase shift directly as intensities are evaluated. However, the phase gradient $\frac{d\varphi}{dx}$ described in Equation 2.8 is related by Equation 2.7 to the deflection angle ε by

$$\varepsilon = \frac{h}{2\pi p_0} \cdot \frac{d\varphi}{dx} \tag{2.10}$$

using the paraxial approximation $\sin(\varepsilon) \approx \varepsilon$ [77]. Concluding Figure 2.4, the rigid shift of the BF disk resulting from present homogeneous electric fields can be described in the particle as well as in the wave-optical picture. Both show that the deflection angle of the electron probe is linearly related to the electric field which can be either explained by the transferred momentum (particle description) or by the phase gradient (wave description). The atomic potentials of atom in a specimen are, however, not homogeneous across the beam diameter. This is particularly the case when DPC imaging is combined with state-of-the-art lens aberration correction, as electron beam diameters smaller than the Bohr radius ($a_0 = 52\,\mathrm{pm}$) are readily achieved. This enables to probe the electric field between the (screened) atomic nuclei and the electron clouds [5, 8, 24, 80].

However, as the beam electrons experience a varying electric field, this results in a redistribution of intensity within the BF disk, which exhibits a pronounced inner structure. Still, the magnitude of intensity redistribution depends on the relative position of the electron beam within the inhomogeneous electric field and thus the causing electric field can be deduced as described in the following.

Figure 2.5 schematically illustrates the imaging of atomic electric fields using DPC. If the electron probe is far away from an atom during the scanning, the electrons within the electron beam do not experience the atomic electric field and the BF disk with homogeneous intensity distribution is centred on the segmented detector (Figure 2.5 a). Notably, the BF disk in Figure 2.5 a) is only a simplified representation of the BF intensity distribution during STEM-DPC imaging at atomic resolution. When analysing crystalline specimens with a finite thickness, the BF disk at atomic resolution typically exhibits a rich inner structure of intensity variations due to (dynamical) diffraction, such as electron (multiple) scattering, influenced by the specimen thickness and tilt as well as probe parameters [4, 5]. During scanning, the sharp electron probe comes close to a nucleus and penetrates the atoms electron cloud surrounding and screening the positively charged nucleus. Depending on the position to the atomic nucleus, the attractive Coulomb force between the

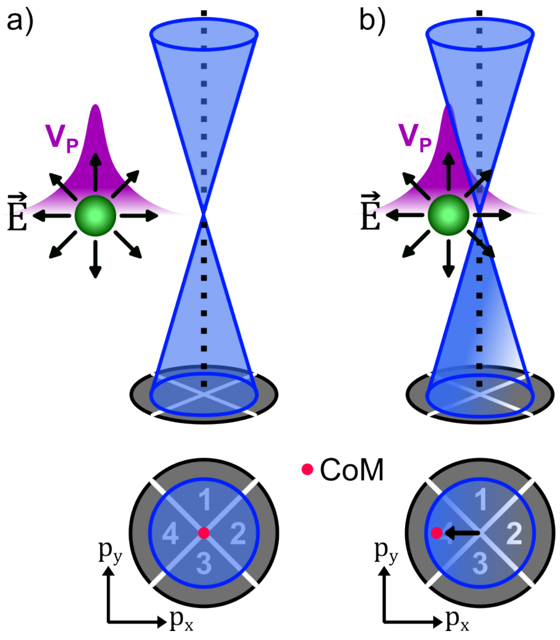

Figure 2.5: Schematic illustration of the intensity distribution within the BF disk when the electron probe is a) far away from an atom or b) is close to an atom. An illustration of the projected atom potential V_P is indicated by purple curve. The centre-of-mass (CoM) of the intensity distribution on the detector is indicated by the pink dot.

not-fully-screened positively charged nucleus and the beam electrons leads to an intensity redistribution within the BF disk with preferential direction towards the nucleus [4–6, 8]. This situation is illustrated in Figure 2.5 b): If the electron probe is located to the right of an atom the Coulomb interaction leads to an increased intensity on the left of the detector and a reduced intensity on the opposite side. Thus, the atomic electric fields do not lead to a shift of the BF disk on the segmented detector but to a complex intensity redistribution. However, the DPC signal can still be accessed by the shift of the centre of mass (CoM) of the intensity distribution indicated by the pink dot in Figure 2.5.

In accordance with the wave-optical description of STEM imaging introduced in Chapter 2.3, the incident electron wave can be defined by a wavefunction $\Psi_0(\vec{p})$ with $\vec{p}$ a vector of the momentum space related to the real space coordinate $\vec{r}$ by a Fourier transform. The electron wave interacts with the electric field $\vec{E}$ of the specimen stemming from varying specimen potentials $V(\vec{r})$ in the specimen which are related to the electric field by $\vec{E}(\vec{r}) = -\nabla\vec{V}(\vec{r})$. Using the WPOA, the electron wave experiences a phase shift $-i\sigma V_P$ introduced by the interaction with the projected potential V_P [28]. The modified electron wave after the interaction within this approximation is described by $\Psi_{\text{exit}} = \Psi_0 e^{-i\sigma V_{\text{P}}}$ (Chapter 2.4). In contrast to the illustrated deflection of the phase front in homogeneous electric fields illustrated in Figure 2.4 d) the phase shift is neither constant nor linear over the beam diameter but exhibits a curved phase front of the exit wave. As a result an intensity redistribution in the detector plane can be observed depending on the beam position on the specimen [28].

To quantitatively relate this complex intensity redistribution on the detector to the causing atomic electric fields Müller et al. proposed a quantum mechanical approach [4]. Using the Ehrenfest theorem, which links the quantum mechanical expectation values to the classical equations of motion, the expectation value of the momentum transfer $\langle\vec{p}_\perp\rangle$ can be related to the expectation value of the projected electric field $\langle\vec{E}_\perp\rangle$ at the scan position $\vec{R}$ by

$$\langle\vec{E}_\perp\rangle(\vec{R}) = -\frac{v_{\text{rel}}}{e\cdot t}\cdot\langle\vec{p}_\perp\rangle(\vec{R}) \tag{2.11}$$

with e as the electron charge, v_{rel} as the relativistic velocity and t the specimen thickness [4, 7]. The quantum mechanical expectation value of the momentum $\langle \vec{p}_{\perp} \rangle$ is given by

$$\langle \vec{p}_{\perp} \rangle = \int \vec{p}_{\perp} I(\vec{p}_{\perp}) dp_{\mathrm{x}} dp_{\mathrm{y}} \tag{2.12}$$

where $I = \Psi^*_{\mathrm{exit}} \Psi_{\mathrm{exit}}$ is the intensity distribution of the exit wave Ψ_{exit} in the detector plane and the subscript $\perp$ indicates the x- and y-components perpendicular to the incident propagation direction [4, 7]. Equation 2.12 represents a centre-of-mass calculation of the lateral momentum $\vec{p}_{\perp}$ weighted with its probability density given by the intensity distribution $I(\vec{p}_{\perp})$. It therefore reduces the detailed intensity distribution of the BF disk into an average momentum [4]. Therefore, the expectation value of the transferred momentum $\langle \vec{p}_{\perp} \rangle$ can be experimentally accessed by calculating the shift of the centre-of-mass of the post-specimen intensity distribution in the detector plane [4, 7]. This shift of the CoM corresponding to the average momentum transfer $\langle \vec{p}_{\perp} \rangle$ can be related to the projected electric field $\langle \vec{E}_{\perp} \rangle$ inside the specimen using Equation 2.11. Therefore, recording the intensity distribution in the diffraction plane using a suitable detector enables the quantitative measurement of inhomogeneous electric fields for which no rigid deflection of the bright-field disk is observed, even with a spatial resolution at the sub-atomic level.

It is important to note that Equation 2.11 is only valid under the WPO approximation which reduces the three-dimensional electric field inside the specimen to a projection along the beam propagation direction. Thus, any beam broadening or propagation inside the specimen is neglected [7]. As beam broadening is a function of specimen thickness, this approximation only holds for thin and weak scattering specimens with a thickness of about less than 2 nm (Chapter 2.4) [28].

Furthermore, the projected electric field distribution inside the specimen measured with STEM-DPC allows to derive a projected charge density. Using Maxwell's equation, the overall charge density ρ of protons and electrons can be calculated by

$$\rho = \epsilon_0 \cdot \nabla \cdot \vec{E}_{\perp} \tag{2.13}$$

with ϵ_0 being the vacuum permittivity and ∇ the two-dimensional Nabla operator. Since the derived electric field is convolved with the electron probe, the same holds for the charge density.

Hence, the derived STEM-DPC images are sensitive to different microscope- and specimen-related parameters, such as lens aberrations and probe parameters [26, 82–84].

Up to now in this description, no assumptions have yet been made about the detector. Equation 2.12 describes the calculation of the centre of mass using an integral that sums up the intensity weighted by the momentum in infinitesimal steps in momentum space. However, to experimentally access the detailed intensity distribution and to enable a CoM determination, a position-sensitive detector is needed [5, 77, 85]. This detector in the diffraction plane can either be a pixelated or segmented detector which both are located on the optical axis but consist of a different number of segments. The pixelated detector is similar to a camera that consists of a reasonably large number of pixels to record the full intensity distribution at each position of the scan. For this detector type the integral expression of the CoM calculation in Equation 2.12 can be replaced by a summation over the number of pixels.

Segmented detectors are circular or annular round shaped detectors which typically consist of four to 16 segments split into quadrants. Due to the reduced number of segments compared to the pixelated detector, segmented detectors exhibit a reduced momentum space resolution and only give an approximation of the CoM as the intensity distribution of the BF disk within a segment cannot be evaluated.

In the theoretical description, the type and shape of the detector is included by a detector response function which describes the way the detector intersects the intensity distribution in momentum space and thus collects the intensity. For a segmented detector the detector response function $D_\alpha(\vec{k}_\perp)$ is given by

$$D_\alpha(\vec{k}_\perp) = \begin{cases} k_{\alpha,i}^{CoM} & \text{for } \vec{k}_\perp \text{ within the i-th segment} \\ 0 & \text{otherwise} \quad , \end{cases} \tag{2.14}$$

where α denotes the x or y components and $k_{\alpha,i}^{CoM}$ denotes the α component of the geometrical centre of mass of the i-th detector segment [5, 86]. The wave vector $\vec{k}_\perp = (k_x, k_y)$ is related to the transferred momentum by the de-Broglie equation $\vec{p}_\perp = \hbar\vec{k}_\perp$. The DPC signal $I_\alpha(\vec{R})$ acquired using a segmented detector is then given by

$$I_{\mathrm{DPC},\alpha}(\vec{R}) = \sum_i \Big[\int \tilde{I}(\vec{k}_\perp, \vec{R}) D_\alpha(\vec{k}_\perp) d\vec{k}_\perp \Big] = \sum_i k_{\alpha,i}^{CoM} \tilde{I}_i(\vec{R}). \tag{2.15}$$

where $\tilde{I}_i(\vec{R})$ indicates the intensity detected by the i-th detector segment [5, 86]. The detector response function is of great importance for the interpretation and quantitative analysis of DPC images. However, not only the detection of the intensity is of interest for quantitative DPC imaging but more important the transfer of the phase information by the detector. Therefore, the (phase) contrast transfer function ((P)CTF) describes how the phase information is related to the detected intensity and therefore describes the accuracy of the derived electric fields. The CTF of segmented detector is in contrast to the CTF of pixelated detectors not isotropic but exhibits an anisotropic behaviour due to the segmentation of the detector, which means that the sensitivity to measure the CoM is influenced by the direction of the CoM shift. Depending on the segment geometry, the number of segments and their orientation, an anisotropic transfer of phase information for certain directions is observed [28, 86, 87]. In general, the CTF $\mathcal{T}(\vec{K})$ is given by

$$\begin{aligned} \mathcal{T}(\vec{K}) =& i \cdot \int A(\vec{k}_\perp) D(\vec{k}_\perp) \big[A(\vec{k}_\perp - \vec{K}) \exp\{-i\chi(\vec{k}_\perp - \vec{K}) + i\chi(\vec{k}_\perp)\} \\ & - A(\vec{k}_\perp + \vec{K}) \exp\{i\chi(\vec{k}_\perp + \vec{K}) - i\chi(\vec{k}_\perp)\} \big] d\vec{k}_\perp \end{aligned} \tag{2.16}$$

with the detector response function $D(\vec{k}_\perp)$ given for a segmented detector in Equation 2.14 and the spatial frequency of the scan position $\vec{K}$ [86]. The CTF is further influenced by the incident electron probe described by the aperture function $A(\vec{k}_\perp)$ and the lens aberration function $\chi(\vec{k}_\perp)$ [28, 86]. Thus, the CTF varies with the experimental setup, illumination conditions, and present lens aberrations. To illustrate the mentioned anisotropy in the CTF of a segmented detector, Figure 2.6 a) depicts an exemplary representation of a CTF of an eight-fold segmented detector as illustrated in Figure 2.7 b). The calculation is adapted from the work of Bekkevold et al., who provide an interactive Python script for the calculation of the CTF of segmented detectors for different detector and probe parameters [88]. Further details on the parameters used for the calculation of this CTF are given in the Appendix 9.1. Figure 2.6 a) shows the anisotropic contrast transfer of an eight-fold segmented detector with a cross-like feature of high contrast transfer in the centre of the image with tips parallel to the k_x- and k_y-directions (yellow pixels in Figure 2.6). This indicates a high contrast transfer for spatial frequencies along these directions whereas for spatial frequencies at 45° to these directions a reduced contrast transfer indicated by the more orange pixel colour is observed. Thus, the contrast transfer of an eight-fold segmented detector exhibits a certain symmetry influencing the resulting electric field distribution obtained by STEM-DPC. Overall, the CTF decreases from the centre of the image which corresponds to small spatial frequencies to the edges indicating high spatial frequencies. Unlike to a segmented detector, the CTF of a pixelated detector depicted in Figure 2.6 b) shows an isotropic contrast transfer in all directions, gradually decreasing from the centre. To illustrate the signal generation and the calculation of DPC images using a segmented detector, Figure 2.7 depicts a STEM-DPC image simulation of strontium titanate (STO) in [001] zone-axis orientation. The simulation is done using the multislice approach explained in the following Chapter 2.6 and shows the HAADF image and the intensity on individual segments of the outer "Layer" of an eight-fold segmented detector (sketched in the centre of Figure 2.7). Based on the HAADF image, the atomic structure of STO in [001] zone-axis orientation is identified and atomic column positions are exemplarily marked by the coloured circles.

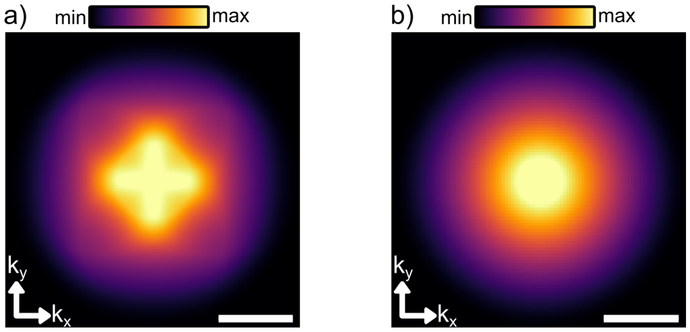

Figure 2.6: (Phase) Contrast transfer function of a) an eight-fold segmented detector and b) a pixelated detector. The scalebars correspond to 0.7 Å^{-1}.

The HAADF image only shows bright intensities for the strontium atomic columns and the mixed titanium and oxygen columns, but the pure oxygen columns are not visible. This is due to the weaker scattering power of the light-Z oxygen atomic columns at high angles compared to the high-Z Sr and Ti atomic columns as explained in Chapter 2.2 [8]. The different segments $S_{5\text{-}8}$ of the outer Layer of the segmented detector show images with

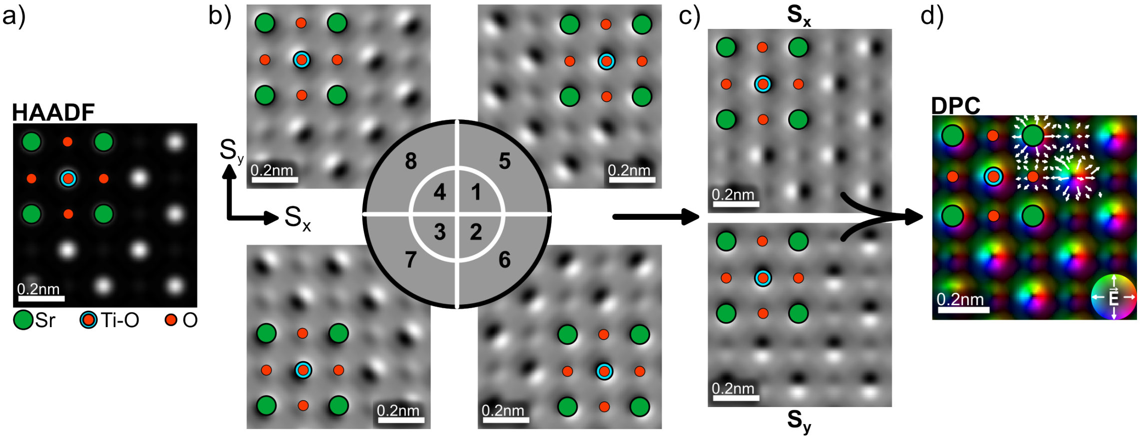

Figure 2.7: STEM-DPC Multislice image simulation of a STO specimen in [001] zone-axis orientation which has a thickness of one unit cell. a) shows the HAADF image acquired with the high-angle annular dark-field detector. b) shows a sketch of an eight-fold segmented detector and depicts the images derived from the outer segments 5 to 8. c) Difference signals obtained from the outer segments in x- and y-direction. d) Colour-coded DPC image which represents a map of the electric field distribution. The atomic column positions are marked by green, red and blue dots for Sr, O and Ti atomic columns, respectively. The simulation parameters can be reviewed in Table 9.2. A unit cell of STO is shown in Figure 2.3.

different intensity distribution (Figure 2.7 b) which are dominantly visible close to the atomic column positions. These differences arise due to the intensity redistribution within the BF disk when the electron beam is close to an atomic column. By calculating the signal difference of opposing detector segments pixel by pixel, the difference signals denoted as $\mathrm{S_{x,y}}$ in Figure 2.7 c) can be obtained. Depending on the number of segments and the geometry of the segmented detector different approaches are used to calculate the difference signals. For segmented detector with a comparable geometry as depicted in Figure 2.7 b) the difference signals can be calculated in a bisected way using

$$S_{x,y} = \frac{S_5 \pm S_6 - S_7 \mp S_8}{S_5 + S_6 + S_7 + S_8} \tag{2.17}$$

which is a common approach for accessing homogeneous electric fields by STEM-DPC [16, 77, 78]. The electric field maps can then be calculated by the pixel-wise vectorial superposition of the two difference signals $\mathrm{S_x}$ and $\mathrm{S_y}$ using a calibration factor to relate the Signals $\mathrm{S_{x,y}}$ to a deflection angle ε or transferred momentum $\vec{p}_\perp$ and the specimen thickness. The determination of calibration factors based on the evaluation of diffraction patterns of crystalline materials with known scattering vectors is described in detail in Ref. [84]. The result is a colour coded DPC image which represents the projected electric field distribution within the specimen (Figure 2.7 d). This electric field map indicates the direction of the projected electric field by a colour, the magnitude of the electric field by the saturation of the respective colour. For reference, a so-called colour wheel depicted in the bottom right of the image is used to assign the colours to the field vectors. Else, the electric field can also be represented by a vector map which is partially plotted on top of the DPC image and marked by the white arrows.

The DPC image reveals rotational symmetric electric field distributions around each individual atomic column position. The electric field always points away from the positively charged nucleus. This is expected as the deflection is dominated by the (screened) positively charged atomic nuclei of the atomic columns [4, 5, 24]. In contrast to the HAADF image in Figure 2.7, the DPC image not only reveals the high-Z atomic columns but rotational symmetric electric field distributions are also observed at the position of the pure oxygen atomic columns (indicated by the red dots in Figure 2.7) which highlights the capability of STEM-DPC to measure light and heavy atoms simultaneously [6, 8].

2.6 Multislice STEM Image Simulation

High-resolution STEM images, particularly high-angle annular dark-field images, can qualitatively be interpreted intuitively due to the Z-contrast. The quantitative interpretation of STEM image contrast in general and the quantitative interpretation of STEM-DPC images in particular is more complex as it is rather sensitive to the imaging parameters such as unavoidable lens aberrations (Chapter 2.2 and 2.5). Therefore, image simulations are necessary to correctly interpret DPC images and identify subtle differences due to lens aberrations. Within this work, the image simulations are done using two different programs which both rely on the multislice algorithm. The first simulation software is called “Dr. Probe” and was implemented by J. Barthel [63]. The second software package is called “abTEM” and was designed by J. Madsen and T. Susi [89]. Both simulation programs aim to calculate high-resolution (S)TEM images of arbitrary crystal structures using the multislice algorithm, but they differ in the atomistic modelling methods and the implementation of atomic potentials. In the following, the basic principle of the multislice algorithm and the STEM image simulation are discussed. Differences between the two open-source simulation programs are then discussed with respect to the different approaches for the atomic potentials.

In general, an incident electron wave interacts with the crystal structure of the three-dimensional crystal in different ways by elastic and inelastic scattering. These scattering processes are caused by the Coulomb interaction with the atoms in the specimen and lead to a deflection of the incident electron (Chapter 2.2). In the wave-optical description such a deflection of electrons corresponds to a phase shift of the incident electron wave. Furthermore, depending on the thickness of the material multiple scattering may occur which results in a complex beam-specimen interaction. The incident electron wave interacts with the first layer of atoms, is diffracted and transmitted and then interacts with the subsequent atomic layer following in direction of propagation [63, 67, 89]. The simulation of these processes in a three-dimensional system is complex. To numerically simplify and describe the interaction of the electron wave with the specimen the multislice algorithm is often used for STEM image simulations. Analogous to Chapter 2.2, the simulations are done using the wave-optical description. The multislice algorithm divides the three-dimensional electrostatic potential of the specimen into multiple thin slices along the beam propagation direction and, therefore, reduces the description to a set of two-dimensional potential slices (Figure 2.8). Each two-dimensional slice j with a thickness $t(j)$ contains the

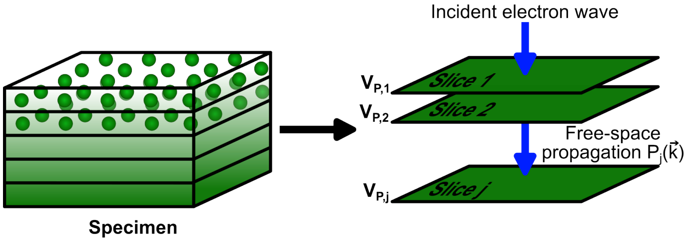

Figure 2.8: Illustration of the multislice approach which shows the decomposition of the 3D specimen in j potential slices with a projected potential $V_{\mathrm{P,j}}$.

projected potential $V_{\mathrm{P,j}}$ of the atoms within this slice. The projected potential is calculated by calculating the infinite integral $V_{\mathrm{P,j}}(\vec{r}) = \int_{-\infty}^{+\infty} V_{\mathrm{j}}(x, y, z)dz$. Thus, the whole atomic potential is projected into a slice of thickness $t(j)$ and contributions from atoms of other slices extending to the current slice are neglected [63, 89]. In addition, abTEM allows a finite integral to be taken only along the slice thickness $t(j)$. However, the contributions of atoms in previous or subsequent slices are not considered. Although the finite projection of atomic potentials is more accurate, only the infinite projection is used to ensure comparable simulations from abTEM with Dr. Probe.

The interaction of the incident electron wave with the j-th slice of the specimen is then described using a transmission function $T_{\mathrm{j}}(\vec{r}) = \exp(i\sigma V_{\mathrm{P,j}}(\vec{r}))$ with which the impinging wave is multiplied. Here, σ represents the interaction constant already introduced in Chapter 2.4. Thus, each slice introduces a phase shift to the electron wave which is related to the projected potential of the slice by the WPOA described in Chapter 2.4 [67]. The exit wave of the j-th slice is then propagated to the (j+1)-th potential slice by using a Fresnel free-space propagator $P_{\mathrm{j}}(\vec{k})$ [63, 67, 89]. These two processes, the scattering with a slice described by the transmission function and the subsequent propagation, are iteratively repeated until the desired specimen thickness is reached [67].

For the final image simulation, various detectors can be implemented, which are characterised by polar and azimuthal angle ranges. The intensity in the detector plane is calculated and recorded for each scan position of the simulated electron beam, based on the exit wave calculated by the multislice algorithm.

The multislice algorithm is a straight-forward description of the interaction between the electron wave and the specimen. Although the iterative process of the algorithm is always the same, there are different approaches for the calculation of potentials. The first approach is the so-called independent atom model (IAM) which simplifies the calculation of the specimen potential by assuming isolated single atoms. By this, the specimen consists of a set of independent atoms and any charge redistribution due to bonding effects is neglected [67, 89, 90]. The specimen potential is calculated as a superposition of spherical symmetrical atomic potentials [67, 89, 90]. This approximation is suitable for high-angle scattering as the scattering process is dominated by the atomic nucleus. However, the asymmetry of the atomic potential due to bonding effects is not considered. Thus, the influence of bonding, which becomes important for low-angle scattering used in DPC imaging, is not included in the IAM-based potentials.

The second approach to calculate the specimen potential is using the density functional theory (DFT), which is based on the more accurate calculation of the specimen potential using the exact electron density.

In general, DFT solves the problem of the theoretical description of the materials electronic structure for interacting many-particle systems commonly of interest in solid state physics and chemistry. With the work of P. Hohenberg and W. Kohn in 1964 the fundamental concept of DFT was presented by introducing a functional of the electronic charge density, which fully describes the energetic ground state of the system, thus eliminating the necessity of solving the Schrödinger equation for N electrons [91, 92]. By this, the system is fully characterized by the electron density without using any approximations, however, the form of this energy functional of the electron density is unknown. Thus, a central part of DFT is to find a suitable expression. Especially, the correct description of the exchange-correlation energy, which accounts for any quantum mechanical effects of an interacting many-electron system, e. g. Pauli exclusion principle, is challenging [92]. A route to solve for the charge density was introduced by Kohn and Sham with a set of self-consistent equations which include the exchange and correlation effects in an approximated way by assuming an auxiliary non-interacting system with the same ground state energy as the interacting system [92, 93]. By this the N-particle problem is simplified to N single-particle equations [93, 94]. With the work of Hohenberg, Kohn and Sham, the theoretical framework is given to describe the electronic density and by this the whole system, however, approximations are needed to describe inhomogeneous charge distributions such as in the vicinity of atomic nuclei.

Among the variety of different numerical methods to solve these equations accurately is the (grid-based) projector augmented-wave ((G)PAW) method introduced by Blöchl [95]. This approach aims to describe the different regions of charge density of an atom by introducing smooth auxiliary wavefunctions to accurately describe the high density close to the atomic nuclei as well as the bonding regions between atoms [95, 96]. The PAW approach combines different wavefunctions for the different regions and, therefore, numerically describes the bonding region and the region near the atomic nucleus. This approach uses pseudo-potentials where the all-electron information is restored but the singularity at the atomic core is approximated by a cut-off radius [96]. A detailed description of the PAW method and the implementation is beyond the scope of this work and the reader is referred to Ref. [95, 96] for more details.

With the theoretical framework given by DFT and the implementation to solve for the electron density by the (G)PAW method, the DFT-based potentials include possible charge redistribution due to bonding. Therefore, using DFT potentials allow for a highly accurate simulation of (S)TEM images including scattering effects due to charge redistributions and bonding effects. Thus, the accuracy of (S)TEM image simulations benefit from the detailed description provided by DFT calculations. However, compared to the IAM-based simulations, the DFT-based simulations are computational intensive and not always necessary in terms of imaging sensitivity of STEM imaging. A detailed description of the integration of GPAW to the STEM image simulation software abTEM is given in Ref. [89].

2.7 2D Transition Metal Dichalcogenides

Among the variety of 2D materials, transition metal dichalcogenides (TMDs) comprise their own material family which exhibits interesting layer-number dependent optoelectronic and electrical properties [31–33]. Unlike many other 2D materials, such as graphene with a zero band gap [97–99] or boron nitride with indirect band gap [98, 100], TMD monolayers have a direct band gap E_g in the visible range ($E_\mathrm{g} = 1 - 2\,\mathrm{eV}$) [101, 102] which decreases with increasing number of layers and changes into an indirect band gap for the bulk TMD [103–105]. Besides by the number of layers, the band gap of TMDs can further be tuned by stacking of layers into homo- and heterostructures [106–108], by strain [109–111] and by applying external electric fields [112]. In combination with their semiconducting properties and inherently low thickness, they are promising candidates for future optoelectronic devices, such as ultra-thin photodetectors and transistors [32, 113–118].

Unlike graphene or boron nitride, monolayers of TMDs with the stoichiometric formula $\mathrm{MX_2}$ consist of three covalently bonded atomic planes rather than one. In these materials, the transition metal atomic plane (e.g. Mo, Ti, W) is sandwiched between the two chalcogenide atomic planes (e.g. S, Te, Se). Figure 2.9 shows the top and side view of the crystal structure of a TMD monolayer, exemplified by the TMD tungsten diselenide ($\mathrm{WSe_2}$). Figure 2.9 a) depicts the lattice structure in [0001] orientation showing the hexagonal arrangement of atoms which, for tungsten diselenide leads to alternating selenium (green spheres) and tungsten (grey spheres) atomic columns. The lattice constant a, indicated by black arrows in Figure 2.9 a), is equal to 0.329 nm [119, 121]. Figure 2.9 b) shows a $\mathrm{WSe_2}$ monolayer in [$1\bar{1}00$] orientation, which corresponds to a side view showing the triatomic structure of the monolayer, with one tungsten atomic plane enclosed between two selenium atomic planes. Similar to other 2D materials, the bulk crystals of TMDs consist of these triatomic monolayers stacked on top of each other and only bonded by weak van der Waals (vdW) interaction [98]. The lattice constant c of bulk unit cell of $\mathrm{WSe_2}$ is 1.298 nm and contains a bilayer which results in a reduced lattice constant of about $\frac{c}{2}$ =0.65 nm for $\mathrm{WSe_2}$ monolayers. The Se-Se distance in a $\mathrm{WSe_2}$ monolayer amounts to 0.33 nm. The additional space in the cell of a monolayer accounts for the vacant space when stacking TMD monolayers into multilayer and bulk systems.

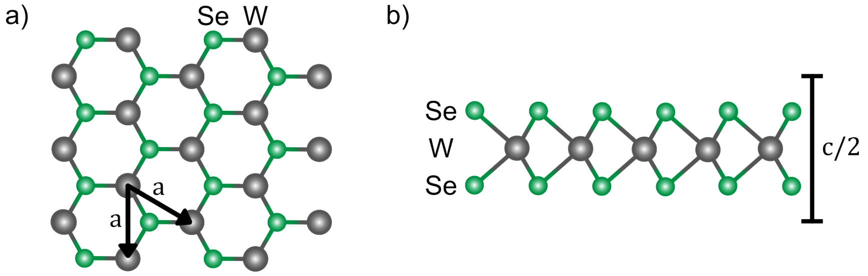

Figure 2.9: Schematic illustration of the $\mathrm{WSe_2}$ crystal structure in a) top view and b) side view of a monolayer. The orientations are [0001] and [$1\bar{1}00$], respectively. The lattice constants of $\mathrm{WSe_2}$ are a = 0.329 nm and c = 1.298 nm [119–121]. Selenium atoms are indicated by green and tungsten atoms are marked by gray spheres.

2.7.1 Stacking Configurations of TMDs

The electronic and optical properties of TMDs change depending on the number of layers stacked on top of each other, which provides the opportunity to adjust physical properties such as band structure [122, 123] and band gap energy [102]. The monolayer of WSe_2 shows a direct band gap of 1.6 eV. With increasing number of stacked layers the band gap becomes indirect with a reduced band gap energy of about 1.2 eV [102]. In addition to the number of layers, the stacking order of the layers also influences the materials properties [122–124]. Due to the weak interlayer interactions, different high-symmetry stackings of two or more TMD layers are possible which differ in the order of atoms along the *c*-axis of the crystal lattice and change the interlayer distances [124–126] as well as the excitonic response [123, 127]. The different stacking of the individual monolayers alters the optoelectronic properties such as the band gap energy [125, 126] as well as the charge carrier mobility [128]. Figure 2.10 illustrates the five possible high-symmetry stacking configurations of TMD bilayers. The nomenclature is adapted from Ref. [129] and is consistently used within this thesis.
The first two stacking configurations in Figure 2.10 a) and b) retain the hexagonal structure in the top view but differ in the stacking sequence of atoms along the *c*-axis direction.
For the AA stacking configuration, metal and chalcogenide atoms of the first layer are aligned with the same type of atoms in the second layer which results in atomic columns consisting either purely of metal atoms or purely of chalcogenide atoms.
In the AA' stacking configuration, the two monolayers are rotated by 60° to each other which leads to a different stacking of atoms. The metal atoms of one layer are now aligned with the chalcogenide atomic column of the other layer which results in atomic columns consisting of both atomic species (Figure 2.10 b)).
In addition, a lateral displacement of one layer with respect to the other results in three more stacking configurations called AB', AB and A'B. In top view, atoms are located within the centre of an upper or lower atomic hexagon. These three stacking configurations exhibit a different alignment of atoms along the c-axis (indicated by the three differently dotted and dashed lines in the side view). For the AB' stacking shown in Figure 2.10 c), this stacking results in atomic columns either consisting of four selenium atoms or a single tungsten atom. Contrary, the AB stacking configuration exhibits pure selenium and pure monoatomic tungsten atomic columns as well as mixed atomic columns containing one tungsten and two selenium atoms (Figure 2.10 d). The A'B stacking configuration consists of pure tungsten atomic columns containing two tungsten atoms and selenium atomic columns consisting of two selenium atoms. Even though the five stacking configurations consist of the same type of atoms and number of layers stacked on top of each other, these configurations differ in their stability. Due to the weak vdW interaction and electrostatic interaction between the layers, the AA' and AB stacking configuration are energetically the most stable configurations [124]. The other stacking configurations exhibit a significantly higher total energy and are therefore less stable and less frequently naturally observed [124]. The different configurations also exhibit different structural, optical and electric properties [124]. Not only the interlayer distance changes but also the band structure and the band gap as well as the interband transitions are altered by the different stackings [124, 126, 127, 130,

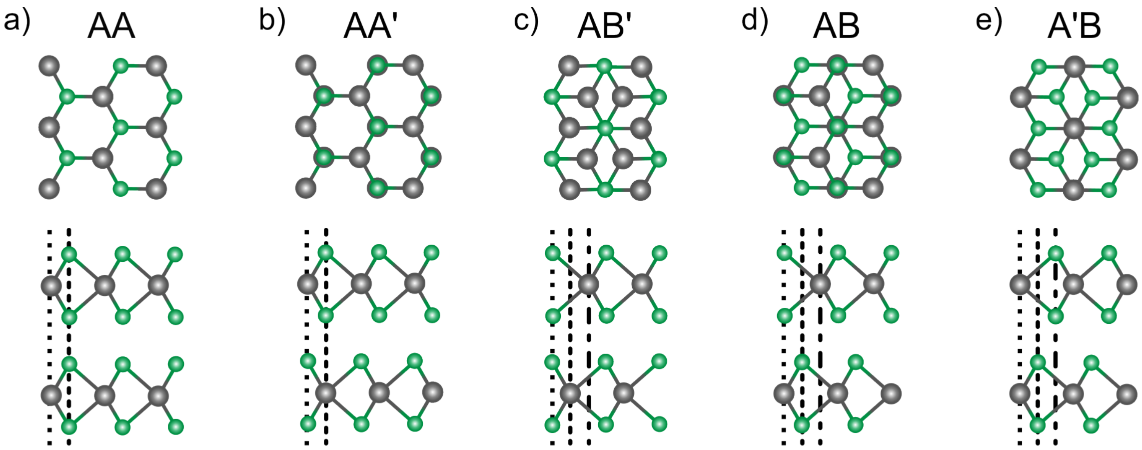

Figure 2.10: Different stacking configurations of a TMD bilayer in top (upper panel) and side (bottom panel) view denoted in accordance to Ref. [129]. The configurations are illustrated for WSe_2, but the same applies for other TMDs. Green spheres are used to denote the chalcogenide atoms (e.g. Se, Te, S), whereas grey spheres are used to indicate the transition metal atoms (e.g. W, Ti, Mo).

131]. Furthermore, the stacking of TMDs influences the non-linear optical properties as the symmetry of the system changes [127, 132]. By reducing the TMD thickness to a monolayer, the inversion symmetry of AA'-stacked TMDs is broken resulting in a strong non-linear optical response, e. g. to a strong second harmonic generation in MoS_2 monolayers [132, 133].

Vertical stacking of monolayers of TMDs is not only limited to the high-symmetry stacking of layers of the same material, as shown in Figure 2.10. Layers of different TMDs can also be artificially stacked with arbitrary orientation, enabling a versatile platform for new 2D heterostructures with tunable optoelectronic properties [131, 134]. Due to the weak vdW interaction between the layers these heterostructures exhibit atomically sharp interfaces without the constraints of lattice mismatch known for conventional semiconductor heterostructures. In addition to the stacking of layers, the rotational alignment of the layers offer another degree of freedom to tailor the optoelectronic properties by the twist angle between the layers. Therefore, these so-called Moiré structures and vdW heterostructures are currently highly investigated and potential material systems for future optoelectronic heterostructure nanodevices [108, 135, 136].

2.7.2 Defects in 2D TMDs

The potential device performance as well as the electronic and optical properties of TMD monolayers are strongly influenced by defects in the crystal structure [137–139]. Due to the reduced dimensionality of 2D materials defects significantly influence the electronic and optical properties [140–143]. On the one hand, the different kinds of defects such as vacancies, interstitials and substitutional impurities can reduce the optical response as electrons are trapped by the introduced defect states [139, 140, 143, 144]. On the other hand, introducing defects systematically allows to locally change the band structure and allows to generate additional states within the band gap [143]. Therefore, defect engineering

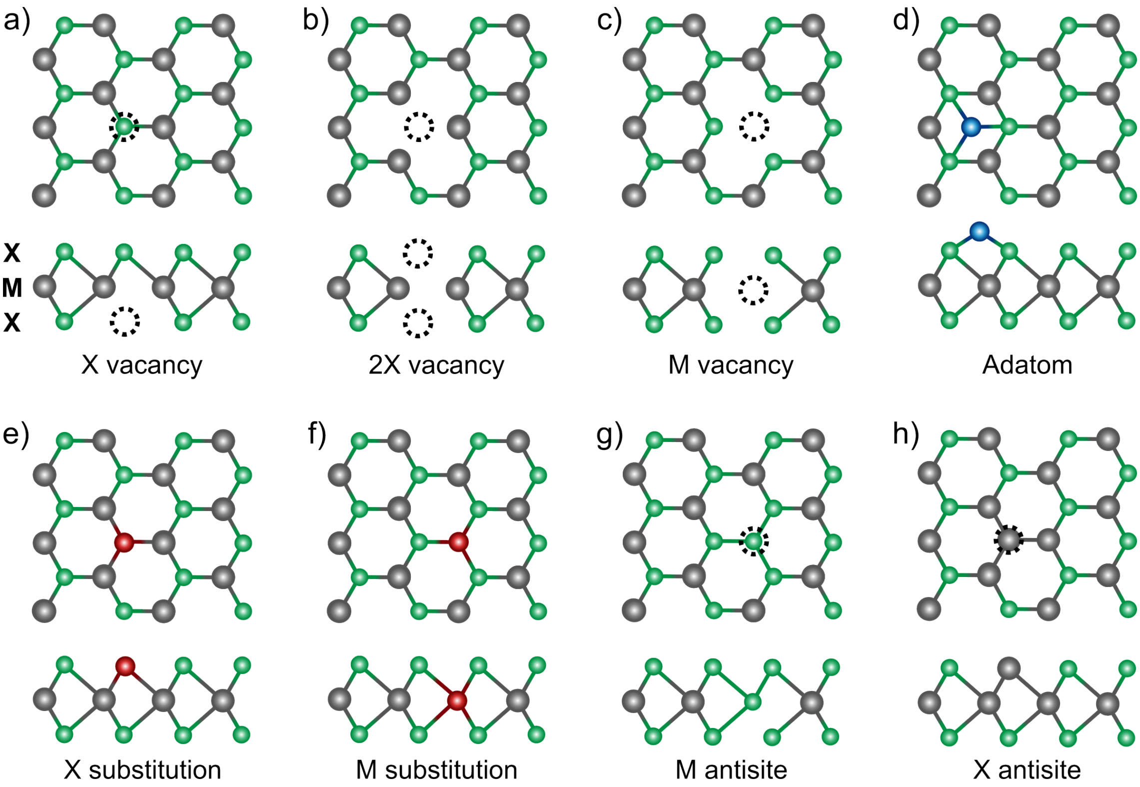

Figure 2.11: Different point defects in a TMD monolayer. The green spheres indicate the chalcogen atoms (X) and the grey spheres mark the metal atoms (M).

in 2D TMDs enables an additional opportunity to tailor the materials' optoelectronic properties [140, 143, 144].

Just like in other materials, a finite number of defects is present in 2D materials due to thermodynamics [140, 142, 143]. However, the physics of defect formation is different from bulk systems as these monolayers mainly consist of surface atoms. Consequently, the dynamics of defect formation and the influence of different defects on the physical properties of 2D materials are currently subject of intense investigations [139, 145]. Although a variety of different defect types such as point and line defects as well as grain boundaries are possible in 2D materials, the most investigated ones are point defects as these have a lower formation energy than defects of higher dimension [140, 143]. Point defects in 2D materials are assumed to promote single photon emission as observed in 2D-WSe$_2$ [44, 124, 146] and are therefore of great interest for quantum optical applications [147].

Figure 2.11 illustrates the different point defects in a triatomic TMD monolayer where the green spheres indicate the chalcogen atoms (X) and the grey spheres indicate the metal atoms (M). Single chalcogen vacancies (V$_\mathrm{X}$) are the most prominent defect type in 2D-TMDs because they exhibit the lowest formation energy [141, 143, 144, 148]. This type of defect has only one missing chalcogenide atom as illustrated in Figure 2.11 a). As the chalcogen atoms are surface atoms, these atoms are more easily removed from their lattice site than the metal atoms which are sandwiched between the two chalcogen atomic planes [141]. Therefore, the formation energy of a single chalcogen vacancy is lower than the formation of a single metal vacancy (V$_\mathrm{M}$) [141, 144]. However, if a transition metal vacancy is created, it tends to form a vacancy cluster as the binding energy of neighbouring chalcogen atoms is reduced [149].

The formation of a double chalcogen vacancy (V_{2X}), which in a TMD monolayer is a completely missing chalcogen atomic column as illustrated in Figure 2.11 b), is energetically less favourable than two single chalcogen vacancies but still more likely than a metal vacancy [150]. Chalcogen vacancies in TMDs, either single or double vacancies, are currently of great interest as they introduce mid-gap states in the electronic band structure supporting strong defect luminescence [43, 151, 152] and single photon emission [153, 154].

In addition to missing atoms, additional atoms can adsorb on the structure, forming a different class of point defects. For example, an adatom can be adsorbed on the surface of the 2D-crystal (indicated by the blue sphere in Figure 2.11 d). Note that these adatoms do not substitute one of the MX_2 atoms or occupy an atomic lattice position of the crystal structure.

In contrast, if a host atom of the WSe_2 layer is substituted by another atom, this point defect is called substitutional defect. The substitutional atom is incorporated into the crystal lattice and occupies an atomic lattice position which can be either a chalcogen or transition metal atomic position (indicated by the red sphere in Figure 2.11 e) and f). Depending on the introduced atomic species the optical behaviour can be tuned, e. g. substitutional oxygen atoms lead to an enhanced photoluminescence, e. g. in a MoS_2 monolayer [155]. If the substitutional atom is an atom of the host material and replaces an atom of the other atomic species, this is called an anti-site defect (indicated by the black dashed circle in Figure 2.11 f) and g). An anti-site appears when a chalcogen occupies a transition metal lattice position and vice versa [140]. This defect type is currently of great interest as it introduces local magnetism due to strong spin-splitting [112] and gives a new platform for qubit applications [156].

It is therefore desirable to be able to artificially generate different types of defects in order to precisely tailor the properties of TMDs to a specific application. However, as the exact defect formation processes are complex and involve several thermodynamic and kinematic factors, a whole research field evolved around this topic called defect engineering [149, 157]. Defect incorporation and density optimization can be achieved during growth, since the intrinsic defect density depends on process parameters such as temperature, pressure, and atmosphere [140, 141, 152]. It can also be achieved by post-growth treatments such as chemical etching [158] or thermal annealing processes [43, 159], laser [160, 161] or plasma treatments [162–164] as well as the irradiation with energetic electrons or ions [143, 152, 165]. A detailed description of these processes to create and modify defects in TMDs is beyond the scope of this work, however, an introduction of the defect formation under electron irradiation is given in Chapter 2.8 as the defect formation is part of the damage process of TMDs under prolonged irradiation during STEM investigations.

2.8 Specimen Damage under Electron Irradiation

Since the wavelength of electrons in transmission electron microscopy can be adjusted by changing the acceleration voltage, the spatial resolution can be increased almost arbitrarily by increasing the energy of the electron beam. However, the increase in beam energy, and therefore the possible increase in spatial resolution, is limited by specimen damage induced by the interaction of the high energetic electron beam with the specimen. Due to scattering processes, energy is transferred to the specimen and results in damage and degradation of the material which, in addition to diffraction, further limits the spatial resolution in transmission electron microscopy [166]. The description of specimen damage is divided into five different processes which lead to beam-induced changes of the specimen. These processes are categorized by the underlying scattering process.

Knock-on Damage

Even though elastic scattering is commonly assigned to a scattering process without energy transfer, this only holds in case of low-angle scattering ($\leq 1°$) [48]. This is a reasonable assumption for TEM imaging techniques as the transmitted electrons are used, however, elastic scattering can also result in scattering angles of more than 90°. In this elastic high-angle scattering the energy transfer is not negligible anymore [167, 168]. The energy E transferred from the electron to the atomic nucleus depends on the deflection angle θ as well as the incident beam energy E_0 and is given by

$$E = E_{\max} \sin^2(\theta/2) \tag{2.18}$$

$$E_{\max} = E_0(1.02 + E_0/10^6)/(465.7A). \tag{2.19}$$

The energies are given in units of eV and A corresponds to the atomic mass number which gives the total number of protons and neutrons in the atomic nucleus [167]. $E_{\max}$ is the maximum possible energy which can be transferred to the atom in a head-on collision and depends on the energy of the incident electrons E_0 and the atomic mass number A of the atom involved [167]. Therefore, the energy transfer is dependent on the atoms involved in the scattering process and can be in the range of several eV for high electron beam energies and high scattering angles. This direct energy transfer from the electron to the nucleus can lead to a displacement of the atomic nucleus if the transferred energy E exceeds a certain displacement energy E_{d}. This process is called knock-on damage. The threshold for knocking atoms out of their atomic site depends on the bond strength, the atomic species involved, the lattice structure as well as the atomic environment such as interfaces and surfaces [167–169]. If the energy transfer exceeds the binding energy, a displacement of an atom at specimen surfaces might even lead to a sputtering process by which the atom leaves into vacuum. As described by the Equation 2.19, the energy transferred to the atom mostly depends on the incoming electron beam energy E_0. Reducing the beam energy by lowering the acceleration voltage, leads to a reduction or even a suppression of knock-on damage [166].

Radiolysis

The second defect formation process is based on an indirect displacement of atoms resulting from an inelastic interaction of beam electrons with atomic electrons [168]. The inelastic interaction of beam electrons with the atomic electrons can lead to an excitation of valence electrons which necessitates an energy transfer of a few eV or can lead to an ionization of inner atomic shells which requires an energy transfer of up to hundreds of eV depending on the atom [166, 168]. The excitation leads to a configurational instability which relaxes by bond breaking [166, 169]. This process is often called ionization damage or radiolysis. Contrary to the knock-on damage, reducing the beam energy results in an increase in radiolysis processes as the probability of inelastic scattering is inverse proportional to the beam energy [166, 168]. However, not only the beam energy determines the amount of radiation damage but also the electron dose rate which describes the number of electrons per area and the illumination/irradiation time [167, 168].

Specimen Heating

Besides the active displacement or ejection of individual atoms and the subsequent structural changes of the specimen, phonons can introduce changes of the specimen. Phonons are generated by inelastic scattering which dissipate as heat inside the specimen. Even though the increase in temperature does not significantly damage inorganic specimens, it becomes important for biological specimens and can degrade these specimens. The only way to counteract this beam-induced damage is by cooling down the specimen.

Contamination

Another damage process includes the beam-induced polymerization of hydrocarbons on the specimen surface [170]. Under electron irradiation these contaminations built up and lead to a loss in image contrast and spatial resolution [169]. Furthermore, contaminations are supposed to be involved in chemically-assisted knock-on damage even for energies below the knock-on damage threshold as the presence of adatoms leads to a local weakening of the chemical bonds [171, 172].

Electrostatic Charging

Another beam-induced damage mechanism which is less common but especially for insulating materials important is the electrostatic charging of specimens. Although, most of the incident beam electrons leave the specimen, the generation and emission of secondary and Auger electrons leads to an accumulation of charge inside the specimen resulting in a local electric field [167, 173, 174]. In an insulating material, the imbalance of charge can not be restored by a migration of surrounding charge. As a consequence of the electrostatic field, ionized atoms can migrate inside the specimen resulting in the creation of holes [167, 174].

Most of the described beam-induced damage processes not only depend on the energy of the incident electrons but also on the electron dose defined by product of beam-current density and exposure time resulting in a quantity which gives the number of incident electrons per unit area [167, 173]. In addition, the time in which these electrons impinge on the specimen area influences the generation of damage. Since all these different beam-induced damage processes alter the specimen during STEM investigations it is important to adjust the electron energy, dose and dose rate to minimize the specimen damage. However, suitable imaging conditions can not be stated out in general as the damage processes are highly dependent on the material under investigation. There are possibilities to minimize the beam-induced damages but it is mostly a trade-off in resolution. Reducing the acceleration voltage to suppress knock-on damage reduced the spatial resolution and reducing the dose to minimize radiolysis damage reduces the signal-to-noise ratio [167, 175].

Although beam-induced damage to bulk TEM specimens has been studied, investigations of 2D materials by (S)TEM reveal unexpected behaviours of 2D materials under electron irradiation which resulted in a novel research field of defect engineering in 2D materials by high energetic electron beams [139, 176]. For different 2D materials, e.g. MoS_2, WS_2 and graphene, knock-on damage is observed even for electron energies far below the displacement energy threshold [177–181]. The reason for the changed behaviour under electron irradiation of 2D materials is not completely understood, yet, but is presumably ascribed to the low dimensionality [140]. Due to the planar geometry and a thickness of only one or a few atomic layers sputtering processes are more likely than in bulk systems and the energy dissipation changes significantly [140, 177]. The occurrence of beam-induced defects even below the displacement energy threshold might be due to the combination of electronic excitation in combination with a knock-on damage mechanism [179]. S. de Graaf and B. J. Kooi found that the beam-induced damage in WS_2 even increases by a factor of two when halving the electron beam energy from 60 keV to 30 keV [181]. Furthermore, they showed that the type and density of defects strongly depends on the dose. With prolonged illumination, and thus with increasing accumulated electron dose, the density of point defects remains almost constant but the density of line defects and holes increases which illustrates the migration of vacancies to defect cluster [181].

Furthermore, 2D materials inherently exhibit a certain number of defects which depends on the fabrication process. It is shown that the displacement energy of atoms in the vicinity of such defects is drastically lowered [177]. In combination with the high mobility of defects in 2D materials, an accumulation of defects under prolonged irradiation is commonly observed [157, 182]. Therefore, imaging conditions such as acceleration voltage, electron dose and dwell time must be carefully selected according to the 2D material under investigation.

For 2D-WSe_2, knock-on damage is theoretically not expected below an acceleration voltage of 200 keV beam energy as the displacement threshold for selenium atoms is around 6.4 eV [165, 183]. However, radiation damage with displacement of selenium atoms is commonly observed in high-resolution STEM imaging of WSe_2 monolayers [165, 182]. But despite the creation of electron beam-induced defects a self-healing of single selenium vacancies is observed for monolayer WSe_2 [183]. As the diffusion energy barrier on a WSe_2 monolayer is only of about 0.23 eV the migration of surface adsorbed selenium atoms can heal defects by an electron-beam induced diffusion [183]. However, the investigation of healing of selenium vacancies shown by Li et al. was done in a Se-rich environment [183]. In general, a high accumulated electron dose results in more selenium defects and more extending defects with prolonged electron illumination [182]. Thus, in high-resolution STEM imaging of WSe_2 monolayer the formation of selenium defects can be reduced by short illumination times and low beam currents but is typically unavoidable for atomic resolution imaging with reasonable signal-to-noise ratio.

Chapter 3

Experimental Details

3.1 Microscope Properties & Layout

The following chapters deal with the layout and specifications of the microscope used as well as the different detectors employed for quantitative STEM-DPC investigations. The transmission electron microscope used is a probe-side C_S corrected microscope called *JEM-ARM200F ACCELARM* manufactured by *JEOL Ltd.* (Tokyo, Japan). Figure 3.1 depicts the schematic layout of the electronoptical components of the TEM column including different lenses, apertures and detectors necessary for DPC imaging and analytical (S)TEM modes. The microscope is equipped with a cold field emission gun (short: CFEG) located at the top of the TEM column. The CFEG is followed by an acceleration tube which allows to accelerate the electrons to pre-aligned energies of 30 keV, 60 keV, 80 keV and 200 keV. In STEM, the sharp electron beam is focused onto the specimen by the probe-forming lens system including the two condenser lenses (CL1 and CL2), and the two condenser apertures, the C_S-corrector and well as the condenser mini lens.

The C_S-corrector is a so-called *ASCOR* manufactured by *CEOS GmbH* (Heidelberg, Germany) which allows to correct lens aberrations up to the fifth geometrical order (Chapter 2.3). The subsequent condenser mini-lens is used to converge and focus the electron beam on the specimen.

The specimen is inserted into the TEM column using a dedicated double-tilt holder (EM01360RSTHB or EM01040RSTHB) from *JEOL Ltd.* The goniometer stage of the microscope enables the specimen to be moved in the x-, y- and z-directions, and allows it to be tilted in the x- and y-directions. The double tilting capability is an important feature to precisely align and orientate the specimen in zone-axis orientation. The subsequent lens system projects the electron beam onto the detector. The excitation of the projection lens system defines the illumination of the detectors and is therefore important for STEM imaging. The projection of the beam intensity can be described by a camera length L which defines the virtual distance between the specimen and the detector (see dashed green line in Figure 3.1). The camera length in the microscope determines the magnification of the post-specimen intensity and is given by the excitation of the post-specimen lens system.

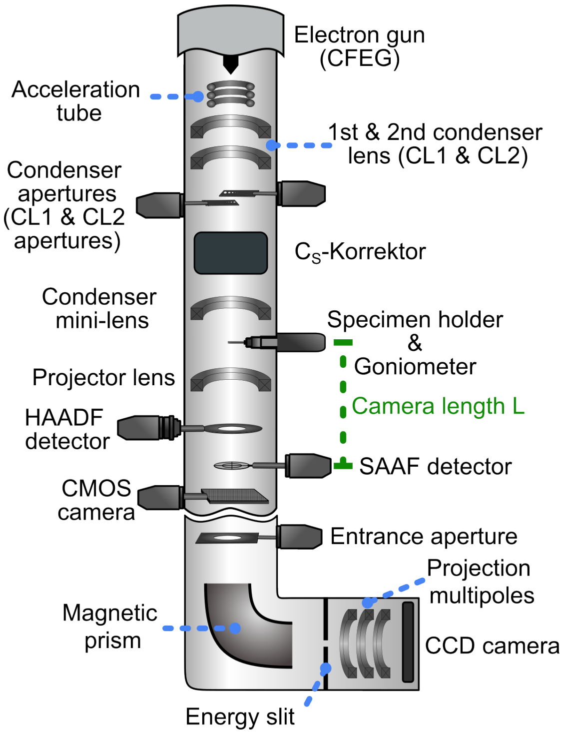

Figure 3.1: Schematic layout of the transmission electron microscope including analytical components.

The high-angle annular dark-field (HAADF) detector and the segmented detector used for STEM-DPC imaging are both located underneath the specimen. The HAADF detector is a ring-shaped detector centred around the optical axis and the segmented annular all-field (SAAF) detector is a disk-shaped detector centred on the optical axis. Both are manufactured by *JEOL Ltd.* A detailed description about the layout and specifications of the segmented detector as well as signal acquisition will be given in the following chapter. Due to the different positions of both detectors, HAADF and DPC measurements are possible simultaneously. For analytical (S)TEM investigations, the microscope is additionally equipped with an energy filter named *GIF Quantum ER* from *Gatan GmbH* (California, United States). The energy-filter consists of an entrance aperture to reduce off-axial contributions, a focussing 90° magnetic prism as well as a slit in the energy dispersive plane of the 90° prism to filter certain energy losses. Sets of multipole lenses project the intensity distribution onto a CCD camera. As the energy filter is located underneath the segmented detector, energy-filtering of the electron beam and DPC measurements are not simultaneously possible. Thus, the energy filter is not used in this work, but it is included here for the sake of completeness. The measurements on the 2D materials WSe_2 and MoS_2 were performed using an acceleration voltage of 80 keV to prevent beam damage of the specimen. A CL1 aperture of 150 μm and a CL2 aperture of 40 μm were used, resulting in a convergent semi-angle of 30 mrad. A camera length of L=12 cm is used. At this camera length the collection angles of the HAADF detector span a range from 54 mrad to 191 mrad and the SAAF detector extents to 36.1 mrad. For all high-resolution STEM investigations and DPC measurements residual lens aberrations are of great importance as they influence the shape of the electron beam and introduce artefacts in the measured electric field distribution [26]. Thus, the C_S-corrector was tuned using a reference sample of gold nanoparticles on graphite right before STEM-DPC investigations.

3.2 Segmented Detector and Signal Acquisition

Segmented detectors used for STEM-DPC investigations are typically disk- or annular-shaped detectors centred on the optical axis. In this thesis, a JEOL segmented annular all-field (SAAF) detector which consists of two concentric rings with four quadrants each (Figure 3.2) and has a diameter of about 10 mm. The SAAF detector is a scintillator based detector where the segments consist of lutetium oxyorthosilicate (LSO) single crystals which are individually fibre-coupled to photomultipliers and 32-bit analog-digital converters. This allows to adjust the gain for each segment individually.

The eight segments of the SAAF detector can be combined to two “Layers”. The inner four segments (1-4) comprise a disk as illustrated in Figure 3.2 a) which is denoted as Layer 1. The outer four segments (5-8) are denoted as Layer 2. The detector segments can be described by the inner and outer collection angles as well as the azimuthal collection angles. Due to the splitting in quadrants, each detector segment spans over an azimuthal range of 90°. Furthermore, the detector can be rotated about the optical axis between 0° and 90° with a precision of 0.01° allowing to tailor the azimuthal collection angles to the CBED pattern.

The illumination of the segmented detector with the CBED pattern is determined by the camera length which defines the collection angles of Layer 1 and Layer 2. For the acceleration voltage of 80 keV used in this thesis, the inner collection angle of Layer 2 is $\beta_{\text{inner}} = 18.2$ mrad and corresponds to the outer collection angle of Layer 1. The outer collection angle of Layer 2 is $\beta_{\text{outer}} = 36.1$ mrad. This is achieved at camera length of L=12 cm, for which the bright-field (BF) disk of the CBED pattern illuminates about half of the outer layer of segments. Unless otherwise stated, all layers are used for signal acquisition.

Figure 3.2 a) exemplarily shows a simulated CBED pattern of a WSe_2 monolayer overlaid with the segmented detector. The bright-field disk is indicated by the white dashed circle. Although, most intensity is found within the BF disk, some electrons are scattered out of the BF disk (visible by the colour variations in the region outside the BF disk). The CBED pattern shows a complex intensity distribution across the bright field disk and also some intensity variations outside the BF disk corresponding to the scattered and diffracted electrons. The CBED pattern shows a higher intensity located on segment 7 compared to the other four segments of the outer layer. This intensity redistribution within the CBED pattern is the basis for the calculation of the electric field distribution in the specimen. In general, DPC images are obtained by calculating difference signals from intensities on opposing detector segments in a bisected way where the quadrants are combined along the x-and y-direction resulting in a split into halves of the detector. For the eight-fold segmented detector the difference signals are given by

$$S_{x,y} = \frac{S_5 \pm S_6 - S_7 \mp S_8}{S_5 + S_6 + S_7 + S_8} \tag{3.1}$$

with S_i indicating the intensity on the individual segments $i \in \{1, ..., 8\}$. The directions K_x and K_y are given by the upper ($\pm$) and lower ($\mp$) case and indicated in Figure 3.2 a). As can be seen from Equation 3.1, the signals are normalized by the intensity of all segments reducing the influence of different scattering probabilities across the scan.

To quantitatively relate the intensity differences to an electric field present at a certain scan position, a calibration of the detector is needed. There are two approaches for the DPC signal calibration, which are both used in this thesis and are described in the following.

The first approach is a signal-based calibration utilizing a previously determined calibration

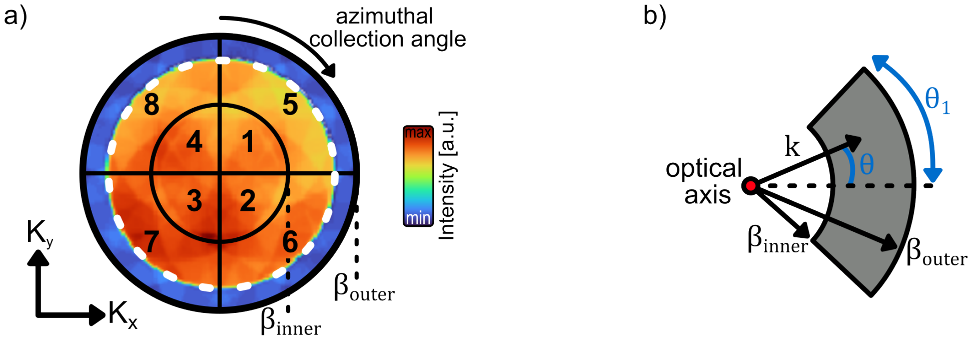

Figure 3.2: a) Schematic sketch of the eight-fold segmented annular all-field detector with a simulated CBED pattern overlaid. The region of the bright-field disk is indicated by the white dashed circle. b) Description of the centre-of-mass calculation for the signal processing (adapted from [5, 84]).

factor which relates the shift of the CoM of the intensity distribution to a deflection angle. For this, the difference signals $S_{x,y}$ are calculated using Equation 3.1. The deflection can be then calculated using $\varepsilon_{x,y} = \frac{S_{x,y}}{c_{\text{cal}}}$ with c_{cal} being a calibration factor or using $\varepsilon_{x,y} = \frac{K_{x,y}}{k_0}$. This calibration factor is determined previously using the momentum-space calibrated CMOS camera located underneath the SAAF detector (Figure 3.1). This calibration is done by manually deflecting the electron beam once across the SAAF detector and with the same steps once across the camera using the beam deflection coils. As the camera is calibrated, the change in the differential signals $S_{x,y}$ can be related to a deflection angle ε [26]. For the microscope parameters used for the DPC measurements the calibration factor amounts to $c_{\text{cal}} = 1.306 \cdot 10^8\,\text{mrad}^{-1}$.

The second approach is based on the geometrical centre of mass (gCoM) of the detector segments and is denoted as k-space calibration. This calculation is adapted from Ref. [5, 84] and utilizes the angular extension of the detector segments defined by their polar and azimuthal collection angles. Figure 3.2 b) shows an illustration of a segment of a quadrant detector. To simplify the calculation of the gCoM, it is assumed that each segment spans over an azimuthal range of $2\theta_1$ with $\theta_1 = \pi/4$ centred around $\theta = 0$ (Figure 3.2 b). The polar angle is defined by a corresponding wave number k. The wave number range of each detector segment is given by the inner and outer collection angles β_{inner} and β_{outer}. The polar component of the gCoM $k_{i,\text{Polar}}$ of the i-th segment can hence be calculated as:

$$k_{i,\text{Polar}} = k_0 \frac{\int_{-\theta_1}^{\theta_1} \int_{\beta_{\text{inner}}}^{\beta_{\text{outer}}} k \cos(\theta)\, dk\, d\theta}{\int_{-\theta_1}^{\theta_1} \int_{\beta_{\text{inner}}}^{\beta_{\text{outer}}} k \quad dk\, d\theta} \qquad [5]. \tag{3.2}$$

The same calculation can be done for the inner layer of the eight-fold segmented detector when using an inner collection angle $\beta_{\text{inner}} = 0$. The individual wavenumber components $k_{i,x/y}$ for the gCOM of each detector segment are then calculated using $k_{i,x} = k_{i,\text{Polar}} \cdot \cos(\theta - \gamma)$ and $k_{i,y} = k_{i,\text{Polar}} \cdot \sin(\theta - \gamma)$ with the azimuthal angle θ and the detector rotation γ [84]. Finally, the DPC signal is obtained by the sum of the intensities on individual segments weighted with the individual gCoMs. Thus, the components of the lateral transferred momentum are given by $p_{\perp,x,y} = \hbar \cdot k_{x,y}$.

The k-space calibration of the DPC image is used for all the experimentally obtained DPC images and mostly for the simulations, as no previous calibration measurements of the segmented detector are needed. However, some simulations are calibrated by the first approach using a signal-based calibration. For all DPC measurements and simulations the calibration type used is indicated in the respective table in the appendix.

3.3 Image Post-Processing

For the analysis of the STEM-DPC images, different post-processing steps are necessary. All the image post-processing steps are done using a *Matlab* software developed within the research team. A detailed description of several basic post-processing steps can be found in Ref. [84]. In the following, a short overview is given and self-written functions specifically tailored to the analysis of 2D materials are described.

3.3.1 Basic Image Corrections

The post-processing is typically initiated with a rotation correction of the deflection directions necessary due to three contributions.
1) The post-specimen lens system rotates the CBED pattern due to the interaction of the electron beam with the electromagnetic field of the lenses via the Lorentz force. This rotation alters the derived electric field distribution in direction. This contribution can therefore be compensated by a basic rotation angle which is experimentally determined by acquiring a DPC image in vacuum without any sample. Scan and detector rotations are set to zero for this image acquisition. Comparing the obtained DPC image with the expected image without any further rotation due to the projector lens system allows to determine the basic rotation angle which amounts to $\phi_{\mathrm{Basic}} = 180° \pm 1°$ at 80 kV.
2) The scan rotation ϕ_{Scan} determines the orientation in which the electron probe is scanned over the specimen. Therefore, any non-zero values change the orientation between the direction of the scan and the direction of the CBED pattern.
3) The detector rotation angle γ changes the way how the segments intersect with the CBED pattern and therefore changes the signal on the different segments. The influence of the detector rotation on the derived DPC images will be investigated in detail in Chapter 4.3.2.
To take these three influences into account, the rotation of DPC images is corrected by modifying the signals $\mathrm{S_x}$ and $\mathrm{S_y}$ ($\mathrm{K_x}$ and $\mathrm{K_y}$) with trigonometric functions (sin and cos) and the corresponding angle defined by $\phi_{\mathrm{Correction}} = \phi_{\mathrm{Basic}} + \phi_{\mathrm{Scan}} + \gamma$ [84].
Previous to the DPC measurements the electron beam is manually centred on the detector using an alignment tool implemented in the software of the SAAF detector by the manufacturer. However, microscope instabilities and slight misalignment will introduce dominating directions in the DPC images due to the no longer perfectly centred electron beam on the detector. This imperfect beam centring however can be corrected in a post-processing step by subtracting an average signal corresponding to an offset, when analysing atomic electric fields. This average signal is determined using a 2D histogram of the DPC image, the so-called scattergram. Further information on the scattergram is given later in this chapter. This procedure readily enables a post-measurement correction of slight misalignments of the beam centring present during DPC measurements [84].

3.3.2 Denoising and Correction of Specimen Drift

During STEM investigations different kinds of distortions and noise are present which alter the image quality. Besides the noise, scan distortions and specimen drift influence the resulting image. In the following, three post-processing steps are described to reduce the influence of these distortions on the DPC images. To reduce image noise, a Gaussian filter can be used. This corresponds to a convolution of each image pixel with a Gaussian function of a certain standard deviation. The standard deviation gives the extension of the Gaussian function and sets the size of the convolution kernel determining the contribution of neighbouring pixels.
Although the Gaussian filter reduces the influence of noise, it also reduces the spatial image

resolution due to the convolution process. In contrast to this method, a denoising algorithm based on a registration of images or image segments followed by an averaging of intensities of individual pixels retains the spatial resolution of the image while reducing the image noise [184–186]. For this process, two images of the same object are translatively overlaid by a rigid registration algorithm using a cross-correlation coefficient as parameter for the quality of the registration. For the highly symmetric atomic resolution images used in this work, there is no need of taking two or more STEM images of the same object area to obtain a rigid registration. Instead, segments of the HAADF and DPC image are registered, overlaid and averaged. For the typically 512 × 512 px atomic-resolution images, an image area of a dimension between 80 × 80 px up to 200 × 200 px can be chosen as a reference image. This reference image is then scanned pixel bx pixel across the full area of the STEM image. For each step, the cross-correlation coefficient between the reference image and the current image area is calculated (based on the HAADF image contrast). If the cross-correlation coefficient is higher than a certain threshold value, the image area is registered. Thus, the threshold in cross-correlation coefficient determines whether an object area is registered to the reference image or discarded if the equality is below the threshold value. Therefore, by manually adjusting the threshold for the image registration the number of overlaid images can be tailored. Finally, the mean values of all registered image areas are calculated for each pixel.

Besides the rigid image registration process an additional non-rigid registration process can be used [184, 185]. In contrast to rigid registration which only uses translational operations for the image registration, non-rigid registration also includes deformations of the image to achieve a high similarity to the reference image. This is beneficial when registering images with distortions, which lead to an elongation or distortion of image features [186]. However, as the image registration is based on a symmetry or repeating features within the image, it is only suitable for the post-processing of the highly symmetric pristine images. For denoising DPC images containing crystallographic defects, only the described Gaussian filtering can be applied.

Specimen drift can also be corrected using a self-developed algorithm based on the atomic column positions in high-resolution HAADF images. Specimen drift leads to a distortion of the crystal structure in the HAADF image. By manually readjusting the atomic columns, the influence of the specimen drift in the image can be reduced. This is done by drawing a line over the atomic column positions. The angle between this line and the expected arrangement of the atomic columns without specimen drift is corrected by rotating the image. In case, the drift leads to strong distortion (e.g. elongation or compression in one direction) of the lattice visible in the HAADF images, this can be slightly adjusted by adjusting the pixel size in one direction. By comparing the distances of atomic columns along a direction with the ideal distance given by the perfect crystal lattice, a factor can be found to readjust the pixel size in this direction. Due to the interpolation between pixels, the drift correction slightly alters the pixel magnitudes while preserving the features in the DPC images. The influence on the absolute values is therefore negligible compared to the features of interest. A detailed description of the drift correction procedure is given in the Appendix 9.2.

3.3.3 Quantitative Analysis of DPC Images

Finally, the DPC images and related electric field and charge density maps can be calculated as described in Chapter 2.5. In addition, atomic column positions are determined by fitting 2D gaussian functions to the bright image intensity of HAADF images. These positions are marked in the other image types for visual guidance.

Figure 3.3 displays the different quantities derived from a DPC data set, here exemplarily for a multislice image simulation of a STO unit cell. The simulation is the same as shown in Figure 2.7 in Chapter 2.5. The DPC image representing the electric field distribution in direction and magnitude is shown in Figure 3.3 a) and the atomic column positions are exemplarily indicated by the coloured disks. As the DPC image contains a lot of information, it is useful to only extract the magnitude of the electric field. The electric field magnitude map is shown in Figure 3.3 b) where areas with high electric field magnitude are observed close to the atomic column positions. Furthermore, due to the overlap of opposing electric fields of neighbouring atomic columns local field minima are observed along the connecting direction between two individual atomic columns (exemplarily marked by the white arrow in b). In addition to the electric field distribution, using Maxwell's equation (Equation 2.13) the charge density can be derived by the vacuum permittivity and the calculation of the two-dimensional divergence of the electric field. The charge density of a STO unit cell received using STEM-DPC is shown in Figure 3.3 c). The charge density map is colour coded: red pixels indicate a positive charge density and blue pixels represent a negative charge density. This colour code is applied to all charge density maps throughout this thesis. It is important to note that the charge density maps show an overall net charge density, which has contributions from the positively charged nucleus and the negatively charged electron cloud. Thus, the net positive charge density is localized at the position of the atomic columns arising from the presence of protons at the (partially screened) atomic nuclei. The negative charge density is delocalized surrounding the nuclei [4, 27, 34, 79].

Figure 3.3 d) shows a so-called scattergram which is the 2D histogram of the DPC image displaying the number of pixels with similar magnitude and direction of beam deflection. The scattergram can represent any quantity of the DPC images, such as beam deflection, wavevector or the electric field in magnitude and direction. Here, the description is exemplarily done for the beam deflection.

Each pixel of the DPC image is represented within the scattergram and can be interpreted in terms of the beam deflection, transferred momentum or electric field as these quantities are interlinked by constant factors. The deflection magnitude is given by the distance from the scattergram centre. The direction of deflection of a scattergram feature can be deduced from the reference colour in the outer ring. For the shown scattergram of a unit cell of STO, a star-like feature close to the centre of the scattergram (red dot in Figure 3.3 d) is observed, indicating a large number of pixels with a weak deflection but pronounced in the direction of green, yellow, blue and magenta. This finding can be explained by

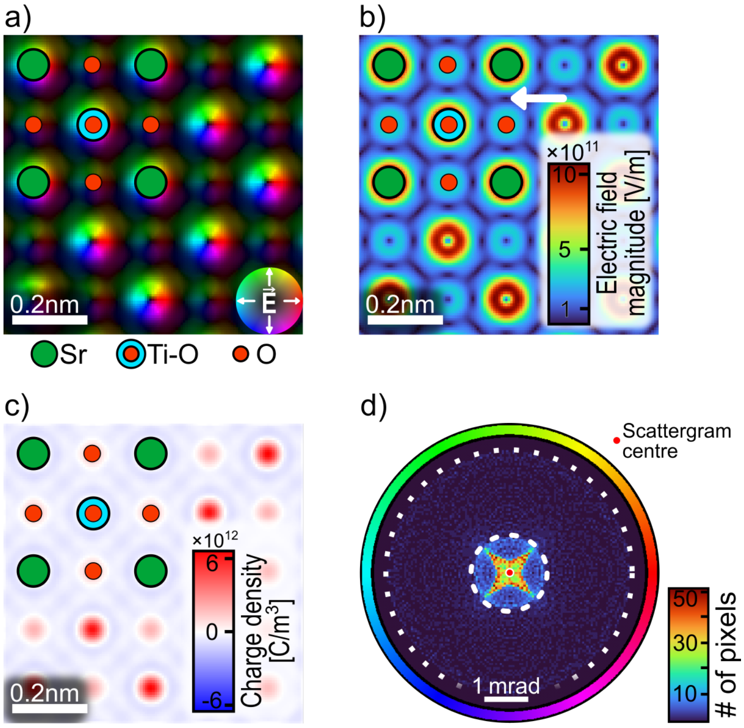

Figure 3.3: a) Colour-coded DPC map and b) the electric field magnitude map of the simulated STO lattice described in Chapter 2.5. The positions of some pure Sr and O as well as mixed TiO atomic columns are marked as indicated in a). c) Charge density distribution derived from the DPC map (a) using the Maxwell's equation. d) Scattergram as the histogram of the number of pixels with a deflection in a certain deflection interval.

the corresponding features in the DPC image. These features correspond to ones on the diagonally connecting line between neighbouring atoms. As the distance of diagonally arranged (e. g. [110]) atoms is larger than the directly adjacent ones, the deflection at positions on the diagonal connecting axis are less suppressed by the overlap of electric field components. Thus, the star-like feature arises due to the four-fold lattice symmetry and reduced overlap of individual atomic fields in certain directions. Furthermore, a disk with comparable deflection magnitudes as the star-like feature is observed and marked by the white dashed line in Figure 3.3 d). This indicates that the overlap of fields does not lead to a complete compensation of opposing fields and a small number of pixels in the DPC image exhibits a deflection even for the directions of overlapping fields. This round-shaped feature with medium deflection magnitude but homogeneous in all direction corresponds to the weak deflection of the oxygen atomic columns. Furthermore, a disk-shape diffuse background is visible in the scattergram and marked by the white dotted circle. As the radius of the disk is large, these pixel correspond to a high beam deflection arising from beam deflections close to the atomic column positions, especially from the pronounced Sr and Ti-O atomic columns [84]. The scattergram is therefore a compact representation of the DPC image neglecting the atomic structure which makes it a suitable tool to detect lens aberrations [26], which in the case of the simulation shown were set to zero.

3.4 Specimen Preparation

Within this thesis two different kinds of 2D materials, namely WSe_2 and MoS_2, are investigated. For WSe_2, both, mechanically exfoliated and CVD grown mono- and multilayers are used. The CVD grown WSe_2 samples are purchased from *2DSemiconductors* (Arizona, United States), which are already transferred to the TEM grids by a polymer-based transfer process. For the mechanical exfoliation of WSe_2 mono- and multilayers, bulk crystals with a dimension of a few millimetres are purchased from *2DSemiconductors*. The bulk crystal is mechanically exfoliated and thinned down using the adhesive tape 224PR-MJ from *Nitto Denko* (Osaka, Japan). The exfoliation process is based on the so-called Scotch tape method and adapted from Ref. [187]. The thickness of the TMD flakes on the Nitto tape can be estimated using the transmission mode of a visible light microscope. In a next step, the thinned TMD flakes are transferred to a PDMS stamp. To transfer the exfoliated flakes to TEM grids, a PDMS-based transfer process widely applied in literature on 2D material transfer [187, 188] was adapted and tailored to the substrates and materials used here. It is applicable to WSe_2 and MoS_2 and most likely many other TMDs. The PDMS stamp itself is fabricated using the elastomer Sylgard™ 184 from *The Dow Chemical Company* (Michigan, United States). This is an elastomer with a ratio of 10:1 of base and curing agent. The stamps are prepared by pouring the PDMS on a silicon wafer in a petri dish. To achieve a flat surface, residual air pockets, resulting from the pouring, are released by degassing under vacuum for 10 min. The PDMS is then cured at 130 °C for 15 min on a hotplate.

PDMS stamps are cut and released from the wafer and placed upside down on a cleaned glass slide. By this the flat surface which was in contact with the silicon wafer is facing upwards. The adhesive tape with the thinned TMD flakes is pressed by hand on to the PDMS stamp and the whole stack is placed on a hot plate for a heat treatment at a temperature of about 60 °C for about 2 min. This ensures a good contact between the PDMS and the TMD monolayer. The stack is then cooled down to room temperature and the adhesive tape is quickly pulled off. Parts of the 2D TMD flakes which were initially attached to the adhesive tape will stick to the PDMS. The thickness of the flakes on the PDMS is investigated by the contrast in the transmission mode of an optical light microscope.

The flakes can then be transferred from the PDMS to a holey silicon nitride TEM grid for the (S)TEM investigations. The silicon nitride TEM grids by Pelco® are purchased from *Plano GmbH* (Wetzlar, Germany) and consist of a 200 μm thick silicon substrate with a 0.5 × 0.5 mm window. The windows is spanned with a 200 nm thick holey membrane of amorphous silicon nitride. The holes have a diameter of 200 nm and a centre-to-centre distance of 400 nm. Therefore, the free-standing TMDs layers can be investigated within the 200 nm holes in the amorphous membrane. For the transfer of the monolayer flakes to the membrane of the TEM grids, a digital microscope (VHX-X1) from *Keyence Corporation* (Osaka, Japan) is used with an in-house built transfer stage. Figure 3.4 shows a schematic illustration of this transfer stage. The stage itself consists of piezo-driven stepper motors which allow to move the stage in x- and y-direction. Furthermore, the stage can be rotated about the stage axis which is parallel to the z-axis and can be heated by an integrated peltier element. The TEM grid is fixed on top of the stage by using an adhesive carbon tape. Above the stage, the glass slide with the PDMS stamp can be fixed and moved in z-direction. Since the complete system is placed under the optical microscope, the position of the flakes and the transfer process itself can be controlled with great precision. The 2D material on the PDMS is then brought in contact with the TEM grid by carefully lowering the glass slide. The 2D material flakes are positioned on the TEM grid in a way, that parts of the flake are placed on the substrate and only the region of interest is placed on the membrane of the window in the TEM grid. By this the adhesion of the flake is improved as the interaction of the 2D material is stronger with the flat substrate than with the membrane due to its flexibility. The contact of the PDMS with the TEM grid is observed by a change in contrast. To further enhance the adhesion between the 2D material and the TEM grid, the stage is heated up to about 80 °C. As the PDMS expands during the heating, the stage needs to be slightly lifted up again to prevent a breakage of the membrane. To start the release process of the 2D material, the PDMS stamp is lifted up step-wise until a movement of the contact line is observed. It is important that the lifting up is rather slow to fully exploit the viscoelastic properties of the PDMS. Typical transfer times amount to at least four hours. The successful transfer can again be confirmed by the optical light microscope. To reduce the built up of contamination during the STEM investigations, the TEM grids with transferred 2D materials are heated under vacuum condition ($p=5\cdot10^{-7}$ mbar) for about 20 h at a temperature of 150 °C. Although this beakout process does not eliminate residual polymer contaminations on the specimen surface, but it reduces the amount of volatile hydrocarbon contaminations.

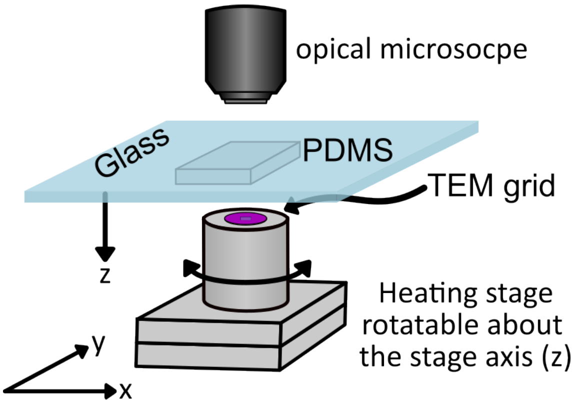

Figure 3.4: Schematic illustration of the transfer stage used to transfer the 2D material from the PDMS to the TEM window grid. The stage can be moved in x- and y- direction and rotated about the stage axis (z-axis).

Chapter 4

Electric Field and Charge Density Distributions in a WSe_2 Monolayer

4.1 Quantitative STEM-DPC Investigations of a WSe_2 Monolayer

In this chapter, STEM-DPC measurements of a WSe_2 monolayer are shown and discussed with focus on the atomic electric field and charge density distribution. The experimental DPC measurements are compared with corresponding multislice image simulations using the software abTEM [89], and a quantitative analysis is done. Furthermore, different microscope and specimen-related influences are discussed.

Figure 4.1 a) depicts a measured (left) and a simulated (right) STEM-HAADF image of a WSe_2 monolayer in [0001] zone-axis orientation. Both HAADF images show a hexagonal arrangement of spots with alternating high and dim intensity which correspond to the two different atomic columns in WSe_2. The intensity distribution observed is in agreement with the one expected in case of Z-contrast for HAADF imaging, as discussed in Chapter 2.2. The variation in HAADF intensity of the different atomic columns is analysed in detail by the integrated line profiles over the two dumbbells of WSe_2 depicted in Figure 4.1 b) for the measurement (blue line) and the simulation (orange line). The line profiles are integrated over the region indicated by the blue and orange boxes in a) and normalized to the maximum intensity. Both line profiles show four peaks resulting from the high scattering probability of the atomic columns. Each dumbbell exhibits one peak with a high HAADF intensity (right peak) and one peak with a lower HAADF intensity (left peak). Based on the Z-contrast of HAADF images, the high intensity peaks correspond to an atomic column with a higher atomic number projected along the beam propagation direction whereas the lower intensity peaks result from a smaller projected atomic number. Although the selenium atomic columns consist of two selenium atoms stacked above each other in beam propagation direction, the projected atomic number $Z_{2Se} = 68$ is still smaller than the projected atomic number of the tungsten atomic columns consisting of only one single tungsten atom ($Z_W = 74$). Therefore, the two different atomic species of WSe_2 can clearly be identified by the HAADF images. The peaks with the higher HAADF intensity are identified as tungsten atoms and the peaks with reduced intensity are identified as the selenium atomic columns. From the ratio of measured HAADF intensities of the selenium and tungsten atomic columns and the projected atomic numbers the exponent for the Z-contrast imaging is determined to be 1.8 for the used experimental imaging parameters. This value is in good agreement with the finding of Yamashita et al. who investigated the atomic number dependence for the (HA)ADF imaging of 2D materials [72]. The atomic column positions and species identified by the HAADF image intensity are marked by green and grey dots for selenium and tungsten atomic columns, respectively, and are also plotted on the other images to highlight the atomic column positions.

Figure 4.1 c) shows the measured (left) and simulated (right) colour-coded DPC images. The colour of a pixel represents the direction of the electric field. The saturation of the respective colour indicates the magnitude of the electric field. The directions and magnitudes can be deduced from the inserted colour legend shown as a colour wheel. Quantitatively, the measurement shows an overall smaller electric field magnitude compared to the simulation.

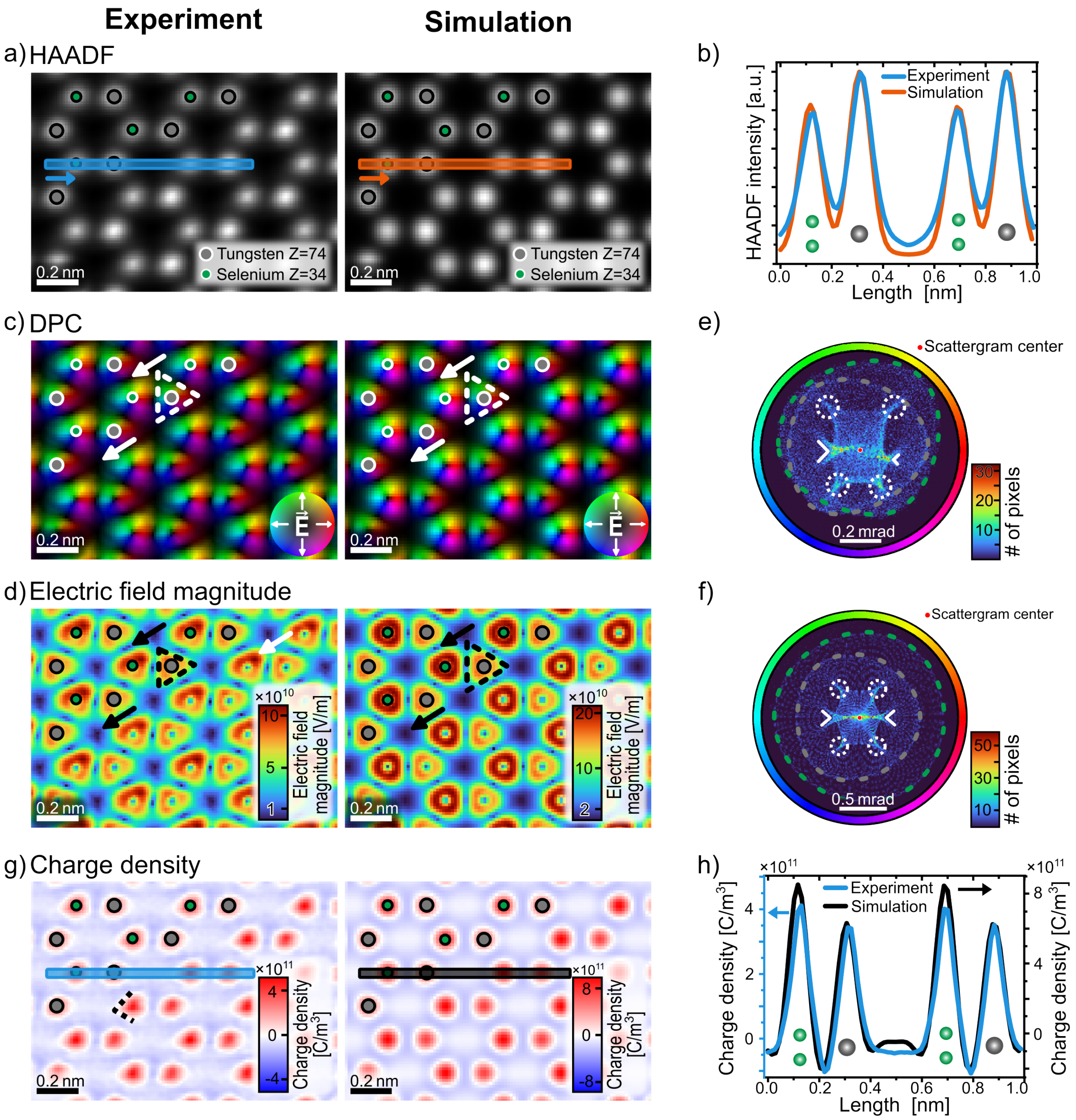

Figure 4.1: STEM-DPC investigation of a WSe$_2$ monolayer. a) Measured (left) and simulated (right) HAADF images of a WSe$_2$ monolayer in [0001] zone-axis orientation. b) Line profiles of the normalized HAADF intensity integrated over the blue and orange boxes indicated in a) for the measurement and the simulation. c) Experimental and simulated Colour-coded DPC images of the electric field distribution and d) the corresponding electric field magnitude maps. Scattergram of the DPC images for e) the measurement and f) the simulation with a coloured frame to readily identify the corresponding azimuthal electric field directions of scattergram features. g) Experimental and simulated charge density maps and h) line profiles integrated over the blue and black boxes in g). Atomic column positions are exemplarily given by the green and grey dots for selenium and tungsten atomic columns, respectively.

The measured values are in the same order of magnitude but differ by a factor of about two. This behaviour is also observed in publications on other 2D materials, e. g. MoS_2 [37]. The overall smaller electric field magnitudes in the measurement might be due to residual lens aberrations or contamination on the monolayer, blurring the DPC signal.

For both, measurement and simulation, rotational symmetric electric field distributions comparable to the reference colour wheel are found around each atomic column position. This is due to the high positive charge of the atomic nucleus dominating the electron beam deflection. Such atomic field distributions are expected and described in literature for different materials [4, 7, 8, 24, 27, 34, 37]. At the centre of these rotational symmetric electric field distributions a local field minimum can be observed. As STEM-DPC is only capable of measuring the transferred momentum perpendicular to the beam propagation, no momentum transfer can be observed at the centre of the atom as the electric field emerging from the nucleus is parallel to the beam propagation direction [8, 34]. Local field minima are also observed along the connecting directions of each pair of neighbouring atomic columns and within each hexagonal W-Se ring (white arrows in Figure 4.1 c). These local field minima are due to an overlap of opposing electric fields. Due to the close distance of neighbouring atomic columns, the local field minima appear sharp along the connecting directions between two atomic columns whereas the field is gradually decreasing towards the centre of a W-Se ring. The potential overlaps also lead to a deformation of the expected rotational symmetric field distributions at atomic columns and result in triangular-shaped electric field distributions around atomic columns. This triangular shape is indicated in Figure 4.1 c) by the dashed triangles and has been observed in STEM-DPC images for other, comparable materials with such a hexagonal structure, e.g. graphene [34], hBN [35] and MoS_2 [27].

The triangular shape of the electric field distribution is more pronounced in the corresponding electric field magnitude map depicted in Figure 4.1 d). Here, the triangular shape is clearly visible and indicated by the black dashed triangle in the measured and simulated images. Furthermore, the discussed local electric field minima due to field compensation are indicated by black arrows.

For both, the measurement and the simulation, the extension of the triangular regions with high electric field magnitude is different for selenium and tungsten atomic columns. For selenium atomic columns these triangular regions are slightly larger than those of tungsten atomic columns. Furthermore, the electric field magnitude of these regions is different. Unexpectedly, the electric field distribution shows a higher electric field magnitude for the selenium atomic columns than for the tungsten atomic columns. This is unexpected as tungsten atomic columns have a higher atomic number and should therefore lead to higher electric field magnitudes. Although it is not easily identified in the DPC images, this higher electric field can also be observed in the DPC images in Figure 4.1 c). There, the rotational symmetric colour wheels at selenium atomic column positions show a slightly higher saturation than the electric field distribution around tungsten atoms, corresponding to a higher electric field magnitude.

Although, the experimental and simulated HAADF images in Figure 4.1 a) look almost identical, the electric field magnitude maps disclose several small differences worth looking at. The simulated electric field magnitude map (Figure 4.1 d) right) shows a triangular electric field magnitude around each atomic column position with an almost homogeneous electric field magnitude distribution. However, the corners of the triangles exhibit slightly higher electric field magnitudes than the edges. In contrast, the measured electric field magnitude map shows a deformation of the triangular electric field distribution in form of an elongation of triangles to the upper right, especially visible for the selenium atomic columns. In addition, a non-homogeneous magnitude is observed with a local field magnitude maximum observed for the upper right corner (white arrow) and a reduced electric field magnitude is observed for the lower right corner. Furthermore, the electric field magnitude at tungsten atomic column positions exhibits a reduced magnitude along the lower edge. The larger differences between measured and simulated images in case of STEM-DPC compared to STEM-HAADF are due to the higher sensitivity of STEM-DPC to the atomic number, specimen tilt, and residual lens aberrations [26, 189]. The observed effects presumably arise due to specimen tilt and residual lens aberrations. It is noteworthy that these parameters affect the DPC signal more strongly than the HAADF signal as STEM-DPC uses primarily the direct beam [26, 189]. Features introduced by lens aberrations and specimen tilt are therefore more readily observed in DPC images. The impact of lens aberrations is studied in more detail in Chapter 4.2.

Figure 4.1 e) and f) display the scattergrams of the measured and simulated DPC images. Both scattergrams are obtained from a region of about $1.2 \times 1.2\,\mathrm{nm}^2$ for a better statistics, as the DPC images shown in Figure 4.1 c), d) and g) are only sections of a larger scan area. The two scattergrams show an inner rich structure with high intensity, resulting from the DPC signals with high occurrence, and outer disk-shaped features of pixels with low intensity. The inner part exhibits a structure which is a vertically elongated hexagon. Due to the close distance to the scattergram centre, these hexagons are related to interatomic pixels where the electric field magnitude is small. The six tips at the corners including the two y-shaped tips of the hexagon-like feature show a pronounced intensity in the measurement and the simulation (indicated by the four white dashed circles and the two angled solid lines in Figure 4.1 e) and f). The higher intensity at these positions indicates a high number of pixels in the DPC image which correspond these deflections in the magnitude and direction interval i. e. pronounced yellow, red, pink, blue, cyan and green areas. Due to the hexagonal lattice structure and the overlap of neighbouring atomic electric fields, some directions are slightly suppressed compared to others, e. g. the direction corresponding to an orange or purple pixel colour. This results in the hexagonal tapering of the inner feature.

Overall, the hexagon-like feature of the scattergrams is centred around the scattergram centre and extends to a maximum deflection magnitude of about 0.14 mrad for the measurement and about 0.23 mrad for the simulation. Here again, measurement and simulation differ quantitatively by a factor of about two as explained for the electric field magnitude maps. Besides the different deflection magnitudes, the scattergram of the measured DPC image shows a slight deformation in the vertical direction. There, the hexagon top edge is found at a slightly larger distance to the scattergram centre than the bottom edge. This means a higher deflection magnitude for the electric field direction corresponding to pixel colour of yellow and green. Such preferential directions are typically introduced by different kinds of residual lens aberrations, as discussed later in Chapter 4.2.

In addition to the extending corners at the top and bottom of the inner feature, both hexagons show two y-shaped local maxima on the left and right of the centre which are indicated by the white v-shaped lines. In the scattergram of the simulation, these y-shaped maxima are exactly horizontally aligned with the scattergram centre and exhibit the same extension resulting in a symmetric appearance of the inner hexagon-shaped feature (Figure 4.1 f). However, the scattergram of the measured DPC image shown in Figure 4.1 e) is slightly deformed, resulting in an imperfect horizontal alignment of the y-shaped features. The right y-shaped local maximum in scattergram intensity is shifted downwards and exhibits a less pronounced y-shape.

From the pronounced scattergram intensities of the two hexagons, it can be deduced that most of the DPC image pixels have a weak deflection. These features close to the scattergram centre with weak deflection magnitudes correspond to interatomic pixels in the DPC image. As these interatomic pixels are strongly influenced by the neighbouring atomic fields, the overlap of opposing electric field components is clearly reflected by the hexagonal shape.

Both scattergrams additionally show two diffuse disk-shaped features with a ring of slightly higher pixel intensity than the average scattergram intensity (indicated by the dashed green and grey lines). Due to the large extension of the rings they correspond to higher deflection magnitudes than the hexagon. The scattergram obtained from the simulation in Figure 4.1 f) shows an inner disk (grey dashed line) and an outer disk (green dashed line). Both disks are mostly circular with a minimal triangular deformation. In accordance with the discussed difference in electric field magnitude between tungsten and selenium atomic columns, the outer disk is assigned to selenium atomic columns and the inner disk with a slightly lower deflection magnitude to the tungsten atoms. The triangular shape is again due to the suppression of certain electric field directions due to the field compensation. The scattergram obtained from the measurement also shows the two disks corresponding to deflections introduced by selenium (green dashed line) and tungsten (grey dashed line) atomic columns. It shows that selenium atomic columns have a pronounced beam deflection in the upper right direction corresponding to a yellow pixel colour. These two features are not clearly separated as it is the case for the simulation but are slightly deformed presumably due to residual lens aberrations in the measurement.

Figure 4.1 g) depicts the measured (left) and simulated (right) charge density maps calculated from the corresponding electric field distributions using Maxwell's equation (Chapter 2.5). These charge density maps indicate a net positive charge density by red pixels and a negative charge density by blue pixels. As expected, the positive charge density is localized at the position of the atomic columns due to the strong influence of the positively charged nucleus [27, 34]. The negative charge density is delocalized and surrounds the atomic columns. In contrast to the almost perfectly circular positive charge density of the simulated charge density map, the measured charge density map shows deformed spots of positive charge density at the position of the atomic columns. The deformation is more pronounced for the selenium atomic column positions where the positive charge density exhibits a spike-like feature at the left of the selenium atomic columns (exemplarily indicated by the dashed black line in g). Compared to this, the positive charge density at tungsten atom positions are only slightly elongated. The deviation from the perfectly round-shaped positive charge distribution is presumably due to the presence of residual lens aberrations.

For quantitative analysis, Figure 4.1 h) displays line profiles of the charge density for the simulation (black line) and the experiment (blue line). The line profiles are integrated over the regions indicated by the black and blue boxes in Figure 4.1 g). It can be seen that the measured and simulated charge densities are different, but again in the same order of magnitude. More importantly they exhibit a similar behaviour. Both line profiles show four peaks of positive charge density corresponding to selenium and tungsten atomic columns, which can be grouped in two peaks stemming from the Se-W dumbbell structure. Based on the HAADF line profile shown in Figure 4.1 b) the left peak of the charge density of a W-Se dumbbell corresponds to the selenium atomic column and the right peak to a tungsten atomic column. Between the peaks of one atomic dumbbell the charge density drops to negative values. Between the two dumbbells, which corresponds to the area in a W-Se hexagonal ring, the charge density is only slightly negative or almost neutral.

Unexpectedly, the selenium peaks of the two dumbbells show a higher positive charge density than the tungsten peaks of the dumbbells. This suggests that the selenium atomic columns consisting of two selenium atoms exhibit a higher projected charge density than the single tungsten atoms. This is an unexpected observation as the projected atomic number of two selenium atoms is still lower than the projected atomic number of the single tungsten atom. Based on the DPC theory and the described linear Z-dependency of the DPC contrast mechanism, one would expect the tungsten atom to show a higher charge density than two selenium atoms as DPC imaging is sensitive to the projected potential which is assumed to be proportional to the projected atomic number and the number of atoms in the atomic column (Chapter 2.5). This unexpected finding for the ratio of positive charge densities is also observed for other transition metal dichalcogenides (e. g. MoS_2 [27, 42]), where the chalcogen atomic columns with lower projected atomic number show a higher charge density than the metal atomic column. The origin is attributed to residual lens aberrations, in particular the three-fold astigmatism [40, 42]. However, since the simulation shown here is performed without any residual lens aberrations but still exhibits the unexpected charge density ratio, lens aberrations cannot be the origin for the here observed unexpected charge density distribution in the WSe_2 monolayer.

As seen by the comparison of the measured and simulated DPC images of a WSe_2 monolayer shown in Figure 4.1, a high similarity in electric field and charge density distributions is achieved. However, differences remain, whose origins need to be investigated to ensure a correct interpretation of the derived quantities. As described in this section, the following differences between simulation and measurement as well as unexpected behaviours are found:

i) The measured electric field magnitude map exhibits lower absolute values than the simulated electric field magnitude map.

ii) A deformation of the triangular-shaped electric field around atomic columns with a non-uniform distribution of the electric field magnitude within these triangles is observed in the measurement.

iii) In the scattergram of the measurement, the outer ring-shaped features are triangularly distorted and overlap with each other.

iv) The inner structure of the scattergram is asymmetric with the upper half showing higher deflections than the lower half for the measurement, unlike in the simulation.

v) The two local y-shaped maxima near the scattergram centre are not horizontally aligned in the experimental case.

vi) The expected circular positive charge density at selenium atomic columns shows spike-like features in the measurement which are not visible in the simulation.

vii) For both, the measurement and the simulation, the charge density of selenium atomic columns is higher than that of tungsten atomic columns.

There are several possible origins which might lead to these observed and unexpected features in the DPC images: (a) Scan distortions and specimen drift are common problems in high-resolution STEM imaging but are not considered in the shown simulation. Based on the great agreement between DPC measurement and simulation it is not expected that these cause such pronounced and directional features in the electric field distribution. (b) Since the simulation was performed using the same microscope and detector parameters as in the experiment but without any lens aberrations, the features described in i)-vi) most probably arise due to residual lens aberrations present during the measurement. (c) Furthermore, the segmented detector and its geometry might alter the measured and simulated electric field distribution and may lead to unexpected features in the atomic electric field distribution for a WSe_2 monolayer. Thus, different microscope- and imaging-related parameters such as lens aberrations and the detector geometry need to be investigated to correctly interpret the derived DPC images.

As lens aberrations are assumed to have the strongest influence on STEM-DPC images and their presence may lead to the observed artefacts in the electric field magnitude, Chapter 4.2 investigates the influence of different lens aberrations and their combinations on the electric field and charge density distributions. First, a general overview of the influence of the two most prominent lens aberrations is given and then a combination of lens aberrations is discussed to explicitly describe the features observed in the measurement of the WSe_2 monolayer.

Moreover, the unexpected charge density ratio between selenium and tungsten atomic columns described in point vii) can presumably not be explained by lens aberrations as it is also observed for the simulation without any residual lens aberration. This finding must therefore have a different origin. It might arise from the detection of DPC signals using a segmented detector which has a limited momentum space resolution due to the limited number of segments (Chapter 2.5). Furthermore, the illumination of the detector and the segments used for signal processing might introduce this unexpected behaviour as both influence the sensitivity of the measurement. Chapter 4.3.1 and 4.3.2 will therefore investigate the influence of the limited number of segments and the geometry of a segmented detector.

Another possible reason for the unexpected charge density distribution might be in the material structure itself. Like all TMD monolayers, WSe_2 consists of three atomic planes at different z-positions with respect to the incident electron beam, where the metal atomic plane is sandwiched between the two chalcogenide atomic planes (Chapter 2.7). Selenium atomic columns consist of two atoms instead of one single atom for tungsten atomic columns and the tungsten has another z-position than the selenium atoms. Therefore, the electron beam propagation is likely to be altered differently by the two selenium atoms compared to a single tungsten atom. To gain an insight into the quantitative analysis of DPC images, the influence of different atoms and the stacking of atoms is investigated in Chapter 4.4.

Section summary

- The STEM-DPC measurement of a WSe_2 monolayer shows rotational symmetric electric field distributions around each individual atomic column which exhibit a triangular shape due to the overlap of opposing electric field components from neighbouring atomic columns. The observed field distribution is in good agreement with the atomic electric field distribution obtained by the multislice image simulation.

- The electric field magnitude map highlights the triangular-shaped field distributions around the individual atomic columns and shows a non-uniform distribution with local maxima at the upper left corner in the vicinity of selenium atomic columns.

- Quantitatively, measured and simulated electric field and charge density distributions differ by a factor of about two. This factor is already reported in literature but the origin is not known yet.

- The derived charge density distribution shows positive charge densities at the position of the individual atomic columns and negative charge densities surrounding the atomic column positions. A good agreement of measurement and simulation is observed.

- Unexpectedly, a higher electric field magnitude and a higher positive charge density is found at selenium atomic columns compared to the tungsten atomic columns. This is in contrast to the linear relationship of the DPC signal magnitude to the projected atomic number (Chapter 2.5). This unexpected behaviour is observed in both, the measurement and the simulation.

- Several aspects in terms of microscope and imaging related parameters as well as the specific atomic structure of WSe_2 need to be studied to understand the observed unexpected features in the above results.

4.2 Influence of Lens Aberrations on quantitative DPC Imaging of 2D Materials

Lens aberrations limit the resolution in STEM imaging, however, owing to state-of-the-art lens aberration correctors, a spatial resolution in a sub-atomic regime is possible. Although these correctors allow to significantly minimize lens aberrations up to a high geometrical order, residual lens aberrations are still present in STEM imaging. Since DPC imaging uses the coherent part of the post-specimen intensity distribution, i. e. mostly the direct beam, DPC imaging is sensitive to lens aberrations [26, 189]. It is even more sensitive to lens aberrations than HAADF imaging, which is based on the incoherently scattered electrons. As the electric field distribution obtained by DPC is a convolution of the specimen potential and the electron probe, any change in the shape of the electron probe due to aberrations will be transferred to the DPC image, also altering the measured electric field distribution. Changes introduced by lens aberrations do not correspond to an actual change in electric field distribution as they arise due to a deviation of the electron probe from an ideal round-shaped spot. Therefore, the investigation of the influence of lens aberrations on the DPC signal is of great important for a detailed understanding of experimentally obtained electric field distributions. Bürger et al. theoretically studied the influence of different low-order lens aberrations and their combination by DPC image simulations of 20 nm thick $SrTiO_3$ [26]. The paper gives a great overview over the general changes in DPC signal and arising features in the electric field distribution for the most prominent lens aberrations during STEM measurements. Their analysis focuses on a range of specimen thicknesses and only one material system. However, the artefacts induced by lens aberrations might depend on the specimen thickness and the atomic structure, as dynamic diffraction effects for different structures including a different overlap of atomic potentials might drastically impact the DPC image features which are induced by lens aberrations. The following discussion therefore focuses of the influence of lens aberrations and their combination on the electric field distribution of just a single WSe_2 monolayer. To understand the general impact of lens aberrations on DPC imaging, the two most common lens aberrations, defocus as well as 2-fold and 3-fold astigmatism, are investigated by DPC image simulations using the software Dr. Probe [63]. As these two lens aberrations are only stable for a few minutes and need to be corrected manually by the operator, different combinations of lens aberrations are simulated. Based on the simulations, lens aberration combinations are evaluated to investigate the introduced artefacts in the electric field distribution. By this, an estimation of the residual lens aberrations present in the previously shown DPC measurement of a WSe_2 monolayer is done (Figure 4.1).

To investigate the influence of 2-fold astigmatism (A1) and defocus (f) on the electric field and charge density distributions of a WSe_2 monolayer multislice image simulations were done using the software Dr. Probe. Except of the two lens aberrations, all other parameters remain constant. Defocus and astigmatism were varied between -3 nm and +3 nm in steps of 1 nm. For the defocus positive values correspond to an overfocus and negative values correspond to an underfocus. The simulation parameters are given in

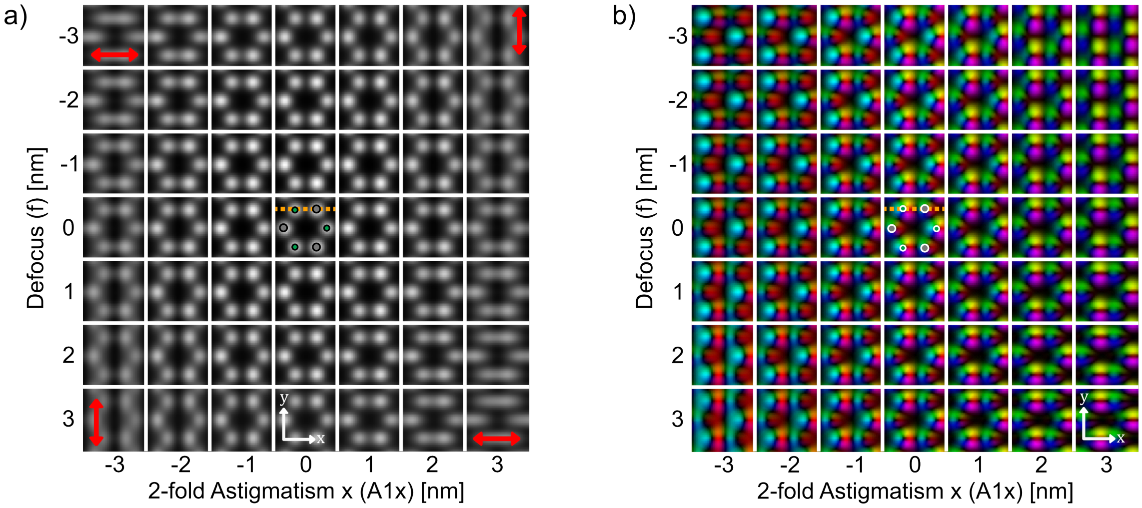

Figure 4.2: a) HAADF and b) DPC image simulations of a WSe_2 monolayer for different combinations of 2-fold astigmatism and defocus. Both lens aberrations where varied between -3 nm and +3 nm in steps of 1 nm. The 2-fold astigmatism is applied in x-direction, which is parallel to W-Se dumbbell axis indicated by the dotted orange line. For the lens aberration free simulation, the atomic column positions are marked by green and grey dots for selenium and tungsten, respectively. Positive focus values correspond to an overfocus and negative correspond to an underfocus. The individual DPC images are normalized to their respective maximum value.

Table 9.4 in the Appendix. Figure 4.2 a) depicts HAADF images for different combinations of defocus and 2-fold astigmatism. In the absence of 2-fold astigmatism, defocus leads to a non-directional blurring of the HAADF image contrast. The individual atomic columns can still be identified even though the contrast is reduced. This is visible by the reduced brightness of pixels close the atomic column positions compared to the pixels at vacuum regions. As expected, negative defocus values which correspond to an underfocus lead to slightly less blurry image compared to the same values of overfocus due to the reshape of the electron beam inside the specimen. For small over- and underfocus values (≤ 2 nm) the influence is difficult to identify in the HAADF images.

For the depicted values of 2-fold astigmatism, a non-directional blurring of the atomic columns is observed in the absence of defocus (f=0 nm).

Depending on the orientation of the lens aberrations in reference to the atomic structure of WSe_2, different directions are expected to result in differently shaped features in the images. Positive values of 2-fold astigmatism in x-direction in combination with overfocus lead to a blurring pronounced in horizontal direction which results in merging of the HAADF image intensity of the two dumbbell atomic columns. Negative values of 2-fold astigmatism in combination with overfocus show a directionality in the vertical direction which results again in a blurring pronounced in this direction but due to the larger distance between the atoms along this direction compared to the W-Se dumbbell distance the individual atomic columns can still be distinguished. Changing the defocus value in presence of 2-fold astigmatism changes the direction of the blurring from horizontal to vertical and vice versa depending on the combination of the sign of defocus and 2-fold astigmatism. Therefore, for the hexagonal structure of WSe_2 with its six-fold symmetry the direction of lens aberrations

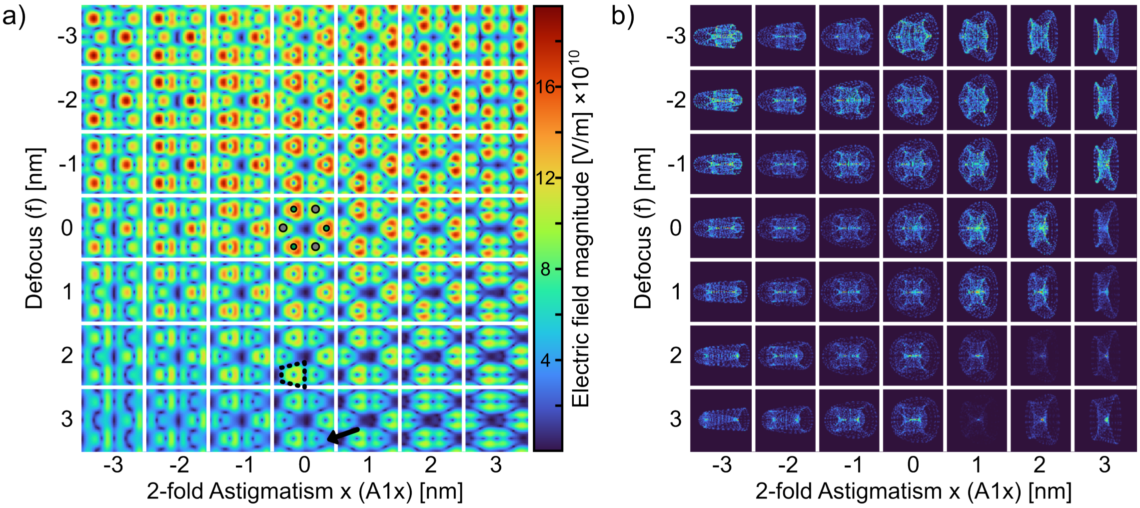

Figure 4.3: a) Electric field magnitude maps and b) scattergrams for the different combinations of 2-fold astigmatism and defocus. The individual scattergrams are normalized to their respective maximum value.

is of great importance. Overall, the combination of 2-fold astigmatism and defocus leads to an increase of the influence of astigmatism which results in stripe-like features for the highest shown values of lens aberration (indicated by the red arrows in Figure 4.2 a).
The HAADF image tableau for the different combination of defocus and astigmatism in Figure 4.2 a) shows that the influence is only visible for absolute values above 2 nm which makes it difficult to identify these lens aberrations during the measurement especially in context to the typically more noisy HAADF images.
Figure 4.2 b) shows the corresponding tableau of colour-coded DPC images. The influence of defocus in the absence of 2-fold astigmatism is barely visible within the DPC images as the rotational symmetric electric field distribution around atomic columns almost remain the same as without lens aberration. However, for 2-fold astigmatism at zero defocus the influence can be observed even for ±1 nm of astigmatism by the change in colour distribution around the atomic columns. For -1 nm astigmatism, the rotational symmetric electric field distribution is compressed along the vertical direction with pronounced cyan areas. For the corresponding positive value of astigmatism the electric field distribution around the atomic columns is compressed in horizontal direction leading to pronounced purple colour. With increasing values of astigmatism the electric field distribution around the atomic columns gets more compressed and some colours along the compression direction even vanish e.g. red and cyan for +3 nm astigmatism. Again, for the combination of the two lens aberrations, the effect is again enhanced as can be seen from the DPC images at the corners of the tableau in which individual colour wheels at the atomic column positions can not be identified.
To investigate the impact of the two lens aberrations on the electric field magnitude, Figure 4.3 a) shows the corresponding electric field magnitude maps for the different combination of defocus and 2-fold astigmatism. For the highest values of astigmatism and defocus, the electric field distribution is distorted and no triangular-shaped electric field magnitude around the atomic columns can be identified. Furthermore, a compression

of the triangular-shaped electric field magnitude around the atomic columns along the vertical direction for negative values of 2-fold astigmatism and along horizontal direction for positive values of 2-fold astigmatism is evident. The electric field magnitude itself changes in dependence on the combination of astigmatism and defocus which is expected due to the aberration induced changes of the wave front of the electron beam. This change of the wave front leads to a (directional) broadening of the electron probe intensity on the specimen. As a broader probe interacts with a larger specimen area, potential variation across the electron beam diameter lead to a blurring of the atomic fields in the DPC image. The electric field magnitude tableau shows that an overfocus (positive defocus values) always results in a reduction of the maximum electric field magnitudes despite local directional enhancements of the measurable electric field magnitude by 2-fold astigmatism. The reduction in the maximum electric field magnitude compared to a focus of zero is about 54% (A1x=0 nm and f=3 nm). This finding possibly – or at least partially – explains the difference in the electric field magnitudes of the measurement and the simulation of the WSe_2 monolayer shown in the previous Chapter 4.1 which differed by a factor of about 2. The presence of 2-fold astigmatism in combination with underfocus in the considered range, however, leads to an increase of about 7% of the maximum electric field magnitude (A1x=-1 nm and f=-1 nm) compared to the simulation without lens aberrations. Thus, overfocus has a stronger influence than underfocus for the same range of absolute values close to ideal focus conditions. Comparing the tableau of the HAADF images in Figure 4.2 a) and the tableau of the electric field magnitude maps in Figure 4.3 a) for the different combinations of lens aberrations shows that the DPC imaging is more sensitive to small residual lens aberrations than HAADF imaging. Since DPC imaging uses primarily the direct beam and is therefore comparable to bright-field imaging this is an expected behaviour [26, 189]. Therefore, it is difficult to find optimum defocus conditions during the experiment and slight variations in the electric field magnitude between the measurements are therefore inevitable.

Furthermore, the electric field magnitude maps reveal significant changes in the shape of the electric field distribution around atomic columns even if only defocus is present. For high overfocus, the initially triangular-shaped electric field magnitude around the atomic columns gets more trapezoidal with vanishing contrast at the tips (indicated by the black dotted box and the black arrow in Figure 4.3 a). Contrary, for high underfocus values the triangular-shaped electric field magnitude around the atomic columns mostly remains its shape, but the tips get slightly more pronounced.

The electric field magnitude map reveals more artefacts induced by the lens aberration, however, the change in direction can not be identified from the magnitude maps. In addition, it is difficult to access the impact of residual lens aberrations on the complete DPC image by analysing only individual features of the DPC images. Therefore, a representation of the whole electric field distribution within the image including the direction and magnitude would be more suitable for the identification of lens aberrations and their influence on the electric field distribution. Bürger et al. introduced the so-called scattergram and applied it to analyse residual lens aberrations in DPC images by the shape and features of the scattergram [26]. The scattergram is a 2D histogram of the DPC image revealing the number of pixels in a certain deflection direction and magnitude interval. The histogram displays the direction by the azimuthal position as well as the magnitude by the distance to the scattergram centre. Figure 4.3 b) displays the tableau of scattergrams for the DPC image simulations with different lens aberration combinations (Figure 4.2 b). Each individual scattergram is normalized to the maximum intensity for better visibility. In presence of 2-fold astigmatism a compression of the scattergram is observed which is directly related to the electric field distribution. Depending on the direction, either a horizontal or a vertical compression is observed. In addition, even changes in defocus are distinguishable by the scattergram. For overfocus values, the maximum scattergram intensity shifts towards the centre of the scattergram meaning that more pixels of the DPC image have a smaller deflection magnitude. This is in accordance to the observed electric field magnitude reduction visible in the tableau of the electric field magnitude maps in 4.3 a). For overfocus in the absence of 2-fold astigmatism pronounced y-shape features at the horizontally aligned tips of the inner hexagon form. The y-shape is more pronounced for the left side compared to the right. This behaviour is comparable with the observed different extension of the y-shaped features in the measurement, indicating that about 1 nm of overfocus was present during the measurement.

Interestingly, the compression of the scattergram either in horizontal or vertical direction for high values of 2-fold astigmatism is independent of the defocus. This contrasts the observed changes in the blurring of the HAADF image, where in presence of 2-fold astigmatism the direction of pronounced blurring changes by 90° between over- and underfocus (red arrows in Figure 4.2 a). This highlights the completely different behaviour of the introduced artefacts of lens aberrations for coherent DPC imaging and conventional, incoherent STEM imaging. Therefore, a detailed analysis of the influence of lens aberrations on the DPC signal is important for a correct interpretation of atomic electric field distributions.

Besides the electric field distribution the charge density distribution is another quantity of interest derived from DPC measurements. Even though the charge density distribution is derived from the electric field distribution, it is interesting to study the impact of lens aberrations on the charge density distribution as the differentiation when calculating the charge density from the electric field distribution alters the influence and features introduced. The tableau of charge density maps for different combinations of defocus and 2-fold astigmatism in x-direction is shown in Figure 4.4. The charge density maps reveal a response on the presence of residual defocus and 2-fold astigmatism which is comparable to the one of HAADF images shown in Figure 4.2 a). For the highest absolute values of the two lens aberrations, the positive charge density at the atomic column positions becomes elongated. For high values of defocus in combination with 2-fold astigmatism, the positive charge density features merge together with neighbouring atomic columns. Again, a directionality in horizontal or vertical direction, similar to the HAADF images, is observed. The direction depends on the combination of over- and underfocus with 2-fold astigmatism and is indicated by the black arrows in Figure 4.4. Not only the positive charge density at the atomic columns gets elongated but also stripe-like features occur within the negative charge density due to the change in the incident wave front introduced by the

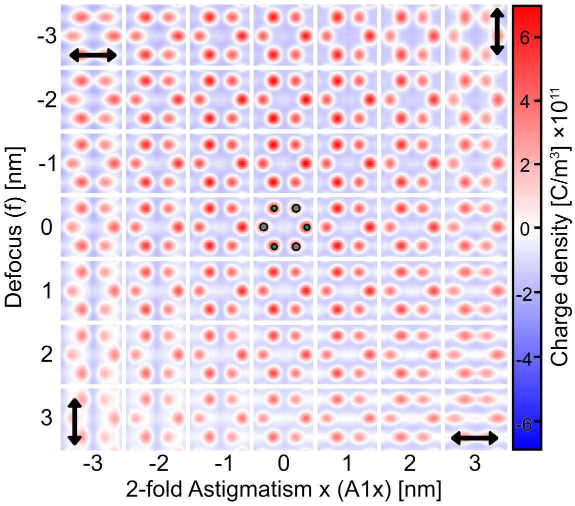

Figure 4.4: Tableau of the charge density maps for different combinations of defocus and 2-fold astigmatism in x-direction.

lens aberrations. The overfocus leads to a reduction in the measured charge density not only for the positive but also in the negative charge density. Compared to the electric field magnitude maps and the scattergrams, the influence of 2-fold astigmatism is less visible in the charge density distributions and the introduced features are comparable to the features in the HAADF images. The influence of 2-fold astigmatism can be recognized for higher values compared with the stronger impact on the electric field magnitude maps and the scattergrams.

Although the combination of defocus and astigmatism leads to an elongation, the previously seen spike-like features in the measurement in Figure 4.1 g) are not observed in the here shown simulations. Thus, also other lens aberrations must be present during the measurement.

To identify the lens aberrations present during the measurement multislice images simulations of various combination of different lens aberrations and orientations were done which can be reviewed in the Appendix 9.14. Here, only a selection of lens aberration combinations and images are shown to understand the features in the measured electric field distribution of the WSe_2 monolayer discussed in the previous chapter. Figure 4.5 a) depicts the electric field magnitude maps influenced by 2-fold astigmatism in x-direction and 3-fold astigmatism in y-direction. In general, the influence of a lens aberration reduces with increasing geometrical order (Chapter 2.1) [26]. Therefore, higher values of the higher geometrical order lens aberration are used for 3-fold astigmatism compared to the values used for 2-fold astigmatism. The presence of 3-fold astigmatism in y-direction without any 2-fold astigmatism leads to a local increase of the electric field magnitude at one corner of the triangular-shaped field distribution around the atomic columns and to local reduction on the opposite edge of the triangle. These local field reductions and enhancements are indicated by black arrows in Figure 4.5 a) for positive aberration values. The same trend is observed for negative values but the position of the local maxima and minima is changed. In combination with 2-fold astigmatism of ±1 nm, the triangular shaped electric

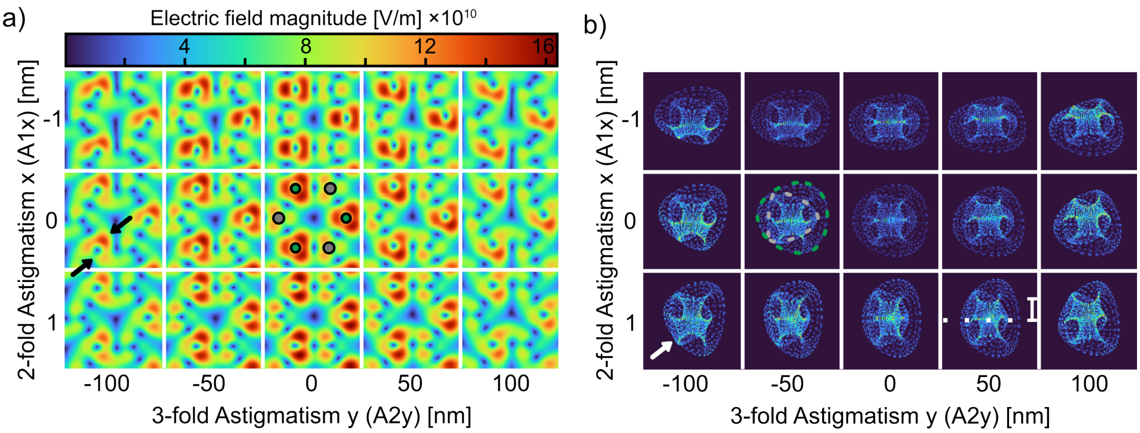

Figure 4.5: a) Electric field magnitude maps and b) normalized scattergrams for different combinations of 2-fold astigmatism and 3-fold astigmatism. The atomic column positions are exemplarily marked by green and grey dots for selenium and tungsten, respectively. The individual scattergrams are normalized to their individual maximum for a better visibility of the features.

field distribution is further distorted and starts to vanish in combination with ±50 nm of 3-fold astigmatism. The local field maxima induced by 3-fold astigmatism in y-direction is in great agreement with the local field maxima observed in the monolayer measurement (Figure 4.1 d).

To estimate the amount of residual 3-fold astigmatism, the scattergram of the measurement is compared with the scattergrams of the here shown simulations. Figure 4.5 b) shows the tableau of scattergrams for the DPC image simulations with different combinations of 2- and 3-fold astigmatism. It is clearly visible, that the here shown values of both lens aberrations lead to drastic changes in the scattergram. Even for only 1 nm of 2-fold astigmatism, the scattergram is significantly elongated in vertical direction. Furthermore, the 3-fold symmetry of 3-fold astigmatism is reflected in the scattergrams even for only 50 nm 3-fold astigmatism in y-direction by the inner 3-fold structure. The shown scattergrams are more strongly distorted by the lens aberrations than the obtained scattergram from the measurement (Figure 4.1 d) which means that the amount of lens aberrations can be estimated with this tableau. It also means that the residual 2-fold and 3-fold astigmatism in the experiment is at least smaller than 3 nm and 100 nm, respectively. The actual lens aberrations in the experiment hence surpass the values specified by the corrector manufacturer with $A1 \leq 10$ nm and $A2 \leq 100$ nm. Moreover, the tableau indicates trends of scattergram distortion depending on the lens aberration.

The most obvious scattergram deformation due to 3-fold astigmatism is visible by the shape of the inner scattergram structure. With increasing 3-fold astigmatism the inner hexagonal structure is deformed to a three-fold rotor. Depending on the sign of the aberration this rotor-like feature is flipped by 180°. In absence of 2-fold astigmatism, the initially hexagonal inner rich structure of the scattergram transforms to a three-fold structure when 3-fold astigmatism is present. This is in agreement to the phase shifts of the wave front introduced by 3-fold astigmatism as shown in the Figure 2.2 b) in Chapter 2.3.

In addition, it introduces an asymmetric elongation of the scattergram which leads to the situation, that one half of the inner scattergram structure extends more to higher deflections than the other. This is exemplarily indicated in Figure 4.5 by the dotted white (inner) and dotted green (outer) lines. This was also observed in the measurement even though it was less visible than for the here shown combination of 50 nm 3-fold astigmatism and 1 nm 2-fold astigmatism.

Furthermore, the 3-fold astigmatism also affects the outer ring-shaped distributions assigned to selenium and tungsten atomic columns, respectively. Starting with almost round-shaped outer rings as described in the previous chapter, 3-fold astigmatism induces a triangular shape. This is indicated by the green and grey dashed shapes in Figure 4.5 b). Furthermore, the rings overlap when 2-fold astigmatism is present, which is exemplarily indicated by the white arrow. The triangular distortion and the overlap of the outer rings in the scattergram were also observed for the WSe_2 measurement, however the distortion of the inner scattergram structure was not that pronounced.

All these trends, such as the triangular shape in the outer rings of the scattergram and the overlapping rings resulting from selenium and tungsten atoms as well as the elongation of the scattergram in vertical direction, were also observed in the measurements which leads to the suggestion that both of these lens aberrations were present during the measurement. As the simulated scattergrams with different lens aberrations shown are more distorted than the one of the measurement, it can be assumed that less than 50 nm of residual 3-fold astigmatism and less than 1 nm of 2-fold astigmatism were present during the DPC measurement of a WSe_2 monolayer (Figure 4.1). Differences presumably stem from a slight overfocus.

Although the aberration correctors allow to compensate these lens aberrations, the here found values of residual lens aberrations are below the specifications of residual lens aberrations defined by the corrector manufacturer e.g. 100 nm for 3-fold astigmatism and 10 nm of 2-fold astigmatism [52, 190]. Even though these values alter the DPC measurement significantly they are not observable in the HAADF images which is due to the lower sensitivity of HAADF imaging on lens aberrations compared to DPC imaging [26, 189]. This makes it difficult to correct them experimentally. Thus, slight values of residual lens aberrations are inevitable. Therefore, a precise knowledge of the influence of lens aberrations on DPC images is important for a correct understanding of the electric field and charge density distributions.

Especially 3-fold astigmatism, with its 3-fold symmetry, is found to strongly influence the high-resolution STEM imaging of 2D TMDs with similar symmetry. Due to the specific symmetry of the 3-fold astigmatism superimposed with the three-fold symmetry of the 2D TMDs in [0001] zone-axis orientation, this residual lens aberration leads to contrast artefacts in conventional STEM images and even results in an inversion of the potential and charge density in STEM-DPC images [40, 42, 190]. For MoS_2, the observed higher charge density at the lower-Z sulphur atomic sites compared to the higher-Z molybdenum atomic sites observed in different experimental DPC measurements [27, 37, 42] is ascribed to be an artefact introduced by a certain orientation of residual 3-fold astigmatism with respect to the crystal structure by Martis et al. [42]. Furthermore, Dosenovic et al. showed

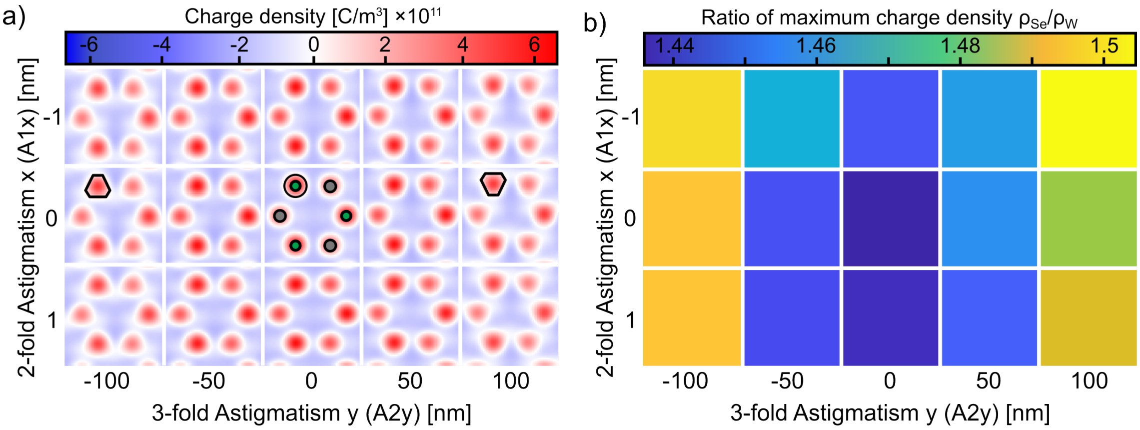

Figure 4.6: a) Charge density maps for the combination of 2-fold and 3-fold astigmatism. The atomic column positions are exemplarily marked by green and grey dots for selenium and tungsten, respectively. b) Ratio of the maximum charge density at the atomic column positions between selenium and tungsten atomic columns.

a comparable behaviour for the projected potential of a WSe_2 monolayer where the introduction of certain values and orientations of 3-fold astigmatism result in an inversion of the projected potential of the two types of atomic columns [40]. Therefore, the presence of 3-fold astigmatism possibly explains the observed unexpected charge density ratio in the measurement of the WSe_2 monolayer shown in Figure 4.1. Thus, the charge density at the selenium and tungsten atomic columns in presence of 3-fold astigmatism is investigated in detail.

Figure 4.6 a) shows the charge density maps for the different combinations of 2-fold and 3-fold astigmatism. The atomic column positions and the type of atomic columns are marked by green and grey dots for selenium and tungsten atomic columns, respectively, and are determined from the charge density map derived from the simulation without any lens aberrations present (A1x=0 nm & A2y=0 nm). In the absence of 2-fold astigmatism, the 3-fold astigmatism leads to a deformation of the positive charge density at the position of the atomic columns which is only barely visible (highlighted by the black shapes in the middle row in Figure 4.6 a). Although the influence of ±1 nm of astigmatism was clearly visible in the electric field distribution shown in Figure 4.5 a), the charge density distribution is less influenced by 2-fold astigmatism. This is presumably due to the additional differentiation of the projected electric field to calculate the charge density. Thus, the charge density is less sensitive to lens aberrations than the electric field distribution.

With increasing 3-fold astigmatism the overall charge density gets slightly reduced as expected for the presence of lens aberrations due to the convolution with an extended probe but the higher positive charge density at the selenium atomic columns compared to the tungsten atomic columns remains for any shown value of 3-fold astigmatism. For a detailed investigation of the influence of 3-fold astigmatism on the positive charge density at the atomic column positions, Figure 4.6 b) shows the ratio in the peak charge density between selenium atomic columns and tungsten atomic columns. For the calculation of these ratios, the maximum charge density at the selenium and tungsten atomic column positions are determined by fitting Gaussian functions to the atomic column positions. This is done for both types of atomic columns, respectively, and the mean value of maximum positive charge density is calculated for each type of atomic column. The ratio between the maximum positive charge density is then calculated by the quotient between mean value of the maximum charge density at selenium atomic columns and the mean value of maximum charge density at tungsten atomic columns. This procedure is done for each charge density map shown in Figure 4.6 a) and displayed as a colour-coded map in Figure 4.6 b). Values of the charge density ratio greater than 1 indicate a higher positive charge density at selenium atomic columns and values below 1 indicate a higher positive charge density at the tungsten atomic columns compared to selenium atomic columns.

In Figure 4.6 b), the ratio is indicated by a colour, where the minimum ratio of 1.44 is indicated by blue and the highest ratio of charge density is 1.5 and indicated by yellow. It can be clearly seen, that the presence of 3-fold astigmatism increases the charge density ratio between selenium and tungsten atomic columns and the smallest value with 1.44 is found for the charge density map in the absence of any lens aberration (A1x=0 nm & A2y=0 nm). Apparently, the ratio in maximum charge density does not drop below 1 for any shown combination of 3-fold astigmatism and 2-fold astigmatism. Therefore, the unexpected ratio is not explained by the presence of residual 3-fold astigmatism. Furthermore, the fact that the charge density map derived from a multislice image simulation without any lens aberrations shows a ratio of 1.44 indicates that the unexpected charge density ratio is not an artefact introduced by residual lens aberrations. However, Ref. [42] and [40] claim that the direction of the 3-fold astigmatism is of importance for the resulting inversion of charge density and potential. Since even the aberration-free simulation show the unexpected behaviour, it does not originate from residual lens aberrations.

But since the orientation of the 3-fold astigmatism is expected to have a strong influence on the introduced artefacts in the DPC measurements, multislice image simulations for different orientations of 3-fold astigmatism are shown in Figure 9.27 in the Appendix 9.14. An analysis of the ratio of maximum charge density between selenium and tungsten atomic columns shows no inversion of the charge density at selenium and tungsten atomic columns (Appendix 9.14). Although Dosenovic et al. used the same material system and the same acceleration voltage, their results on the influence of 3-fold astigmatism differ with the results shown here [40]. This is presumably due to slightly different microscope imaging parameters used, especially the different semi-convergence angles defined by the apertures used. As the aperture limits the contribution of aberrations to the probe by cutting off parts of the probe tail, the variation of the aperture might result in the different observation of the influence of 3-fold astigmatism [191]. Therefore, the influence of different lens aberrations on the electric field and charge density distributions obtained with phase-retrieval methods, such as STEM-DPC and 4D STEM, strongly depend on the specific microscope parameters.

All in all, the unexpected charge density between selenium atomic columns and tungsten atomic columns can not be explained by the residual lens aberrations. Even though different combinations of lens aberrations lead to a distortion of charge density, an inversion of the peak charge density ratio, i. e. a higher positive charge density at the lower-Z selenium atomic columns compared to the one of higher-Z tungsten atomic columns, is not observed.

Section summary

- A qualitative comparison of the HAADF an DPC tableaus indicates a stronger influence of lens aberrations on the electric field and charge density distribution than on the conventional HAADF images.
- 2-fold astigmatism can mainly be seen by the deformation of the rotational symmetric electric field distribution around atomic column positions. The direction of deformation which leads to an elongation at small values depend on the direction of the astigmatism in combination with defocus. A suppression and enhancement of field components is already observed for astigmatism values of less than ±1 nm.
- Although the influence of 2-fold astigmatism is clearly visible in the electric field distribution and magnitude maps, as well as in the scattergram, it is comparable difficult to detect the influence of 2-fold astigmatism in the charge density distribution. There a visible difference is observed for higher values of astigmatism.
- 3-fold astigmatism strongly alters the electric field magnitude within the triangular-shaped features of high field magnitude around the atomic column instead of a deformation of field distribution as it was observed for the 2-fold astigmatism. The 3-fold astigmatism introduces local field enhancements in the triangular-shaped electric field magnitude distribution around individual atomic columns and is therefore identified to be present in the previously shown measurement of the WSe_2 monolayer.
- The lens aberrations not only alter the shape of the field distribution but also the overall magnitude. Typically, an overall reduction of the obtained electric field magnitude is observed in the presence of residual lens aberrations.
- Although 3-fold astigmatism reduces the overall charge density it only slightly influence the ratio of maximum charge density between selenium and tungsten atomic columns. It does not lead to an inversion of the charge density ratio and thus does not explain the observed unexpected charge density distribution of selenium and tungsten atomic columns.

4.3 Influence of the Detector Configuration and Detector Rotation on DPC Images of 2D Materials

When using a segmented detector, different combinations of the segments can be used to calculate the difference signals S_x and S_y (K_x and K_y) for the quantification of electric field distributions. Depending on the detector geometry, i.e. the number and shape of segments as well as the collection angles, different intensities are utilized to acquire a DPC image and, thus, the different detector configurations can introduce artefacts in the obtained electric field distribution. The reason for these artefacts is the weighting of the intensity on the detector with the (phase) contrast transfer function ((P)CTF) which, in dependence of the detector geometry and number of segments, exhibits an anisotropic behaviour for specific spatial frequencies of the object imaged [27, 28, 77, 80, 86, 192, 193]. This anisotropy leads to a non-equal transfer of spatial frequencies to the DPC image and depends on the angle between the spatial frequency vector and the direction of the opposing detector segments [87]. Thus, the way the segmented detector intersects the CBED pattern will alter the DPC image. Theoretically, this anisotropy is described by using the (phase) contrast transfer function which, for segmented detectors, shows the highest contrast transfer along the axes of opposing detector segments [87]. Theoretical considerations of the phase contrast transfer function for multi-segmented detectors in comparison to pixelated detectors can be reviewed elsewhere [83, 87].

The CTF of the segmented detector, or the way of how the segments intersect the CBED pattern, can be changed by rotating the sample or the detector itself [83, 84]. Especially for thin specimen, the symmetry of the detector is assumed to have no significant influence since the CBED pattern is expected to exhibit mostly an intensity gradient than a complex inner rich distribution. For thick specimen diffraction effects typically introduce intensity variation in the central disk of the CBED pattern which exhibit a certain symmetry related to the crystal structure. However, diffraction effects and the resulting symmetry of the inner rich intensity distribution need to be considered even for 2D materials [194, 195]. The superposition of the symmetry of the CBED pattern, introduced by diffraction effects, and the symmetry of the detector, determined by its geometry, gives rise to artefacts in the measured electric field distribution even for specimen as thin as monolayers of TMDs. Therefore, the following chapter briefly discusses the different detector configurations of an eight-fold segmented detector and the influence of the detector rotation for the investigation of 2D-WSe_2.

The investigations are carried out using a 4D-STEM simulation of a WSe_2 monolayer simulated with the software Dr. Probe [63]. By projecting virtual detector segments onto the CBED pattern at each position of the scan, arbitrary detector configurations as well as rotation angles can be extracted. For each scan position and for each detector segment, the signal is then calculated by summing up the CBED intensity within the range of this virtual detector segment. The microscope and detector parameters used for the simulation are comparable to the one experimentally achieved with the microscope and detector used and are listed in Table 9.5. For the acquisition of the virtual signals, the detector

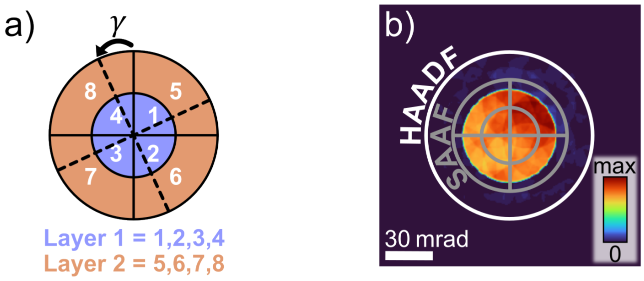

Figure 4.7: a) Layout of the segmented detector consisting of two layers with four quadrants each. The rotation of the detector is given by γ and exemplarily indicated by the dashed lines. b) Simulated CBED pattern of the 4D-STEM data set overlaid with the segmented detector.

configuration shown in Figure 4.7 a) is projected on the CBED pattern and the individual signals are extracted based on the enclosed pixels. The calculation of the DPC signal uses the calibration based on the centre of mass of the detector segments (Chapter 3.2). As the SAAF detector consists of two layers and can be rotated between 0° and 90° as described in Chapter 3.2, the following discussion is restricted to the possible detector configurations and rotation angles. Figure 4.7 a) shows a schematic of the eight-fold segmented detector consisting of Layer 1 (L1) and Layer 2 (L2) which are indicated by the blue and orange segments. The detector rotation is given by γ and corresponds to a counter-clockwise rotation around the detector centre.

For this kind of segmented detector, most commonly a bisected configuration using only Layer 2 is used for DPC image calculation. Thus, the following discussion is restricted to the two layers. Figure 4.7 b) shows a simulated CBED pattern and the projection of the detectors. The segmented detector and the HAADF detector are indicated by the grey and white circles. The detector extension reflects the experimental conditions. The bright field disc of the CBED pattern illuminates about half of the outer layer of the segmented detector and only a small fraction of intensity is scattered to higher angles due to the thin specimen thickness. As can be seen in Figure 4.7 b) the CBED pattern exhibits a complex intensity distribution with a certain geometry dominated by the periodic lattice structure of the WSe_2 monolayer. Due to the size of the individual segments, the intensity of one segment is averaged, although the CBED pattern exhibits a richer structure.

In the following, the influence of the detector configuration on the derived DPC images of a WSe_2 monolayer (Chapter 4.3.1) as well as the influence of the detector rotation are investigated (Chapter 4.3.2).

4.3.1 Influence of the Detector Configuration on DPC Images of 2D Materials

In this chapter, the influence of the different possible detector configurations on the electric field distribution is studied for a fixed orientation between CBED pattern symmetry and detector symmetry. Since the detector configuration alters the contrast transfer function, it also influences the measured electric field distribution and is, thus, of importance for a correct interpretation of DPC images (Chapter 2.5). The following discussion aims to find the detector configuration of an eight-fold segmented detector which generates DPC images with the highest similarity to a DPC image of WSe_2 acquired with a pixelated detector. The scope of this discussion is limited to the three possible configurations achievable by the eight-fold segmented detector at a detector rotation of 0° which are defined as only using Layer 1 (L1) or only Layer 2 (L2), and using both of the layers (L1+L2). Furthermore, the semi-convergence angle is fixed to 30 mrad which is similar to the experimental conditions. A detailed description of the influence of the semi-convergence angle and the influence of different number of segments can be found elsewhere [84, 86, 87]. When performing DPC measurements experimentally, STEM images are acquired for all segments. However, the calculation of the DPC images is typically only done for the segments of the outer layer in a post-processing step. It is suggested to neglect the intensity on the inner layer to reduce image noise as only weakly scattering features are found in the centre of the direct beam [196]. Even though this is reasonable and might be a good compromise for thick specimen, it is not necessarily reasonable to omit parts of the DPC signal for thin specimens such as monolayers of 2D materials.

The CoM-based images, corresponding to images acquired using a pixelated detector, are utilized as reference as the pixelated detector is assumed to represent ideal detection condition due to the higher momentum space resolution [87]. Figure 4.8 shows the DPC image, the electric field magnitude and charge density maps from left to right for the different detector configurations. As a reference the corresponding CoM-based images are depicted in the first row of Figure 4.8 a, e, i), followed by b, f, j) only using Layer 1, c, g, k) only using Layer 2, and d, h, l) using both layers. All these images are acquired from the same 4D-STEM data set, and the segmented detector is virtually generated by the projection of the segments on the data set.

The CoM-based DPC image shows pronounced rotational symmetric electric field distributions around the atomic columns. Due to the small distance between the atoms, a slight triangular shape is observed, which is introduced by the overlap of opposing electric fields of neighbouring atomic columns. However, the influence is barley visible.

Comparing the acquired DPC images (first column in Figure 4.8 a)-d) for the different detector configurations reveals differences in the electric field distribution. For all the different detector configurations, rotational symmetric electric field distributions are found around the atomic column positions. The most distinct changes in the electric field distribution compared to the CoM-based field distribution are observed for using only Layer 1, where pronounced electric fields are visible in the W-Se rings at interatomic pixels in the DPC image (Figure 4.8 b). There, a weak, halo-like electric field distribution surrounding the pronounced rotational field distribution around the atomic columns is visible (indicated by the white hexagonal-shape in Figure 4.8 b). In this region, an additional colour wheel-like field distribution is observed in the hexagonal-shape with the tips extending between two neighbouring atoms and exhibiting different colours as indicated in Figure 4.8 b). The colours indicate a field which points away from the centre of the W-Se ring towards the atomic column positions.

Furthermore, the rotational electric field distribution close around the atomic columns is not perfectly round-shaped, but exhibits a triangular shape, which is more pronounced than for the CoM-based DPC image. The tips of the triangular field distribution point towards the neighbouring atomic columns. A comparable behaviour is also observed for the DPC image acquired by using only Layer 2 shown in Figure 4.8 c), but rotated by 60° compared to the electric field distribution obtained using Layer 1. The triangular shape presumably arises from the superposition of the CBED symmetry with the symmetry of the detector and the anisotropic contrast transfer.

For the electric field distribution acquired with Layer 2, no weak, colour wheel-like field distribution within the W-Se ring is visible and only the colours of the individual atomic columns slightly leak into this interatomic region as exemplarily indicated in Figure 4.8 c) by the white ellipse.

In addition, for both detector configurations (L1 and L2), the triangular-shaped electric field distribution is more pronounced for the tungsten atomic columns (marked by grey dots) than for the selenium atomic columns (marked by green dots). Since this is also observed in the CoM-based DPC image although less pronounced, this is no artefact introduced by the detector configuration. This is presumably due to the different interaction of the electron beam with the atoms within the atomic column, as tungsten atomic columns only consist of one atom and selenium atomic columns exhibit two atoms above one another in case of a WSe_2 monolayer. Here, the investigation is focused on the influence of the detector configuration, but further research about the influence of two atoms above each other is presented in Chapter 4.4. Despite the different rotation of the triangular shaped electric field distribution, the DPC images acquired using either Layer 1 or Layer 2 differ in the extension of the electric fields around the atomic columns. For Layer 1, the atomic electric field distributions are more extended than the atomic electric field distributions around obtained using Layer 2 or the pixelated detector (Figure 4.8 a) & c).

In contrast to only using Layer 1 or only using Layer 2, the DPC image shown in Figure 4.8 d), which is calculated using both layers, does not exhibit this pronounced triangular shape around the atomic columns but is very similar to the electric field distribution of the CoM-based DPC image. Furthermore, no artefacts of extending electric fields at interatomic positions, e. g. within the W-Se ring, are observed. Thus, the pronounced triangular shape seems to be introduced by the limited number of segments using only one layer and omitting parts of the CBED pattern.

The electric field magnitude maps (middle column in Figure 4.8 e)-h) give greater insight into the specific shapes of the atomic electric field distribution. Again, for the CoM-based electric field magnitude map in a) the highest electric field magnitude around the selenium

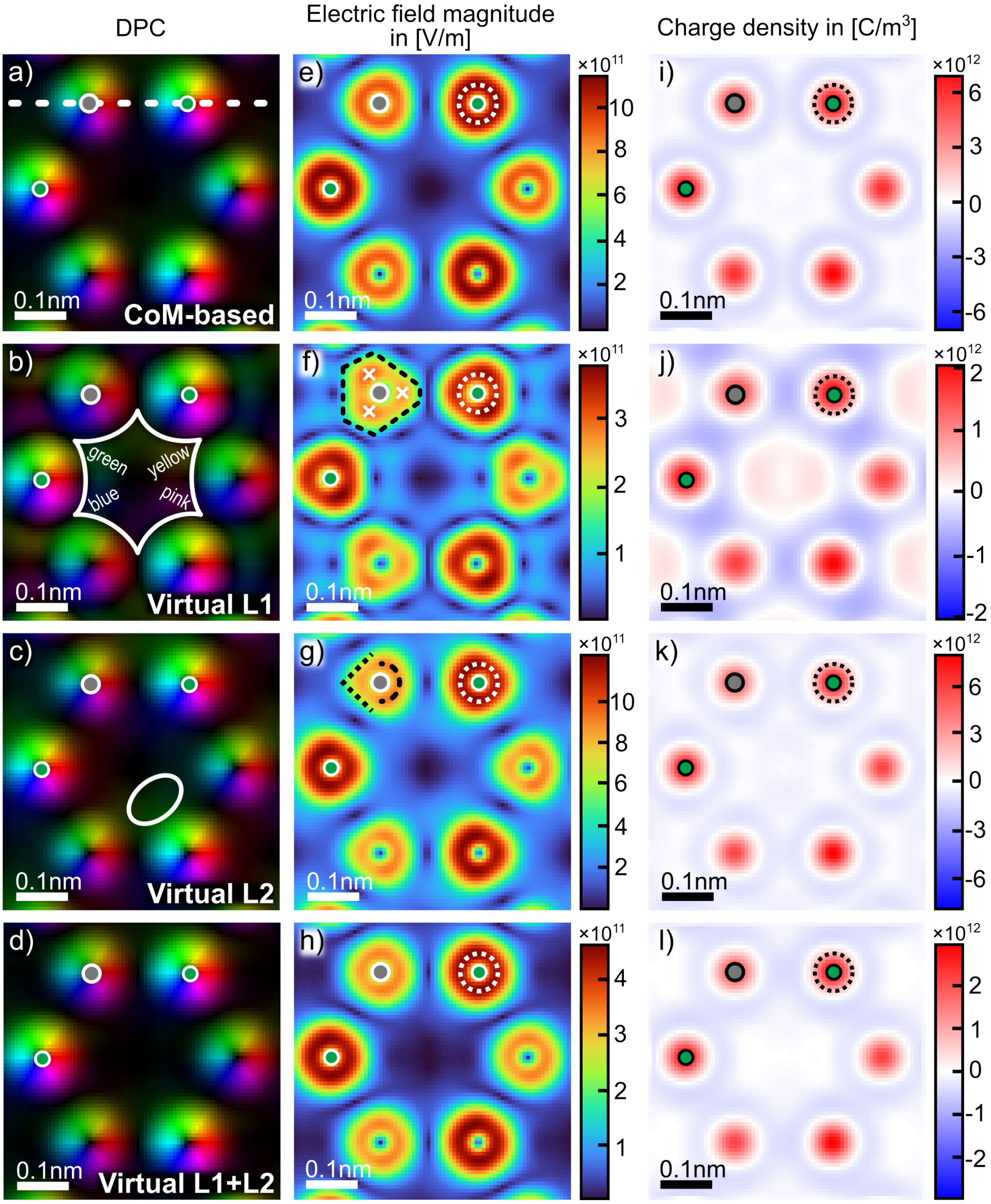

Figure 4.8: a)-d) The colour-encoded DPC images, e)-h) the electric field magnitude maps, and i)-l) the charge density map for different detector configurations. a, e, i) Reference images acquired with a CoM-based approach using a pixelated detector. For the segmented detector b, f, j) only the inner layer L1, c, g, k) only the outer layer L2, and d, h, l) both layers (L1+L2) are used. Green and grey dots mark the atomic column position of selenium and tungsten atomic columns, respectively.

atomic columns is round-shaped (white dashed circle) and the electric field distribution shows only slight triangular shape for the field distribution further away from the atomic column positions. However, the triangular shape is clearly visible when using only Layer 1 (black dashed shape in Figure 4.8 f). There, the electric field distribution around selenium atomic columns deviates from a round shape. Furthermore, the triangular-shaped electric field magnitude around tungsten atomic columns exhibits three pronounced local field maxima at the tips of the triangular shape (exemplarily marked by white crosses). These local field maxima at are not visible when only using Layer 2 (Figure 4.8 g). Thus, these maxima presumably arise due to extension of Layer 1 and by only using the central part of the CBED pattern where the intensity redistribution due to the deflection is less pronounced and superimposed with diffraction contrast. In contrast to Layer 1, the electric field magnitude map obtained only using Layer 2 does not show these local maxima and exhibits more round-shaped atomic electric field distributions around atomic columns. Between a horizontally aligned pair of W and Se atomic columns, the field magnitude in direction of the neighbouring atom is round-shaped (black dashed crescent), comparable to the CoM-based magnitude map, but exhibits for both atomic columns peaks to the opposite direction (black dotted tip). The position of this round-shaped crescent depends on the detector rotation and will be discussed in Chapter 4.3.2.

The triangular shape of the atomic electric field magnitude as well as the pronounced local maxima in the field magnitude at atomic columns are artefacts introduced by using only Layer 1 or only Layer 2 and mostly vanish when using both layers (L1+L2) shown in Figure 4.8 h). For this detector configuration, the electric field magnitude map is almost the same as for the pixelated detector. However, a difference in the electric field magnitudes is observed. The electric field magnitudes acquired with a segmented detector are reduced compared to the electric field magnitude derived of the CoM image but still are in the same order of magnitude.

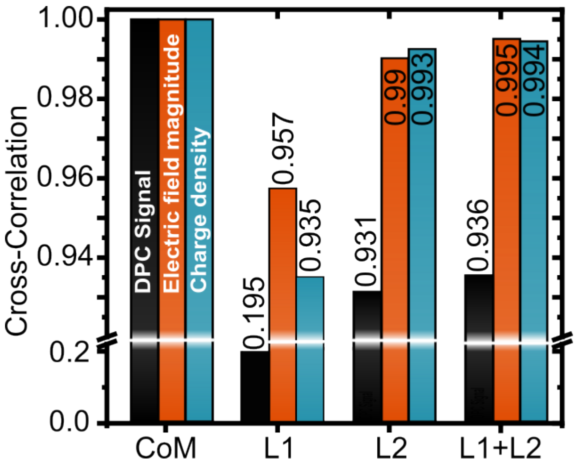

Figure 4.9: Cross-correlation coefficients of the DPC signal (black), the electric field magnitude (orange) and the charge density (blue) calculated in reference to the CoM-based images for the three different detector configurations.

In contrast to the electric field magnitude, the charge density distributions in Figure 4.8 i)-l) reveal only minor changes that are introduced by using the different detector configurations. For all detector configurations, the positive charge density around the atomic column positions is mostly round-shaped and exhibits only a slight triangular deformation when using Layer 1 (Figure 4.8 j). Furthermore, for Layer 1, a positive charge density distribution can be found at interatomic pixels, i. e. in the W-Se ring, where no atom is located. Using only Layer 1 for the DPC image acquisition, thus, leads to delusive artefacts and alters the electric field and charge density distribution significantly in comparison with the ideal CoM-based images. Using only Layer 2 gives a less negative charge distribution around the atomic columns compared to the CoM-based image. Again, using both layers results in a charge density distribution similar to the one obtained from a pixelated detector (CoM-based) (compare Figure 4.8 i) and l).

From the charge density distribution it is further apparent, that the ratio of maximum positive charge density between the two atomic species is not significantly altered. A higher positive charge density is observed for selenium atomic columns compared to tungsten atomic columns for all detector configurations. Therefore, these investigations show that even though the electric field distribution is altered by the detector configuration, the charge density ratio between tungsten and selenium atomic columns discussed in Chapter 4.1 is not reversed. Thus, the observed charge density ratio is not an artefact of the detector configuration.

To quantitatively find the detector configuration resembling the CoM image best, the cross-correlations coefficients of the different DPC images are calculated between the three detector configurations and the CoM-based reference images. Figure 4.9 shows the cross-correlation coefficients for the DPC image (black), the electric field magnitude map (orange), and the charge density distribution (blue). The lowest cross-correlation coefficients for all three image types can be found when only using Layer 1. For this detector configuration, the comparison of DPC images only gives a cross-correlation coefficient of about 0.2 which is due to the halo-like electric field distribution observed within vacuum, indicating a field pointing towards the atomic columns. Since the cross-correlation coefficient of the DPC image is calculated as the product of the cross-correlation coefficient of the direction and the magnitude, the pronounced halo-like field in the W-Se ring for Layer 1 significantly reduces the similarity in field direction. However, the corresponding electric field magnitude and charge density maps give cross-correlation coefficients of about 0.96 and 0.94, respectively. For the electric field magnitude, this is an unexpected high value, as the introduced artefacts discussed previously are clearly visible and even the charge density map showed a positive charge density distribution in vacuum regions.

In contrast to Layer 1, using Layer 2 or both layers results in cross-correlation coefficients of 0.93 or higher. It is to note, that for all detector configurations, the cross-correlation coefficients of the DPC image are significantly lower than the corresponding cross-correlation coefficients of electric field magnitude or charge density maps. This is due to the fact, that the DPC images combine electric field direction and strength within one image and thus changes in both can be detected. Using Layer 2 or both layers leads to cross-correlation coefficients of electric field magnitude and charge density of 0.99, indicating a high similarity to the corresponding maps obtained using a pixelated detector. As expected the use of both layers leads to the highest possible cross-correlation coefficients. Qualitatively this was described previously based on the electric field magnitude map which shows only minor differences compared to the CoM-based electric field magnitude map. For this case, a cross-correlation coefficient of about 0.94 is observed for the DPC image. This is in good agreement with the observations made by J. Bürger for a 30 nm thick silicon specimen where the use of both layers reduces the influence of dynamical diffraction effects [84]. However, here it is shown that even for 2D materials, where dynamical diffraction effects can be neglected, the optimum configuration to achieve the highest similarity with a pixelated detector is to use both layers for the DPC image calculation.

Section summary

- The different possible detector configurations of an eight-fold segmented detector influence the obtained electric field and charge density distributions.
- Using an eight-fold segmented detector introduces a triangular shape of the atomic electric field distribution for all three detector configuration.
- Using only the inner layer, Layer 1, leads to a halo-like field distribution around the atomic columns and positive charge density values in vacuum regions.
- The triangular shaped field magnitude distribution around the individual atomic columns rotates by 60° when using only one of the two layers.
- Mostly the derived charge density distribution in surrounding the atomic columns is influenced by the chosen detector configuration, but the positive charge density at the atomic column positions is not drastically affected resulting in comparable charge density ratio between selenium and tungsten atomic columns as observed before.
- The highest similarity in electric field and charge density distribution to the CoM-based images is found when using both layers which leads to a cross-correlation coefficient of 0.99.

4.3.2 Influence of Detector Rotation on DPC Images of 2D Materials

Due to the specific geometry of the segmented detector, the segmented detector exhibits an anisotropic information transfer as theoretically illustrated in Ref. [28, 87] which introduces artefacts in the measured electric field distribution. Besides the theoretical considerations, the influence of the detector rotation is experimentally and theoretically only shown for 30 nm thick silicon by J. Bürger [84]. There, the influence is significant and directly visible in the electric field maps. It is found that the detector rotation introduces changes mostly for interatomic pixels [84]. For the 30 nm silicon specimen, the electric field distribution was influenced by dynamical diffraction effects, resulting in strong intensity variations across the detector segments. For a monolayer of WSe_2 the influence of the detector rotation is expected to be different compared to silicon as dynamical diffraction effects are assumed to be negligible due to the thin specimen thickness of only a few atoms. In addition, the CBED pattern of WSe_2 has a different geometry than silicon due to the different crystal structure, which will possibly alter the influence of detector rotation.

Thus, the influence of detector rotation on the DPC image, the electric field components and magnitude as well as the charge density distribution is investigated for detector rotations between 0° and 80° in steps of 10° in counter-clockwise direction (Figure 4.7 a). Even though the detector configuration with the highest similarity to a pixelated detector was found when using both layers, the following investigation of the influence of the detector rotation is done using only Layer 2. Many segmented detectors are ring-shaped detectors which only consist of one layer with a central hole. Using an annular segmented detector was expected to increase the signal-to-noise ratio [196]. Therefore, the following discussion is based using Layer 2 to maintain a comparable configuration and to facilitate a more general discussion.

To quantify the influence of the detector rotation, cross-correlation coefficients of the DPC images of different detector rotations and the CoM-based image are calculated. All images are acquired from the same 4D-STEM data set by projecting a segmented detector on each CBED pattern (Chapter 3.3). Using the cross-correlation coefficient allows to quantify the similarity between the images obtained using a pixelated detector and a segmented detector. Figure 4.10 a) shows these cross-correlation coefficients of the two components of the electric field (E_x and E_y), the electric field magnitude maps and the charge density maps for the different detector rotations of the segmented detector.

First of all, it is to note that the cross-correlation coefficients are above 0.986 for all the here shown detector rotations. This means that a high similarity between the images of a segmented detector and the ones from a pixelated is found for all detector rotations. Even though the segmented detector offers only a reduced momentum-space resolution due to the limited number of segments compared to the pixelated detector, it seems to be sufficient to quantitatively investigate specimens with a specimen thickness of only a few atoms. However, depending on the detector rotation variations in the cross-correlation coefficients can be identified. For example, the electric field magnitude (black line) shows the highest cross-correlation coefficient of about 0.99 for a detector rotation of 0°, but additionally exhibits two local maxima with a cross-correlation coefficient of 0.989 for a detector rotation

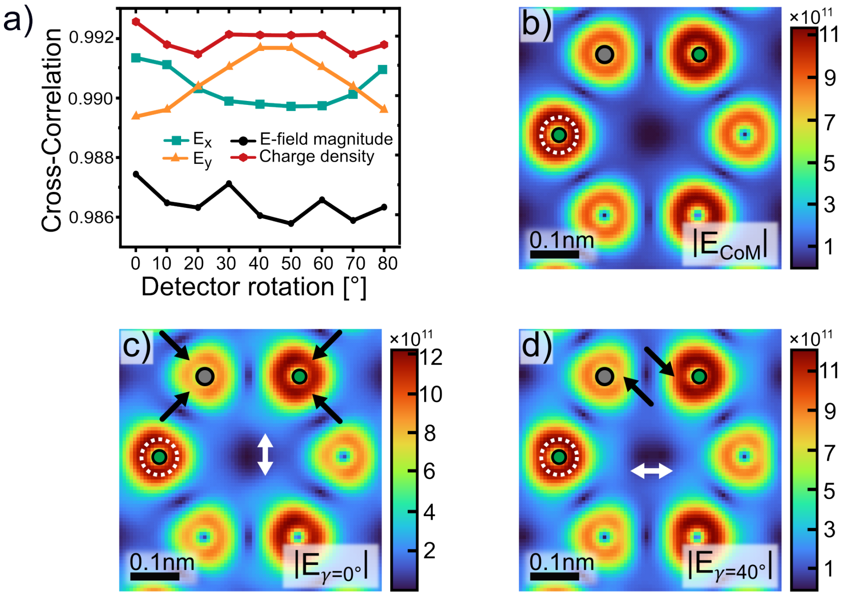

Figure 4.10: a) Cross-correlation coefficients calculated in reference to the CoM-based images of the x- and y-components of the electric field (blue and orange), the electric field magnitude (black) and charge density (red) for the different detector rotations. b-d) Electric field magnitude maps obtained with b) a pixelated detector, c) a non-rotated segmented detector, and d) a segmented detector rotated by 40°. The electric field magnitude is given in units of V/m.

of 30° and 60°. This is due to the specific symmetry of the CBED pattern and the way the detector segments intersect the intensity distribution, leading to optimum conditions for DPC measurement with a segmented detector when the detector is rotated by $n \cdot 30°$ to any W-Se dumbbell axis ($n \in \mathbb{N}$). The pronounced contrast transfer for these detector rotations can also be explained by the CTF of the detector which for segmented detector gives a high contrast transfer if the spatial frequency vector is parallel to the direction of the detector partitioning [87] (Chapter 2.5).

Another important finding is the difference in cross-correlation coefficients for the electric field components in x- and y-direction. Here, the electric field component in x-direction (green line) shows decreasing coefficients for increasing detector rotations which increase again for detector rotations higher than 40°. Conversely, the y-direction of the electric field distribution exhibits a contrary behaviour where an increase of the cross-correlation coefficients is observed for detector rotations between 20° and 50°. The electric field in y-direction even shows a higher maximum cross-correlation coefficient compared to the maximum cross-correlation coefficient of the x-component. Generally, the difference of the two electric field components is due to the anisotropy of the contrast transfer function of segmented detectors which exhibits a non-equal phase contrast transfer for the different directions [86, 87, 193]. However, still the cross-correlation coefficients are in the range of high similarity to a CoM image.

The highest similarity can be found for the charge density maps, which is for most of the detector rotations almost constant. This might be due to the fact that the charge density distribution is calculated by a divergence operator applied to the electric field distribution which potentially reduces the influence of the anisotropic CTF of the detector. Overall, the highest cross-correlation value for the charge density maps is found for a non-rotated detector and yields up to 0.993.

Taking into account the cross-correlation coefficients of all four image types, the most suitable detector rotation for the investigation of a WSe_2 monolayer is 0° where the x-axis is orientated parallel to a dumbbell axis. As all detector rotations achieve a high cross-correlation, the question arises, which changes are introduced by the detector rotation. Figure 4.10 b)-d) depict the electric field magnitude maps calculated for b) a pixelated detector (CoM-based), c) a segmented detector at a rotation of 0° and d) 40° using only Layer 2. Comparing the absolute values of the electric field maps reveal that the magnitudes are in the same order of magnitude for the three different electric field magnitude maps. However, the segmented detector introduces some artefacts due to its anisotropy in the CTF. Comparing the electric field distribution acquired with the pixelated detector and the segmented detector at 0° detector rotation gives an insight into these artefacts (Figure 4.10 b) & c). For the CoM-based electric field distribution, the highest electric field distribution is almost rotational distributed symmetrically around the atomic columns (white dashed circle) without any directional weakening. But along the connecting direction of neighbouring atomic column the round-shaped electric field is slightly reduced due to the overlap of opposing electric fields resulting in a slightly triangular shape of the outer field distribution around the atomic column. For a non-rotated segmented detector shown in Figure 4.10 c), the triangular shape is even more pronounced. Furthermore, the high electric field magnitude around the atomic columns is not evenly distributed but shows areas with reduced electric field magnitude. For no detector rotation, these areas with attenuated field magnitude are located on the left for tungsten atomic columns and on the right for selenium atomic columns (indicated by the black arrows). However, rotating the detector leads to a change of the position of these features. For 40° detector rotation shown in Figure 4.10 d), these features merge together and are located along the dumbbell axes between tungsten and selenium atomic columns (black arrows).

Furthermore, the local field minima in the centre of the W-Se ring change from round-shaped minima for the CoM-based case to slightly vertical elongated minima for the non-rotated segmented detector and to horizontally elongated minima for the 40° rotated detector (indicated by the white arrows in Figure 4.10 c) & d). It is evident that, even though the cross-correlation of the electric field magnitude with reference to the CoM image yields high values and thus a high similarity, there are still recognizable artefacts introduced by using a segmented detector and by the rotation of the detector with respect to the CBED pattern. To investigate these artefacts further, difference maps are calculated and shown in Figure 4.11. The difference maps of the electric field magnitude comparing two different detector rotations, namely a detector rotation of 40° and 80°, with a non-rotated detector ($|E_{\gamma=0°}|$) are depicted in Figure 4.11 a) and b), respectively. These colour-encoded maps show the absolute difference calculated by the subtraction of the electric field magnitude distribution of a non-rotated detector with the one of the rotated detector. Pixels with values above zero correspond to a lower electric field magnitude and values below zero correspond to a higher electric field magnitude of the DPC image derived with a rotated detector. Figure 4.11 a) shows the difference map between the electric field magnitude map of a non-rotated detector and the one for a detector rotation of 40°. Here, artefacts introduced by the change of the detector orientation with respect to the CBED pattern are identified. A pronounced difference in the electric field distribution can be observed between the W-Se dumbbells, where a reduced electric field magnitude is present (white dashed cross-shaped region in Figure 4.11 a). There, the electric field map obtained with the rotated detector shows a lower electric field magnitude compared to the electric field distribution derived with a non-rotated detector.

Furthermore, s-shaped regions with higher electric field magnitude are observed and indicated by the white dashed curve. These vertically line artefacts of an enhanced electric field are located on the right of the selenium atomic columns and on the left of the tungsten atomic columns. Comparing the values of the difference, which are in the range of about $1 \cdot 10^{11}$V/m and about an order of magnitude lower than the absolute electric field magnitude, it can be roughly deduced that rotating the detector alter the DPC signal locally by up to 9 % even for a monolayer of WSe_2.

Figure 4.11 b) shows the difference map for a detector rotation of 80° and the non-rotated detector. Here, completely different artefacts can be found. The difference map calculated with a detector rotation of 80° shows extended regions of higher electric field magnitude horizontally aligned (white dashed line). Furthermore, pronounced positive values are located nearby selenium atomic columns (marked by a black arrow in Figure 4.11 b). In contrast to the difference map calculated using a detector rotation of 40°, the influence of the detector rotation of 80° is lower, leading to a maximum relative change of about 3 %. This

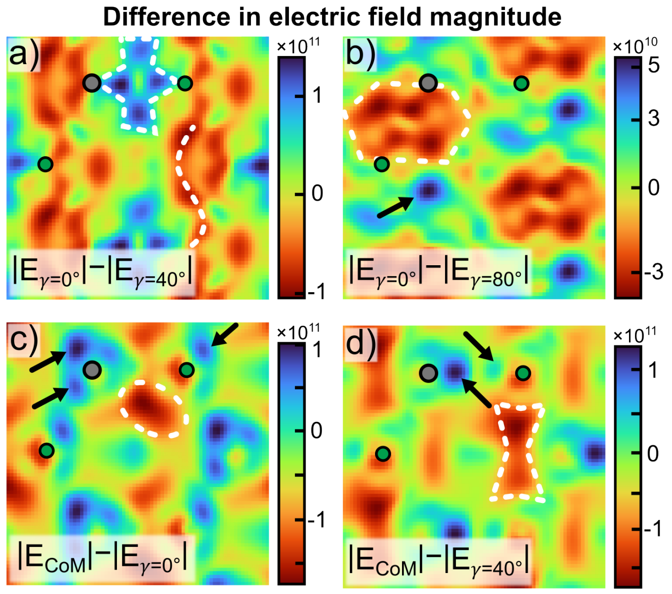

Figure 4.11: Difference maps of the electric field magnitude for different detector rotations. Difference map of the electric field magnitude for a) 40° and b) 80° detector rotation with respect to the non-rotated detector. Difference maps of the electric field magnitude with reference to the CoM-based image for a detector rotation of c) 0° and d) 40°. The difference is give in absolute values in units of V/m.

is due to the relative orientation of the CBED pattern to the detector segments. For the used arrangement of the detector segments (indicated in Figure 4.10 a), a detector rotation of 90° corresponds to the non-rotated configuration. Therefore, the detector rotation of 80° practically corresponds to a detector rotation of only 10° which explains the reduced impact.

Summarizing the findings above, the detector rotation of a segmented detector has a non-negligible influence on the electric field magnitude and leads to slight changes in the electric field distribution. With a relative change of up to 10% depending on the specific detector rotation, these introduced changes need to be considered for detailed quantitative analysis, especially when investigating charge redistribution or bonding effects.

Using a non-rotated segmented detector as a reference for the shown difference maps gives insight into the influence of the detector anisotropy under rotation, but the general influence of the detector geometry and the limited number of segments is not included. Therefore, the discussion is now done using the corresponding CoM-based electric field magnitude map ($|\mathrm{E}_{\mathrm{CoM}}|$) as a reference. Figure 4.11 c) and d) show the difference maps calculated for the CoM image and a detector rotation of 0° and 40°, respectively. In contrast to the previous discussion, where only the segmented detector was considered, the following discussion will include effects not only due to detector rotation but also due to the limited number of segments. Figure 4.11 c) depicts the difference map between the CoM image and the segmented detector with a detector rotation of 0°. A pronounced difference in the electric field magnitude can be observed on the left of tungsten atomic columns and on the right of selenium atomic columns. As indicated by the black arrows, a lower electric field magnitude is observed for the electric field map derived by the segmented detector compared to the electric field magnitude of the CoM image. However, on the opposing side of the atomic columns slightly higher values of the electric field are present. In the centre of the W-Se ring a region with enhanced electric field magnitude are found (exemplary marked by a white dashed circle). At the atomic column positions a higher electric field magnitude can be found compared to the CoM-based image. Thus, the segmented detector slightly overestimates the electric field directly at the determined atomic column position.

The electric field magnitude difference is of an order of magnitude lower than the absolute values of the electric field magnitude obtained by the CoM reference image, however, the relative change still yields to about 15%. Even though the cross-correlations in Figure 4.10 a) indicate a high similarity, the difference between a CoM image and an image acquired with a segmented detector is still significant. As the simulation is done for perfect illumination conditions and without any scan distortions, specimen drift or lens aberrations this difference map demonstrate the influence introduced by the limited momentum space resolution and the anisotropic CTF of a segmented detector. It is noteworthy that introducing a blurring, which is currently experimentally unavoidable due to the finite probe size, will result in slightly reduced difference values and a vanishing of the detailed features. Still, the described pronounced features of higher and lower electric field magnitude will remain for reasonable.

The features and artefacts introduced by the segmented detector will change in dependence of the detector rotation. This can be seen in Figure 4.11 d) showing the difference map for a detector rotation of 40°. Again, there are two highly pronounced artefacts introduced by the detector rotation. 1) There are some areas indicating a reduced electric field magnitude. These are again located in the vicinity of the atomic columns and indicated by the black arrows. In contrast to the non-rotated detector, the areas are now opposing each other. One area, indicating a reduced electric field magnitude, is located on the right of tungsten atomic columns and another is located on the left of the selenium atomic columns. Thus, along the connecting axes of a W-Se dumbbell the rotated segmented detector yields a lower electric field magnitude compared to the CoM-based approach of a pixelated detector. 2) Within the centre of the W-Se rings a higher electric field can be recognized for images obtained with a segmented detector rotated by 40°. The relative change in the electric field magnitude with reference to the corresponding CoM image is again about 15%. Although the shape and position of these two features change for the detector rotations shown here as examples, they remain the same for the other detector rotations.

Concluding the findings above, the investigation shows a significant influence of the detector rotation on the deduced electric field magnitude map even for a monolayer of WSe_2. The relative change in electric field magnitude and distribution can reach up to 15% in reference to the electric field magnitude of the CoM-based DPC image from a pixelated detector. Thus, the influence of the rotation of a segmented detector with respect to the CBED pattern should carefully be considered especially for quantitative investigations of bonding effects or charge redistribution. When aiming to measure bonding effects using DPC, even weak artefacts alter the interpretability of observed electric field and charge density distributions.

As the shown simulations were done without any image distortion introduced by specimen drift, lens instabilities resulting in lens aberrations, the following discussion shows experimental results on the influence of the detector rotation. Here, the influence of the detector rotation is qualitatively discussed for the obtained electric field distribution of a WSe_2 monolayer using an eight-fold segmented detector and compared with a corresponding simulation. The simulation is again a 4D-STEM data set of a WSe_2 monolayer and analysed in the same way as discussed above. In contrast to the previous simulation of the detector rotation, a pixel size comparable to the measurement is used, and the detector is rotated in counter-clockwise direction similar to the experiment. Details about the experiment and simulation parameters can be found in Table 9.5.

Figure 4.12 shows the experimental (left) and simulated (right) HAADF images and electric field magnitude maps for different detector rotations. The atomic column positions of tungsten and selenium atomic columns are indicated by the grey and green dots, respectively. Figure 4.12 a) and b) depict the HAADF images which shows the atomic structure of a WSe_2 monolayer in [0001] zone-axis orientation. The electric field magnitude maps derived using a non-rotated detector are shown in Figure 4.12 c) and d) for the measurement and simulation, respectively. A sketch of the detector is provided on the left of the images. As expected, the electric field magnitude maps obtained using the non-rotated detector show triangularly shaped electric field distributions around the atomic column positions.

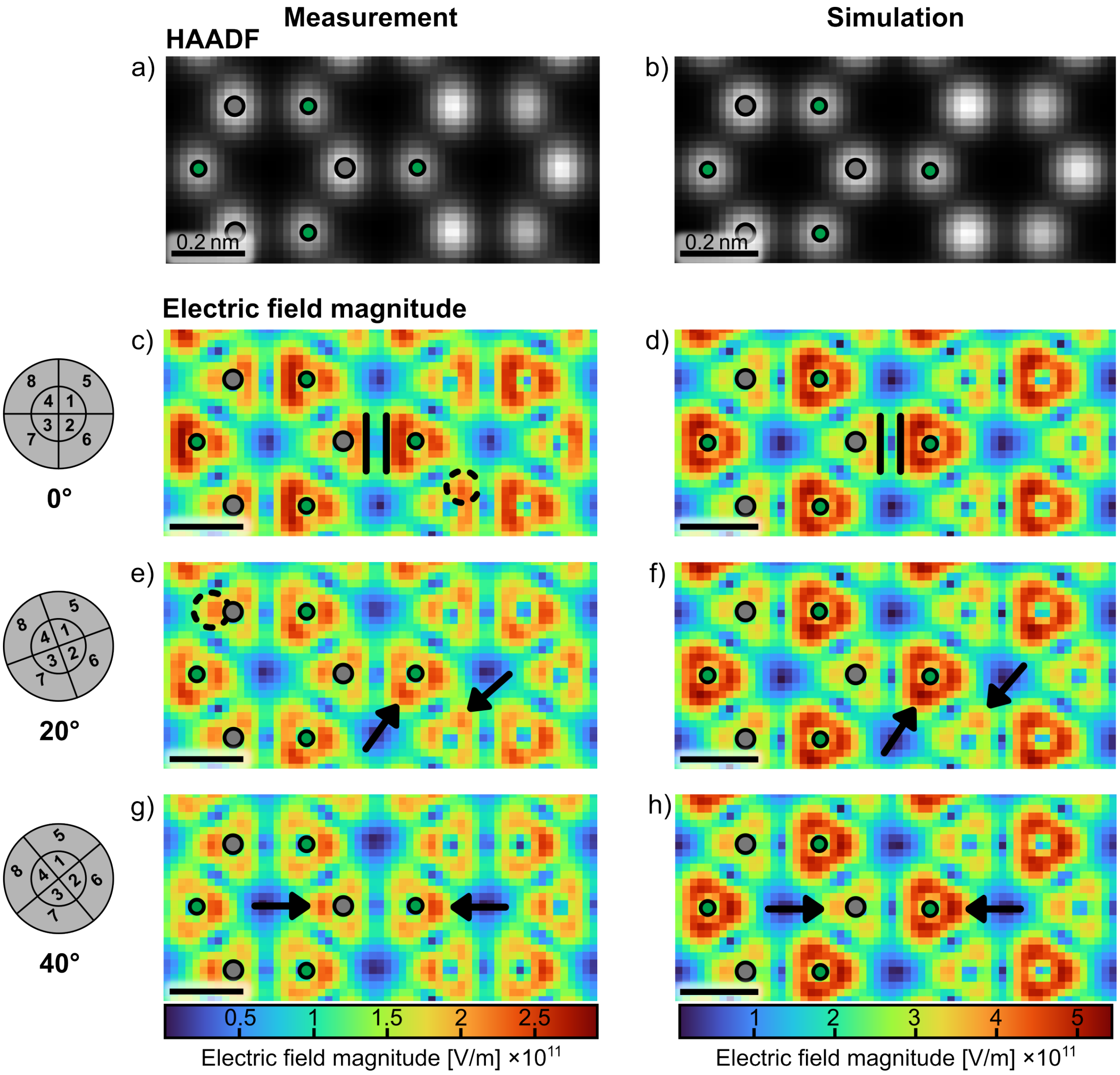

Figure 4.12: Influence of detector rotation on the electric field distribution. a) & b) depict the measured and simulated HAADF images of a WSe_2 monolayer in [0001] zone-axis orientation. c)-h) show the electric field distribution of the measurement and the simulation acquired using different detector rotations indicated by the sketches to the left. Tungsten and selenium atomic column positions are determined from the HAADF image and marked by grey and green dots, respectively. The scale bar corresponds to 0.2 nm and the colormap is given at the bottom.

However, the electric field magnitude is not evenly distributed within this triangular feature, but exhibits some local maxima. For a non-rotated detector, the measurement shows a pronounced electric field magnitude on the right of the triangular feature around tungsten atomic columns and on the left of the triangular feature around selenium atomic columns. Locally enhanced electric field magnitudes are observed at the edges of the triangular-shaped field distributions vertical to the connecting direction of W-Se dumbbells for both the measurement and the simulation. This artefact is marked by two black lines in Figure 4.12 c) and d). As the simulation is performed without any residual lens aberrations and specimen tilt, this locally pronounced electric field distribution is not introduced by lens aberrations but by the detector geometry itself. In contrast to the simulated field magnitude map, the experimentally derived electric field magnitude map shows a slightly higher electric field magnitude for the upper part of this line artefact than the simulation (Figure 4.12 c) black dashed circle). This is due presumably due to a non perfectly centred beam on the detector during the measurement. However, the similarity of this artefact is distinctive.

By rotating the detector, the electric field distribution close to the atomic columns significantly changes which is recognizable by the change of the position of the local maxima within the triangular-shaped field magnitude around atomic columns. In contrast to the parallel aligned pronounced field magnitude of tungsten and selenium vertical to the dumbbell axis, a 20° detector rotation leads to a pronounced electric field magnitude of one tip of the triangular feature around the atomic columns. In Figure 4.12 e) and f), this pronounced electric field magnitude due to a detector rotation of 20° is indicated by the two black arrows. For the tungsten atomic columns the upper right tip of the triangular shaped feature is more pronounced than the two other tips. For selenium, the lower left tip indicates a higher electric field magnitude than the other two. This influence of a detector rotation can be clearly observed for the simulated electric field magnitude maps, but is also visible for the measurement even though it is again slightly less localized than for the simulation. For the measurement, the two less pronounced tips of the triangular-shaped region around atomic columns do not show an almost equal magnitude as it is the case in the simulation. Instead, they show one tip with a slightly higher magnitude than the other (indicated by the black dashed circle in Figure 4.12 e). This again is due to some misalignment during the measurement such as a slightly off-centred electron beam on the detector.

A further rotation of the segmented detector to 40° leads to a different position of the local enhanced electric field magnitude within the triangular shaped regions around atomic columns. A pronounced electric field magnitude can be found at the horizontally aligned tips of the triangular features. For selenium atomic column this corresponds to an enhanced magnitude in the right tip of the triangle and for tungsten atomic columns the enhanced electric field magnitude can be found at the left tip. For the simulation and the measurement, these introduced artefacts are marked by the black arrows in Figure 4.12 g) and h). The experimental data for the influence of the detector rotations is in good agreement to the corresponding simulations. The detector rotation introduces artefacts close to the atomic column positions and significantly alters the local electric field magnitude within the triangular shaped regions around the atomic columns. Even though unavoidable misalignments during the experimental measurements lead to minor distortion of the artefacts introduced by the detector rotation, the influence of the detector rotation is still recognizable under experimental illumination conditions even for a WSe_2 monolayer. Thus, the detector geometry and the rotation of the detector with respect to the object imaged introduces characteristics in the electric field distribution which can not be related to the material. Therefore, the investigation of charge redistribution or bonding effects using segmented STEM-DPC is hindered by the detector itself.

Section summary

- The way how the segmented detector intersects the CBED pattern strongly influences the obtained atomic electric field distribution.
- The symmetry of the detector and the symmetry of the CBED pattern result in an optimum transfer of information for detector rotations that are integer multiples of 30°.
- The anisotropy of the segmented detector results in a pronounced triangular shape of the local electric field magnitude around the atomic column positions with reduced values in certain direction.
- The highest cross-correlation coefficients of electric field magnitude and charge density distribution between a (rotated) segmented detector and a pixelated detector (CoM-based) is found at a detector rotation of 0° with a value of 0.99.
- The detector rotation leads to a rotation of these introduced artefacts of reduced field magnitude.
- The detector rotation introduces changes in the electric field magnitude with a relative difference of about 10% compared to the non-rotated detector and 15% relative difference in comparison to the electric field magnitude acquired with a pixelated detector.
- Qualitatively, the artefacts due to the detector anisotropy are experimentally observed for a WSe_2 monolayer.
- The experimentally observed triangular field magnitude around the atomic column positions shows local minima and maxima which change their position around the atomic column position in dependence of the detector rotation.
- The significant influence of the anisotropy of the eight-fold segmented detector hinders the measurement of bonding effects or charge redistribution.

4.4 Investigation of the Influence of single and multiple Atoms on quantitative DPC Imaging

The previous sections show that lens aberrations, the limited resolution in momentum space of the segmented detector as well as the anisotropy of a segmented detector influence the electric field and charge density distribution measured using STEM-DPC. Still, even for the most suitable detector configuration, using both layers of a segmented detector or even a pixelated detector, the unexpected charge density distribution in a WSe_2 monolayer with a higher charge density at selenium atomic columns compared to tungsten atomic columns is observed. Thus, it is neither an artefact introduced by the anisotropy of the segmented detector nor introduced by lens aberrations. The origin of this charge density is therefore presumed to be resulting from the actual interaction of the electron beam with different types of atomic columns, which in WSe_2 consist of different elements, i. e. different projected atomic numbers, and also differ in the number of atoms in the atomic columns. Thus, the electron beam propagation close to selenium atomic columns is expected to be influenced not only by the different projected atomic numbers but is additionally altered by the two atoms stacked above each other and separated along the beam propagation direction by a certain distance.

Therefore, the influence of the different atomic numbers of the two atomic columns in a WSe_2 monolayer as well as the influence of the different number of atoms within an atomic column are investigated in the following using multislice image simulations of individual atoms using the software abTEM [89]. In Chapter 4.4.1, the influence of the (projected) atomic number on the DPC signal is investigated using DPC image simulations of one and two atoms with different atomic numbers between Z=1-85. These simulations are done with a fixed vertical distance between the two atoms stacked along the beam propagation direction. The influence of the separation distance is investigated in Chapter 4.4.2. In Chapter 4.4.3, the influence of the number of atoms in atomic columns of a WSe_2 mono- and multilayer is investigated by increasing the number of atoms of the pure tungsten and selenium atomic column while having a fixed vertical distance between the atoms. Detailed information on the multislice image simulations for the different structures and atoms can be reviewed in the Appendix in Chapter 9.11.

In addition to the investigation of the DPC signal, the difference in the electron beam propagation close to the two different atomic columns in a WSe_2 monolayer and its evolution while the electron beam transmits the specimen are investigated in Chapter 4.4.4 using a simulation of the real space probe intensity after the interaction with a single or multiple selenium or tungsten atoms. Detailed information on these simulations are given in the Appendix 9.11.

To identify the relation of the DPC signal and related quantities with the actual atomic potential, the atomic potentials of atoms with different atomic number and the projection of atomic potentials are investigated in Chapter 4.4.5 and compared to the observed DPC signal.

4.4.1 Influence of the Atomic Number

It is assumed in literature that under ideal illumination conditions without lens aberrations, the projected potential, governed by the atomic number and the number of atoms, is linearly connected to the observable DPC signal. However, it has been observed in Chapter 4.1 that the projected atomic numbers of the two different atomic columns in a WSe_2 monolayer are close to each other with $Z^{\mathrm{proj}}_{\mathrm{2Se}} = 68$ and $Z^{\mathrm{proj}}_{\mathrm{1W}} = 74$, a higher charge density is observed for selenium atomic columns than for the higher Z tungsten atomic columns. This is unexpected due to the assumed linear dependency of DPC signal to the projected atomic number Z (Chapter 2.5). Therefore, the influence of the atomic number on the DPC signal is investigated using multislice image simulations of individual atoms with different atomic numbers Z. For elements with an atomic number between Z=1 and Z=85, multislice image simulations of a single atom within a scan area of $0.4\,\mathrm{nm} \times 0.4\,\mathrm{nm}$ are conducted using the IAM potentials based on the parametrization of Lobato [197] as well as using DFT-based potentials (Chapter 2.6) [89]. The element group of lanthanides (Z=57-70) is omitted in the simulations. For the simulations an ideal electron probe without lens aberrations, an acceleration voltage of 80 kV, and collection angles of the eight-fold segmented detector similar to the experimental values are used (Chapter 3.1). In addition, the simulations are repeated for two atoms of the same atomic species stacked on top of each other in beam propagation direction with a fixed distance of 0.6 nm. This value was arbitrarily set for simulations of various elements, yet it is consistent with the interlayer spacing of two tungsten atoms in WSe_2. Further information on the simulation parameters are given in Table 9.6 in the Appendix 9.11.

To compare the simulations, the arithmetic mean value of the beam deflection of the complete DPC image is calculated. This allows to quantitatively investigate the influence of two atoms stacked on top of each other on the DPC signal in dependence of the atomic number.

Figure 4.13 a) shows the atomic number dependent arithmetic mean value of the beam deflection calculated over the whole image simulation. An image simulation of a single W atom is exemplarily depicted in the inset. The mean beam deflection of a single atom in dependence of the atomic number is plotted as a black line for the simulations using the IAM-based potentials and as a blue dotted line for the simulations using the DFT-based potentials in Figure 4.13 a). For both used types of potential, the mean beam deflection shows a non-monotonic behaviour with increasing atomic number. Although the overall tendency shows an increase in mean beam deflection with increasing atomic number, local minima are observed for certain atomic numbers, such as for the atoms of the noble gas group as well as for atomic numbers of 24, 29 and 46. The same non-linear behaviour with local minima in the mean beam deflection is observed for two atoms stacked on top of each other as indicated by the pink solid and green dashed line for IAM- and DFT-based potentials, respectively.

Furthermore it is to note that for the single atom simulations no significant difference in the mean beam deflection between the simulations with IAM potentials and DFT potentials can be observed. This is an expected observation, since the influence of possible charge redistri-

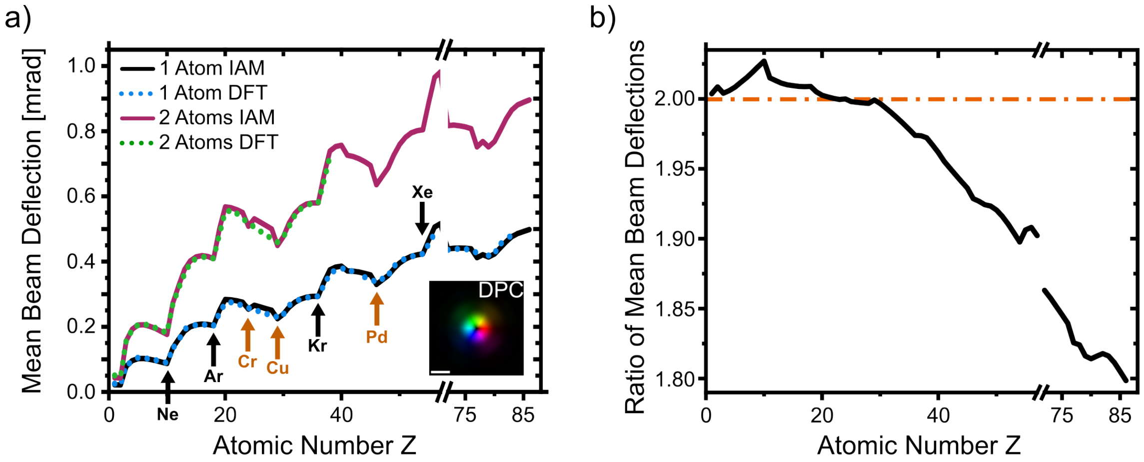

Figure 4.13: a) Mean beam deflection in dependency of the atomic number between Z=1-85 simulated using IAM-based potentials (black line) and DFT-based potentials (blue dotted line). The mean beam deflection for two atoms of the same atomic species is indicated by the solid magenta line for the IAM potentials and indicated by a green dotted line for the DFT-based potentials. The inset exemplarily shows a simulated DPC image of a single selenium atom over a scan area of 0.4 nm × 0.4 nm. The mean beam deflection is calculated by the arithmetic mean of these DPC image for each atomic species. b) Ratio of mean beam deflection in dependency of the atomic number for atomic numbers between Z=1-85.

bution due to bonding which is included in DFT potentials but neglected in IAM potentials, is irrelevant for single atoms. The non-monotonic behaviour of the mean beam deflection in dependence of the atomic number is quantitatively investigated by fitting a power function to the mean beam deflection of a single atom for atomic numbers between 1 and 57. This gives the overall tendency of the mean beam deflection with increasing atomic number. Based on the fit a $Z^{0.61}$-dependency is found, which is similar to the $Z^{0.6}$-dependency of bright field (BF) imaging generally assumed [67, 198, 199]. A comparable dependency on the atomic number is further found for other phase-related techniques such as ptychography [199] and annular bright-field phase imaging [198]. Thus, the mean beam deflection derived from DPC imaging with a segmented detector is not linearly related to the atomic number but shows a comparable relation to the atomic number as BF imaging. This might be expected as DPC imaging exploits the BF signal and DPC detectors extend to slightly higher collection angles than typical BF detectors. However, a more linear relationship was expected as the DPC signal is assumed to be proportional to the projected potential which is determined by the number of atoms and the type of atoms within an atomic column (Chapter 2.5).

For one and two atoms, the non-monotonic behaviour of the mean beam deflection shows some pronounced minima for certain atomic species which are marked by the black and orange arrows in Figure 4.13 a). The black arrows indicating local minima in the beam deflection are found at positions of elements from the noble gas group. For these elements, the mean beam deflection drops to a local minimum which is possibly caused by the characteristic noble gas electron configuration. All these elements exhibit an electron shell which is fully occupied by electrons. This electron configuration is the most stable and energetically most favourable configuration. As the electron configurations determines the occupation of the electron shells it also influences the atomic potential.

Furthermore, local minima in the mean beam deflection are also observed for chromium, copper and palladium atoms (marked by orange arrows in Figure 4.13 a) which do not belong to the group of noble gases. However, for these elements, exceptions are made for filling the electron shells, resulting in a lower energy and more stable electron configuration. Therefore, the local minima in the mean beam deflection are presumably related to the electron configurations of the elements. This is reasonable as the electron configurations will alter the atomic potential which is then used for the simulations.

The increase in mean beam deflection with increasing atomic number even for light atoms and the sensitivity to the electron configuration and thus to the actual atomic potential shows the capability of STEM-DPC to image light and heavy atoms and relate the measured signal to the atomic potentials. However, due to the non-monotonic behaviour an identification of the atomic species by the DPC signal is not straight forward. This finding is in agreement with BF imaging showing a comparable Z-dependence of the signal [67].

To investigate the DPC signal of two atoms of the same atomic number stacked on top of each other, Figure 4.13 b) shows the ratio of mean beam deflection of two and one atom, also assuming ideal conditions. The ratio is calculated for the mean beam deflection of one and two atoms shown in Figure 4.13 a). As DFT-based and IAM-based simulations result in similar mean beam deflections, the ratio is only calculated from the IAM-based simulations.

For the lightest atoms, the ratio of the mean beam deflection is slightly above two for the lightest atom and is increasing with increasing atomic number until a maximum of about 2.03 for $Z=10$ is reached. For $Z \geq 10$, the ratio decreases and falls below a factor of two when $Z \geq 22$. For heavy atoms, the ratio of mean beam deflection is less than two which should be the ideal values for the expected linear dependency of DPC imaging. Thus, the DPC signal of two heavy atoms ($Z \geq 22$) is smaller than twice the DPC signal of one atom. Note that this applies for the simulation parameters and atomic spacings used, but this behaviour might be different for other acceleration voltages. The ratio in mean beam deflection shows neither a constant nor a linear relationship which indicates that the stacking of two atoms of the same Z alters the DPC signal differently depending on the atomic number. As the ratio is always above one, the DPC signal of two atoms is in general higher than the DPC signal of one atom but the additional beam deflection due to the additional atom is decreasing for heavy atoms. Therefore, STEM-DPC imaging is not linear with respect to the number of atoms within an atomic column.

As charge densities can be calculated from the DPC signal, it is interesting to investigate the influence of Z as well as the impact of the stacking on the obtainable charge densities. Thus, the following discussion describes the influence of the atomic number on the charge density. Figure 4.14 compares the maximum charge density for one and two atoms stacked on top of each other. The maximum charge density is calculated for each simulation and is typically found at the centre of the atomic column position. In Figure 4.14 a), the maximum charge density for a single atom (solid black line) and for two atoms of the same atomic number (dotted black line) increases with increasing atomic number. Although the

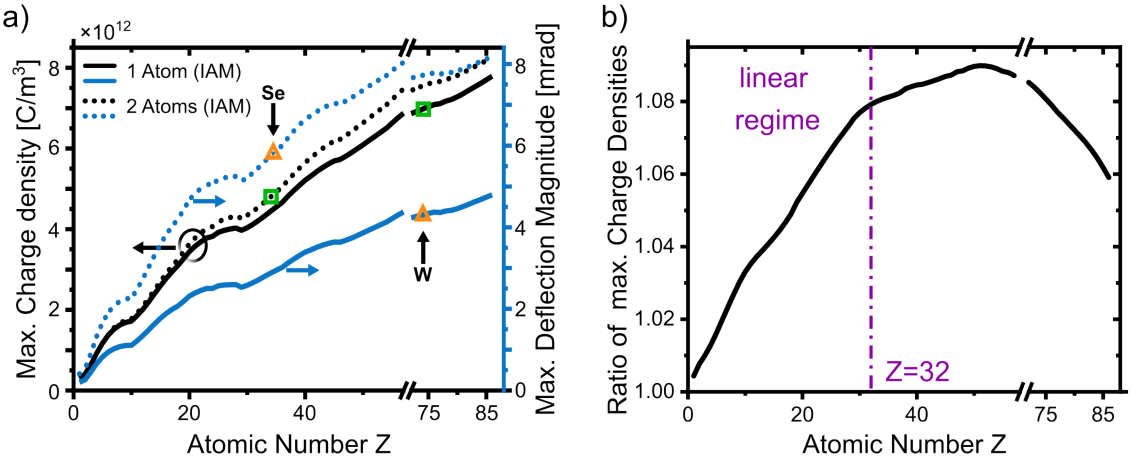

Figure 4.14: a) Maximum charge density (black lines and left y-axis) and the maximum beam deflection (blue lines and right y-axis) for increasing atomic number between Z=1-85. Both quantities are shown for one (solid lines) and two atoms (dotted lines), respectively. The yellow triangles indicate the values of the maximum beam deflection for the selenium and tungsten configuration in a WSe_2 monolayer and the green squares highlight the corresponding values for the maximum charge density for two selenium atoms and a single tungsten atom. b) Ratio of the maximum charge densities between one and two atoms of the same atomic species.

increase in maximum charge density increases almost linearly with the atomic number, several deviations from the linear trend are observed for the same atomic species for which a local minimum in the mean beam deflection was previously found, namely for the noble gas elements and chromium, copper, and palladium. As these local minima are also observed for the DPC signal from which the charge densities are derived, this observation is expected. Despite the local minima for these positions which are only slightly visible, the overall trend follows a linear increase for both the maximum charge density of one atom and the maximum charge density of two atoms. By comparing the charge density of one and two atoms it becomes evident that the charge density of two atoms is also smaller than twice the charge density of one atom (also discussed later). Especially for light atoms with a low atomic number, the maximum charge density shows almost no difference between one and two atoms. With increasing atomic number, the difference of the charge density between one atom (solid black line) and two atoms (dotted black line) increases such that a higher maximum charge density is observed for two atoms than for only one atom.

Figure 4.14 a) additionally shows the maximum beam deflection to compare its behaviour to the behaviour of the maximum charge density. The maximum beam deflection is indicated by the blue solid and dotted line for one and two atoms, respectively.

The maximum deflection magnitude of single atoms increases almost linearly with the atomic number. Again, for noble gas elements and elements with a specific electron configuration, local minima in maximum beam deflection are observed. In contrast to the maximum charge density, the difference in maximum beam deflection between one and two atoms is significantly larger.

Although the projected atomic number of two selenium atoms is less than the atomic number of one tungsten atom, the maximum deflection magnitude indicates a larger deflection for two selenium atoms compared to one tungsten atom (marked by the orange triangles in Figure 4.14 a). Despite the higher deflection magnitude of two selenium atoms compared to one tungsten atom, the higher charge density is found at the single tungsten atom compared to the charge density of two selenium atoms (marked by the green squares). Comparing the findings of the single atom simulations and the observed unexpected charge density of selenium and tungsten atomic columns in a WSe_2 monolayer, it is evident that the unexpected charge density ratio can not be explained by the maximum charge density and the maximum beam deflection.

To get an insight into the actual change of the maximum charge density depending on the atomic number, the ratio of the maximum charge density of two atoms and the maximum charge density of one atom of the same atomic species is calculated and shown in Figure 4.14 b). The ratio increases almost linearly for an atomic number up to Z=32. For heavier atoms, the slope changes and reaches a maximum of about 1.09 for Z=51. Heavier elements with $Z \geq 51$ exhibit a reduced charge density ratio. While, the overall change in the charge density indicated by the ratio is small, it is noteworthy that the values of the maximum charge density ratio indicate that the maximum charge density of two atoms is always smaller than twice the maximum charge density of one atom. The unexpected small change in maximum charge density between one and two atoms is possibly due to an intensity redistribution inside the electron beam caused by the first atom. Surprisingly, this could possibly mean that the DPC signal is already dynamically affected if only two atoms are present instead of one. As the ratio of charge densities is only linear for light atoms ($Z \leq 32$) and drastically non-linear for heavier atoms, it is difficult to interpret DPC measurements when light and heavy atoms are present.

All in all, the unexpected charge density ratio of tungsten and selenium atomic columns can not be explained by the shown results from the single atom simulations. However, the findings are of great importance for the correct interpretation of DPC image and give an insight into the DPC signal when different atomic species are present in a measurement. Furthermore, the non-monotonic behaviour of the mean beam deflection with increasing atomic number shows the difficulty of a correct quantitative analysis. Thus, STEM-DPC allows to distinguish between light and heavy atoms but a direct identification of the atomic species is not straight forward.

Section summary

- The mean beam deflection in dependence of the atomic number shows a non-monotonic linear behaviour with local minima observed for specific elements, i. e. elements of the noble gas group as well as chromium, copper and palladium.
- These local minima in beam deflection are due to the electron configuration with energetically more stable electron shells filled.
- Overall, the mean beam deflection increases with $Z^{0.61}$.

- The ratio of the mean beam deflection for one and two atoms on top of each other shows neither a constant nor a linear ratio which is below two for atoms with an atomic number higher than 22. For light atoms the ratio is even above a factor of two. The increase in beam deflection with an additional atom in the atomic column is non-linear and depends on the atomic species.
- The maximum charge density increases almost linear with the atomic number, however, local dips are also observed for the elements of the noble gas group as well as chromium, copper and palladium.
- For low-Z atoms, the maximum charge density only marginally increases upon the addition of a second atom, which makes it difficult to quantitatively analyse the charge density distribution introduced by additional atoms such as adatoms of contamination.
- The ratio in maximum charge density between one and two atoms shows a non linear behaviour and a ratio below a factor of two indicating that two atoms do not show twice the charge density than one atom of the same species.
- Only for light atoms with an atomic number below Z=32, the maximum charge density increases almost linear when a second atom is added.
- The shown maximum charge density of single atoms can not explain the unexpected charge density ratio in a WSe_2 monolayer.

4.4.2 Influence of the Distance of Atoms

The obtainable DPC signal is presumably also influenced by the vertical distance of the atoms, as beam propagation along the atomic columns is affected by the distance between the atoms within the column. With different interatomic distances, the intensity distribution on the second atom will change due to the intensity redistribution at the first atom and the subsequent propagation of the electron wave. This propagation will presumably also alter the non-linearities observed in Chapter 4.4.1. Although the distance between two atoms in a crystal can typically not be changed experimentally, missing atoms within an atomic column such as defects result in an effective change of the vertical distance between atoms. In addition, the distance of atoms in beam propagation direction is also influenced by the orientation of the specimen. Hence, the impact of the distance between two atoms on the DPC signal is important to investigate, especially for quantitative analysis of defects. Therefore, the influence of the distance between atoms is investigated in the following using comparable multislice image simulations, here limited to a maximum of two atoms per atomic column – either tungsten or selenium atoms – using the IAM-based potentials. The multislice image simulations shown in the following consider interatomic distances d between 0.1 nm and 2.4 nm along the beam propagation direction as indicated in the sketch in Figure 4.15. Further information about the simulations is given in the Appendix 9.11 in Table 9.7.

Figure 4.15 a) reveals the influence of the distance of two atoms on the maximum beam deflection magnitude. This is achieved by plotting the ratio of maximum beam deflection from two atoms at varying distance and the one imposed on the beam by a single atom. The ratio of maximum beam deflection is indicated by a solid green line for selenium atoms and by a solid grey line for tungsten atoms. For both atomic species, the ratio of maximum beam deflection magnitude increases with increasing distance until a maximum is reached. Afterwards, the ratio then drops again. The maximum ratio is observed at a distance $d = 0.7\,\text{nm}$ for selenium atoms and at $d = 1.2\,\text{nm}$ for tungsten atoms. The ratio of maximum beam deflection magnitude shows that the maximum ratio shifts towards larger atomic distances d. This finding is presumably due to the stronger interaction of the electron beam with the higher atomic potentials resulting in a pronounced intensity redistribution. In addition, the maximum ratio is not found at the vertical distance of the tungsten and selenium atoms in WSe_2 (indicated by the two dashed lines in Figure 4.15 a). Furthermore, the ratio of maximum beam deflection is overall higher for selenium than for tungsten at any distance between the two atoms. For selenium, the ratio starts at 1.8 and increases up to approximately 2, implying that the maximum beam deflection for selenium is closer to twice that of a single atom at any given distance. In contrast to selenium atoms, the maximum beam deflection of two tungsten atoms is always lower than two times the beam deflection of one atom. Starting from a ratio of 1.3 for the smallest W–W spacing, the ratio increases to a maximum of 1.9. Therefore, the stacking distance between two atoms has especially for heavy atoms a drastic effect on the observed maximum beam deflection. Quantitatively, two heavy atoms do not result in twice the beam deflection of one atom which again highlights the non-linear behaviour of DPC signal. The always smaller ratio

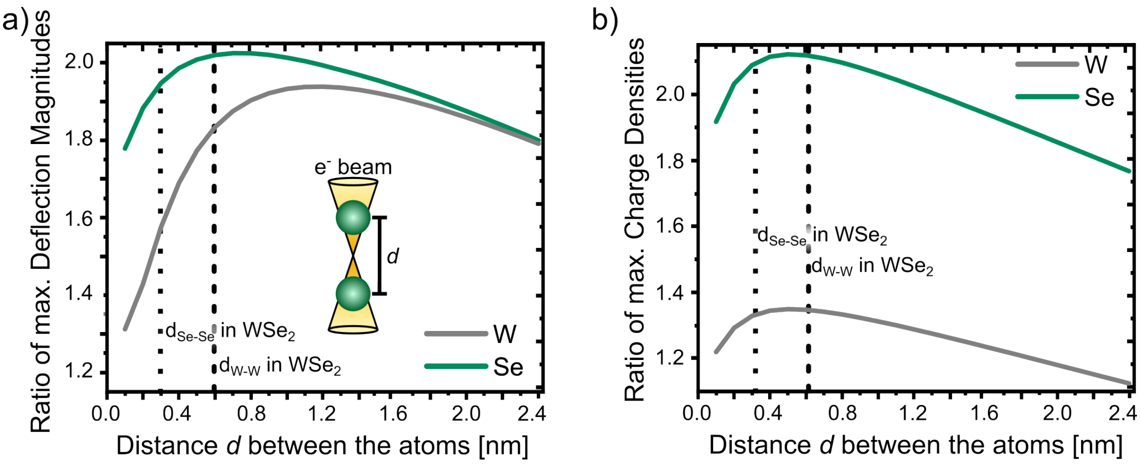

Figure 4.15: a) Ratio of the maximum beam deflection of two atoms stacked on top of each other in dependence of the vertical distance d between each other in reference to the maximum beam deflection of a single atom. b) Ratio of the maximum charge density for two atoms in reference to a single atom for different distances d between the two atoms. Green solid lines indicate selenium atoms and grey solid lines indicate tungsten atoms. The dotted and dashed lines indicate the vertical distance between selenium atoms and tungsten atoms in WSe_2.

of maximum beam deflection of tungsten compared to selenium can be explained by the fact that the higher atomic number, and, therefore, the higher atomic potential, leads to a stronger intensity redistribution inside the electron beam. Thus, the influence of a second tungsten atom results in a more pronounced change in the intensity redistribution than for two selenium atoms which is emphasised by the greater changes in the ratio of the maximum beam deflection.

To further investigate the influence of the distance of two atoms on the DPC signal, Figure 4.15 b) shows the charge density ratio of two atoms stacked on top of each other in reference to the charge density of a single atom. The charge density magnitude are derived from the same simulations as in Figure 4.15 a). The distance is again varied between 0.1 nm and 2.4 nm but the number of atoms remains the same. As the calculation of the charge density requires a specimen thickness, a constant thickness of 1 nm is used for the calculation of the charge density for comparability. By this, the influence of the distance can be solely investigated without the influence of variations in specimen thickness. In addition, the specimen thickness is only a constant factor and therefore does not change the course of the calculated charge density ratio.

For the smallest distance between two selenium atoms the ratio in maximum charge density starts at 1.9 and increases to a maximum of 2.12 at a distance of $d = 0.5$ nm. For larger distances than 0.5 nm, the ratio decreases almost linearly with increasing distance. In comparison to the previously discussed beam deflection ratio, the maximum of the charge density ratio is found at smaller distances between the two atoms. An analogous behaviour is observed for the maximum charge density ratio tungsten atoms. The charge density ratio for the smallest distances starts at about 1.2 and only slightly increases up to a ratio of 1.35 at the same distance of $d = 0.5$ nm, where the maximum ratio of two selenium atoms is found. Overall, the charge density ratio of tungsten atoms is again lower compared to the one of selenium atoms over the considered distance range. Comparing the actual distances of atoms in WSe_2 indicates that for two selenium atoms with the typical distance of $d_{\mathrm{Se-Se}} = 0.33\,\mathrm{nm}$ in WSe_2 the observed ratio in charge density, which is about 2.1, is more than twice the charge density ratio of one selenium atom whereas for a typical distance of tungsten atoms $d_{\mathrm{W-W}} = 0.65\,\mathrm{nm}$ in WSe_2, the charge density ratio is only of about 1.4. Thus, it can be assumed that the observed charge density of two atoms is always lower than twice the maximum charge density of one tungsten atom. In contrast, the measured maximum charge density of two selenium atoms can even be higher than twice the maximum charge density of one single selenium atom.

In addition to possible charge redistribution due to the defect changing the DPC signal, the changed distance between the remaining atoms within the atomic column will also affect the DPC signal. The findings highlight the difficulty of quantitative DPC analysis of light and heavy atoms.

Section summary

- The vertical distance between two atoms influences the measured maximum beam deflection as the intensity distribution on the second atom is affected by the intensity redistribution at the first atom and the following beam propagation.
- For any distance between two selenium or two tungsten atoms, the maximum beam deflection is less than twice the maximum beam deflection of a single atom. In contrast to tungsten atoms, two selenium atoms reach a ratio of two for a certain distance.
- The ratio of maximum beam deflection is for any distance between the atoms lower for tungsten than for selenium illustrating the stronger intensity redistribution in the electron beam in presence of two tungsten atoms.
- The maximum charge density ratio between one and two selenium atoms is even above 2 for a certain distance between the two atoms and drops for increasing distances. The maximum ratio of charge density for two tungsten atoms is significantly lower with only 1.35.
- Due to the significant influence of the distance between two atoms on the maximum beam deflection and resulting charge density, a quantitative investigation of defects with single atoms missing in an atomic column is hampered. As a missing atom changes the distance between the atoms leading to a non-linear change in the beam deflection, a correct interpretation of the field distribution is difficult.

4.4.3 Influence of the Number of Atoms

The DPC signal is described to be related to the specimen's projected potential, which in turn depends on the atomic number and the number of atoms along the beam propagation direction (Chapter 2.5). It is expected for thin specimens within the WPO approximation, that the projected potential is linearly related to the number of atoms within an atomic column [4, 6, 30]. In the previous two chapters, the influence of the atomic number on the DPC signal was investigated in great detail. In addition, also the influence of the distance between atoms stacked along the beam propagation direction was considered. However, the simulations where limited to one or two atoms stacked above each other. Thus, the following discussion will investigate the influence of the number of atoms in an atomic column on the DPC signal. For this, multislice image simulations of tungsten and selenium atomic columns with varying number of atoms and a fixed distance of 0.6 nm between the atoms were conducted. The atoms were stacked on top of each other along the beam propagation direction and for each stack the defocus was set to the middle of the atomic column.

Figure 4.16 a) depicts the mean beam deflection in dependence of the number of atoms in a selenium atomic column (green solid line) and a tungsten atomic column (grey solid line), respectively. The mean beam deflection is acquired in the same way as described in Chapter 4.4.1, i. e. calculated by the arithmetic mean of the DPC image over the whole simulated area of $0.4\,\mathrm{nm} \times 0.4\,\mathrm{nm}$. For both atomic species, an increasing mean beam deflection with increasing atomic number is observed. Independent of the number of atoms in the atomic column, the mean beam deflection is always higher for tungsten atomic columns than for selenium atomic columns. Other than described in literature, the increase in mean beam deflection is not fully linear as visualized by the inserted linear regressions (dashed lines). From Figure 4.16 a) it can be deduced that the deviation from a linear dependency is more pronounced for tungsten than for selenium atomic columns. It is also noteworthy, that the linear regressions exhibit a y-axis offset for both atomic species. This offset is higher for tungsten ($y^{\mathrm{W}}_{\mathrm{offset}} = 3.6 \cdot 10^{-4}\,\mathrm{mrad}$) than for selenium ($y^{\mathrm{Se}}_{\mathrm{offset}} = 1.2 \cdot 10^{-4}\,\mathrm{mrad}$) indicating the pronounced non-linear behaviour for the heavier tungsten atomic columns. Although not shown here, one can expect that the non-linear behaviour of the mean beam deflection gets stronger with increasing atomic number. This is in accordance with the validity of the WPO approximation which holds for larger thicknesses if light atoms are present and breaks down even for small specimen thicknesses in case of heavy atoms present [28].

Figure 4.16 b) shows the maximum beam deflection magnitude in dependence of the number of atoms within a selenium and tungsten atomic column indicated by the green and grey solid lines, respectively. Overall, the maximum beam deflection increases with increasing number of atoms within the atomic column. However, it behaves differently compared to the mean beam deflection shown in Figure 4.16 a). For the selenium atomic column, the maximum beam deflection increases linearly for only a few atoms in the atomic column but for larger number of atoms within the atomic column the curve flattens and the slope decreases. For the tungsten atomic columns, the maximum beam deflection increases linearly but shows a non-monotonic behaviour for large number of atoms. To analyse

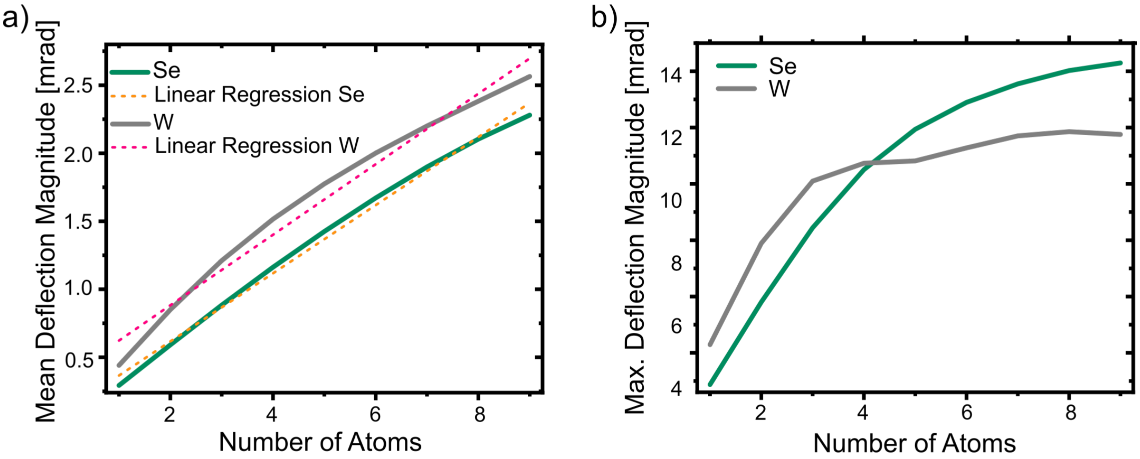

Figure 4.16: a) Mean beam deflection for selenium and tungsten atomic columns as a function of the atoms within an atomic column. The defocus is set to the middle plane of the stacked atoms. b) Maximum beam deflection for selenium and tungsten atomic columns with increasing number of atoms. Green and grey solid lines indicate selenium and tungsten atomic columns, respectively.

the linearity of the maximum beam deflection with increasing number of atoms and to identify the possible deviations from a linear behaviour, linear regressions are used. Several linear regressions are fitted for different number of atoms within the atomic column for tungsten and selenium atomic columns, respectively. The different linear regressions are given in the Appendix 9.4. Starting with a linear regression between one and two atoms and step-wise increasing the number of atoms contributing to the fit, a starting point for the non-monotonic behaviour can be identified. The quality of the linearity of each regression is quantified by the R^2-value. Each regression is defined as linear if the R^2-value is greater than 0.99. For selenium atomic columns, a linear increase in maximum beam deflection is observed for up to four selenium atoms above each other. For more than four selenium atoms, the deviation from a linear regression increases and the slope of the maximum beam deflection is reduced significantly. For the tungsten atomic column, no linear increase in maximum beam deflection with a reasonable R^2-value of about 0.99 is observed. Thus, the linear regression is only reasonable for the first two atoms. For more atoms the R^2-value drops below 0.99 and the maximum beam deflection increases with a less steep slope. The change of the linear increase in the maximum beam deflection observed for selenium and tungsten atomic columns gives an insight into the break-down of the WPO approximation necessary for quantitative DPC imaging (Chapter 2.5). For tungsten, the observed non-monotonic behaviour in maximum beam deflection for more than two tungsten atoms indicates that the WPO approximation is not valid for more than two tungsten atoms. Although the fast break-down of the WPOA for heavy atoms was already indicated by Müller-Caspary et al. [28], the observed break down for just two tungsten atoms is surprising. It is noteworthy that the non-monotonic behaviour of the maximum beam deflection is observed for selenium atomic columns comprising more than four atoms, which corresponds to a WSe_2 bilayer with a specimen thickness of only 1.2 nm. In comparison to other specimens, these thicknesses are fairly low and it was expected that mono- and few-layers of 2D materials inherently fulfil the WPOA. However, Figure 4.16 b) shows that this is not the case and quantitative DPC imaging is only reasonable for mono- or bilayers of WSe_2. For other 2D materials with a combination of lighter atoms than tungsten and selenium, presumably more layers are suitable for quantitative DPC imaging. However, for WSe_2 the simulations of the number of atoms indicate that quantitative DPC imaging is only reasonable for up to a bilayer.

In conclusion, the number of atoms in an atomic column changes the resulting DPC signal, but the increase in DPC signal is not linear even for only a few atoms stacked on top of each other. For a selenium atomic column, the increase in DPC signal increases linearly for up to four selenium atoms which corresponds to the selenium atomic columns in a WSe_2 bilayer. For tungsten no linear behaviour can be observed and even a non-monotonic behaviour is found for four tungsten atoms.

The simulations show the break-down of the WPO approximation for more than two tungsten atoms and for more than four selenium atoms stacked on top of each other. As the WPOA is a requirement for quantitative DPC imaging, for the investigation of electric field and charge density distributions in WSe_2 using STEM-DPC the number of layers should not exceed a bilayer. However, none of the shown single atom simulations was able to explain the unexpected charge density ratio between tungsten and selenium atomic columns in a WSe_2 monolayer. Therefore, the following Chapter 4.4.4 investigates beam propagation along the two atomic columns in WSe_2.

Section summary

- The mean beam deflection increases for increasing number of atoms in the atomic column. However, the increase is not linear highlighting the influence of the intensity redistribution and the beam propagation along atomic columns.
- The maximum beam deflection in dependence of the number of atoms in a selenium or tungsten atomic column shows a non-monotonic increase for more than four selenium or more than two tungsten atoms. This illustrates the break-down of the WPO approximation necessary for quantitative DPC imaging.

4.4.4 Influence of the Beam Propagation

Although the simulations of single atoms in dependence of the atomic number, the number of atoms, and the distance between the atoms, provided insight into how these parameters influence the DPC signal, the unexpected higher electric field magnitude and charge density at selenium atomic columns compared to tungsten atomic columns are not yet clarified. These single atom simulations revealed that the mean beam and maximum beam deflection is higher for two selenium atoms compared to one tungsten atom. Thus, the unexpected ratio of electric field and charge density observed in the DPC measurements of a WSe_2 monolayer shown in Chapter 4.1, is consistent with the behaviour of the individual atoms. Despite this agreement, the finding contradicts the general dependency on the projected atomic number as the two selenium atoms have a lower projected atomic number than the one tungsten atom.

Due to the stacking of atoms it might be possible that the two selenium atoms alter the incident electron probe stronger than one tungsten atom even though the projected atomic number is smaller. Thus, the actual beam propagation along the atomic columns is of importance for a correct understanding of quantitative DPC imaging.

For example, the channelling effect – defined as the tendency of the incident electron beam to propagate preferentially close to an atomic column – leads to a certain intensity redistribution, which might result in an overestimation of the beam deflection in DPC imaging. The channelling of electrons along atomic columns is well known for crystalline materials orientated in zone-axis orientation where the incident electrons tend to be trapped close to the atomic cores due to the atomic potential [200–204]. This channelling results in an oscillation of the probe intensity depending on the propagation depth inside the specimen. However, the channelling effect not only influences the intensity distribution but also the angular distribution of the incident electron probe [205]. As this effect is introduced by the atomic potential of the atoms, the atomic number strongly determines the strength of this effect [201, 205].

For small specimen thicknesses and in combination with the sensitivity of STEM-DPC imaging on the deflection of the electron beam, this effect might also play a role for the quantitative investigation of atomic fields in 2D materials. Especially if the specimen thickness is as small as one monolayer but the number of atoms for the different atomic columns varies, the influence of channelling effects might become important.

Therefore, the evolution of the electron probe intensity inside the specimen is investigated. This is achieved by using multislice simulations of the real space distribution of the electron probe intensity which can be analysed after each interaction with a potential slice. Individual selenium and tungsten atomic columns consisting of six atoms are simulated using the software Dr. Probe [63]. The intensity of the electron probe in real space is obtained after the interaction with a slice leading to a stack of seven images of the real space probe intensity for each scan position.

Figure 4.17 a) shows the HAADF image of a selenium atomic column consisting of six atoms. The scan area is about 0.2 nm × 0.2 nm with 20 × 20 scan positions which result in a pixel size of 20 pm. Even though this pixel size is experimentally not feasible, it is used here to phenomenologically investigate the beam propagation and possible channelling effects for specimens as thin as 2D materials. The atoms within the atomic column are separated in beam propagation direction by a distance of 0.3 nm. As each slice of the multislice simulation consist of only one atom, the distance between the atoms also corresponds to the slice thickness. Figure 4.17 b) illustrates the slicing of the selenium atomic column used for the simulation.

The electron probe is focused on top of the first slice as illustrated by the blue triangle in Figure 4.17 b). The probe size is diffraction-limited by the electron wavelength and the aperture used which are set by the acceleration voltage of 80 kV and the semi-convergence angle α of 30 mrad. No residual lens aberrations are used in the simulations. Thus, the full width at half maximum (FWHM) of the incident electron probe, as determined by the diffraction-limited Airy function, is 71.6 pm. More information on the simulation parameters are given in Table 9.9 in the Appendix.

To investigate the beam propagation in the vicinity of the selenium atomic column in dependence of the specimen thickness, three beam positions of the scan are selected and indicated by the three dots in the HAADF image. In Figure 4.17 a), the first scan position (“Pos. 1”) marked by the mint green dot is about 0.18 nm on the left of the atomic column position. This distance is comparable to the distance between a selenium and a tungsten atomic column in the W-Se dumbbell configuration. The second scan position under investigation is marked by the pink dot (“Pos. 2”) and is close to the atomic core. The distance is about 0.06 nm. The third scan position which is analysed in the following is placed almost directly on the atomic column position and indicated by the yellow dot (“Pos. 3”). For all three beam positions, the real space intensity distribution of the electron probe is extracted after each slice. By this, the influence of the interaction after each atom can be visualized. To display the 2D intensity distribution in dependence on the specimen thickness, 1D line profiles for each image of the real space probe intensity are extracted along the horizontal line centred at the initial position of the incident probe. Therefore, negative x-coordinates in the real space correspond to a position on the left of the initial beam position and positive values correspond to a position on the right of the initial beam position. Seven real space probe intensity images, one before any interaction and six after each atom within the column, are derived. For each of the seven probe intensity images line profiles are extracted and plotted in z-direction and shown in Figure 4.17 c, e, g) for the three beam positions under investigation.

Figure 4.17 c) depicts the evolution of the real space probe intensity for Position 1. The overall maximum of the intensity distribution can be found at the entrance slice which corresponds to the intensity distribution of the incident electron beam (highlighted by the white arrow in Figure 4.17 c). With increasing specimen thickness, the electron probe intensity almost remains the same. Only the maximum intensity reduces due to elastic scattering, which is considered in the simulation by the absorptive from factors. As the intensity of the incident probe is defined as one, the probe intensity after the interaction with an atomic slice is less than one.

To identify even small changes in the intensity distribution of the electron probe, Fig-

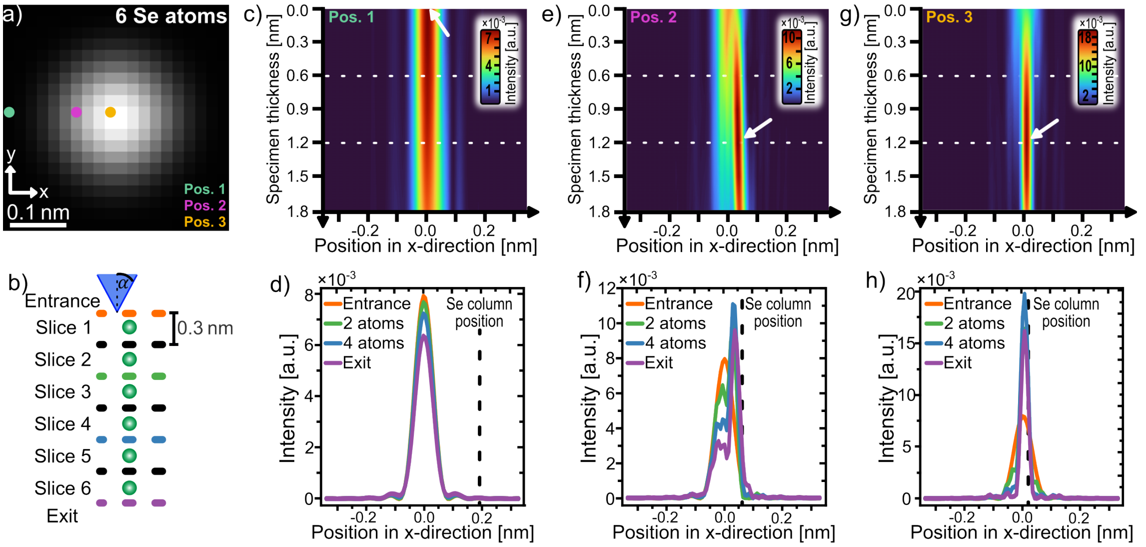

Figure 4.17: Investigation of the electron beam propagation at a selenium atomic column. a) HAADF image of the selenium atomic column with the three beam positions used for the analysis marked by the coloured dots. b) Illustration of the six selenium atomic column and the slicing used for the multislice algorithm approach used for the multislice image simulation. Each slice consists of one selenium atom and has a thickness of 0.3 nm which leads to an equidistant spacing between the six selenium atoms along the beam propagation direction. c, e, g) Probe intensity distribution along the x-direction in real space coordinates for the three different beam positions indicated in the HAADF image in a). d, f, h) Line profiles of the real space probe intensity along the x-direction for the three different positions. The selenium atomic column position is indicated by the black dashed line. Each plot contains four line profiles extracted from specific specimen thicknesses. The corresponding specimen thicknesses are indicated in the sketch in b) and also indicated by white dashed lines in the corresponding probe intensity distribution in c, e, g).

ure 4.17 d) shows the line profiles of the intensity distribution at different specimen thicknesses. The specimen thicknesses from which the line profiles are extracted are also indicated by the different colours of the dashed lines in the sketch in Figure 4.17 b). Here, line profiles are extracted from the entrance plane before any interaction, after the interaction with the two and four selenium atoms (marked by the white dashed lines in c), and at the exit plane after the interaction with all six atoms.

All four line profiles in Figure 4.17 d) show a similar shape corresponding to the ideal airy-shaped electron probe. However, the maximum probe intensity from the entrance plane (orange line) is reduced by about 20 % after the interaction with the six selenium atoms (purple line). As the shape of the intensity distribution remains the same, the influence of the atomic column is negligible at this distance to the atomic cores. The distance of about 0.18 nm from the atomic column is comparable to the distance between the atoms in a W-Se dumbbell. As no significant changes in the electron probe intensity due to the presence of the atomic column can be identified, this finding shows that the selenium atomic potential in the W-Se dumbbell configuration does not influence the beam propagation close to the neighbouring tungsten atomic column.

When the incident beam is close to the atomic column position, the atomic potential is expected to have a stronger impact on the intensity of the incident probe. Figure 4.17 e) depicts the corresponding evolution of the probe intensity at the beam position indicated by the pink dot ("Pos. 2") in the HAADF image at a distance of about 0.06 nm distance to the atomic column which is about half of the covalent atomic radius of a selenium atom ($r_{\mathrm{Se}} = 0.12\,\mathrm{nm}$ [206]). Thus, this scan position is located within the atomic potential and a strong intensity redistribution of the incident probe intensity is expected.

In contrast to the first scan position, the probe intensity distribution changes significantly already after the interaction with the first two selenium atoms. The intensity distribution splits up into two local maxima. With increasing specimen thickness and further interaction with the subsequent atomic potentials, a global maximum of probe intensity is formed, which is shifted towards positive x-position values (marked by the white arrow in e). The corresponding line profiles shown in Figure 4.17 f) show that a maximum probe intensity higher than the maximum intensity of the incident probe is formed after the interaction with four selenium atoms. The line profiles after the interaction with two, four and all six selenium atoms show the split into two maxima, however the maximum at the initial beam positions (orange line) vanishes with increasing specimen thickness, whereas the maximum shifted towards the atomic column position increases up to a global maximum after the interaction with four selenium atoms (blue line) and then starts to drop with further increasing specimen thickness. The newly formed global maximum in electron probe intensity exhibits an intensity which is about 40 % higher than the maximum intensity in the initial electron beam. It is important to note, that the total probe intensity is less than one due to intensity conservation. However, more intensity is confined to a single point, resulting in a larger maximum probe intensity after the interaction with the atoms.

The electron probe intensity does not show a channelling effect for the here investigated specimen thickness, which would be visible by an oscillation of the probe intensity, but instead the electron beam intensity gets refocused after the interaction with four selenium atomic potentials. The here shown refocussing effect can be quantified by the FWHM of the intensity distribution. The incoming electron beam with its airy-shaped intensity distribution exhibits a FWHM of 71.6 pm which is in accordance to the diffraction-limited FWHM. However, after the interaction with selenium atoms, an intensity redistribution takes place resulting in a global maximum in probe intensity and a reduced FWHM of only 34 pm which is below the FWHM of the diffraction-limited incident probe. Although, some intensity is still visible at the initial probe position, the main proportion of intensity is now located within this new formed intensity maximum. Thus, the subsequent atoms are now probed by an electron beam with a smaller diameter than incident electron probe on the first atom. Note, that the probe position additionally no longer matches the initial beam position of the probe, i. e. a measurable deflection arises from a different area than the initial beam position.

The third beam position ("Pos. 3") is located almost directly at the atomic column position. The distance with about 0.02 nm from the atomic column positions is even less than the Bohr radius ($a_0 = 0.052\,\mathrm{nm}$). The evolution of the real space intensity distribution of the electron probe in dependence of the thickness is shown in Figure 4.17 g). Here, the formation of a local intensity maximum is directly visible after the interaction with four selenium atoms (marked by the white arrow) which exhibits an even higher intensity than observed for the beam position 2. In contrast to the previously shown intensity distribution at scan position 2, this local maximum is only slightly shifted towards the position of the atomic columns (positive x-position values). However, this can be explained by the close distance of the scan position to the atomic column position. The electron beam is mostly parallel to the electric field components of the atoms and therefore the deflection perpendicular to the beam propagation direction is reduced [8, 34]. However, the influence of the atomic electric field is still strong enough to refocus the intensity of electron probe into a global maximum. Again, after the incident electron beam has interacted with four selenium atoms the maximum intensity increases significantly by about 150 % (blue line). Furthermore, the intensity distribution narrows from the ideal FWHM of 71.6 pm for the incident intensity distribution to a FWHM of 30 pm. Despite the formation in a global maximum, the intensity distribution at this scan position is more focused than for the beam position 2 where two local maxima are observed and a diffuse but pronounced background intensity evolves at the initial beam position for increasing specimen thicknesses.

For specimens with thicknesses of several tens of nanometre, also a shift of the intensity distribution close to atomic columns as well as a broadening of the electron beam due to the scattering of electrons at the atomic potentials are observed. However, no comparable investigations are found for small specimen thickness or individual atoms. Therefore, the observed evolution of the electron beam intensity in dependence of the specimen thickness is highly unexpected. A refocussing of the incident electron beam instead of a beam broadening is observed in case of only a few atoms stacked on top of each other. This refocussing effect of single atoms is barely investigated but was observable in a comparable way by J. M. Cowley in 1997 in Ref. [207] where the channelling effect results in a reduction of the incident beam diameter below 50 pm in the vicinity of heavy atoms. However, the consequences for quantitative STEM-DPC imaging are not discussed.

Therefore, the subsequent atomic potentials are neither probed by the same airy-shaped electron probe with a certain beam diameter as incident on the specimen, nor are they probed by a broader electron probe but instead the following atomic potentials are probed by an electron probe with a smaller diameter.

The re-focused electron probe might influence the measurement of the deflection as a larger number of electrons (due to the new global maximum) probe a certain part of an inhomogeneous field to the right of the scan pixel whereas the left of the pixel with a different field is probed by less electrons. The resulting average deflection of the electron beam at this pixel might differ from the arithmetic average value due to the inhomogeneous intensity distribution in the electron probe. However, it is difficult to relate the observed behaviour of the real space probe intensity to the DPC signal, as on the one hand the DPC signal is calculated from the intensity distribution in the reciprocal space at the plane of the detector, and on the other hand the experimental specimen conditions are different in terms of thermal vibration and crystal structure. For comparable simulations of the electron probe intensity, Wu et al. show not only the oscillatory behaviour of the probe intensity

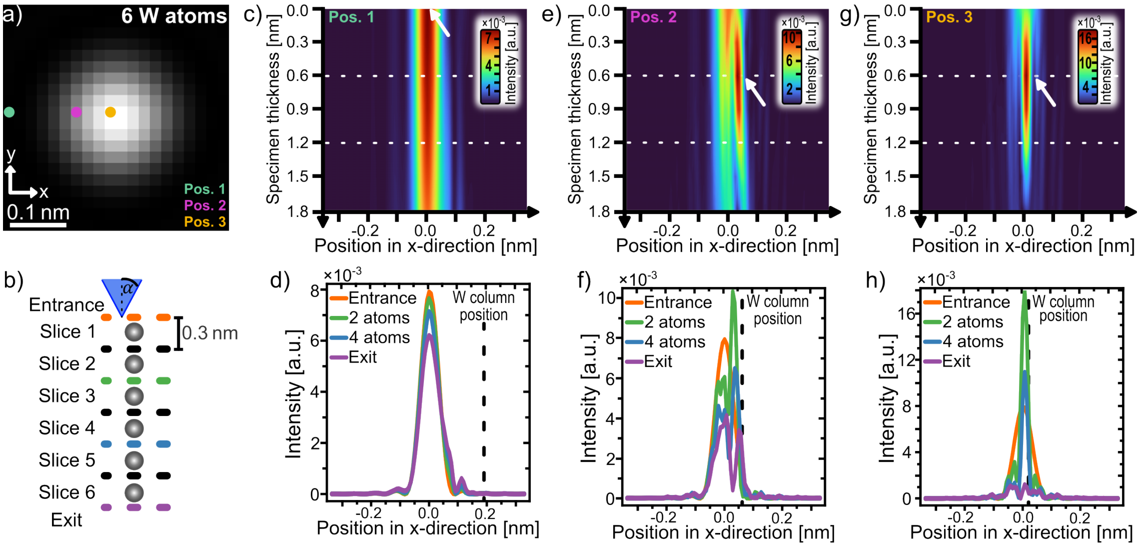

Figure 4.18: Investigation of the electron beam propagation at a tungsten atomic column. a) HAADF image of the tungsten atomic column with three spots marked by the coloured dots. b) Illustration of the six tungsten atomic column and the slicing used for the multislice algorithm approach used for the multislice image simulation. Each slice consists of one tungsten atom and has a thickness of 0.3 nm which leads to an equidistant spacing between the six tungsten atoms along the beam propagation direction. c, e, g) Distribution of the probe intensity distribution along the x-direction in real space for the three different spots indicated in the HAADF image in a). d, f, h) Line profiles of the real space probe intensity along the x-direction for the three distinct positions with respect to atomic column position which is indicated by the black dashed line. Each plot contains four line profiles extracted from specific specimen thicknesses. The corresponding specimen thicknesses are indicated in the sketch in b) and also indicated by white dashed lines in the corresponding probe intensity distribution in c, e, g).

with increasing specimen thickness, but also indicate an increase of the beam intensity for small specimen thicknesses of high-Z atomic columns such as gold atomic columns. As the evolution of the real space intensity distribution strongly depends on the atomic number, as described by Wu et al. [205], the influence of a tungsten atomic column on the electron probe is shown in Figure 4.18. The previously described simulations are repeated for a pure tungsten atomic column consisting of six tungsten atoms stacked on top of each other. Each slice contains one tungsten atom and has a thickness of 0.3 nm which results in a distance of 0.3 nm between the tungsten atoms along the beam propagation direction. The corresponding HAADF image is shown in Figure 4.18 a) and the scan positions under investigation are again marked by the three coloured dots. Figure 4.18 b) illustrates the slicing of the tungsten atomic column for the multislice image simulation. The real space probe intensity as a function of the specimen thickness is investigated in the same way as described for the selenium atomic column. Figure 4.18 c, e, f) depict line profiles of the real space probe intensity distributions as a function of specimen thickness. For the first beam position, the intensity distribution is comparable to intensity distribution at the same beam position in presence of the selenium atomic column (Figure 4.17 c). At this scan position and distance of the electron probe to the atomic column position, the atomic potentials barley influence the intensity distribution. Thus, the line profiles for the four different specimen thicknesses shown in Figure 4.18 d) resemble the behaviour of the incident airy-shaped intensity distribution. In contrast to the intensity distribution close to selenium atomic columns, a sidelobe of slightly higher intensity towards the atomic column positions forms. This can readily be seen by the small local maximum in beam intensity in the purple line in Figure 4.18 d) which occurs towards the atomic column position after the interaction with all six tungsten atoms. Thus, in contrast to the selenium atomic column, the tungsten atomic column slightly influences the electron probe even at a distance of about 0.18 nm from the atomic core. This is due to the larger extension of the tungsten atomic potential compared to the extension of a selenium atomic potential.

The real space probe intensity distribution in dependence of the specimen thickness for the second scan position at a distance of 0.06 nm to the atomic column is shown in Figure 4.18 e). This position is within the atomic radius defined as $r_{\mathrm{W}} = 0.16\,\mathrm{nm}$ for a tungsten atom [206]. Here again, the interaction with the first tungsten atoms results in a splitting of the intensity distribution into two local maxima. After the interaction with two tungsten atoms, a global maximum is formed (highlighted by the white arrow). In contrast to the selenium atomic column, less tungsten atoms are needed to focus the electron beam into a global intensity maximum. In addition, this maximum is also shifted towards the atomic column position by about 7 pm. Furthermore, the intensity of this focused electron beam increases by about 25 % and the FWHM reduces down to 30 pm. For the same beam position, the selenium atomic column leads to a reduction in the FWHM of only 34 pm. Thus, the refocusing action of two tungsten atoms is stronger, which results in a smaller beam diameter, than the refocussing action of the lower-Z selenium atoms. For increasing specimen thickness, the intensity reduces for both parts of the partitioned intensity distribution.

For a beam positioned at a very close distance to the atomic column, the real space probe intensity distribution behaves similar to the same scan position in case of selenium atoms. The real space probe intensity and the corresponding line profiles are displayed in Figure 4.18 g) and h). Again, the electron probe is focused to a global intensity maximum after the interaction with two tungsten atoms (marked by the white arrow) but rapidly vanishes for increasing specimen thicknesses. For this scan position a vanishing intensity distribution is observed after the interaction with six tungsten atoms. No significant peak can be identified. The refocusing action of the two tungsten atoms leads to a FWHM of about 26 pm with weak corona-like intensity distribution on the left and on the right of the global intensity maximum.

Summarizing the findings above, the simulated real space probe intensity of a convergent electron probe in STEM is strongly influenced by the presence of selenium and tungsten atomic columns especially if the scan position is close to the atomic column position. Here, the investigation of the evolution of the real space probe intensity was aimed for specimen thicknesses of only a few atoms to visualize the electron beam propagation in 2D materials. In contrast to existing literature, which show the electron probe intensity for several tens of nanometres specimen thickness, the influence of individual atoms is investigated in great detail. Unexpectedly, the electron probe intensity is reshaped in the vicinity of the atomic column and refocused into an electron probe with a FWHM smaller than the incident electron probe. Thus, the commonly expected beam broadening is not observed for the specimen thickness of only a few atoms but instead the intensity distribution is changed to a more focussed and concentrated intensity distribution close to an atomic column. This might be a part of the channelling effect described in literature, however, the introduced smaller FWHM of the electron probe due to the interaction with only a few atoms and the resulting smaller electron probe incident on the following atoms is only described by Cowley et al., and not related to the interpretation of STEM and DPC imaging itself [207]. The here shown beam propagation for the tungsten and selenium atoms is dominated by the atomic potentials as can be seen by the different focusing action of tungsten and selenium atomic columns. The influence of the observed redistribution of probe intensity is difficult to relate with measured DPC signals. For the STEM-DPC investigation of a WSe_2 monolayer discussed in Chapter 4.1, two selenium atoms exhibit a higher electric field and charge density compared to a single tungsten atom. Comparing the different real space probe intensity distributions shown in Figure 4.17 and 4.18 of two selenium atoms with one tungsten atom, the electron probe distributions are comparable with each other. In both cases, the initial electron beam intensity distribution splits into two local maxima and thus qualitatively comparable in intensity distribution.

To briefly investigate the beam propagation in a WSe_2 monolayer for the individual atomic columns, Figure 4.19 depicts the line profiles of the real space probe intensity of the incident electron beam (orange line), after the interaction with two selenium atoms (green line) and after the interaction with one tungsten atom (grey line) derived from the two sets of simulations shown previously in Figure 4.17 and 4.18. Both line profiles are extracted from the scan position “Pos. 2”, which is close to, but not directly on, the atomic column.

The direct comparison of probe intensity distribution for the same scan position for two selenium atoms and one tungsten atoms, highlights the impact of the refocussing of the probe intensity. The intensity distribution after the interaction with one tungsten shows a lower peak intensity than the distribution after the interaction with two selenium atoms. Although the tungsten atoms exhibit a higher refocussing action as shown previously and described by Wu et al. for high-Z atoms, the higher number of selenium atoms leads to a greater refocussing and a higher beam intensity in the new global maximum [205]. Thus, for two selenium atoms, more intensity is refocussed into a new global maximum which is slightly shifted from the initial beam position towards

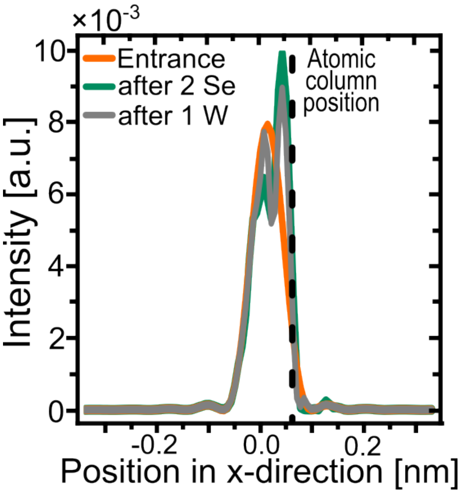

Figure 4.19: Line profiles of the real space probe intensity incident on an atomic column (orange solid line), after the interaction with two selenium atoms (green solid line), and after the interaction with one tungsten atom (grey solid line). The black dashed line indicates the position of the atomic columns.

the atomic column. This higher refocussing action might explain the higher mean beam deflection of two selenium atoms shown in Chapter 4.4.1 compared to one tungsten atom despite the lower projected number. In a WSe_2 monolayer, the two selenium atoms more strongly alter the shape of the electron beam and refocus the incident probe than the single tungsten atom which is in accordance to the observed higher mean beam deflection. Thus, the channelling effect, here only investigated for a few atoms, leads to a refocussing of electron beam intensity which results in a smaller electron beam probing the subsequent atoms.

It is described by Wu et al. that the channelling of the electron beam intensity and hence presumably also the observed refocussing of probe intensity, are related to a change in the angular distribution of the incident electron beam and thus will influence the DPC signal. The influence of these changes in the real space probe intensity distribution on the STEM-DPC images and the derived electric field distribution is difficult to quantify as the experimental conditions are more complex. These conditions include a non-ideal electron probe which is affected by residual lens aberrations. In addition, thermal vibration of the atoms and microscope instabilities also affect the measured DPC signal. Still, the important finding that a few (high-Z) atoms focus the real space probe intensity into a global maximum with high beam intensity instead of a beam broadening can also be expected in the experiments.

Neither the electron propagation seem to be drastically different close to tungsten and selenium atomic columns in a WSe_2 monolayer, nor do lens aberrations, the distance between atoms or the number of atoms within an atomic column solely explain the higher electric field and charge density of selenium atomic columns compared to tungsten atoms. The following chapter therefore investigates the atomic potentials in greater detail.

Section summary

- The beam propagation of the electron beam in terms of the real space probe intensity distribution is investigated in dependence of the distance towards an atomic column, the propagation depth and the atomic number of the atoms within the atomic column.
- The intensity redistribution strongly depends on the position of the incident electron beam and its distance to the next atomic column.
- For a position of the electron probe outside the atomic radius (“Pos. 1”), no significant intensity redistributions are observed in the presence of selenium atoms, and only slight changes in the airy-shaped probe intensity are observed in presence of tungsten atoms. After the interaction with six tungsten atoms, a local maximum shifted towards the position of the atomic column is formed.
- For the intermediate position of the electron beam to the atom (“Pos. 2”), the interaction wit the atomic potentials leads to the formation of a global maximum with increased beam intensity compared to the incident electron

beam and to a shift of the beam position. For selenium, the interaction leads to a global maximum after the interaction with four selenium atoms shifted towards the atomic column position. For tungsten, the global maximum in beam intensity forms after the interaction with two tungsten atoms. The maximum beam intensity is also shifted towards the atomic column position.

- For initial beam positions close to the atomic column ("Pos. 3"), the influence of the atomic potentials becomes stronger leading to an intensity redistribution which results in the formation of a global intensity maximum after the interaction with four selenium or two tungsten atoms. These maxima exhibit a higher intensity and a smaller FWHM than the incident probe. For this position, no shift of the maximum beam intensity towards the atomic column position is observed.
- For the third beam position ("Pos. 3"), the incident electron beam is refocused by the atomic potential below the diffraction limit resulting in a FWHM of 26 pm after the interaction with two tungsten atoms and of 30 pm after the interaction with four selenium atoms illustrating the different interaction strength due to the different atomic number of tungsten and selenium atoms. The subsequent atoms within an atomic column are therefore probed with an even smaller electron probe then the incident probe.
- For the specific situation in a WSe_2 monolayer with one atomic column consisting of two selenium atoms and one atomic column containing only on tungsten atom, the evolution of the real space probe intensity shows a stronger intensity redistribution resulting in a more focussed electron probe for the two selenium atoms than for the single tungsten atom. This is a possible explanation for the observed higher beam deflection for selenium atomic columns than for tungsten atoms.

4.4.5 Investigation of the Atomic Potential and the Influence of the Crystal Structure

In this chapter, the atomic potentials and the projection of the crystal structure is investigated to further analyse the unexpected charge density observed for tungsten and selenium atomic columns in a WSe_2 monolayer. This is achieved using the software *abTEM* which allows to directly access the potential of each slice used for the multislice image simulations from Chapter 4.4.1. Figure 4.20 shows the mean potential for one (green plot) and two atoms (orange plot) in dependence of the atomic numbers. With increasing atomic number, the mean potential increases though the increase is not monotonic. Instead, the mean potential shows a behaviour comparable to the observed mean beam deflection shown in Figure 4.13 with local minima for specific atoms. These local minima are observed again for the elements of the noble gas group as well as for chromium, copper and palladium. This finding emphasises that the mean beam deflection derived by STEM-DPC reflects the mean potential of the single atoms.

In contrast to the mean beam deflection, the mean atomic potential of two atoms above each other is exactly twice the mean potential of one atom. This was not the case for the mean beam deflection derived by STEM-DPC. Although, the potentials used for the simulations fulfil the linearity in dependence of the number of atoms, the resulting quantities derived from DPC measurements are strongly influenced by the intensity redistribution or beam propagation which lead to the non-linear behaviour (Chapter 4.4.3).

Figure 4.20 b) shows the corresponding maximum potential of the individual atomic potentials used for the multislice image simulation of the DPC images which corresponds to the maximum potential located at the centre of the atomic column. Here, the maximum potential for one (green solid line) and two atoms (orange solid line) stacked on top of each other increases linearly with increasing atomic number. In accordance to the observed linearity of the mean potential with the number of atoms, here again, the ratio between the maximum potential of two atoms and the maximum potential of one atom is exactly a factor of two. Thus, the non-linearity of the beam deflection with the number of atoms is

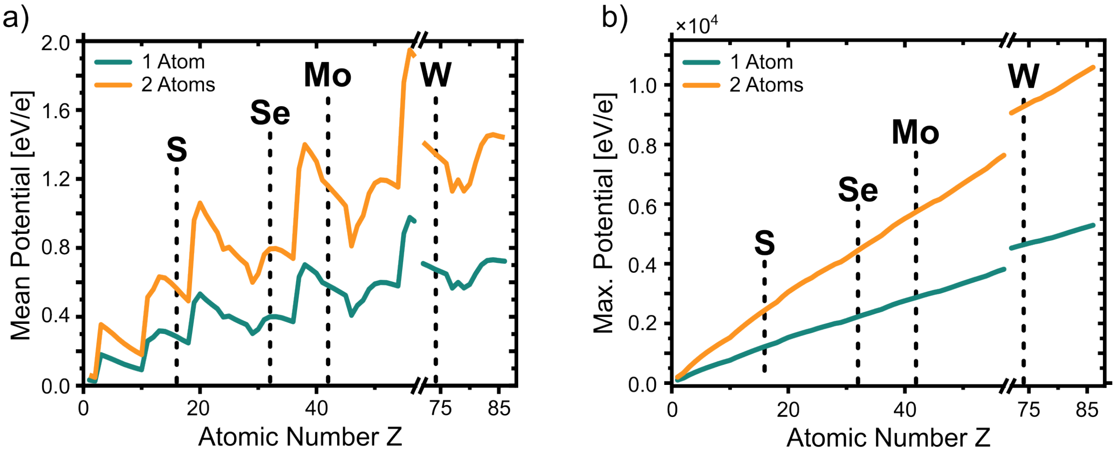

Figure 4.20: a) Mean and b) maximum potential of one (green) and two (orange) atoms for increasing atomic number Z.

V(Z)	1 atom		2 atoms	
	slope	intercept	slope	intercept
Z $\leq$ 56	64 ± 1	156 ± 12	129 ± 1	313 ± 24
Z $\geq$ 72	54 ± 1	593 ± 59	109 ± 2	1186 ± 119

Table 4.1: Parameters of the linear regression for the two regions with atomic numbers of Z$\leq$56 and Z$\geq$72. All values are in the unit of eV/e.

not introduced by the projection of the atomic potentials in the simulations but must result from the influence of the beam propagation at beam positions close to the atomic columns leading to a redistribution of intensity on the detector. This finding is of great importance as it highlights that STEM-DPC is reflecting the individual atomic potentials, but does not allow for a direct interpretation of quantitative analysis. In other words, the assumption that for thin specimens the interaction between electrons and specimen can be estimated using the projected specimen potential is erroneous even for extremely thin specimens, i. e. it makes a difference if the charge at which a beam electron is scattered is concentrated in one single nucleus, or if it is split between two nuclei along the beam direction.

While the ratio of maximum potential between one and two atoms on top of each other is constant for all atomic numbers, the slopes of the linear increase of the maximum potential is different for high-Z atoms (Z$\geq$72) compared to low-Z atoms (Z$\leq$56). Again, linear regressions are used for the two regions to identify the behaviour of the maximum atomic potential in dependence of the atomic number for one and two atoms, respectively. The results of the four different linear regressions are compiled in Table 4.1. Comparing the slopes for the low-Z regions of one and two atoms shows that the maximum potential of two atoms is twice the maximum potential of one atom. The same holds for the high-Z region where the factor between the slope of the linear regression for one atom and the slope of the linear regression for two atoms differ by a factor of two. Unexpectedly, the slopes between the lower Z and higher Z region differ slightly. For the high-Z region (Z$\leq$72) the slope of the maximum potential for one atom is lower than the slope for the low-Z region (Z$\geq$56). Thus, the maximum potential of heavy atoms increases less with increasing atomic number than the maximum potential of light atoms. This unexpected difference is also observed for tungsten and selenium atoms. Although the potential of one selenium atom is only of about V(1Se)=2353 eV/e, the maximum potential of two selenium atoms (V(2Se)=4706 eV/e) is higher than the maximum potential of one tungsten atom (V(1W)=4633 eV/e). Thus, this finding of the unexpected behaviour of the maximum of the atomic potentials might explain the higher positive charge density at the selenium atomic columns compared to the charge density at the tungsten atom in a WSe_2 monolayer. However, it contrasts the observed charge density for the same simulations of single selenium and tungsten atoms shown in Figure 4.14 where the higher charge density is observed for the tungsten atom and not for the two selenium atoms. As this is in contrast to the observed charge density ratio observed in the measurement shown in Figure 4.1 in Chapter 4.1, the potential of a WSe_2 monolayer is investigated for each atomic slice used for the multislice image simulations. As the single atom simulations are not affected by the neighbouring atomic potentials, the higher potential of two selenium atoms might be true for single atoms, but can be altered

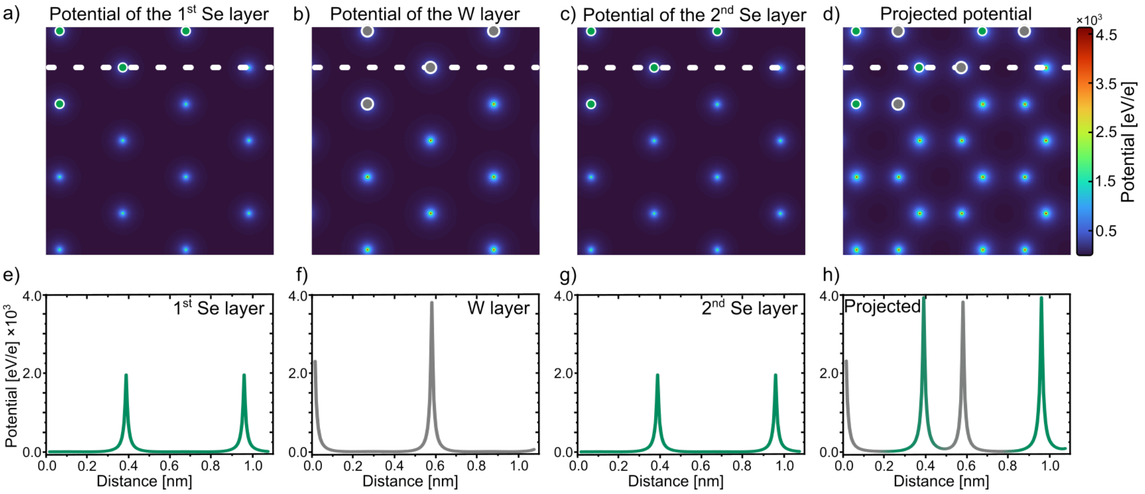

Figure 4.21: Potential of the three individual slices used for the multislice image simulation of a WSe_2 monolayer. a-c) Potentials of the first selenium atomic layer, the tungsten atomic layer, and the second atomic layer, respectively. The atom positions are marked by the green and grey dots for selenium and tungsten respectively. d) Electrostatic potential of the WSe_2 monolayer structure projected along the beam propagation direction including all contributions from the three atomic layers. The colorbar is the same for all four potential slices. e-g) Line profiles of the potential along the line indicated by the white dashed line in all three potential slices a-c). h) Line profile of the projected potential along the region indicated by the white dashed line in d).

by the overlap of other atomic potentials in a crystal. Therefore, Figure 4.21 shows the crystal potential of a WSe_2 monolayer. The potentials of the three different slices used for the multislice algorithm are shown in Figure 4.21 a-c) for the first selenium atomic plane, the tungsten atomic plane, and the second selenium atomic plane. As the potentials of atoms are completely projected into the corresponding slice no contributions of atoms from below or above a certain slice are present. Only the contribution of the atoms within the slice are considered in the individual slice. For all potential slices, the atomic positions of selenium and tungsten are indicated by the green and grey dots. For all three potential slices, the atomic potentials are visible as bright spots. As the colorbar is the same for all potential slices, a direct comparison between the selenium potential slice and the tungsten potential slice can be achieved. The tungsten potential landscape shows slightly brighter spots which are also slightly broader than the atomic potentials of the selenium potential slices. However, this is only barely visible in the projected potential landscape shown in Figure 4.21 d), which corresponds to the projection of the three individual potentials slices. The projected potential is defined as the sum of all potential slices of the structure. As STEM-DPC is sensitive to the projected potential, the potential landscape in Figure 4.21 d) is expected to determine the DPC images, although the quantitative values are strongly influenced by the previously shown effects (Chapters 4.2–4.4.4). Due to the projection of the two selenium slices, the difference in the bright spots between tungsten and selenium atoms of the individual slices is not observed as significant as before. However, to quantitatively investigate this in detail, Figure 4.21 e-h) show corresponding line profiles along the white dashed lines in Figure 4.21 a-d). From the line profiles of the individual atomic layers, again a single selenium atom (e & g) exhibits a lower maximum atomic potential than one tungsten atom (Figure 4.21 f). The line profile of the projected potential shows that the projection of two selenium atoms leads to a higher potential at the selenium atomic column compared to a single tungsten atom (Figure 4.21 h). The projected maximum potential at the position of selenium atomic columns is about $V_{proj}(2Se)=(4135\pm433)$ eV/e compared to the projected potential of tungsten with about $V_{proj}(1W)=(3883\pm655)$ eV/e. Based on this finding, it is reasonable to observe a higher positive charge density at selenium atomic columns using DPC imaging. Furthermore, the refocussing of the electron beam close to the selenium atomic column containing two atoms with a certain vertical distance to each other enhances the observed higher DPC signal at these lower-Z atomic columns. Thus, the observed higher electric field magnitude and positive charge density at the lower-Z atomic columns is a combinatorial effect of the projected potential, the changes in beam propagation due to the two atoms stacked in a certain way on top of each other, with the resulting refocussing action of the two atoms depending on the distance between them.

Section summary

- The mean atomic potential shows a non-monotonically increasing potential with increasing atomic number similar to the observed behaviour of the mean beam deflection with local minima for noble gas atoms and chromium, copper, and palladium.

- In contrast to the mean beam deflection, the mean potential of two atoms is twice the mean potential of one atom. The same holds for the maximum potential. The observed non-linearity in mean beam deflection in dependence of the number of atoms is therefore due to the beam propagation. Thus, the assumption of the projection of the potential for thin specimen in DPC imaging introduces errors even for extremely thin specimens.

- The increase in maximum potential in dependence of the atomic number is not fully linear. Still, it is almost linear for atoms with an atomic number below $Z\geq56$ and linear for atoms with an atomic number $Z\leq72$.

- The maximum potential of two selenium atoms is higher than the maximum potential of a single tungsten atom.

- The projected potential of a crystalline WSe_2 monolayer exhibits a higher potential at the selenium atomic columns compared to the tungsten atom positions, which is in good agreement with the observation in the DPC measurement of a WSe_2 monolayer.

4.5 Influence of Contamination on DPC Images

Contamination is a well-known problem in high-resolution STEM imaging as it influences the spatial resolution and degenerates the specimen (Chapter 2.8). Specimen contaminations typically originate from the sample preparation or the residual gas atmosphere in the microscope column [170].

For the transfer 2D materials, often a polymer-based transfer process is used which typically utilizes PDMS, PMMA or PVA. These polymers leave residuals on the 2D material layer, which then influence the measurable electric field distribution due to the additional nuclei on top or below the material of interest. Although, cleaning routines can be applied to reduce the amount of residuals, these procedures themselves might introduce additional contaminations or damage the specimen. Especially for 2D materials, the cleaning is challenging as conventional techniques, such as plasma treatments, are not applicable as they might destroy the mono- and few-layer samples. Therefore, small amounts of residual contamination atoms on top or below the 2D material are usually unavoidable. Thus, it is important to know the influence of residual contamination on the STEM-DPC investigation to correctly interpret the atomic electric field distribution. The contamination present in the measurement arises most probably from the polymer-based transfer process of the 2D material to the TEM grid. The introduced atoms are most likely low-Z atoms from the commonly used polymers such as PMMA, PVA or PDMS contain hydrocarbons, oxygen and silicon. Therefore, amorphous carbon is exemplarily used for the simulation of the possible contamination.

In the following, the influence of amorphous carbon contamination on top or below a WSe_2 monolayer on the atomic electric field distribution is investigated. The analysis is done using multislice image simulations of a WSe_2 monolayer with a varying amount of contamination. Figure 4.22 shows the top (a) and side view (b) of an exemplary structure used for the simulation of the influence of contamination. The top view includes the atomic structure of the WSe_2 monolayer which is indicated by the green and grey dots for selenium and tungsten atomic columns, and the additional carbon atoms indicated by the blue dots. The red rectangle highlights the scan area used for the simulations.

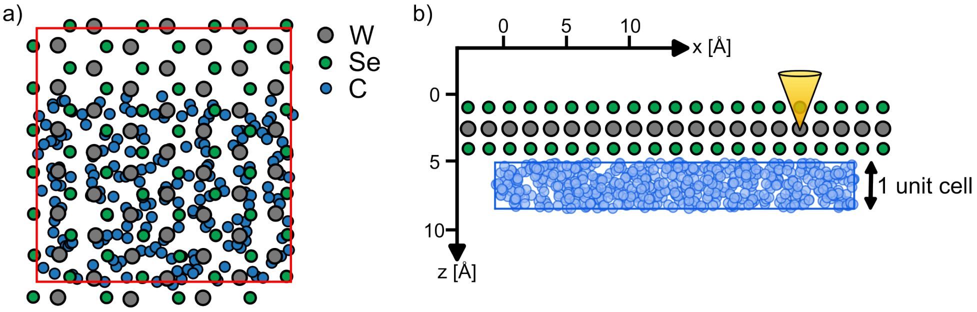

Figure 4.22: a) Top and b) side view of the structure stack of WSe_2 monolayer and an amorphous carbon layer. The red rectangle indicates the scan frame of $2 \times 2\,\mathrm{nm}^2$. The carbon layer is placed in beam propagation direction underneath the WSe_2 monolayer. The amorphous carbon layer has a thickness of one diamond unit cell t=0.36 nm. The focus is fixed to the layer of the tungsten atomic plane in the WSe_2 monolayer.

Figure 4.22 b) shows the corresponding structure in side view indicating the position of the amorphous carbon layer in beam propagation below the WSe_2 monolayer. The focus is set to the tungsten atomic layer in the WSe_2 monolayer as depicted by the yellow cone in Figure 4.22 b). The amorphous carbon is simulated using a diamond unit cell with cell parameters $a = b = c = 0.356\,\text{nm}$ where the atoms in the cell are randomly displaced by up to 50 % of the bond length. Atoms which overlap by a distance of 0.5 Å are removed. The diamond unit cell is then extended eight times in x- and y-direction. Although, this is not a real amorphous structure it still gives a sufficient insight into the influence of amorphous material on STEM-DPC measurements. Further information on the simulation parameters are given in Table 9.10 in the Appendix 9.11.

Figure 4.23 demonstrates the influence of carbon contamination and compares a measurement of a contaminated WSe_2 monolayer with a multislice image simulation of the atomic structure shown in Figure 4.22. Figure 4.23 a) and b) depict the HAADF images of a contaminated WSe_2 monolayer for the measurement and simulation, respectively. The atomic column types and positions are determined by the HAADF image contrast and indicated by the green and grey dots for selenium and tungsten atomic columns. Both HAADF images show the hexagonal arrangement of selenium and tungsten atomic columns as known for the WSe_2 monolayer in [0001] zone-axis orientation. Contamination is present for both, the measurement and the simulation, although not visible in the HAADF images. For the measurement, the contamination is located in the bottom part of the shown image area. An estimation of the interface between the area with contamination and a contamination-free area is indicated by the blue dashed line in the HAADF image. For the simulation, the contamination is in bottom part of the image area and the upper part is free of contamination. The interface is indicated by the blue dashed line in the HAADF image. The reason for the unrecognizable influence of contamination atoms on the HAADF images despite the atomic resolution is the typically lower atomic number of the contamination atoms compared to the higher-Z atoms of WSe_2. Since the low-Z atoms exhibit a low scattering power, they do not scatter many beam electrons to high angles. In combination with the high collection angles of the HAADF detector, a small amount of amorphous low-Z contamination can not be identified by the HAADF signal. However, the DPC images are more sensitive to residual low-Z atoms as the DPC detector is located on the optical axis and collects electrons scattered under small angles. Thus, for the measurement, the interface between contaminated and contamination-free area is determined by the DPC image, which shows distortions of the atomic fields in presence of contamination. But the determined interface indicated by the dashed line is only an estimation.

Figure 4.23 c) and d) show the corresponding colour-coded DPC images obtained from the measurement and the simulation. Both DPC images show the rotational symmetric atomic electric fields around the individual atomic column positions. However, the atomic field distribution also exhibits distortions, which are introduced by the contamination above or below the WSe_2 monolayer. Depending on the position of the individual contamination atoms with respect to the atomic columns of the WSe_2 monolayer, some atomic electric field distributions are also highly pronounced. This can be seen from the locally enhanced

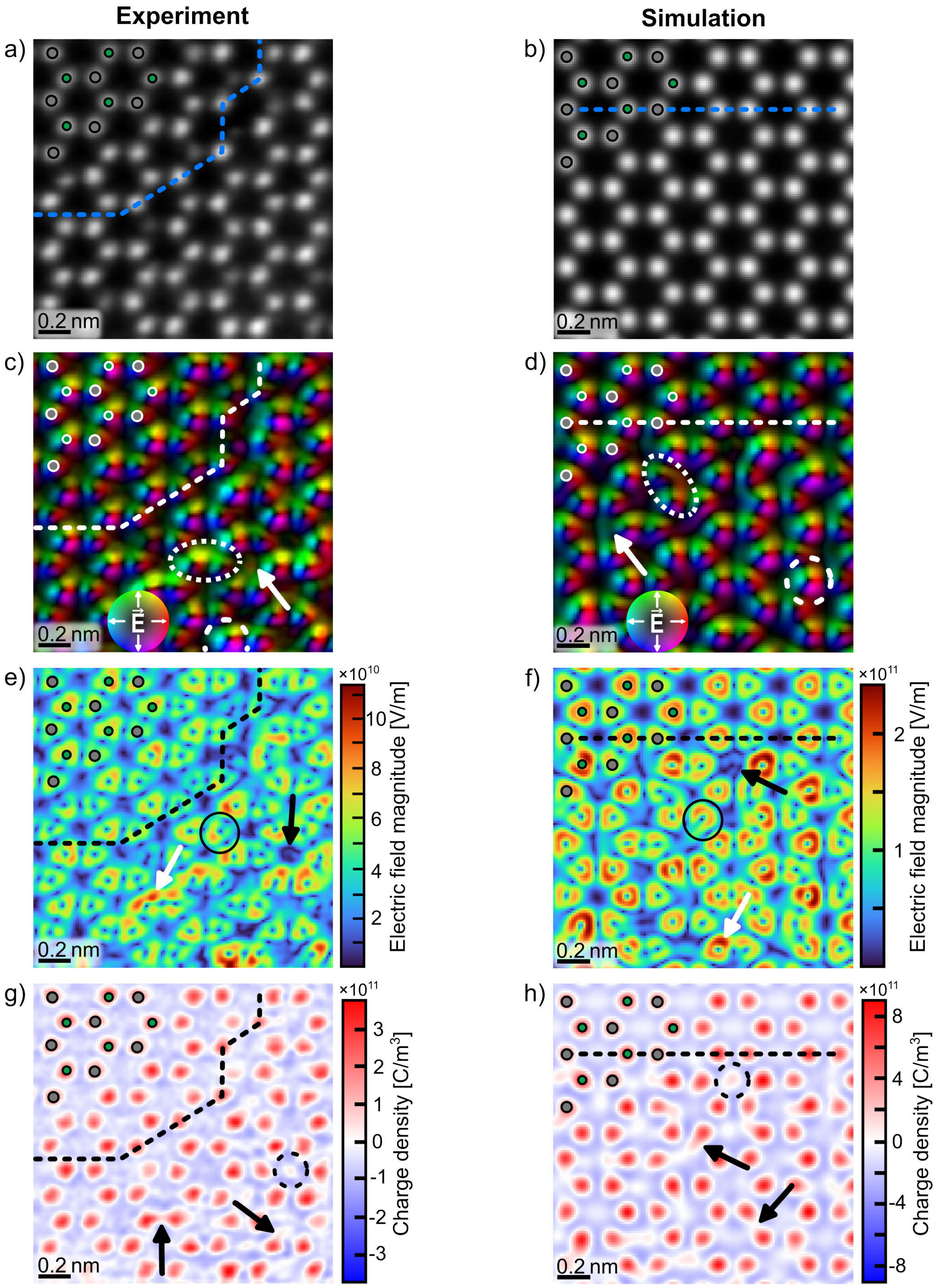

Figure 4.23: Influence of contamination on DPC measurements. From top to bottom the HAADF (a & b), DPC (c & d), and the electric field magnitude maps (e & f) as well as the charge density distribution (g & h) are depicted for the measurement (left) and a corresponding multislice simulation (right). The atomic column positions and species are given by the green and grey dots for selenium and tungsten respectively. Contamination atoms are not marked as they are not visible in the HAADF images.

saturation of the colour in the DPC image indicating an enhanced electric field magnitude in these specific areas. These atomic columns are exemplarily marked by white dashed circles in the measurement and the simulation. This is due to an incidental vertical alignment of contamination atoms with the underlying atomic columns of the monolayer, which results in a higher projected potential at these atomic columns. Due to the amorphous structure, the influence of contamination atoms is also visible at interstitial positions. For example, smeared field distributions are observed in the W-Se rings as indicated by the white arrows in Figure 4.23 c) and d). The individual atomic electric fields and their triangular shape are further distorted and merge with neighbouring atomic field distributions as indicated by the white dotted ellipses.

Based on the distortion of the atomic electric field distribution visible in the DPC image, the region of contamination can be identified and distinguished from the contamination-free area. The interface of contaminated and contamination-free area is indicated by the white dashed line in the DPC images. This estimation assigns the contaminated monolayer region below the dashed line and the contamination-free area above the dashed line. This rough estimation of the interface is used for all other image types shown in Figure 4.23.

The influence of contamination on top or below the specimen on the derived electric field distribution is also visible in the resulting electric field magnitude maps shown in Figure 4.23 e) and f). For the measurement and the simulation, the clean areas located above the dashed lines show the triangular-shaped atomic fields around each individual atomic columns which exhibit comparable shapes and magnitudes for all the columns of the same atomic type in this area. In contrast, the atomic electric field magnitude in the contaminated areas show strong variation in the shape and magnitude around the atomic column positions. Due to the random distribution of contamination atoms on the WSe_2 monolayer, features with moderate electric field magnitudes are found within W-Se rings indicating the presence of low-Z atoms (exemplarily marked by black arrows in Figure 4.23 e) and f). Furthermore, the atomic electric field distributions around individual atomic columns are distorted due to the influence of contamination atoms, which lead to a loss of the triangular shape as exemplarily highlighted by the black circles. In some cases, the field magnitude is locally enhanced leading to pronounced tips of the triangular distribution as exemplarily indicated by the white arrows.

A comparable behaviour is observed in the charge density distribution shown in Figure 4.23 g) and h). The additional low-Z atoms of the contamination introduce additional local positive charge density in the W-Se rings, or lead to charge density features which are continuos across neighbouring atomic columns or fade into the W-Se rings (exemplarily marked by the dashed black circles and the black arrows). Generally, the observed features introduced due to contamination atoms in the measurement are in great agreement with the one observed in the simulation.

To quantitatively investigate the influence of amorphous carbon contamination on the DPC signal, simulations with varying amount of contamination on the WSe_2 monolayer are done. The amount is varied in steps of unit cells of amorphous carbon between zero and three unit cells ($n \cdot 3.56\text{Å}$). As a difference in the influence of contamination is expected whether it is

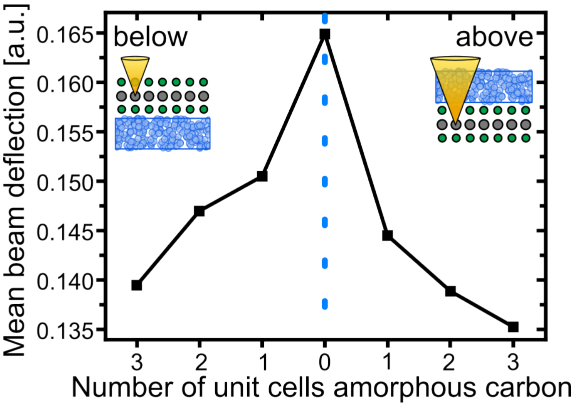

Figure 4.24: Mean beam deflection in dependence of the amount of amorphous carbon contamination given as number of unit cells either above or below the specimen.

above of below the specimen in beam propagation direction, the simulations are conducted for both cases. To quantitatively analyse the influence of the contamination the mean beam deflection is used as a figure of merit. The mean beam deflection is derived from the whole scan area of $1.8 \times 1.8\,\mathrm{nm}^2$ which is fully covered with the amorphous carbon. The defocus is constant and set to the tungsten atomic plane as sketched in Figure 4.24. A sketch of the simulated structure with varying amount of amorphous carbon and the obtained HAADF and DPC images are exemplarily shown in the Appendix in Chapter 9.5 for contamination below the WSe_2 monolayer. Additionally, Chapter 9.5 provides an analysis of the impact of non-rigid registration of contaminated DPC images as an image post-processing step to reduce the influence of contamination.

Figure 4.24 shows the mean beam deflection plotted over the number of unit cells of amorphous carbon atoms. The blue dashed line indicates the simulation without any contamination. On the left of the dashed line, the carbon contamination is placed in beam propagation direction below the specimen, as illustrated by the inserted sketch. On the right of the dashed line, the simulation is done with the carbon contamination on top of the specimen. From Figure 4.24 it is clearly visible, that the highest mean beam deflection is observed for the contamination-free specimen. The mean beam deflection reduces with increasing amount of contamination either above or below the specimen. It is also evident that the influence of the same amount of contamination below the specimen is smaller than the one above the specimen. This can be explained by the beam propagation: For amorphous contamination above the specimen, the electron beam is already altered and broadened by the contamination before it interacts with the crystalline specimen structure of interest. If the amorphous contamination is located below the specimen, the sharp electron beam first interacts with the specimen of interest and gets deflected leading to the DPC signal of a WSe_2 monolayer. The finely focussed probe than enters and interacts with the amorphous contamination which broadens the electron beam. However, the influence is less pronounced than for contamination above the monolayer due to the previous interaction with the potential of the crystalline material.

Summarizing the findings above, it can be concluded that residual contamination drastically influences the electric field distribution measurable by STEM-DPC as it reduces the measurable mean beam deflection. Although not visible in the HAADF image, even small amounts of amorphous carbon, e. g. a unit cell with 0.36 nm thickness, alters the atomic field distribution and results in distorted atomic fields. Thus, using a contamination-free specimen is crucial for quantitative DPC imaging.

Section summary

- Residual contamination of low-Z atoms are typically not visible in the HAADF images due to the low scattering power, but drastically influence atomic electric field distribution in DPC images.
- The individual atoms of amorphous carbon introduce artefacts in the atomic electric field distribution such as a distortion of the triangular shaped atomic field distribution of the atomic columns in a WSe_2 monolayer and locally enhanced fields of individual atomic columns.
- Multislice image simulations of increasing amount of amorphous carbon on top or below the WSe_2 monolayer show that contamination reduces the measurable mean beam deflection.
- Contamination above the specimen reduces the measurable beam deflection more strongly than the same amount of contamination below the specimen. This is possibly due to a diffuse broadening of the electron beam before it is incident on the WSe_2 monolayer.

Chapter 5

Electric Field and Charge Density Distributions in a MoS_2 Monolayer

5.1 Quantitative STEM-DPC Investigations of a MoS_2 Monolayer

Among the variety of different 2D TMDs, molybdenum disulphide is one of the most investigated TMD materials due to its semiconducting properties and high carrier mobility, direct band gap and bound excitons making it a promising candidate for future optoelectronic and semiconductor devices [114, 117, 208, 209]. Hence, the first DPC measurements of atomic electric fields in TMDs were carried out on MoS_2 by Müller-Caspary et al. in 2018 [27]. MoS_2 has a crystal structure similar to that of WSe_2 in which tungsten is replaced by molybdenum and selenium by sulphur. Unlike WSe_2, it consists of elements with much lower atomic numbers (Z(S)=16 and Z(Mo)=42). Thus, the WPOA, necessary for quantitative DPC investigation, is expected to be fulfilled in case of the MoS_2 monolayer and the interaction of the monolayer with the electron beam can be reduced to the projected potential (Chapter 2.4). Thus, the DPC signal is expected to be linear with the projected atomic number of the individual atomic columns [6, 30]. In the following, the electric field and charge density distributions in a monolayer of MoS_2 are investigated by STEM-DPC and directly compared with the results found for a monolayer of WSe_2. The MoS_2 monolayer is mechanically exfoliated and transferred to the TEM grid by the process described in Chapter 3.4. A visible light microscope image of the exfoliated MoS_2 flake is shown in the Appendix 9.6.
Figure 5.1 a) shows the HAADF image of a mechanically exfoliated MoS_2 monolayer in [0001] zone-axis orientation of the measurement (left) and the corresponding multislice image simulation. Comparable to WSe_2, the HAADF images show the hexagonal arrangement of bright spots with alternating bright and dim image intensity corresponding to the two different types of atomic columns, namely molybdenum atomic columns and sulphur atomic columns. With the lower projected atomic number of two sulphur atoms with Z(2S)=32 compared to the atomic number of Z(Mo)=42 for the molybdenum atom, the spots in the HAADF image with lower intensity are identified as sulphur atomic columns and the spots with high HAADF intensity are identified as molybdenum atoms. The atomic column positions and types are exemplarily marked in Figure 5.1 by the orange and blue dots for sulphur and molybdenum atomic columns, respectively.
Figure 5.1 b) depicts the electric field distributions by the colour-coded DPC images for the measurement (left) and the multislice image simulation (right). The atomic column positions determined by the HAADF image are inserted for visual guidance. Similar to the observed electric field distribution of a WSe_2 monolayer, the colour-coded DPC image of a MoS_2 monolayer shows rotational symmetric electric field distributions around each individual atomic column. Due to the close distance between the atoms and the resulting overlap of opposing electric field components, the individual atomic field distributions show a slightly triangular shape (exemplarily indicated by a white dashed triangle in Figure 5.1 b). This overlap of the field components of the individual atomic columns leads to local minima along the connecting directions between neighbouring atomic columns and within each hexagonal Mo-S ring (exemplarily marked by white arrows in Figure 5.1 b). Qualitatively, the measured field distribution is in great agreement with the corresponding

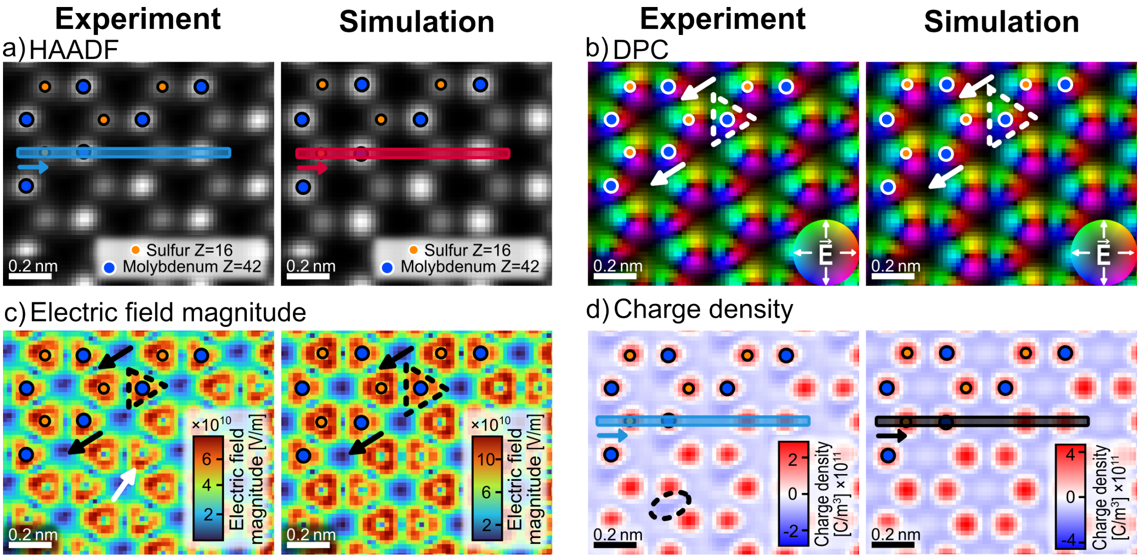

Figure 5.1: a) HAADF and b) DPC images of a MoS_2 monolayer in [0001] zone-axis orientation. c) Electric field magnitude and d) charge density distributions derived from the corresponding DPC signal. On the left of these pairs of images is the measurement shown and on the right the corresponding multislice image simulations. The atomic column types and positions are determined based on the HAADF image contrast and marked by the orange and blue dots for the sulphur and molybdenum atomic columns, respectively.

field distribution of the multislice image.

For a qualitative analysis, Figure 5.1 c) depicts the corresponding electric field magnitude maps for the measurement (left) and the multislice image simulation (right). Here, the triangular shape with enhanced field magnitude around each individual atomic column is clearly visible for both (exemplarily highlighted by black dashed triangles). Furthermore, the local minima in electric field magnitude are found between neighbouring atomic columns and within the Mo-S rings (exemplarily marked by black arrows). Overall, the absolute values of electric field magnitude are again lower for the measurement compared to the simulation.

For the measurement, the electric field magnitude map shows a triangular distribution around the atomic columns with a non-homogeneous distribution in field magnitude which can be seen, e. g. a tip of the triangle with enhanced electric field magnitude: for the sulphur atomic columns (orange dots), an enhanced electric field magnitude is located at the left tip of the triangular-shaped field distribution and for the molybdenum atomic columns (blue dots) an enhanced field is located at the lower left tip of the triangular feature (exemplarily marked by the white arrow in Figure 5.1 c). These locally enhanced field magnitudes are not observed at the same positions in the electric field magnitude map of the corresponding simulation. Still, a slightly pronounced field magnitude is observed at the edges of the triangles between S-Mo dumbbells. In accordance to the observed influence of the detector rotation on the electric field magnitude discussed in Chapter 4.3.2, this difference in the atomic electric field distribution arises from a relative rotation between the detector and the incident CBED pattern. Furthermore, this is presumably also influenced by small values of residual 3-fold astigmatism and star aberration (Chapter 4.2 and Appendix 9.14).

Comparing the atomic electric field magnitude values of the sulphur and molybdenum atomic columns reveals a higher electric field magnitude located at the sulphur atomic columns than at the molybdenum atomic columns. The same is also observed in the electric field magnitude map of the corresponding simulation. This is an unexpected finding as the two sulphur atoms in the MoS_2 monolayer exhibit a lower projected atomic number than the single molybdenum atom. However, it resembles the same behaviour as observed in a WSe_2 monolayer where the higher electric field magnitude is found at the lower-Z selenium atomic columns. This indicates that the chalcogen atomic columns in these two different TMD materials interact more strongly with the incident electron beam resulting in a higher measured electric field distribution despite the lower projected atomic number.

Figure 5.1 d) shows the charge density distribution of the MoS_2 monolayer derived from the measurement (left) and for the corresponding multislice image simulation (right). As expected for the charge density distribution the positive charge density indicated by red pixels is localized at the positively charged atomic columns. The net negative charge density is surrounding the atomic columns. Despite the overall lower absolute values of charge density, measurement and simulation are in great agreement. Only minor influences from detector rotation and lens aberrations are visible in the charge density distribution by the diagonally aligned stripes of slightly more pronounced negative charge density between molybdenum and sulphur atomic columns (exemplarily marked by the black ellipse in the measurement in Figure 5.1 d).

For the quantitative analysis of the charge density distribution in the MoS_2 monolayer, integrated line profiles over two Mo-S dumbbells, indicated by the coloured boxes in Figure 5.1, are used. Figure 5.2 a) shows the line profiles of the normalized HAADF image intensity for the measurement (blue solid line) and the simulation (black solid line) taken over the region marked in the corresponding HAADF images in Figure 5.1 a). Both line profiles show four peaks with different HAADF image intensity corresponding to two Mo-S dumbbells. Due to the lower projected atomic number of two sulphur atoms compared to the atomic number of one molybdenum atom, the peaks with a lower HAADF intensity (left peaks of the dumbbells) correspond to sulphur atomic columns and the peaks with higher HAADF image intensity correspond to the molybdenum atom.

The charge density line profiles shown in Figure 5.2 b) are extracted from the same region as the HAADF line profiles. Therefore, the type of atomic columns are identified based on the previously discussed HAADF intensity and indicated by the orange and blue spheres for sulphur and molybdenum atoms.

The integrated line profiles from the measurement (blue line) and the simulation (black line) show four peaks corresponding to the positive charge density at the atomic column positions for the sulphur and molybdenum atomic columns. Both line profiles qualitatively resemble a similar charge density distribution. However, the charge density line profile derived from the measurement shows an about two times lower overall positive charge density compared to the charge density line profile of the simulation. For the measurement and the simulation, a higher positive charge density is found at the sulphur atomic columns whereas the higher-Z molybdenum atoms exhibit a less positive charge density. By calculating

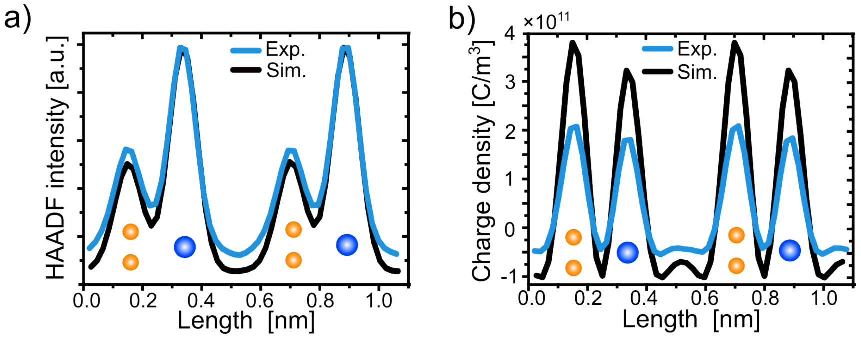

Figure 5.2: Integrated line profiles of the a) HAADF signal and b) the charge density derived from the regions marked by the coloured boxes in Figure 5.1 a) and d). The blue solid line indicates the measurement and the black solid line the corresponding line profile from the simulation.

the mean value of the maximum positive charge density for the sulphur and molybdenum atomic columns for all atomic columns in the image area, the two different types of atomic columns are compared regarding their positive charge density. The mean value of the peak charge density at sulphur atomic columns is $\rho_{2S}^{mean} = (2.73 \pm 0.06) \cdot 10^{11}\,\mathrm{C/m^3}$ and $\rho_{Mo}^{mean} = (2.41 \pm 0.05) \cdot 10^{11}\,\mathrm{C/m^3}$ for molybdenum atomic columns. Despite the lower projected atomic number of sulphur atomic columns with Z(2S)=32 compared to molybdenum atoms with Z(Mo)=42, the positive charge density is higher at sulphur atomic columns by about 13% compared to the charge density at molybdenum atomic columns. Comparable values are observed for charge density distribution of the corresponding multislice image simulation where the sulphuric atomic columns exhibit a positive charge density which is about 15 % higher than the maximum positive charge density of molybdenum atomic columns. A similar behaviour was also found for a WSe_2 monolayer, where the mean peak charge density of the lower-Z selenium atomic columns amount to $\rho_{2Se}^{mean} = (4.7 \pm 0.2) \cdot 10^{11}\,\mathrm{C/m^3}$ and for the higher-Z tungsten atoms to $\rho_{W}^{mean} = (3.9 \pm 0.1) \cdot 10^{11}\,\mathrm{C/m^3}$ (Chapter 4.1). For WSe_2, the difference between the two atomic columns is even more pronounced with the selenium atomic columns exhibiting a positive charge density about 21 % higher than the tungsten atoms. Thus, for both TMD monolayers, the lower-Z atomic columns show a higher positive charge density compared to the higher-Z atomic columns and therefore contrast the linear imaging technique of DPC. A similar behaviour for MoS_2 is also shown in literature but not discussed [27, 38, 210]. Only Martis et al. address this unexpected charge density and discussed its origin to residual 3-fold astigmatism [42]. This contrasts with the multislice image simulations shown in Figure 5.1, which are conducted without any lens aberrations and which resulted in the derived charge density distribution with the same unexpected ratio in charge density between the two atomic columns in a MoS_2 monolayer. Thus, its is a highly unexpected behaviour, although it is comparable to the behaviour observed for the charge density distribution in a WSe_2 monolayer. For both TMD monolayer, the lower-Z chalcogen atomic columns exhibit a higher positive charge density derived by STEM-DPC measurements. But contrary to a WSe_2 monolayer, the MoS_2 monolayer consists of elements with a lower atomic number.

As discussed in Chapter 4.4.5, the maximum atomic potential in dependence of the atomic number shows two Z-regimes with linearly increasing maximum atomic potential, which differ in terms of their slope. For the WSe_2 monolayer, this results in the fact that two selenium atoms indeed have a higher atomic potential compared to a single tungsten atoms. This is not the case for MoS_2. Both atomic species are in the low-Z regime with the same linear behaviour of the maximum atomic potential in dependence of the atomic number. From the investigation of the atomic potentials shown in Chapter 4.4.5 it is found that the maximum projected potential of two sulphur atoms is $V(S)=2452\,eV/e$ which is lower than the maximum potential of one molybdenum with of $V(Mo)=2873\,eV/e$. Therefore, it is not expected to observe a higher electric field magnitude and a higher positive charge density at the sulphur atomic columns than at the molybdenum atomic position. The observed electric field magnitude measured using STEM-DPC therefore contrast the presumed behaviour based on the projected atomic potentials and also contrast with the WPOA.

Although, assuming a direct dependency of the DPC signal and the atomic potentials justifies the higher charge density and electric field at selenium atomic columns in the specific case of a WSe_2 monolayer, it is here shown to not hold for a MoS_2 monolayer. The unexpected high electric field magnitude and charge density at the sulphur atomic columns can not be explained by the atomic potentials.

As the multislice image simulations of the MoS_2 and WSe_2 monolayers show the same behaviour as the DPC measurements, the effect resulting in the higher electric field at the chalcogen atomic columns is considered in the (IAM-based) multislice image simulations. Therefore, the observed higher field at chalcogen atomic columns is not due to charge redistribution in the material as these are not included in the IAM-based multislice simulations. This also excludes lens aberrations as the origin of this unexpected observation as the simulations are done using an ideal electron probe without any lens aberrations present. Although the anisotropy of the segmented detector and the detector configuration influence the electric field distribution close to the atomic column positions, the electric field magnitude and charge density at chalcogen and metal atomic columns remains the same. Thus, the segmented detector and its limited momentum space resolution are not the reason for this unexpected finding.

A possible reason for the influence of the actual beam propagation of the electron beam within the material and the difference in beam propagation close to the different atomic columns as shown in Chapter 4.4.4 with the refocussing action of the different atomic columns in WSe_2. The beam propagation within the material seem to drastically alter the observable electric field distribution leading to a field distribution which can not be explained by a projection of the specimen potential. Therefore, STEM-DPC measurements of the electric field distribution and the quantitative analysis are presumably not linearly related with the projected potential but strongly influenced by the beam propagation within the specimen even for specimen thicknesses of more than one atom. Thus, a quantitative analysis is difficult and hindered by the projection due do the lack of resolution along the thickness of the specimen. Although electron ptychography, i. e. multislice ptychography is capable of reconstructing the specimen potential at each slice and therefore accounts for the beam propagation [211], this technique still has difficulties with the depth resolution currently limited to a few nanometres and influenced by the convergence angle, beam energy and electron dose [211, 212]. To date, it is only possible to a limited extend to account for the influence of the actual beam propagation along the atomic columns i. e. channelling effects and a refocussing of the electron beam. Thus, quantitative DPC imaging is still challenging and further research to correctly account for the different influences is needed.

Section summary

- The quantitative DPC measurement on a MoS_2 monolayer reveals a higher electric field magnitude and charge density at the lower-Z sulphur atomic columns compared to the electric field magnitude and charge density at the higher-Z molybdenum atoms. This finding is similar to the observations made for a WSe_2 monolayer in which the lower-Z chalcogenide atomic column also exhibits a higher positive charge density compared to the higher-Z transition metal atom.
- Still, the finding is unexpected as the atomic species in MoS_2 exhibit a lower atomic number than the atoms in WSe_2 and should therefore better fulfil the WPOA necessary for correct quantitative DPC imaging.
- The comparison with a corresponding multislice image simulations without any residual lens aberrations highlight that this finding is not an artefact introduced by an imperfect electron probe.
- The observed positive charge density at sulphur and molybdenum atomic columns is also in contrast with the maximum atomic potentials. The maximum potentials are in agreement with the respective atomic number and thus show a higher maximum potential for the single molybdenum atom than for the maximum projected potential of the two sulphur atoms.

Chapter 6

Different Stacking Configurations of WSe_2 Bilayers

6.1 Influence of different Stacking Configurations of WSe_2 Bilayers

The layered structure of 2D transition metal dichalcogenides (TMDs) enables the individual layers to be stacked in different configurations on top of each other. The vertical alignment of the atoms in these configurations affects the interaction between the layers, thereby altering various material properties, including the electronic and excitonic properties, and lattice parameters (Chapter 2.7). The specific alignment of the two atomic lattices can result in an enhanced interlayer coupling and a specific band structure which affects the optical response [126, 213]. Therefore, understanding the impact of the stacking configurations of 2D WSe_2 is crucial for tailoring the material properties to a certain application (Chapter 2.7). Among the different high-symmetry stacking configurations of TMDs the most common bilayer stacking configuration is the AA' stacking, in which the transition metal atoms of the first layer are vertically aligned with the chalcogen atoms of the second layer. The same applies for the chalcogen atoms of the first layer and the metal atoms of the second layer. Despite the fact that the AA' stacking configuration is energetically the most favourable one, the AB stacking configuration exhibits only a slightly higher formation energy and is therefore also frequently observed [124]. In this stacking configurations the atoms of the first layer are directly aligned with the atoms of the following layer, but the layers are shifted relative to each other. By this, atoms of the first layer are located on top of the hollow of the second layer.

As the optoelectronic properties are dominated by the internal electric field distribution, which is influenced by the specific stacking configurations, the electric field distribution at the atomic for two different stacking configurations of a WSe_2 bilayer is investigated by STEM-DPC measurements. The following two chapters investigate the electric field distribution in a WSe_2 homobilayer in AA' and AB stacking configurations (Chapter 6.1.1 and Chapter 6.1.2, respectively).

6.1.1 AA' Stacking Configuration

Figure 6.1 a) shows the crystal structure of an AA'-stacked WSe_2 bilayer in top and side view. The two different atomic columns are marked by the dotted and dashed lines. In the AA' stacking configuration, the atomic columns of the first monolayer are aligned with the atomic columns of the second monolayer. As indicated by the dashed and dotted lines in Figure 6.1 a), the tungsten atoms of one layer are vertically aligned with the selenium atoms of the other layer leading to mixed atomic columns. Both types of atomic columns therefore consist of the same number of atoms and exhibit the same projected atomic number. Only the stacking sequence along the vertical direction is different with either a tungsten atom above two selenium atoms or vice versa.

Following the principle of Z-contrast in HAADF imaging, no difference in HAADF image intensity is expected between the different atomic columns. However, recent literature claims different, as conventional STEM investigations on AA'-stacked TMD bilayers reveal a difference in the HAADF image intensity of the different atomic columns [123, 214].

A higher HAADF image intensity is observed if the chalcogen atoms are in the beam propagation direction above the metal atom of the second layer. This is found for MoS_2 [123] and WSe_2 [214] homobilayers, still, the reason for the different HAADF intensities of the atomic columns, despite them having the same projected atomic number, is not explained. It will presumably also depend on the HAADF collection angles, defocus and other residual lens aberrations, as well as the refocusing effect shown in Chapter 4.4.4.
Figure 6.1 b-g) shows the STEM-DPC measurement of a WSe_2 bilayer in AA' stacking configuration. The AA'-stacked bilayer configuration was observed on a CVD-grown monolayer, which exhibited nucleation spots with varying number of layers on top of a monolayer. As the variety of different energy-filtered TEM methods for thickness determination are not suitable for the determination of the number of layers of 2D materials [215], the thickness of the area finally identified as a bilayer is estimated by comparing the average HAADF intensity of the different layers with that of the monolayer region. Although the HAADF image intensity depends on the gain and offset settings manually adjusted at the microscope, still, the step in intensity between mono- and bilayer can be utilized to estimate the number of layers. This is only possible for thin specimens and if contrast variations due to channelling effects can be neglected. Further details about the thickness determination using the HAADF image are given in the Appendix 9.10.
Figure 6.1 b) shows the STEM-HAADF image of a WSe_2 bilayer in [0001] zone-axis orientation. Similar to a sub-atomically resolved WSe_2 monolayer, the HAADF image shows bright spots hexagonally arranged in the AA'-stacked bilayer.
Although the atomic columns exhibit the same number of atoms and the same projected atomic number, the HAADF image intensity exhibits small intensity variations between the two atomic columns which is only barely visible in the HAADF image itself but is clearly evident from the integrated line profile shown in Figure 6.1 g). The line profile depicts the HAADF intensity across two atomic dumbbells as indicated by the blue box in Figure 6.1 b). The left atomic column shows a higher HAADF peak intensity than the right atomic column of the dumbbell. A comparable behaviour was also observed in literature for other TMD bilayers in the AA' stacking, where the vertical order of atoms in the atomic column influences the resulting HAADF peak intensity even though the projected atomic number and the number of atoms is the same within each atomic column. Thus, the influence of the stacking sequence of atoms in 2D materials also plays a role in the resulting (HA)ADF images as shown for WSe_2 and MoS2 bilayer in Ref. [123, 214]. For these TMD bilayers, the HAADF image intensity of the atomic columns with the two chalcogen atoms in the first layer in beam direction exhibits a higher HAADF intensity than the atomic columns with the transition metal atom in the first layer. Hence, the assignment of the atomic columns with respect to the atomic species in the upper layer is adapted from Ref. [214]. Atomic columns with the higher HAADF intensity correspond to a stacking of two selenium atoms above one tungsten atom (2Se+W) in beam propagation direction and are marked be green dots in the HAADF image. Atomic columns with a lower HAADF intensity are marked by grey dots and correspond to a tungsten atom above two selenium atoms (W+2Se). This colour assignment for the type of atomic columns is

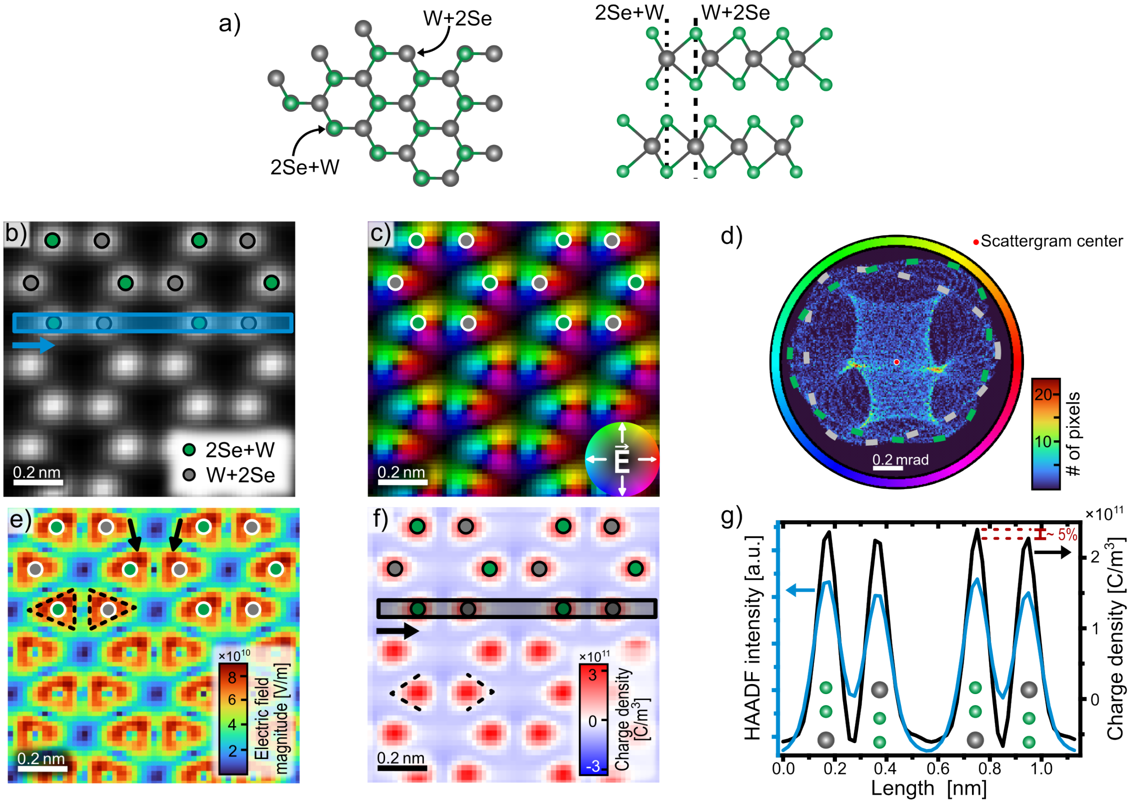

Figure 6.1: a) Structure model of a WSe_2 bilayer in AA' stacking configuration in top (left) and side (right) view. Selenium atoms are marked by green spheres and tungsten atoms are indicated by grey spheres. b-c) HAADF and DPC image of the WSe_2 bilayer in [0001] zone-axis orientation with atomic column positions marked by green and grey dots. d) Corresponding scattergram of the DPC image shown in c). e) and f) Electric field and charge density distribution maps derived from the DPC measurement of the WSe_2 bilayer. g) Integrated line profiles of the HAADF (blue solid line) and charge density (black solid line) derived from the regions marked by the blue and black boxes in b) and f), respectively. It is to note, that the atomic column in this stacking configuration consist of the same number and type of atoms. Therefore, green dots here denote the atomic columns with two selenium atoms followed by one tungsten atom and the grey dots denote the atomic columns with a tungsten atom followed by two selenium atoms.

used for the subsequent images.

Figure 6.1 c) shows the colour-coded DPC image of the bilayer. The atomic column positions and type of atomic columns are exemplarily marked based on the HAADF intensity. The DPC image of this AA' stacking shows rotational symmetric electric fields around each individual atomic column, which are similar to the one measured for a monolayer (Figure 4.1). Due to the overlap of opposing electric fields of individual atomic columns, the rotational symmetric electric field distribution is slightly distorted and exhibits a triangular shape. In contrast to the monolayer, the AA'-stacked bilayer indicates an almost equal electric field magnitude for all atomic columns.

In addition, the scattergram of the DPC signal shown in Figure 6.1 c) is used to investigate the influence of the stacking sequence and possible residual lens aberrations. The scattergram exhibits features which are comparable to the one obtained for the scattergram of the monolayer (Figure 4.1 e) and f). The inner structure of the scattergram exhibits a similar elongated hexagonal feature and two triangularly deformed rings of strong deflections which originate from the mixed atomic columns and are indicated by the green and grey dashed lines. Based on the similar shape of the scattergram no significant lens aberration can be observed. However, in contrast to the scattergram of the monolayer, the two outer rings corresponding to the two types of atomic columns with high deflection, show almost the same extension in the scattergram of the AA'-stacked bilayer. For the bilayer in the AA' stacking configuration, this equal extension of the two outer rings indicates that both types of atomic columns, one with selenium on top of tungsten and the other with tungsten on top of selenium atoms generate DPC image features with similar deflection magnitudes. In Chapter 4.4.4, it was shown that the electron beam propagates differently along selenium atomic column than tungsten atomic columns due to the different refocusing actions of the atomic potentials. Hence, it is expected to observe a difference between the two atomic columns in a dumbbell in the AA'-stacked bilayer.

To quantitatively investigate if a difference in electric field or charge density is observed between the two types of atomic columns due to the different stacking sequence of atoms, the electric field magnitude map and charge density distributions are analysed in the following. Figure 6.1 e) shows the electric field magnitude map of the AA'-stacked bilayer. Overall, the electric field magnitude of the AA'-stacked bilayer is lower than the electric field magnitude of the monolayer (Chapter 4.1). Although theory describes a linear scaling of the DPC signal with the thickness, the normalization of the DPC signal by the specimen thickness to obtain the electric field magnitude leads to a lower electric field magnitude. This explains why the electric field magnitude of the bilayer is lower than the electric field magnitude of the monolayer (Chapter 4.1).

The shown electric field magnitude map exhibits the triangular-shaped electric field magnitude features around each individual atomic column. These triangular-shaped regions around the individual atomic column show a slightly non-uniform electric field magnitude with a locally enhanced electric field magnitude on the upper right tip of the triangle (green dots) and on the upper left (grey dots). The locally enhanced features are exemplarily indicated by the two black arrows in Figure 6.1 e). As shown in Chapter 4.3.2, this is a result of the detector anisotropy and rotation introducing local enhancements in the electric field magnitude depending on the orientation of the detector. In addition, 3-fold astigmatism might also lead to a pronounced field magnitude at the tips of the triangular-shaped atomic field distribution. However, the influence of residual 3-fold astigmatism is not observed in the inner structure of the scattergram shown in Figure 6.1. Both effects can be present simultaneously which makes it difficult to distinguish between both.

The charge density distribution shown in Figure 6.1 f) shows lower magnitudes than observed for the monolayer (Figure 4.1 g). Still, similar features including the positive charge density localized at the atomic column positions and the delocalized negative charge density can be observed. The positive charge densities at the atomic column positions slightly deviate from a perfectly round-shaped distribution as they exhibit spikes on the left for the W atomic column and on the right for the Se atomic column of each W-Se dumbbell. These are tentatively explained by the anisotropy of the detector and residual lens aberrations. As these residual lens aberrations do not strongly alter the rotational symmetry of the features in the electric field distribution and the shape of the inner scattergram feature does not show any directional compression, the residual lens aberrations are expected to be small allowing a further quantitative analysis.

An integrated line profile of the charge density over the region marked by the black box in Figure 6.1 f) is shown in Figure 6.1 g) by the black solid line. Although both types of atomic column consist of the same number of atoms and exhibit the same projected atomic number, the line profile of the charge density shows a difference in maximum positive charge density between the two atomic columns of the dumbbells. A higher positive charge density is observed for the atomic column with two selenium atoms followed by one tungsten atom in beam propagation direction. The relative difference in the maximum positive charge density between the two types of atomic columns is only of about 5 %.

Although the relative difference in maximum positive charge density between the two types of atomic columns is small and presumably affected by image noise, the result highlights the sensitive STEM-DPC imaging to the stacking sequence of atoms in an atomic column. Compared with the single atom simulations and the simulations of the real space probe intensity in Chapter 4.4, the stacking of atoms influences the quantitatively derived charge density distributions due to differences in beam propagation and refocussing by selenium and tungsten atoms.

To further investigate the influence of the stacking configuration on the electric field distribution, the difference between the AA' stacked bilayer and a nearby monolayer is calculated. Using the latter ensures similar imaging conditions. Figure 6.2 a) and b) show the HAADF image of the previously shown bilayer in AA' stacking configuration and the HAADF image of a nearby monolayer region, respectively. For the bilayer, the type of the atomic columns is distinguished by the atomic species of the in beam propagation direction first layer as explained previously. For the monolayer, the type of the atomic column positions are based on the difference in HAADF image intensity between pure selenium atomic columns and the tungsten atom. An illustration of the atomic structure in beam propagation direction is shown in Figure 6.2 c) for the bi- and monolayer. As the bilayer consist of two monolayers stacked on top of each other, the subtraction of a monolayer from this stack would ideally result in a remaining monolayer. Thus, by a careful alignment of the atomic column positions of the monolayer with the atomic column positions of the bilayer, the difference between AA' stacked bilayer and the monolayer is calculated. The alignment of all images types is achieved with a non-rigid registration by exploiting the HAADF images for the alignment calculation. Here, the wave vector magnitude is used. In contrast to the electric field magnitude maps, the wave vector magnitude is not normalized to the specimen thickness. Therefore, the wave vector magnitude maps are more suitable to compare specimen with different thickness, such as bi- and monolayer. The wave vector magnitude maps of the bilayer and the monolayer are shown in Figure 6.2 d) and e), respectively. The wave vector magnitude of the bilayer in AA' stacking configuration shown in Figure 6.2 d) shows similar features as the electric field magnitude map shown

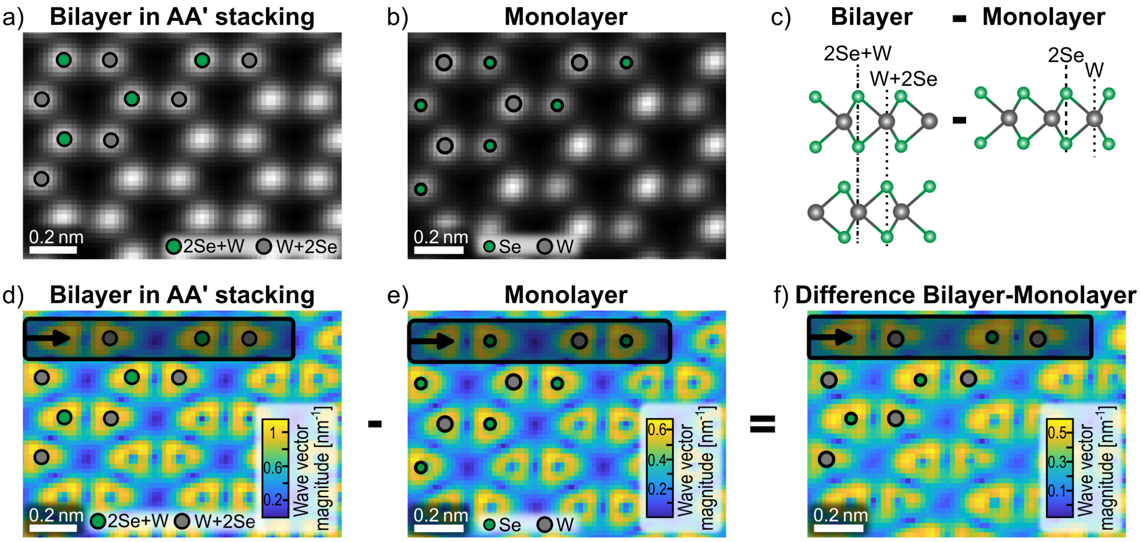

Figure 6.2: a-b) HAADF images of the bilayer in AA’ stacking configuration and a nearby pristine monolayer, respectively. Atomic column positions are marked by green and grey dots. For the atomic composition of the atomic columns, the reader is referred to the legends in both images. c) Sketch of the atomic structure in side view for the bilayer in AA’ stacking and the monolayer. d-e) Maps of the wave vector magnitude for the bi- and monolayer, respectively. The atomic column positions are inserted based on the HAADF image. f) Difference map of the wave vector magnitude calculated by the subtraction of the wave vector magnitude map of the monolayer from the wave vector magnitude map of the bilayer. The types of atomic columns indicate the remaining species of atoms after the subtraction. The black boxes indicate the positions for the integrated line profiles in Figure 6.3.

in Figure 6.1 e). This is expected, as the wave vector, which is related to the transferred momentum or the deflection angle by the Planck constant, is basis for the calculation of the electric field magnitude and therefore resembles the same features. The corresponding wave vector magnitude map of the monolayer is shown in Figure 6.2 e). The wave vector magnitude map shows a comparable behaviour as the electric field magnitude maps of a monolayer discussed in Chapter 4.1 where a higher electric field magnitude was found at the selenium atomic column compared to the field magnitude around tungsten atomic columns. The same is observed for the wave vector magnitude distribution shown in Figure 6.2 e) where the pure selenium atomic columns result in a higher wave vector magnitude and thus a higher transferred momentum than the tungsten atomic columns marked by grey dots. Comparing the two wave vector magnitude maps of the mono- and the bilayer in Figure 6.2 e) and d), respectively, reveals that they qualitatively exhibit the same triangular-shaped features around the individual atomic columns in the hexagonal arrangement. Quantitatively the bilayer overall shows a higher wave vector magnitude than the monolayer.

The difference between wave vector magnitudes of the monolayer and a bilayer is of about a half with slight deviations possibly arising due to noise. Thus, the here shown wave vector magnitude maps for mono- and bilayer show the expected behaviour of increasing transferred momentum or beam deflection with increasing number of atoms within an atomic column. As both, the AA’-stacked bilayer and the monolayer show the expected behaviour in the transferred momentum, a subtraction of the monolayer from the bilayer is expected to give a similar transferred momentum distribution as a monolayer. To analyse this in greater detail, the difference in transferred momentum between bilayer and monolayer is calculated using the two wave vector magnitude maps and shown in Figure 6.2 f). The type of the atomic columns is here identified by the remaining type of atoms after the subtraction. As an atomic column with two selenium atoms followed by one tungsten atoms is subtracted by an atomic column corresponding to a tungsten atom, the remaining signal would arise from two selenium atoms. These atomic columns are denoted by green dots in the difference maps. The other atomic column consists of a single tungsten atom (grey dots). Overall, the difference in wave vector magnitude shows similar features as observed for the monolayer. Features of high wave vector magnitudes, which correspond to a high transferred momentum, are located close to the atomic column positions. These features again exhibit triangular shape. Similar to the wave vector magnitude map of the monolayer, features of a higher wave vector magnitude are located at the remaining selenium atomic columns compared to the remaining tungsten atoms. Thus, the difference of a bilayer in AA' stacking configuration and a monolayer resemble the same features as a monolayer. Based on the described influence of the intensity redistribution and the sensitivity of DPC imaging on the atomic stacking order analysed in the Chapters 4.4.1 and 4.4.2, the observed agreement of the difference map with the wave vector magnitude map of a monolayer itself is rather unexpected. Therefore, all wave vector magnitude maps are further quantitatively analysed using integrated line profiles (black boxes in Figure 6.2). In addition, comparative multislice image simulations are conducted and analogously analysed.

Figure 6.3 a) shows the simulated wave vector magnitude map of a WSe_2 bilayer in AA' stacking configuration. Qualitatively, the distribution is similar to the one observed in the measurement shown in Figure 6.2 a). High wave vector magnitudes are found close to the atomic column positions and no significant difference between the two atomic columns in the AA'-stacked bilayer can be identified. Quantitatively, the wave vector magnitudes of the simulation are overall higher by a factor of about two compared to the measurement. The difference by a factor of two between measured and simulated wave vector magnitude is also observed for the wave vector magnitude of the corresponding monolayer shown in Figure 6.3 b) (simulation) and in Figure 6.2 e) (measurement). The simulated wave vector magnitude map of the monolayer is in good qualitatively agreement with the measured wave vector magnitude map of the monolayer. However, the difference of the wave vector magnitudes between the two different atomic column types is more pronounced in the simulation than in the measurement. This is presumably due to the influence of lens aberrations, especially defocus, which might have significantly impacted the measured wave vector maps. The calculated difference map of the simulated wave vector maps of the bilayer and the monolayer is shown in Figure 6.3 c). Some pixels show a comparable high wave vector magnitude with values up to about $1.8\,\mathrm{nm}^{-1}$ which is above the maximum values of observed for the monolayer. These peaks in the difference map occur due to the alignment of the two images of the bilayer and the monolayer. Qualitatively, the difference map of the wave vector magnitudes shows similar features as the bilayer and the monolayer,

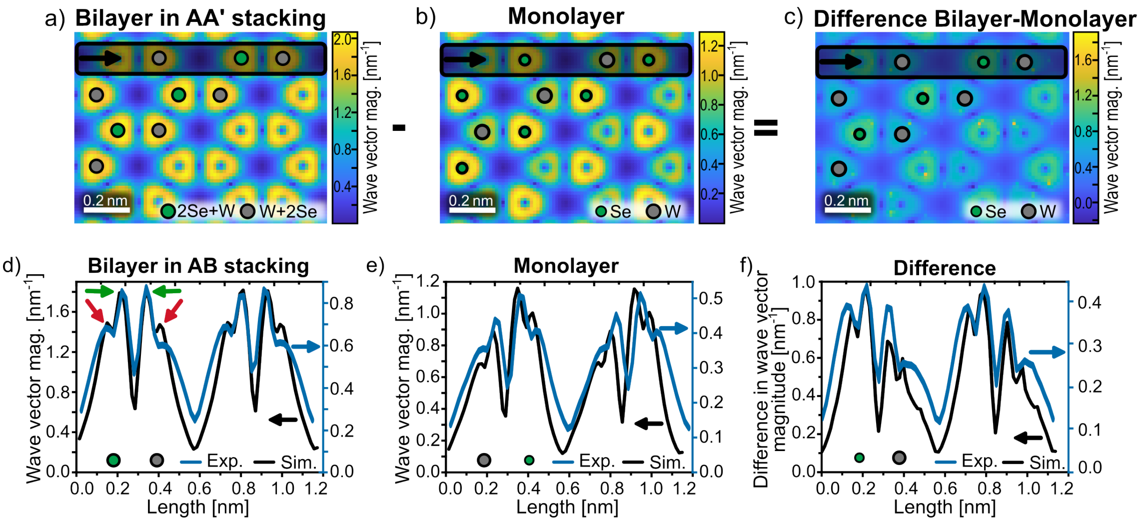

Figure 6.3: a-b) Wave vector magnitude maps of a WSe_2 bilayer in AA' stacking configuration, and a WSe_2 monolayer simulated using the multislice approach. c) Difference map of wave vector magnitude maps calculated by the pixel-wise subtraction of the wave vector magnitude of the monolayer from the wave vector magnitude of the bilayer. d-e) Integrated line profiles of the wave vector magnitude for the bi- and monolayer for the simulations (black solid lines) and the measurements (blue solid lines). The line profiles are integrated over the regions indicated by the black boxes in a-b) for the simulations and in Figure 6.2 a-b) for the measurement. f) Integrated line profiles of the difference in wave vector magnitude for the simulation and measurement. Again, the line profiles are derived from the regions marked by the black boxes in c) and Figure 6.2 c). The left y-axis is ascribed to the simulation and the right y-axis to the measurement. The colour code for the coloured dots highlighting the atomic column positions are explained by the legend of the individual images.

which include hexagonally arranged triangular features of local maxima located close to the atomic columns positions. The difference maps shows a slightly more pronounced wave vector magnitude located at the atomic column which only contains the remaining two selenium atoms after the subtraction of a tungsten atom from the mixed atomic column compared to the atomic column with the remaining tungsten atom. This observation is in great agreement with the observations made for a DPC measurement of a monolayer (Chapter 4.1), where the atomic columns comprising two selenium atoms exhibit a higher DPC signal and thus a higher wave vector magnitude than the one with only a single tungsten atom. Since measurement and simulation show comparable features it can be stated out that the subtraction of a monolayer from an AA'-stacked bilayer results in a similar wave vector magnitude map and related features in the transferred momentum as a pure monolayer.

A detailed investigation of the absolute values is important for gaining insight into the interaction of the electron beam with a bilayer and with a monolayer. Due to the previously discussed non-linear behaviour of DPC imaging with respect to the number of atoms and the stacking sequence of atoms within an atomic column, the measured beam deflection in a bilayer is expected to differ from that in a monolayer.

Figure 6.3 d-f) shows the corresponding integrated line profiles for the AA'-stacked bilayer, the monolayer, and the difference between both for the simulation (black solid lines) and the measurement (blue solid lines), respectively. The line profiles are integrated over 10 px for the simulation and over a comparable region corresponding of 8 px width for the measurement. Thus, the shown values are average values over the integration width.

Despite the quantitative difference by a factor of two, the line profiles for the AA'-stacked bilayer shown in Figure 6.3 d) for the measurement and simulation show a similar behaviour. For both, no significant difference between the two atomic columns can be identified. The line profiles show four pronounced peaks with high wave vector magnitudes which arise from the two atomic dumbbells. Each peak exhibits a pair of local maxima whereas one has a reduced wave vector magnitude (indicated by the red arrows) and the other has a pronounced wave vector magnitude (indicated by the green arrows). The local maxima between the two atomic columns of a dumbbell (green arrows) exhibit higher wave vector magnitudes than the local maxima on the left and on the right of the dumbbell (red arrows). The difference of the local maxima arises due to the detector anisotropy of the segmented detector leading to enhanced magnitudes between the two neighbouring atomic columns (Chapter 4.3.2). Due to the integration width of the line profiles, the outer tips of the triangular-shaped regions on the left and right of the dumbbell are averaged with pixel of lower wave vector magnitude and therefore exhibit reduced wave vector magnitudes in the line profile. Contrary, the inner peaks in between the atoms of the dumbbell are obtained by averaging over the whole edge of the triangular features of high wave vector magnitude. Thus, the difference in wave vector magnitude is introduced by the detector anisotropy and enhanced by the averaging for the integrated line profiles.

Figure 6.3 e) depicts the integrated line profiles for the monolayer. Here, a comparable behaviour of the measurement and simulations as already observed for the AA'-stacked bilayer is found: four peaks corresponding to the two W-Se dumbbells and each peak exhibits two local maxima. In contrast to the bilayer, the left two peaks of the W-Se dumbbell in a WSe_2 monolayer show a lower wave vector magnitude than the right peak i. e. a lower DPC signal at tungsten atomic columns compared to the one of selenium atomic columns. Both, the simulated and the measured, line profiles show the same features and are in good qualitative and quantitative agreement with each other, despite the factor of two between simulation and measurement.

The wave vector magnitudes derived from the monolayer are not half of the maximum wave vector magnitude observed in the bilayer. Instead, the monolayer indicates values in wave vector magnitude which are more than half the values of a bilayer. This possibly arises from the non-linear behaviour of DPC signal with the specimen thickness shown for single atom simulations in Chapter 4.4. For the simulation as well as for the measurement, the changed beam propagation due to atoms stacked on top of each other alters the resulting wave vector magnitude in a non-linear way. Still, this effect does not drastically influence the features of DPC images as the difference maps between bilayer and monolayer reflect the similar features as a wave vector magnitude map of a pure monolayer. This can be deduced from the higher wave vector magnitude at the remaining selenium atoms (in the difference map) and the pure selenium atomic column in the wave vector magnitude map of the monolayer.

This finding is also visible in the integrated line profiles from the two difference maps depicted in Figure 6.3 f). In both line profiles, the left peak of the atomic dumbbells containing two selenium atoms exhibits a higher remaining wave vector magnitude. The peak values are slightly reduced compared to the pristine monolayer (Figure 6.3 e) and f). This is presumably caused by the intensity redistribution and the subsequent beam propagation. For the simulations, a selenium atomic column in a monolayer exhibits a wave vector magnitude distribution around the atomic column with a local maximum of about $1.2\,\mathrm{nm}^{-1}$ whereas the remaining selenium atomic column after the calculation of the difference has a local maxima of only about $0.95\,\mathrm{nm}^{-1}$. A comparable behaviour is observed for the measurement, although the values are overall reduced by about a factor of two.

Another finding of this comparison is that simulation and measurement indicate the same behaviour in the difference maps (bilayer-monolayer). Thus, the beam propagation within the material is well represented by the multislice approach of the image simulation.

The observed reduced values of the difference maps compared to the map of a pristine monolayer can be explained by the non-linear behaviour of the DPC signal for increasing number of atoms within an atomic column resulting in a decreased DPC signal (Chapter 4.4.3). Furthermore, the refocussing of the electron beam shown by the real space probe intensity in Chapter 4.4.4, will influence the observed wave vector magnitude. Although, the simulated illumination conditions used for the investigation of the evolution of the real space probe intensity in dependence of the specimen thickness are not similar to the experimental conditions, as no residual lens aberrations and thermal vibrations are considered. Still, the simulations give an insight into the interaction of the electron beam with the atomic column during the propagation through the specimen. It is shown that the electron probe is focused into an electron probe that is smaller than initially incident probe due to the interaction with a pure tungsten or pure selenium atomic columns. For four selenium atoms and two tungsten atoms, which corresponds to atomic columns in AA-stacked WSe_2 bilayer, the strongest focussing action is observed leading to the smallest probe size. Although the refocussing was shown for isolated atoms and not for a crystal structure, the behaviour is expected to be comparable close to an atomic column as the influence of neighbouring atomic column is assumed to be negligible at these distances. However, the AA’ stacking of a WSe_2 bilayer leads to mixed atomic columns which results in a different focussing action of the atomic columns due to the mixed atomic potentials. Therefore, it is reasonable to expect different DPC signals for the two different atomic columns although the projected atomic number and the number of atoms is the same. Depending on the order of stacking (W on top of two Se or vice versa), after the interaction with the first atom, which is either tungsten or selenium, the subsequent atoms are probed by a different intensity distribution of the probe due to the different atomic potentials.

Section summary

- Qualitatively, comparable features are observed between the atomic electric field distribution of the AA’-stacked bilayer and a monolayer, including rotational symmetry around each atomic column and slight triangular distortion due to the overlap of opposing electric field components.

- In an AA'-stacked WSe_2 bilayer, the two different types of atomic columns, with either two selenium atoms on top of one tungsten atom or vice versa, exhibit a comparable electric field magnitude and the peak positive charge densities differ only by about 5%. The sensitivity of DPC imaging on the stacking of atoms and the change in beam propagation is visible by the difference in the measured charge density distribution, which is presumably caused by the refocussing effect depending on the stacking order and atomic species involved (Chapter 4.4.4).
- The influence of the stacking is further investigated by wave vector magnitude maps of the AA'-stacked bilayer area and a nearby monolayer area. DPC measurements of both are in good agreement with corresponding simulations.
- By the subtraction of the monolayer wave vector magnitude map from the one of the AA'-stacked bilayer, the influence of the beam propagation is investigated. The difference shows features similar to a WSe_2 monolayer including a higher wave vector magnitude at the selenium atomic columns compared to the tungsten atomic columns. The results of the difference-based analysis highlights the fact that for the AA'-stacked bilayer the two layers almost behave like two monolayers stacked on top of each other.
- Quantitatively, the values of the wave vector magnitude of a monolayer are more than half the values of a bilayer which illustrates the influence of the actual beam propagation.

6.1.2 AB Stacking Configuration

Apart from the previously shown highly symmetric AA' stacking configuration, there are several other possible stacking configurations in which the second TMD layer is additionally shifted by a certain fraction of the lattice constant with respect to the first layer. This can result in a stacking for which atomic columns of the first layer are aligned with the centre of a hexagon of the second layer. These specific stacking configurations are denoted as AB-type stacking configurations. The AB-type stacking is further distinguished in three different possibilities of stacking which are illustrated in Figure 6.4, namely AB, AB' and A'B. The top row of Figure 6.4 shows the atomic structure of a bilayer in [0001] zone-axis orientation (top view) and the bottom row shows the corresponding side view. Depending on the lateral displacement between the layers, the resulting atomic columns consist of different number and type of atoms. Each layer itself still exhibits its hexagonal structure, but the stacking of the two layers leads to a more complex arrangement in projection (top view). Although the top view structures of the three AB-type configurations look similar to each other, the different stacking results in different types of atomic columns.

For the AB stacking configuration shown in Figure 6.4 a), the three different atomic columns are one pure selenium atomic column, one mixed atomic column with a single tungsten atom and two selenium atoms stacked on top of each other, and one atomic column of only one tungsten atom. The three different atomic columns are marked by the dotted and dashed lines in the side view sketch in Figure 6.4 a).

For the AB' stacking configuration, each of the three different atomic columns consist only of one atomic species. Two atomic columns consist of a single tungsten atom either from the top or the bottom layer. The third atomic column consists of the remaining four selenium atoms from both layers (Figure 6.4 b).

The A'B stacking configuration also consists of atomic columns that contain only one atomic species. Here, the atomic columns consist either of two selenium atoms or two tungsten atoms (Figure 6.4 c).

In the following, the electric field and charge density distributions of a WSe_2 bilayer in AB-type stacking configuration is investigated. The determination of the number of layers to ensure the presence of a bilayer, is achieved by the HAADF intensity of the assumed bilayer and a monolayer region (Appendix 9.10).

To correctly identify the atomic structure and differentiate between the three possible AB-type stacking configurations of a bilayer, the HAADF image is analysed in detail. Figure 6.5 a) shows the HAADF image of the WSe_2 bilayer in [0001] zone-axis orientation. The HAADF image reveals lines of atomic columns which are expected for the AB-type stacking. Furthermore, three different atomic columns can be identified from the in HAADF contrast. An integrated line profile over the region indicated by the blue box is used to analyse the different atomic columns. This line profile, shown in Figure 6.5 b), exhibits six peaks corresponding to atomic column positions. The six peaks differ in HAADF intensity and pairs of peaks with similar HAADF intensity are observed. Thus, three different types of atomic columns can be identified. The first and the fourth peak exhibit the highest HAADF image intensity and are both followed by two peaks with reduced HAADF intensity.

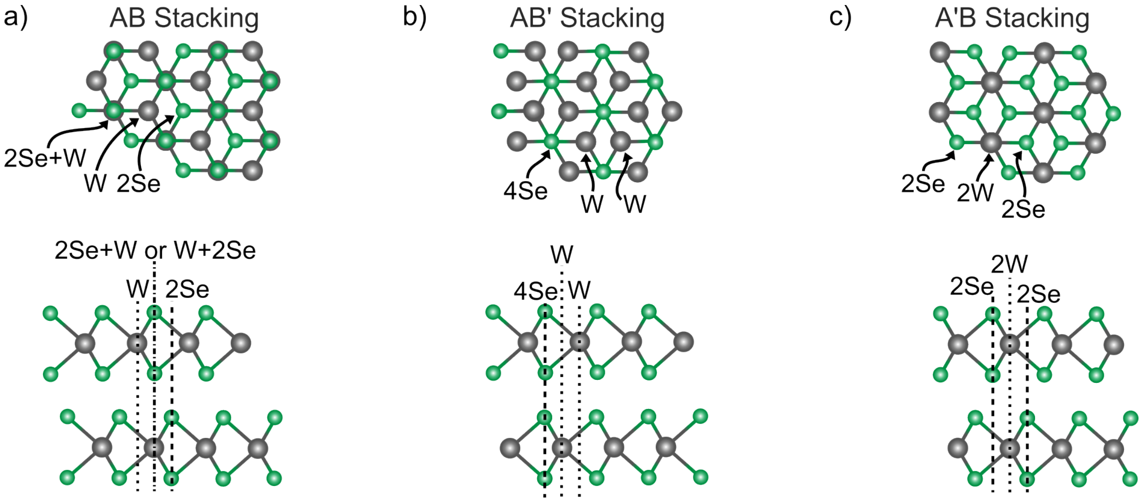

Figure 6.4: Illustration of three different stackings of the AB-type configuration in top and side view with selenium and tungsten atoms marked by green and grey spheres, respectively. a) AB stacking configuration with one mixed atomic column consisting of two selenium and one tungsten atom and two pure atomic columns either of one tungsten atom or two selenium atoms. b) AB' stacking configurations with three pure atomic columns where two atomic columns consist of one tungsten atom and one atomic column which consist of four selenium atoms. c) A'B stacking configuration with three pure atomic columns with two atomic columns consisting of two selenium atoms respectively and one atomic column which purely consist of two tungsten atoms.

The second peak shows a HAADF intensity with is reduced by about 45 % compared to the pronounced first HAADF peak. The third peak shows a slightly higher HAADF intensity compared to the second peak but still exhibits a HAADF intensity which is of about 31 % lower than the first peak of highest intensity.

For the AA' and A'B stacking configurations, two of the three atomic columns consist of the same type and number of atoms. Hence, the HAADF intensity for these two atomic columns in each structure should be almost equal or only slightly modified by the different z-positions along the beam propagation (Chapters 4.2 and 6.1.1). This is in good agreement to the simulated HAADF images and analogous line profiles of multislice image simulations of the three different stacking configuration in the Appendix 9.13. These simulations show an almost identical HAADF intensity for atomic columns of the same atomic type and number, even if their atoms differ in the z-position. Since all three stacking configurations lead to characteristic HAADF image intensities in the simulations due to the different types of atomic columns, the stacking configuration of the experimentally investigated WSe_2 bilayer can be identified by the three peaks in the HAADF line profile and their difference in HAADF intensity. As all the three peaks exhibit significantly different HAADF intensity they do not correspond to the same type of atomic column. Thus, the here shown WSe_2 bilayer is in the AB stacking configurations.

The peaks in the HAADF line profile can be assigned to the different atomic columns in the AB stacking (Figure 6.4 a). The highest HAADF intensity is assigned to the mixed atomic column as it exhibits the highest projected atomic number and, thus, produces the highest HAADF signal. The two peaks with reduced HAADF intensity can then be

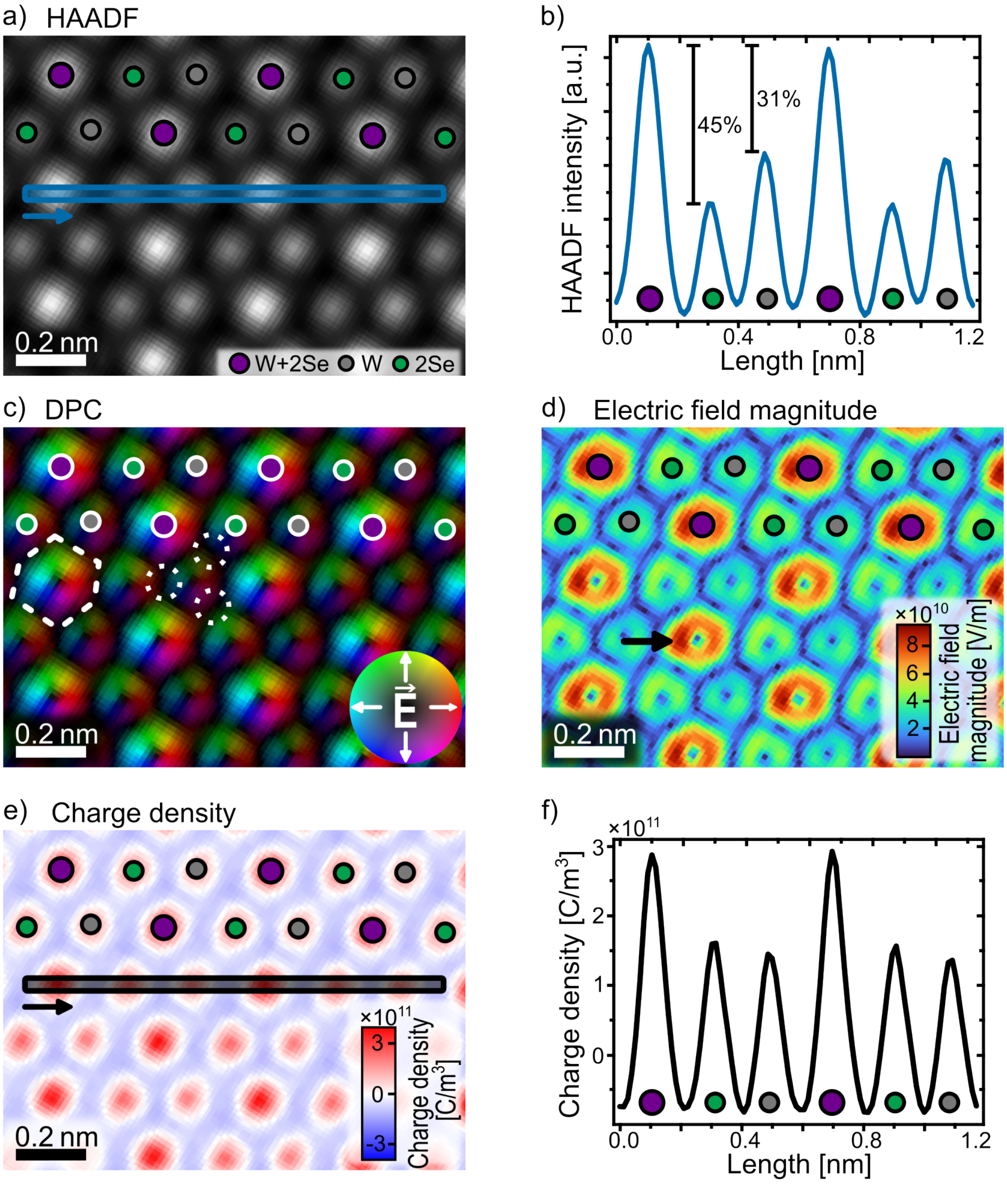

Figure 6.5: Investigation of a WSe_2 bilayer in AB stacking configuration. a) HAADF image of the WSe_2 bilayer with the atomic column positions marked by the coloured dots. The colour code is given in the legend at the bottom of the image. b) Integrated line profile of the HAADF image intensity derived from the region marked by the blue box in the HAADF image in a). c) Colour-coded electric field distribution and d) the corresponding electric field magnitude map. e) Charge density distribution derived from the electric field distribution shown in d) and f) the integrated line profile of the charge density. The line profile is integrated over the region indicated by the black box in the charge density map in e).

identified as the remaining pure selenium and tungsten atomic columns in the AB stacking configuration. The peak with the lowest HAADF intensity corresponds to the selenium atomic column and the peak with a slightly higher HAADF intensity corresponds to the tungsten atom. In the following, the colour code for the type of atomic columns follows the same as in the case of a monolayer, where selenium atomic columns are marked by green dots and tungsten atoms are indicated by grey dots. Additionally, the mixed atomic columns consisting of two selenium atoms and one tungsten atom are marked by purple dots.

The electric field distribution of this WSe_2 bilayer in AB stacking configuration is shown in Figure 6.5 c). The DPC image reveals rotational symmetric electric field distributions around each individual atomic column with one pronounced field distribution around the mixed atomic column (marked by purple dots) and less pronounced field distributions around the selenium and tungsten atomic columns (marked by green and grey dots, respectively). This is expected as the mixed atomic column exhibits a higher projected atomic number which leads to stronger beam deflection compared to the other atomic columns. For the pronounced mixed atomic column (purple dots) a hexagonal shape is observed (marked by the white dashed shape). This contrasts the field distribution observed in a monolayer, where triangular shapes of the individual field distributions around the atomic columns are observed. Furthermore, the selenium and tungsten atomic columns show a slightly triangular shape but with truncated tips along their connecting axis (marked by the three dotted circles in Figure 6.5 c). Although each layer retains its hexagonal structure, the stacking leads to a change of the beam propagation along the atomic columns which results in a measurable change of the extension and shape of the projected electric field distribution. This field distribution is also in good agreement with to the observed electric field distribution of the multislice image simulation shown in Figure 9.21 a) in the Appendix 9.13.

Figure 6.5 d) shows the corresponding electric field magnitude map. The mixed atomic columns have the highest electric field magnitude due to the number and type of atoms within the atomic column. Furthermore, the two atomic columns of pure selenium and the single tungsten atoms show the same quantitative behaviour in electric field magnitude as for the monolayer even though they are not within the same layer and the tips are slightly truncated. The selenium atomic columns show a higher electric field magnitude compared to the tungsten atomic columns. This has been similarly observed for a WSe_2 monolayer. Furthermore, a pronounced electric field magnitude is found on the left of the mixed atomic column which indicates the presence of some residual lens aberrations (exemplarily marked by a black arrow in Figure 6.5 d)). However, as the rotational symmetric field distribution around the individual atomic columns remains its shape the value and impact of residual lens aberrations are assumed to be small and will not hinder a quantitative analysis.

The corresponding charge density distribution is shown in Figure 6.5 e) where positive charge densities are localized at the atomic column positions and the negative charge densities are surrounding the atomic columns. A pronounced positive charge density can be found at the location of the mixed atomic columns which is expected due to the high electric field magnitude. For comparison between the atomic columns, an integrated line profile over the region marked by the black box is shown in Figure 6.5 f). The line profile reveals that the highest positive charge density is located at the mixed atomic columns. Furthermore, the selenium atomic column of the one layer and the tungsten atom of the other layer again resemble the same behaviour as for the monolayer. The selenium atomic columns exhibit a higher positive charge density than the tungsten atom. Overall, the AB-stacked bilayer shows the same features as expected for two monolayers stacked on top of each other.

To quantitatively investigate this further, a difference map of DPC related quantities between this AB-stacked bilayer and a monolayer are calculated. For the calculation a nearby monolayer region is used which was experimentally acquired under similar illumination conditions, i. e. to reduce the influence of lens aberrations. Figure 6.6 a) and b) show the corresponding HAADF images of the AB-stacked bilayer and of the monolayer area, respectively. The atomic column positions are marked by the coloured dots. Based on the HAADF image contrast the two images are aligned by a non-rigid algorithm. Afterwards, the difference map is obtained by calculating the difference of wave vector magnitude for each pixel (Chapter 3.3). Figure 6.6 c) illustrates the subtraction of the monolayer from the bilayer. As the bilayer consists of two monolayers, the subtraction of one monolayer is expected to result in a distribution comparable to the one of the monolayer as described by the AA' stacking in Chapter 6.1.1. Here, the alignment of the image areas for the subtraction is achieved in a way that the tungsten atoms of the monolayer are subtracted from the corresponding tungsten atoms in the bilayer and the selenium atomic columns from the monolayer are subtracted from the mixed atomic columns in the bilayer. The resulting wave vector magnitude difference map is shown in Figure 6.6 f).

Overall, the difference map shows a wave vector magnitude distribution similar to the one of the shown monolayer in Figure 6.6 e). Features with high values of electric field magnitude are found close to the hexagonally arranged atomic column positions which exhibit a triangular shape. Within the hexagonal rings a reduced wave vector magnitude is observed. At this position, a tungsten atom was present in the corresponding AB bilayer. As expected, the subtraction of the tungsten atomic columns results in a local minimum in the difference map indicating a similar wave vector magnitude around the two tungsten atoms in the bi- and monolayer. In contrast to the wave vector magnitude map of the monolayer, the difference map indicates negative wave vector magnitudes along the connecting directions between individual atomic columns (marked by the red dashed ellipse in Figure 6.6 f). These negative values are a result of the subtraction due to the different overlap areas of the atomic columns in mono- and bilayers. As the pronounced features of the wave vector magnitude around the atomic columns in the monolayer have larger extension and a different shape than in the bilayer due to the different overlap of potentials, the subtraction at these overlap region leads to negative values. Another discrepancy between the wave vector magnitude map of a monolayer and the difference map can be deduced from the wave vector magnitude around the individual atomic columns. For the monolayer, the selenium atoms are surrounded by a higher wave vector magnitude compared to the tungsten atoms

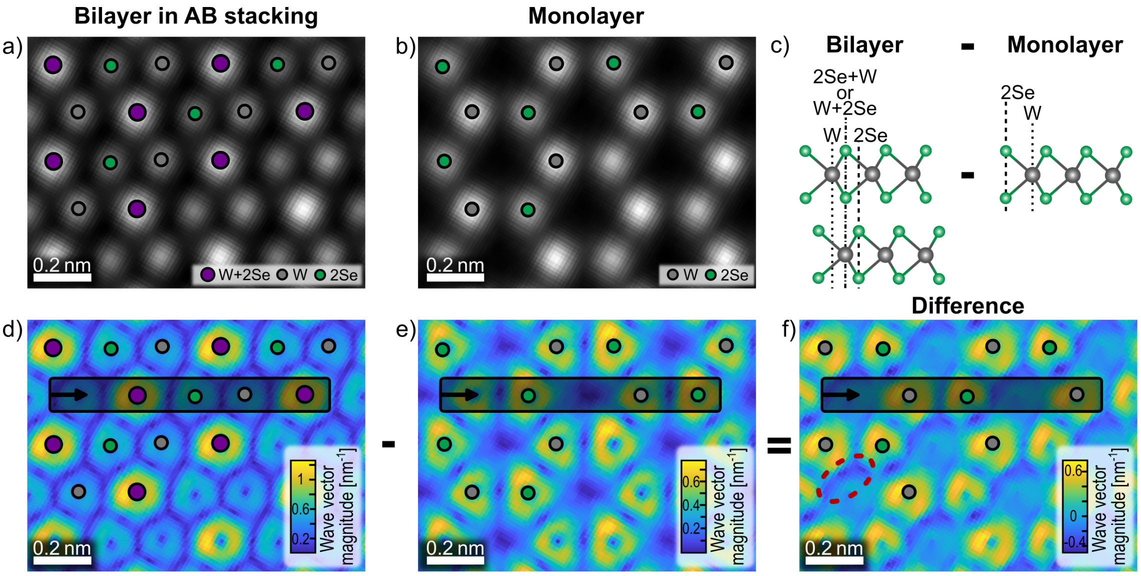

Figure 6.6: a-b) HAADF images of the AB stacked bilayer and the monolayer region, respectively. The atomic column positions are marked by coloured dots and the colour code for the atomic column type is given in the legend of the image. c) Illustration of the stacking of atoms in the bilayer and the monolayer. d-e) wave vector magnitude maps of the bilayer and the monolayer, respectively. f) Difference map of the wave vector magnitude calculated by the pixel-wise subtraction of the wave vector magnitude map of the monolayer from the wave vector magnitude map of the bilayer.

which is in accordance with the electric field magnitude and charge density values discussed in Chapter 4.1. The higher electric field magnitude in the monolayer can be explained by the higher atomic potential of two selenium atoms compared to one tungsten atom as described in Chapter 4.4. In contrast, the wave vector magnitude difference map indicates a reversed behaviour. In the difference map shown in Figure 6.6 f), features of increased wave vector magnitudes are located around the remaining tungsten atoms which were the previously mixed atomic column in the AB-stacked bilayer. Thus, the difference map resembles the wave vector magnitude of a monolayer qualitatively. Quantitatively, a difference between the wave vector magnitudes located at the two types of atomic columns is observed. In addition, the difference values overall indicate a slightly reduced wave vector magnitude compared to the shown monolayer. Still, they are in the same order of magnitude. The difference in absolute values between the monolayer and the bilayer is assumed to occur due to a difference in defocus as there are different optimum defocus for the mono- and bilayer due to the difference in specimen thickness [26, 74]. Furthermore, the beam propagation in the bilayer will also influence the absolute wave vector values. As the electron beam is already altered by the first layer it interacts with the second layer differently as shown by the refocussing effect in Chapter 4.4.4. Thus, a straight summation of two monolayers will not perfectly represent the values of a bilayer. This was also discussed in Chapter 4.4 where the stacking of two atoms on top of each other leads to lower magnitudes than twice the magnitude of a single atom. Although, the simulations of the single atoms gave a good insight into the fundamental behaviour of the quantities derived by DPC imaging, these simulations are idealised using only one atom in a plane under perfect illumination

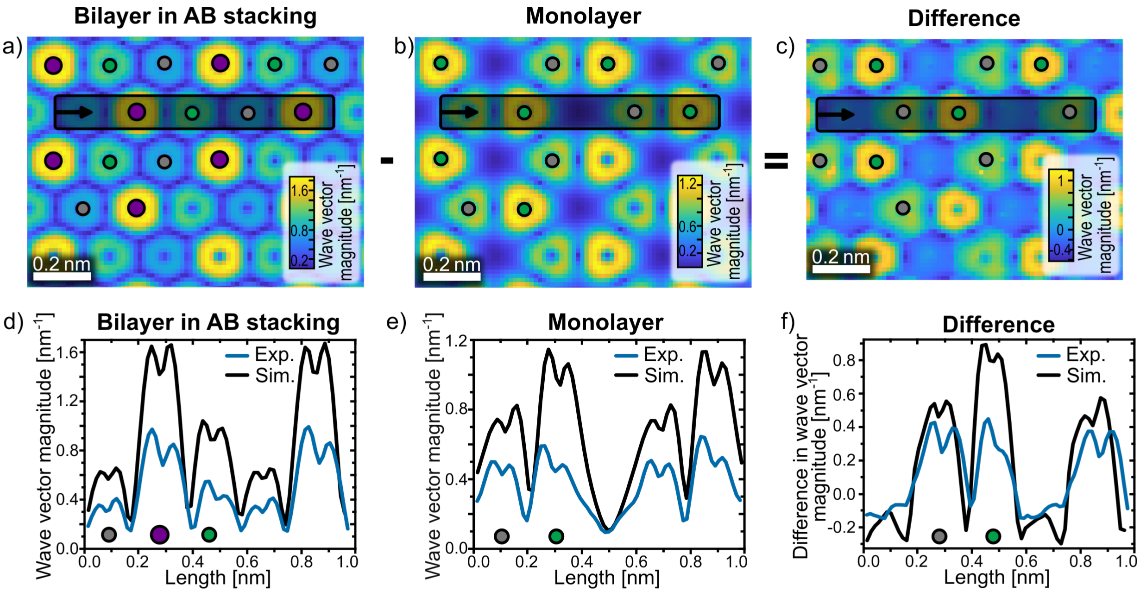

Figure 6.7: a-b) Wave vector magnitude maps of an AB-stacked bilayer and a monolayer derived from multislice image simulations. c) Difference map of the wave vector magnitude calculated by the subtraction of the wave vector magnitude of the monolayer from the one of the AB stacked bilayer. d-f) Integrated line profiles of the wave vector magnitude for the bilayer, the monolayer, and the difference between both, respectively. The line profiles are integrated over the region indicated by the black boxes. Blue solid lines indicate the line profiles taken from the measurement over a comparable region indicated by the black boxes in Figure 6.6. Black solid lines mark the line profiles derived from the measurement.

condition. However, here the difference map of the wave vector magnitude enables to experimentally access the influence of beam propagation.

Analogous, multislice image simulations are conducted. Figure 6.7 a) and b) depict the simulated wave vector magnitude maps of the AB-stacked bilayer and the monolayer simulated. Details of the multislice image simulations are given in the Appendix 9.11. Both images are qualitatively in good agreement with the experimental wave vector magnitude maps shown in Figure 6.6. Quantitatively, the simulations again exhibit higher absolute values of the wave vector magnitude although here it is not a factor of two but about 70 % higher values for the simulation compared to the measurement.

Figure 6.7 c) shows the calculated difference between the wave vector magnitude of the AB-stacked bilayer and the wave vector magnitude of the monolayer. The difference maps are in good agreement with the difference maps derived from the measurement. At the position where the tungsten atom of the AB-stacked bilayer is subtracted by the tungsten atom of the monolayer, a reduced wave vector magnitude is observed with pronounced negative values towards the atoms of a W-Se hexagonal ring. In contrast to the difference map of the measurement, the difference map derived by the simulations shows a different position of features with enhanced wave vector magnitude. Here, the higher wave vector magnitude can be found at the remaining selenium atomic column and reduced wave vector magnitude is observed at the remaining tungsten atom. Thus, the difference map resembles the same wave vector magnitude distribution as the monolayer which was not the case for the measurement. Quantitatively, the difference map of the simulations shows overall smaller wave vector magnitudes compared to the simulated monolayer. This was also observed for the difference map of the measurement. Thus, the influence of the beam propagation in the bilayer is not linear and reduces the values of the wave vector magnitude. For quantitative analysis and a comparison between measurement and simulation Figure 6.7 d-f) show the integrated line profiles for the measurement (blue solid line) and the simulation (black solid line) for the three different wave vector magnitude maps. The line profile of the AB-stacked bilayer shows five peaks with different heights for both, the simulation and the measurement (Figure 6.7 c). As expected the highest wave vector magnitude is found around the mixed atomic column (marked by a purple dot in d) of the AB stacked bilayer followed by the selenium atomic column (marked by a green dot). Despite the overall reduced wave vector magnitude of the measurement, the features in the line profile are in good agreement with the line profile of the simulation. Furthermore, the five different peaks in the line profiles exhibit two local wave vector maxima each. These maxima correspond to the strong wave vector magnitudes on the left and on the right of the atomic column. At the exact atomic column positions, local minima are observed as the transferred momentum parallel to the incident electron beam direction is not measurable. Line profiles derived from the experimental and simulated monolayer are shown in Figure 6.7 e). Again, overall higher wave vector magnitudes are observed for the simulation. Still, both line profiles exhibit similar features. In both line profiles, four pronounced peaks are found corresponding to the two W-Se dumbbells. The left peak of these dumbbells corresponds to a tungsten atom which exhibits a lower wave vector magnitude compared to the neighbouring selenium atomic column. This behaviour is observed for both the simulation and the measurement and is in good agreement with the atomic potentials of two selenium atoms compared to one selenium atom (Chapter 4.4). It is noteworthy that the difference in wave vector magnitude between selenium and tungsten atomic columns is more pronounced for the simulation (black solid line) than for the measurement (blue solid line). As tungsten and selenium atoms have a different z-position along the beam propagation direction, the difference might be due to a different defocus in the measurement and the simulation. Thus, the wave vector magnitude maps of the simulation and the measurement resemble the same features for the mono- and bilayer. However, the calculation of difference maps between mono- and bilayer for the measurement and the simulation results in a discrepancy between the ratio of selenium and tungsten atomic columns. Quantitatively, this is shown by the line profiles in Figure 6.7 f). The integrated line profiles are acquired over the same regions within the difference maps for the simulation and the measurement. The difference in wave vector magnitude derived from the simulations (black solid line) shows the same behaviour in the wave vector magnitude distribution as a monolayer with a higher wave vector magnitude located close to the selenium atoms whereas the tungsten atoms show a lower wave vector magnitude. However, the difference map derived from the measurement shows that the two atomic columns quantitatively exhibit almost the same wave vector magnitude. This is highlighted by the integrated line profile obtained the measurement (blue solid line) which indicates that no clear difference in remaining wave vector magnitudes between the two types of atomic columns can be observed.

Section summary

- The specific stacking configurations of a WSe_2 bilayer is analysed by the HAADF image contrast and identified as AB stacking configurations with three different types of atomic columns.
- The three different atomic columns exhibit an expected electric field distribution with the highest field magnitude located at the mixed atomic column due to the significantly higher projected atomic number compared to the pure selenium and pure tungsten atomic columns.
- A higher field magnitude and positive charge density are observed at the lower-Z pure selenium atomic columns compared to the pure tungsten atomic column which is in good agreement with the same behaviour as in a monolayer despite the fact that these atoms are in different layers of the AB-stacked bilayer.
- The subtraction of the wave vector magnitude map of a nearby monolayer region from the wave vector magnitude map of the AB-stacked bilayer does not result in the wave vector magnitude map of a monolayer as it was observed for the AA'-stacked bilayer. For the AB-stacked bilayer, the close distance of the atomic columns and the different z-positions of the atoms in the different atomic columns strongly influences the beam propagation. Therefore, the AB-stacked bilayer shows a beam deflection which is overall less than the beam deflection of two times a monolayer.

6.2 Moiré Homostructure of a WSe_2 Bilayer

Apart from the previously shown high-symmetry stacking, TMD layers can also be stacked on top of each other with a relative twist angle. This results in a Moiré pattern due to the superposition of the two atomic lattices. In general, Moiré patterns form when two periodic lattices, e.g. monolayers of 2D materials, are stacked on top of each other with either a twist angle or a lattice mismatch. The superposition of the two periodic lattices leads to a Moiré superlattice that has its own periodicity which is larger than the periodicity of the individual atomic lattices. The layered structure of TMDs and the weak van der Waals interaction between the layers facilitate a comparable simple stacking of layers either in homostructures consisting of layers of the same material or in heterostructures containing two or more materials [108]. The weak vdW interaction thereby facilitates the stacking of different layers at arbitrary twist angles or lattice mismatches.

The twisted stacking of TMD single and few layers changes the materials optoelectronic properties and offers a new pathway to tailor the electronic properties of the material stack beyond the number of layers, strain or defects. With the introduction of the large-scale periodicity of the resulting Moiré superlattice, even novel electronic correlation effects arise and new properties are introduced by the stacking of 2D materials, such as Moiré excitons [216] and superconductivity [217]. Especially for homostructures, the twist angle between the layers determines the band structure and the resulting (opto-)electronic properties [108, 218, 219].

Furthermore, the Moiré superlattice also introduces a periodic Moiré potential which superimposes with the atomic potentials but exhibits a larger periodicity than the typical interatomic distances. The periodicity can be tuned by the twist angle between the layers. This Moiré potential is currently of great interest as it leads to a confinement of charge changing the excitonic behaviour of the material in the vicinity of the confinement [220] and even introduces novel physical effects, such as different correlated electron states [221] and superconductivity [217, 219, 222, 223]. Therefore, Moiré structures of TMDs offer a variety of possibilities to tune the materials properties and exploit new physics.

Since the phase-retrieval methods in STEM are sensitive to the potential of the specimen, the introduced Moiré potential can be investigated as shown by Wen et al. for twisted graphene using a pixelated detector [224]. There, the electric field distribution in a trilayer of graphene is investigated, and long-range fields are observed. Therefore, in this chapter the electric field distribution in a twisted WSe_2 bilayer is investigated with focus on the atomic electric fields as well as possible long-range fields introduced by the Moiré superlattice.

Figure 6.8 depicts the STEM-DPC investigation of a Moiré homostructure of a WSe_2 bilayer. This structure was observed on a CVD-grown monolayer purchased from *2DSemiconductors*. Although no detailed information about the growth process and conditions are given by the manufacturer, it can be assumed that this region is a nucleation site for bi- and multilayer growth.

Figure 6.8 a) shows the high-resolution STEM-HAADF image of the Moiré superlattice. The number of layers of this homostructure are determined by the HAADF signal Appendix 9.10. Based on the Z-contrast of the HAADF image, regions with different stacking configurations

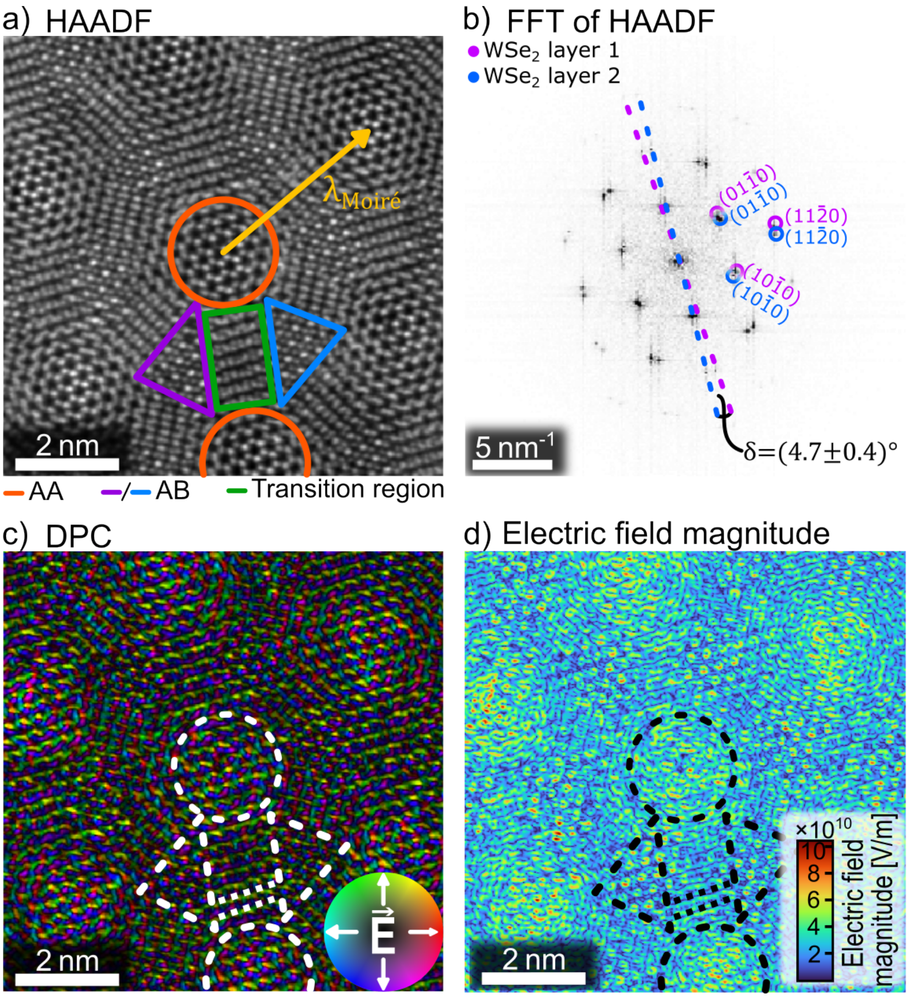

Figure 6.8: a) HAADF image of a twisted WSe$_2$ homostructure showing a Moiré superlattice. The different areas of stacking are exemplarily marked by the orange, purple, blue and green shapes. The wavelength of the Moiré lattice $\lambda_{\mathrm{Moiré}} = (3.93 \pm 0.18)$ nm is indicated by the yellow arrow. b) Power spectrum of the WSe$_2$ homostructure derived from the HAADF image by a Fast Fourier Transformation (FFT). The periodicity of the two WSe$_2$ layers are overlaid with each other resulting in pairs of spots in the FFT indicated by the blue and pink circles for both WSe$_2$ layers. The twist angle between the two layer, determined by the two dotted lines, is $\delta = (4.7 \pm 0.5)\,^{\circ}$. c) Colour-coded DPC image and d) the electric field magnitude map. Information on the experimental imaging parameters and the image post-processing are given in Table 9.12 in the Appendix.

can be identified which are exemplarily marked by coloured shapes. The regions enclosed by the orange (semi-)circles exhibit an AA stacking configuration, the blue and purple triangles indicate the regions with AB stacking configuration and the green square marks the transition region where no high-symmetry stacking can be identified.

The Moiré wavelength of the superlattice is indicated by the yellow arrow and amounts to a $\lambda_{\text{Moiré}} = 3.93 \pm 0.18\,\text{nm}$ and depends on the twist angle between the two sublattices. Here, the twist angle between the two WSe_2 monolayers is determined using the power spectrum of the image derived by a fast Fourier transformation (Figure 6.8 b). The FFT of the HAADF image contains the reciprocal space information of the image and shows distinct spots which correspond to the lattice spacings of the two sublattices. The individual spots of the two WSe_2 sublattices are exemplarily marked by the blue and pink circles for three pairs of spots in the power spectrum. A twist angle of $\delta = (4.7 \pm 0.4)\,^\circ$ is determined from the angle between the spots of the individual lattices which is exemplarily illustrated by the blue and pink dotted lines. For TMD Moiré structures, the twisted stacking leads to different stacking configurations of the layers within the range of the Moiré wavelength. Thus, the atomic stacking changes on a short length scale with transitions regions between the different high-symmetry stackings. Figure 6.8 c) shows the colour-coded DPC map of the electric field distribution in which two different high-symmetry stackings, namely AA and AB, are observed enabling a direct comparison of the different atomic stackings and the resulting atomic field distributions.

Although the number of WSe_2 layers is the same over the whole image area, the DPC image shows variations in the electric field distribution due to the influence of the different stacking of atoms. A pronounced field distribution is visible at the regions with AA stacking configuration which stands out from the other regions and indicates a higher electric field magnitude (exemplarily marked by the white dashed (semi-)circle).

The differentiation between the AB stacking regions and the transition regions is more difficult as the rotational symmetric atomic electric field distribution features are less visible in the DPC image. However, upon closer examination, the AB stacking configuration can be identified by the pronounced rotational symmetric electric field distribution around an individual atomic column, which is surrounded by atomic columns with reduced field distributions (area marked by the white dashed triangles in Figure 6.8 c). The pronounced rotational symmetric field distribution in this region can be assigned to the mixed atomic column consisting of two selenium atoms of one layer and a single tungsten atom from the other layer resulting in the highest projected atomic number for this stacking region, similar to the pure AB stacking discussed in Chapter 6.1.2.

Enclosed by the edges of the neighbouring triangles, transition areas are found which cannot be assigned to any of the five high-symmetry stacking configurations (Chapter 2.7). These transition areas show stripe-like features in the electric field distribution which are exemplarily indicated by the two white dotted parallel lines in Figure 6.8 c). No individual rotational symmetry field distributions around atomic columns can be identified.

For the different stacking regions in the Moiré homostructure, differences in the magnitude of the measured electric field distribution are visible in Figure 6.8 d). Here, a high electric field magnitude is observed for the regions of AA stacking (exemplarily highlighted by the black dashed (semi-)circle). Although some field magnitude variations between the six different AA stacking regions are visible, the trend of an overall higher electric field magnitude in these regions compared to the AB stacking and transitions regions is evident. In the AB stacking regions, individual atomic columns of mixed composition are visible by a pronounced electric field magnitude surrounded by atomic columns with reduced electric field magnitude.

The transition regions show the overall lowest electric field magnitude compared to the two high-symmetry stackings which is due to the missing vertical alignment of atoms. In other words, as the atoms of the two different layers are not perfectly aligned in beam propagation direction due to the twist angle between the two WSe_2 layers, the projected atomic number is lower than in the high-symmetry stacking configurations.

To investigate the influence of the twisted stacking and the different stacking configurations in further detail, Figure 6.9 depicts the three different stacking configurations identified in Figure 6.8 a), namely the AA and AB stacking as well as the transition region. From left to right, Figure 6.9 shows an illustration of the stacking in top as well as side view and sections of the HAADF image, the colour-coded DPC image and the electric field magnitude map. The electric field magnitude maps are displayed with the same colormap and range of values enabling a direct comparison of the colours between the different maps. It is to note, that for the calculation of the electric field magnitude map a fixed thickness of $t = 1.29\,\mathrm{nm}$, corresponding to an interlayer distance of $d_0 = 0.649\,\mathrm{nm}$, is used although the twisted stacking of TMDs leads to a modulation of the interlayer distance [225, 226].

Figure 6.9 a) shows AA stacking region marked by the orange circle in Figure 6.8 a). In this stacking configuration, the atoms of the first layer are vertically aligned with the atoms of the second layer resulting in atomic columns aligned in beam propagation direction. In contrast to the previously discussed AA' stacking configuration, the AA stacking of WSe_2 bilayers leads to atomic columns either consisting only of (four) selenium atoms or (two) tungsten atoms, i. e. no mixed atomic columns. This is determined by the HAADF image intensity. The atomic column positions are marked by green and grey dots for pure selenium and pure tungsten atomic columns, respectively. The HAADF image section shows that the area of almost ideal AA stacking is limited to only a few angströms squared. In the shown image section in Figure 6.9 a) the stacking configuration changes towards the images edges which is apparent from the merging of contrast of adjacent atomic columns.

For the central part of the AA stacking configuration, rotational symmetric electric field distributions around the atomic column positions are observed in the DPC image. With increasing distance from the centre of this AA stacking area, the individual rotational symmetric field distributions around the atomic columns vanish and merge with neighbouring atomic columns into elongated field distributions (exemplarily marked by the white dashed ellipse in the DPC image). This coalescence of the individual field distributions of atomic columns in the edge regions is due to the twist angle between the layers affecting the atomic column alignment perpendicular the beam propagation direction. Thus, atoms of the two layers are not perfectly aligned in vertical direction and the measured projected electric

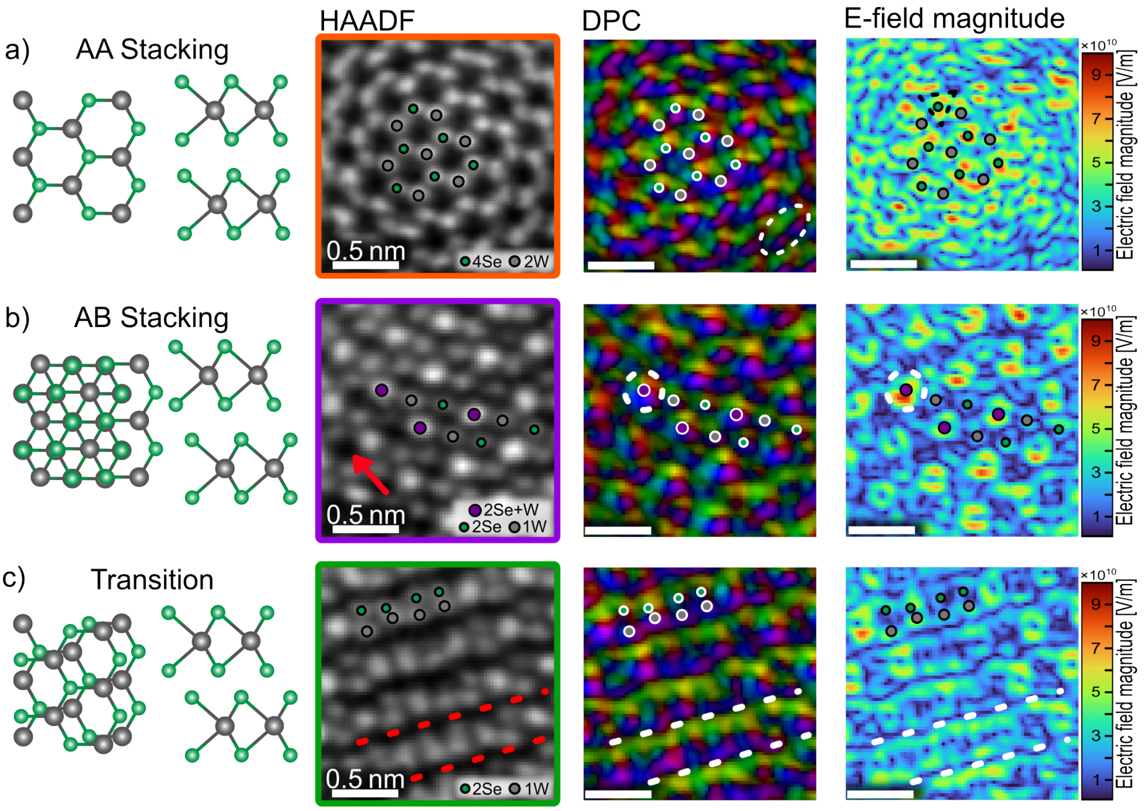

Figure 6.9: Analysis of three different stacking regions in the WSe_2 Moiré structure. From left two right, the atomic structure in top and side view is shown as well as the HAADF and DPC images, and the electric field magnitude maps for a) the AA stacking, b) the AB stacking and c) the transition region. The corresponding regions in the Moiré pattern are indicated in Figure 6.8 a) by the orange, purple and green shapes. The atomic column positions are marked by green, grey and purple dots. The corresponding colour code is given by the legend in the three associated HAADF images. The scale for the colormap of the electric field magnitude maps is the same for all three images which enables a direct comparison of the colours.

field is altered by this not perfectly aligned stacking.

Furthermore, the outer regions of the image section show less saturated colours compared to the central part indicating a reduction in measured electric field magnitude. Thus, the slight variation in stacking from the central to the outer part of the image section already introduces changes not only in the field distribution especially impacting the electric field magnitude. This is in detail visible by the corresponding image section of the electric field magnitude (most right image in Figure 6.9 a). The individual triangular-shaped regions of high electric field magnitude around the atomic columns are difficult to identify even in the central part with the high-symmetry AA stacking. This is presumably due to the presence of contamination located above or below the Moiré structure (Chapter 4.5). However, for some atomic columns the characteristic triangular-shaped electric field magnitude distribution can be found (marked by the black dashed triangle). As expected, the electric field magnitude is the highest for the central part with perfectly aligned atomic columns and is reduced for the edges of the image section where the vertical stacking of atoms in atomic columns is modified by the rotation of the layers. For increasing distance from the centre, the atoms of the two layers are shifted against each other and, thus, the projected atomic number is reduced. Therefore, a reduced electric field magnitude is observed for the edge region of the image section. This shows the sensitivity of the electric field distribution and magnitude derived by STEM-DPC on the local stacking of atoms.

Figure 6.9 b) shows the sketch of the crystal structure and the image sections of the AB stacking region (indicated by the purple triangle in Figure 6.8 a). The atomic stacking matches the AB stacking configuration discussed in Chapter 6.1.2 with atomic columns of one layer located in the W-Se hexagonal ring of the other layer in top view. Additionally, the side view illustrates the vertical alignment of atoms of the different layer resulting in the three different types of atomic columns, namely a pure selenium atomic column with two selenium atoms, a single tungsten atom, and the mixed atomic column containing two selenium atoms and one tungsten atom.

These three different types of atomic columns are distinguished based on the HAADF image contrast and the comparison with simulations done previously for the pure AB stacking discussed in Chapter 6.1.2. Here, the purple dots mark the mixed atomic column, and the green and grey dots indicate the pure selenium atomic columns and the single tungsten atom, respectively. In contrast to the pure AB stacking, the here shown AB stacking region is not perfectly aligned due to the twist between the two layers and the atoms are not straight lines in lateral directions. Furthermore, defects can be observed in the AB stacking regions such as a missing atomic column highlighted by the red arrow. Based on the structure, this defect site is presumably a missing selenium atomic column in one of the two WSe_2 monolayers.

Comparable to the AB stacking observed in the high-symmetry stacking in Chapter 6.1.2, the mixed atomic columns show a pronounced rotational electric field distribution with a high colour saturation in the corresponding DPC image section indicating the higher field magnitude compared to the pure selenium and tungsten atoms (marked by the white dashed circle in the DPC image in Figure 6.9 b). The rotational electric field distribution of the two other atomic columns is less pronounced but still visible.

This is also visible in the corresponding electric field magnitude map. There, the mixed atomic columns, marked by the purple dot, show a high electric field above and below the atomic column positions. Interestingly, enhanced field magnitudes are not evenly distributed around the mixed atomic columns, but local maxima on top and below the atomic column positions can be seen. As an elongation of the electric field magnitude distribution was already observed on the measured pure AB stacking in Chapter 6.1.2, this artefact is most probably introduced by the relative twist angle between the layers leading to a non-perfect vertical alignment in atomic columns. The atoms in the mixed atomic column are shifted with respect to each other and field components from the individual atoms overlap resulting in this direction-dependent reduced field magnitude. In addition, residual lens aberration also influence this field distribution and might enhance the DPC image features at the mixed atomic columns due to the higher number of atoms in the column. Still, as these different stacking regions are derived from the same image, a direct comparison of the different stackings is possible even in presence of residual lens aberrations.

Figure 6.9 c) shows the sketch of the atomic arrangement and the STEM-DPC image sections for the transition region marked by the green rectangle in Figure 6.8 a). For the transition region the two sublattices are not aligned in one of the common five high-symmetry stacking configurations (Chapter 2.7). Thus, the atomic columns of the individual layers are not aligned above each other in beam propagation direction as illustrated by the schematic crystal structure in top and side view. The corresponding HAADF image shows lines of atomic columns (exemplarily highlighted by the two red dashed lines) where the top row of atoms of these lines corresponds to selenium atomic columns and the bottom atomic row consists of tungsten atoms. The close distance of the two rows of atomic columns within a line of atoms leads to strongly overlapping fields visible in the corresponding DPC image section. No individual rotational symmetric field distribution can be observed in this transition region, however, pronounced green and purple areas are visible. For the upper row of atomic columns, consisting of selenium atomic columns, mostly an electric field distribution with pronounced greenish and yellowish colour is observed. For the bottom row of atoms (tungsten atoms), a pronounced dark blue and purple colour distribution is observed. This shows, that the other direction of the field distribution are suppressed due to the close distance of the atomic columns within these lines of atoms. Thus, the projection along the beam propagation direction has a strong influence on the derived electric field distribution even though the in-plane distance between the atoms of each individual layer remains the same. Therefore, the projection along the vertical direction drastically alters the measurable projected electric field distribution. In contrast to the AB stacking, the distance between the atoms and the finite electron probe size limits the capability to separately resolve the individual atomic electric fields.

As described in Chapter 2.7 for the different stacking configurations of TMDs, the interlayer distances change depending on the specific stacking configuration. For Moiré structures, this results in a modulation of the interlayer distance on the length scale of the Moiré wavelength. Bera et al. calculated the interlayer distance for the different stacking regions for a WSe_2 homobilayer at a twist angle of 2°. Under this condition, the AA stacking region exhibits an interlayer distance of $d_0^{\mathrm{AA}} = 0.68\,\mathrm{nm}$, whereas the AB stacking regions exhibit an interlayer distance of $d_0^{\mathrm{AB}} = 0.63\,\mathrm{nm}$ [226]. With the specimen thickness being twice the interlayer distance, the modulation causes a variation in thickness. Thus, the assumed average thickness $\bar{t}$ of twice the monolayer thickness leads to an incorrect calculated electric field magnitude for the different stacking regions in the Moiré superlattice. Instead, the thickness of the Moiré superlattice is a function of the scan position $t(\vec{R})$. Comparing the assumed average thickness $\bar{t}$ with the thickness for the AA stacking regions t^{AA} indicates that the specimen thickness is approximately $5\,\%$ higher in this region than calculated. For the AB stacking configuration the correct interlayer distance gives a specimen thickness t^{AB} which is about $3\,\%$ smaller than the assumed thickness $\bar{t}$. Thus, for the different stacking regions, different specimen thicknesses must be assumed for a correct analysis although the same number of layers and atoms are present.

To investigate the influence of the thickness modulation on the derived electric field magnitude, the relative change in the electric field magnitude is calculated. Since the electric field magnitude is inversely proportional to the specimen thickness t at the specific scan position $\vec{R}$, the thickness modulation results for the AA stacking region in an overestimated and for the AB stacking regions in an underestimated electric field magnitude (Chapter 2.5). Quantitatively, the deviations of the thickness in the range of 3% and 5% would lead to changes in electric field magnitude which are also in the range of $\pm 5\,\%$. These thickness modulations can therefore be here neglected, as the influence of the thickness modulation does not alter the overall trend with the high-symmetry AA stacking exhibiting a higher field magnitude compared to the other stacking regions. With an average electric field magnitude of $|\vec{E}|^{\mathrm{AA}}_{\mathrm{avg.}} = (3.1 \pm 1.5) \cdot 10^{10}\,\mathrm{V/m}$, the AA stacking region exhibits an approximately 23 % higher electric field magnitude than the AB stacking region with an average electric field magnitude of $|\vec{E}|^{\mathrm{AB}}_{\mathrm{avg.}} = (2.5 \pm 1.5) \cdot 10^{10}\,\mathrm{V/m}$. Thus, for STEM-DPC the influence of the interlayer distance is less than the influence of the specific stacking of the atoms in atomic columns.

Comparing the electric field magnitude map of the AA stacking region with the AB stacking region shows one distinct difference: The electric field minimum of the AB stacking $|\vec{E}|^{\mathrm{AB}}_{\mathrm{min}} = 1.2 \cdot 10^{8}\,\mathrm{V/m}$ is overall lower than the overall field minimum of the AA stacking $|\vec{E}|^{\mathrm{AA}}_{\mathrm{min}} = 4.8 \cdot 10^{8}\,\mathrm{V/m}$. This is due to the smaller projected distance between the atomic columns resulting in a stronger overlap of the individual atomic electric fields. Furthermore, also the projected atomic number is lower for two of the three atomic columns in the AB stacking configuration compared to the projected atomic numbers in the AA stacking region. The three different types of atomic columns in the AB stacking configuration exhibit a projected atomic number of 142 for the mixed atomic column, and 68 and 74 for the pure selenium atomic column and the tungsten atom, respectively. However, in the AA stacking both types of atomic columns exhibit a higher projected atomic number with 136 for the four selenium atoms or with a projected atomic number of 148 for the tungsten atomic columns. However, the maximum electric field magnitudes in AA and AB stacking are comparable with $|\vec{E}|^{\mathrm{AA}}_{\mathrm{max}} = 9.9 \cdot 10^{10}\,\mathrm{V/m}$ and $|\vec{E}|^{\mathrm{AB}}_{\mathrm{max}} = 9.0 \cdot 10^{10}\,\mathrm{V/m}$. Thus, the two stackings differ by only 10% in the maximum electric field magnitude. Due to the short periodicity of the Moiré superlattice, only a few atomic columns are perfectly aligned in the AB stacking configuration hindering a quantitative analysis of the electric field magnitude due to a lack of statistics. This is even more hampered by the residual contamination leading to local variation in the electric field distribution and magnitude.

The electric field magnitude map of the transition region shows the lowest electric field magnitude over the image section compared to the two high-symmetry stackings. This is expected as the projected atomic number of the individual atomic columns is the lowest compared to the other stacking configurations. Here again, no triangular-shaped regions of high electric field magnitude are found due to the small distance between the different atomic columns.

All in all, the regions of high-symmetry AB stacking show an electric field distribution comparable to the field distribution of the genuine stacking configuration shown in Chapter 6.1.2. Furthermore, the stacking configurations strongly influence the electric field distribution and magnitude and even slight deviations from the high-symmetry stacking

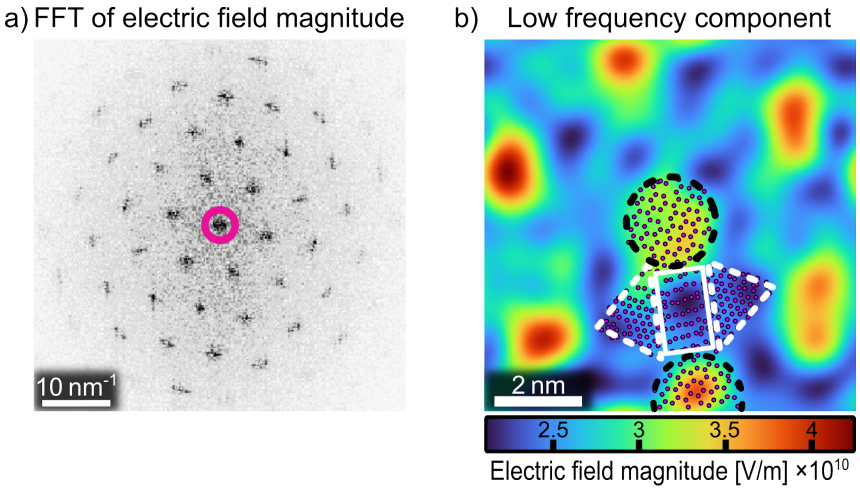

Figure 6.10: a) (Colour-inverted) power spectrum of the electric field magnitude map shown in Figure 6.8 d) derived by an FFT. The inclusive mask for the filtering of the long-range components is indicated by the pink circle. b) Reconstructed low-frequency component of the projected electric field magnitude.

configurations reduce the measured electric field magnitude as shown for the edge regions of the AA and AB stacking sections. This observation is even more visible in the transition regions, where the atoms of the individual layers are not aligned in atomic columns along the beam propagation direction. Therefore, it is noteworthy that the projection of atoms along the beam propagation direction drastically alters the beam propagation and, thus, the projected electric field distribution derived by STEM-DPC. Therefore, the shown Moiré homostructures illustrates the strong influence of the specific stacking of atoms along the beam propagation direction.

Although individual regions of the Moiré superlattice show atomic electric field distributions comparable to the individual high-symmetry stacking, the introduced Moiré potential might introduce an additional long-range electric field which is superimposed with the atomic electric fields from the individual atomic columns. Wen et al. investigated this kind of long-range modulation in the electric field distribution in a twisted graphene trilayer using 4D STEM [224]. There, the low frequency components of the electric field distribution are analysed using the power spectrum derived from an FFT and an inclusive mask for filtering. For the twisted graphene, the reconstructed long-range component of the electric field shows high magnitudes at the regions with high-symmetry stacking [224].

For comparability, a similar approach is applied to investigate the influence of the possibly introduced long-range field in the twisted WSe_2 bilayer. Figure 6.10 a) depicts the power spectrum of the electric field magnitude map shown in Figure 6.8 d). The power spectrum is derived using an FFT and colour-inverted for better visibility. The inclusive mask used for the inverse FFT and the reconstruction of the image is indicated by the pink circle. Since the mask for the filtering is centred around the central spot, high frequencies typically assigned to atomic fields are filtered and only the low frequencies are used for the reconstruction using an inverse FFT. The filtered image of the electric field magnitude map is shown in Figure 6.10 b). The reconstructed image of the low frequencies associated with the long-range field component of the projected electric field shows modulations in the image intensity with high image contrast at the position of the high-symmetry AA stacking of the Moiré structure (exemplarily marked by the black dashed circles in Figure 6.10 b). The influence of the high-symmetry AA stacking configuration is clearly visible by the enhanced field magnitudes (exemplarily marked by the black dashed circles in Figure 6.10 b). These regions show the maximum field magnitude of the filtered long-range field components with about $|\vec{E}^{\mathrm{max}}_{\mathrm{long-range}}| = 4.2 \cdot 10^{10}\,\mathrm{V/m}$ which diminishes for increasing distance to the centre of the AA stacking. For the high-symmetry AB stacking regions and the transition regions, local minima in the derived electric field magnitude are observed (exemplarily marked by white dashed triangles and a white rectangle, respectively). These local minima exhibit an electric field magnitude of about $|\vec{E}^{\mathrm{min}}_{\mathrm{long-range}}| = 2.1 \cdot 10^{10}\,\mathrm{V/m}$. Comparing the maximum and minimum value of the shown electric field magnitude map associated with the long-range component indicates that the modulation of the long-range component is small compared to the modulations introduced by atomic electric fields which are in a field magnitude range of about half an order of magnitude higher. This modulation of the electric field is usually superimposed with the strong atomic electric fields. A comparable behaviour of the long-range field component is also observed by Wen et al. for the twisted graphene trilayer [224].

The pronounced electric field magnitude of the AA stacking regions indicated by the long-range component is in agreement with the expected higher electrostatic projected potential in these regions compared to the other regions of the Moiré stacking. Since the atoms of the two WSe_2 layers are vertically aligned in atomic columns a high potential is expected at this high-symmetry spots as discussed previously. Unexpectedly, no significant difference in the long-range component of the field magnitude is observed between the high-symmetry AB stacking and the transition zone. This is presumably due to the arrangement of atoms in the AB-stacking where the atoms of the two WSe_2 layers are mostly aligned in individual atomic columns and are not vertically aligned with each other. Thus, the vertical stacking of the atoms drastically influences the electric field magnitude.

Section summary

- A Moiré homostructure of a WSe_2 bilayer with a twist angle of $\delta = (4.7 \pm 0.5)\,^\circ$ and a wavelength of $\lambda_{\mathrm{Moiré}} = 3.93 \pm 0.18\,\mathrm{nm}$ is investigated by DPC to analyse the atomic electric field distribution and possible long-range fields introduced by the Moiré superlattice.
- The different stacking configurations introduced by the twisted stacking of the two WSe_2 layers are identified by the high-resolution HAADF image and reveals two high-symmetry stacking regions (AA and AB) separated by transition regions.
- The DPC image shows variation of the electric field distribution and magnitude on the length scale of the Moiré wavelength.

- The high-symmetry AA stacking configuration exhibits the highest electric field magnitude over the image area.
- The regions of different stacking in the Moiré structure do not introduce a long-range field with an extension in the range of the Moiré wavelength and high electric field magnitudes are localized to the atomic column positions.
- The different stacking regions of the Moiré structure illustrate the sensitivity of DPC imaging on the local stacking configuration of atoms in beam propagation direction by the distorted rotational symmetry field distributions for increasing distance from the centre of the high-symmetry stacking.
- The close distance of atoms in the transition regions is smaller than the spatial resolution of the microscope and, thus, no individual atomic electric field distributions can be imaged.
- The investigation of the low frequency components of the electric field magnitude map shows a modulation in the magnitude on the length scale of the Moiré wavelength which is usually superimposed with the atomic field distribution.
- The long-range component of the electric field indicates a higher overall electric field magnitude in the AA stacking regions compared to the other regions indicating the higher projected potential due to the vertical alignment of atoms.

Chapter 7

Defects in a WSe_2 Monolayer

7.1 Single Selenium Vacancy in a WSe_2 Monolayer

According to the second law of thermodynamics, defects are always present in crystalline materials. Depending on their type and density, these defects alter the material's electronic, optical, and mechanical properties [140]. Especially in 2D materials, individual defects influence the optical properties even stronger than in bulk materials due to the low dimensionality of 2D materials [141]. In addition, due to the high surface-to-volume ratio of 2D materials, the defect formation and dynamics differ from the formation of defects in bulk materials. Thus, the precise control, creation and investigation of defects in 2D materials are important for their application in future optoelectronic devices and are currently substance of intensive research [137, 139].

STEM is among only a few techniques that allow investigation of defects in the atomic structure with a spatial resolution down to the sub-atomic level. In combination with DPC, even the atomic electric field distribution can be derived and changes in the electric properties introduced by the defect can be visualized and investigated. Therefore, the following discussion shows STEM-DPC measurements on single and multiple point defects in a monolayer of WSe_2.

Figure 7.1 a) shows the measured (left) and simulated (right) HAADF images of a selenium vacancy in a WSe_2 monolayer. The simulation of the vacancy was achieved using the experimentally determined positions of atoms neighbouring the defect site. Thus, the influence of lattice distortion in the vicinity of the defect is included in the simulation. Both HAADF images show the hexagonal arrangement of atomic columns in WSe_2 in [0001] zone-axis orientation. Based on the HAADF intensity, the atomic column species are determined and indicated by the coloured dots. In the centre of the images an atomic column with reduced HAADF intensity compared to the surrounding atomic columns is identified and marked by a pink dot (see Figure 7.1 a). The reduced HAADF intensity indicates a lower projected atomic number of this specific atomic column. Furthermore, the HAADF intensity of this atomic column is slightly smeared towards the lower tungsten atom, indicating a shift of the atomic column towards the lower tungsten atomic column.

Figure 7.1 b) shows line profiles of the normalized HAADF intensity integrated over the blue and orange boxes in the HAADF images of the measurement and the simulation. The integrated line profiles show two peaks from left to right with low and high intensity corresponding to a selenium and a tungsten atomic column, followed by a small peak with strongly reduced HAADF intensity and a peak with high intensity. Based on the expected alternating low and high HAADF intensities of the Se-W dumbbells, the position with reduced peak intensity is assigned to the position of a selenium atomic column. Comparing the peak intensity of the HAADF peak with reduced intensity with the HAADF peak intensity of the neighbouring selenium atomic column shows that the HAADF peak intensity reduced by about 47 % for the measurement and 55 % for the simulation. The reduced HAADF intensity at the position of a selenium atomic column therefore suggests that one selenium atom of this atomic column is missing, as the resulting projected atomic number is reduced by half. Therefore, the present defect can be identified by the HAADF intensity as a missing selenium atom in a selenium atomic column.

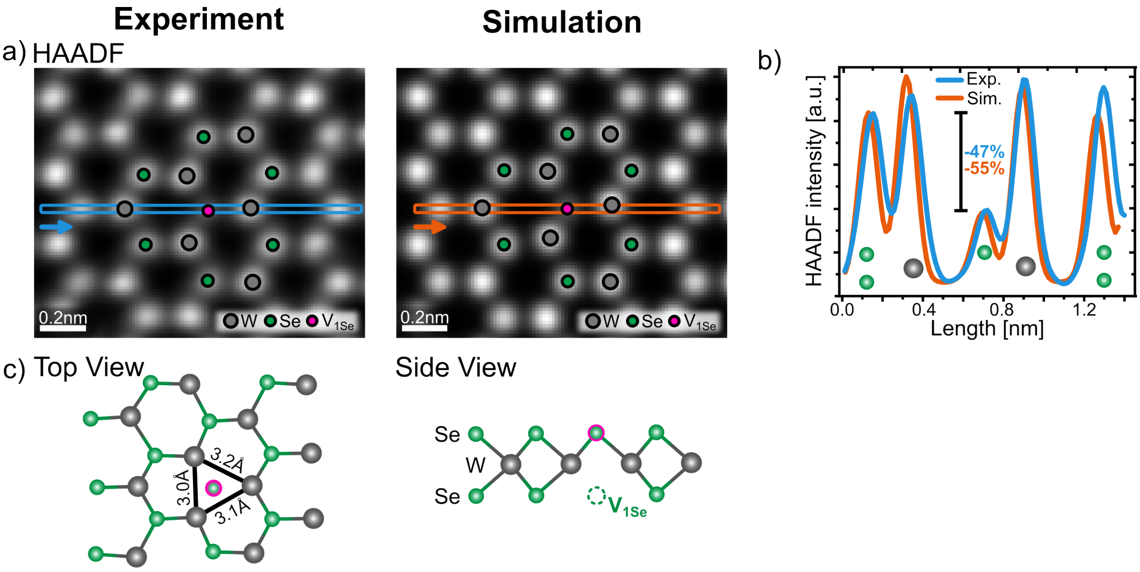

Figure 7.1: a) Measured (left) and simulated (right) HAADF image of a single selenium vacancy in a WSe$_2$ monolayer. Atomic column positions and species are determines by the green and grey dots for selenium and tungsten, respectively. The position of the selenium vacancy is indicated by a pink dot. b) Normalized line profiles of the HAADF intensity integrated over the region indicated by the blue and orange boxes in a) for the measurement and simulation. The HAADF images are also provided in Figure 9.11 in the Appendix, without the coloured dots, to improve visibility of the individual HAADF intensities of the atomic columns. c) Top and side view of a selenium vacancy in the WSe$_2$ monolayer.

Figure 7.1 c) depicts the top and side view structure of a selenium vacancy in a WSe$_2$ monolayer. For the top view image, the experimentally observed atom positions are used. It is visible, that the lattice is slightly distorted in the vicinity of the defect. The mean distance between all tungsten atoms (W) identified by the HAADF image is calculated to $\bar{d}_{\mathrm{W-W}} = (3.29\pm0.11)\,\text{Å}$ which is similar to the ideal lattice constant of a = 3.29 Å. The three tungsten atoms closest to the defect site are not considered for the calculation of the mean W-to-W distance as the defect might introduce additional atomic relaxation. The distance between the three tungsten atoms is indicated in Figure 7.1 c). All three W-W distances differ slightly from the calculated mean W-to-W distance $\bar{d}_{\mathrm{W-W}}$. However, with W-W distances of the three tungsten atoms of about $\bar{d}^{\mathrm{V1Se}}_{\mathrm{W-W}} = (3.1 \pm 0.1)\,\text{Å}$, a significant atomic relaxation is not observed for the single selenium vacancy. However, this is also not expected as the residual atom at the defect site prevents an atomic relaxation of the neighbouring atoms as shown by Ref. [41]. Thus, the observed deviations of the W-W distances close to the defect site are presumable not solely introduced by the missing selenium atom, but might be introduced by additional effects, such as strain due to additional defects in the vicinity. Furthermore, specimen drift during the measurement, which is visible by the not perfectly aligned lines of atomic columns along the horizontal and vertical directions, also influence the measured distances.

As the HAADF images in Figure 7.1 a) do not directly generate information about the position of atoms or lattice distortion in the z-direction, the ideal structure is displayed in the side view image in Figure 7.1 c). Here, the vacancy is marked by the dashed green

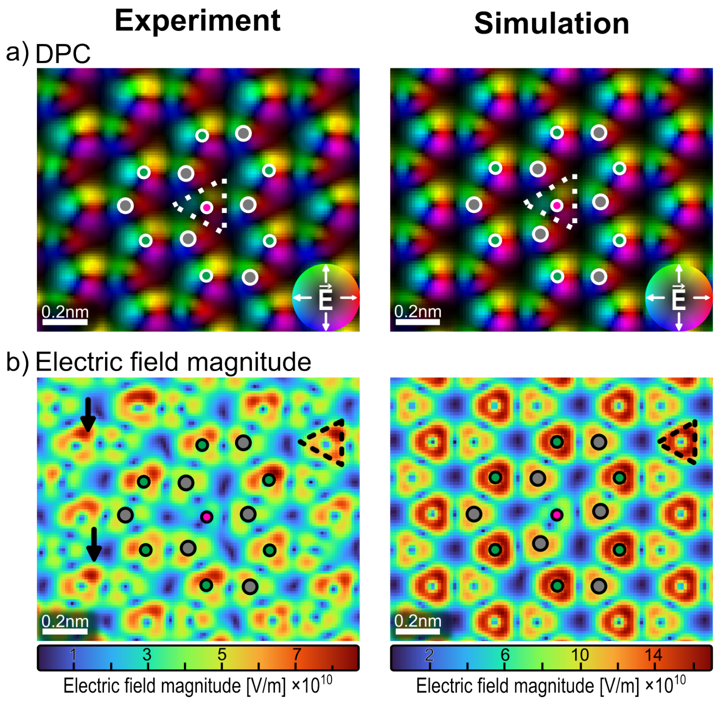

Figure 7.2: a) Colour-coded DPC images of the electric field distribution for the measurement (left) and the corresponding multislice image simulation (right). b) Electric field magnitude maps for the measurement (left) and the corresponding multislice image simulation (right). The DPC images and electric field magnitude maps are also provided in Figure 9.11 in the Appendix, without the coloured dots, to improve visibility of the individual field distributions of the atomic columns.

circle which is located at the bottom selenium layer (last atomic layer in beam direction). For the formation of defects in the upper selenium atomic layer a higher energy is needed as the subsequent selenium layer hinders an escape of the atom [165, 171, 227]. Thus, the probability of selenium vacancies is higher for the bottom selenium layer due to the direction of momentum transfer [227].

Since the number of atoms in the atomic column is reduced by the missing selenium atom, the potential at this position is locally changed. Thus, the electric field and charge density distributions are expected to be altered compared to the pristine structure. Therefore, the following discussion focuses on the analysis of the electric field distribution around the defect site. Figure 7.2 a) shows the colour coded DPC images of the measurement (left) and the simulation (right) of the defect site region shown in Figure 7.1 a). For both, the measurement and the simulation, rotational symmetric electric field distributions around the individual atomic columns are observed which are comparable to the field distributions of the pristine monolayer shown in Figure 4.1. Despite the above-discussed lattice distortion in the vicinity of the defect, the electric field distribution maintain the rotational symmetric field distribution. As described for the HAADF images in Figure 7.1 a), the atomic column positions and species are indicated by the coloured dots. Green and grey dots indicate selenium and tungsten atomic columns and the single pink dot denotes the selenium vacancy position. At the defect site a rotational symmetric electric field distribution comparable to the one around selenium atomic column positions is observed (marked by the white dashed triangle in Figure 7.2 a). However, compared to the surrounding electric field distribution the field at the defect site is reduced which can be deduced from the reduced colour saturation. To investigate the change in electric field quantitatively, the corresponding electric field magnitude maps are shown in Figure 7.2 b) for the measurement (left) and the simulation (right).

The electric field distribution of the simulation shows the triangular shape of enhanced electric field magnitude around the atomic column positions (marked by black dashed triangles in the measurement and the simulation). Here again, an electric field distribution similar to the one of a pristine monolayer is observed, where selenium atomic columns show a higher electric field magnitude than tungsten atomic columns. The same holds for the electric field magnitude of the measurement, though the triangular shape is slightly distorted as discussed below. For the measurement, the electric field magnitude map shows a local electric field maximum in the top right corner of the triangular shaped field magnitude distribution around selenium atomic columns. The maxima are exemplarily highlighted by the black arrows for two selenium atomic column positions. This feature indicates the presence of residual lens aberrations, presumably a combination of defocus and star aberration, leading to a directional enhancement of the measurable electric field (Appendix 9.14). Still, the electric field magnitude map resembles the simulated electric field magnitude map. For both maps, the tungsten atomic columns show a triangular electric field magnitude with increased electric field magnitudes at the tips of the triangular-shaped features which are generally still lower in magnitude than the ones around the selenium atomic columns.

The selenium defect-site itself shows a reduced electric field magnitude for the measurement as well as the simulation. Due to the shift in atomic column position of the defect site towards the bottom tungsten atom, the triangular shape is distorted and only a stronger electric field magnitude on the right and a slightly less pronounced electric field magnitude on the left of the defect site can be observed. As the experimental atomic column positions are incorporated in the simulation, this distortion of the triangular-shaped electric field magnitude at the defect site is also observed for the simulation. Thus, lattice distortions influence the measurable atomic electric fields.

As elaborated for the pristine monolayer, the absolute values of the electric field magnitude between measurement and simulation differ by a factor of about two. To quantitatively analyse the influence of the defect site on the local electric field magnitude for the individual atomic column, the mean value of the local field maxima around the individual atomic columns is calculated for each column type and compared to the local field maxima at the defect site. Close to the measured defect site, the electric field exhibit maxima which are about $|\vec{E}|^{\mathrm{Se}}_{\mathrm{exp.}} = (7.0 \pm 2.2) \cdot 10^{10}\,\mathrm{V/m}$, whereas the local field maxima at pristine selenium atomic columns exhibit values of $|\vec{E}|^{\mathrm{V1Se}}_{\mathrm{exp.}} = (3.4 \pm 0.4) \cdot 10^{10}\,\mathrm{V/m}$ which indicates a reduction in electric field magnitude of 48 %. A similar behaviour is observed for the corresponding simulation where a reduction of 53 % is observed. Thus, measurement and simulation are in good agreement and indicate a reduction in the electric field magnitude by about half compared to a pristine selenium atomic column in a WSe_2 monolayer. This finding is in

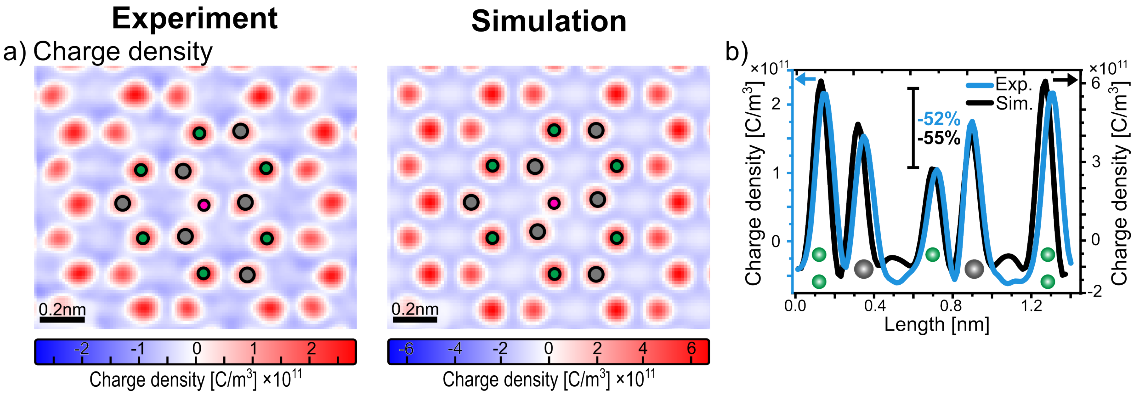

Figure 7.3: a) Charge density maps of the defect site for the measurement (left) and the simulation (right). The charge density maps are also provided in Figure 9.11 in the Appendix, without the coloured dots, to improve visibility of the individual charge densities of the atomic columns. b) Line profiles of the charge density integrated over the region marked by the blue and orange box in Figure 7.1 a). Here, the measurement is indicated as the blue line and the simulation as the black line. The atomic species are denoted by the coloured green and grey spheres for selenium and tungsten atomic columns, respectively.

agreement with the findings shown in Chapter 4.4.3 where the influence of the number of atoms stacked on top of each other was shown. Since the increase in the mean and maximum DPC signal is linear for two selenium atoms, the observed reduction in the electric field magnitude by half is reasonable. Slight deviations from exactly 50 % reduction are attributed to the influence of defocus and residual lens aberrations in the measurement. Not only the electric field is influenced by the missing selenium atom, but also the charge density distribution derived from the electric field distribution. Figure 7.3 a) displays the charge density maps of the measurement (left) and the simulation (right). Both maps show similar charge distributions with positive charge densities localized at the atomic column positions surrounded by the negative charge density. In contrast to the simulation, the positive charge density at the atomic column positions of the measurement arre not round shaped but slightly distorted without a recognizable preferred direction of distortion. This is due to residual lens aberrations already identified in the electric field magnitude map and the lattice distortions.

For a quantitative comparison, Figure 7.3 b) shows the line profiles of the charge density along the area indicated in the HAADF images in Figure 7.1 a). The charge density derived by the measurement is given by the blue line and the left y-axis. The charge density of the simulation is given by the black line and the right y-axis. Both show a similar behaviour with the higher charge density located at the selenium atomic sites as described for the pristine monolayer in Figure 4.1 g). Both line profiles show a reduced positive charge density at the position of the defect site. Compared to the neighbouring left selenium atomic columns, the charge density for the single selenium atom is reduced by 52 % in the measurement and about 55 % in the simulations. As the number of atoms in this atomic column, and thus also the projected atomic number, are both reduced by half, the observed reduction in positive charge density of about 50 % at this atomic columns is expected.

Interestingly, the line profile of the measurement (blue line) indicates a slightly increased

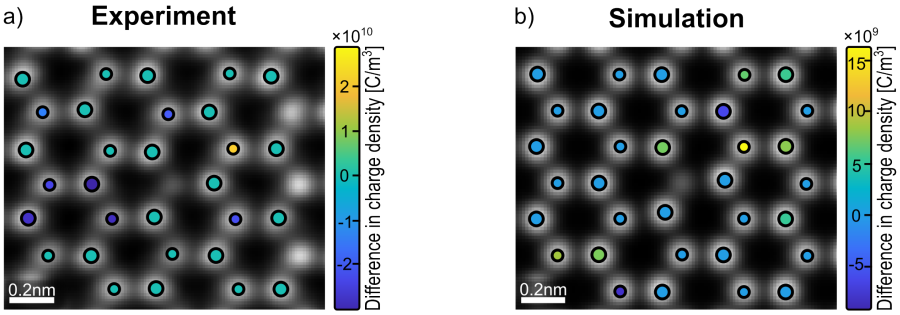

Figure 7.4: Difference in the positive charge density at the atomic column position for a) measurement and b) simulation of a single selenium vacancy in a WSe$_2$ monolayer. The difference is calculated in reference to the charge density of tungsten and selenium atomic column, respectively, of a nearby pristine region.

positive charge density for the nearest tungsten atom compared to the surrounding tungsten atoms. This might be reasonable since a missing atom could potentially change the screening of the neighbouring tungsten atoms. The overlap of the neighbouring potentials is therefore affected leading to a higher measured charge density for the tungsten atom closest to the selenium vacancy.

But to investigate the influence of the missing atom on the charge density of the neighbouring atoms, the difference in peak charge density at the atomic columns is calculated and displayed in Figure 7.4. As a reference, the maximum positive charge density of tungsten and selenium atomic columns of a nearby pristine region are determined for each atomic species separately and the respective mean values and standard deviations are calculated. A mean positive charge density of $\bar{\rho}_{2\mathrm{Se}} = (2.5 \pm 0.2) \cdot 10^{11}\,\mathrm{C/m^3}$ is determined for selenium atomic columns and a mean positive charge density of $\bar{\rho}_{\mathrm{W}} = (2.0 \pm 0.3) \cdot 10^{11}\,\mathrm{C/m^3}$ is determined for tungsten atoms. To identify significant changes in the positive charge density at atomic columns close to the defect, difference values smaller than the respective standard deviation are set to zero, as these are in the range of occurring variations and not necessarily induced by the vacancy.

The calculated difference in maximum positive charge density of the individual atomic columns is displayed in Figure 7.4. For both, measurement and simulation, the difference in the positive charge density at the atomic column positions shows no systematic increase or decrease of the positive charge density at the atomic columns close to the vacancy site. For the measurement, the three tungsten atomic columns closest to the vacancy show no significant difference compared to the positive charge density of tungsten atoms in a pristine lattice. In contrast to this, the simulation indicates one of these atomic columns with a slightly higher positive peak charge density compared to the mean positive charge density of tungsten atoms in a defect-free area (indicated by the positive difference and the green dot).

The atomic columns on the left of the vacancy site in the measurement additionally indicate a negative difference (dark blue dots) in the range of about $-2 \cdot 10^{10}\,\mathrm{C/m^3}$ which is approximately 10 % compared to the absolute positive charge density. These atomic columns, indicated by the blue dots, are not observed in the corresponding simulation

(Figure 7.4 b). Therefore, the reduction in positive charge density for these atomic columns is not caused by the defect itself but might be due to contaminations or defects, e. g. substitutional atoms.

Only one atomic column in the measurement and the simulation shows a significantly higher positive charge density in the vicinity of the defect compared to the corresponding charge density in a defect-free lattice. The selenium atomic column to the upper right of the defect indicated by the yellow dots exhibits a higher positive charge density. The positive charge density for this atomic column shows a higher positive charge density which is increased by about $1.5–2 \cdot 10^{10}\,\mathrm{C/m^3}$ for the measurement and the simulation. This indicates an about 8% higher positive charge density for this atomic column in case of the measurement and about 2% higher positive charge density in the case of the simulation. As the simulation is conducted with the experimental atom positions and with independent atom potentials, i. e. no charge redistribution due to the vacancy is included, the agreement between simulation and measurement is solely due to the change in atomic positions and the changed overlap of individual atomic potentials.

The vacancy itself does not significantly influence the measurable positive charge density at the atomic column positions which is especially evident from the negligible effect on the peak charge density of the three nearest tungsten atoms. This is expected as the positive charge density at the atomic column position is mostly dominated by the present atomic nucleus. Although the single selenium vacancy is not expected to significantly change the positive charge density at the atomic columns it might change the negative charge density distribution in the surrounding.

To investigate the influence of the vacancy on the local electric field magnitude and charge density in the direct vicinity of the defect site, Figure 7.5 depicts difference maps of the electric field magnitude and charge density. These difference maps are obtained by subtracting the electric field distribution of the defect area pixel by pixel from that of a pristine area nearby. In contrast to the previously shown difference in the maximum positive charge density at the atomic column position, these maps show the difference for each pixel in reference to a corresponding pristine region. Before the pixel-wise subtraction, the electric field distributions are aligned based on the corresponding HAADF images using the non-rigid registration algorithm described in Chapter 3.3.

Figure 7.5 a) and b) display the difference maps of the electric field magnitude for the measurement and the multislice image simulation, respectively. The difference maps are calculated by subtracting the electric field magnitude map of a nearby pristine monolayer from the electric field magnitude map of the defective area. The pixel-wise registration of the two maps was conducted using the non-rigid alignment algorithm as described in Chapter 3. The atomic column positions for selenium and tungsten are indicated by the green and grey dots, respectively. The difference between the electric field magnitude of the defective area and a nearby pristine area is given in absolute values where negative values correspond to a reduced electric field magnitude in the defective image compared to the electric field magnitude of the corresponding pristine image. Positive values of the difference indicate a higher electric field magnitude at the defect site compared to a pristine area. At

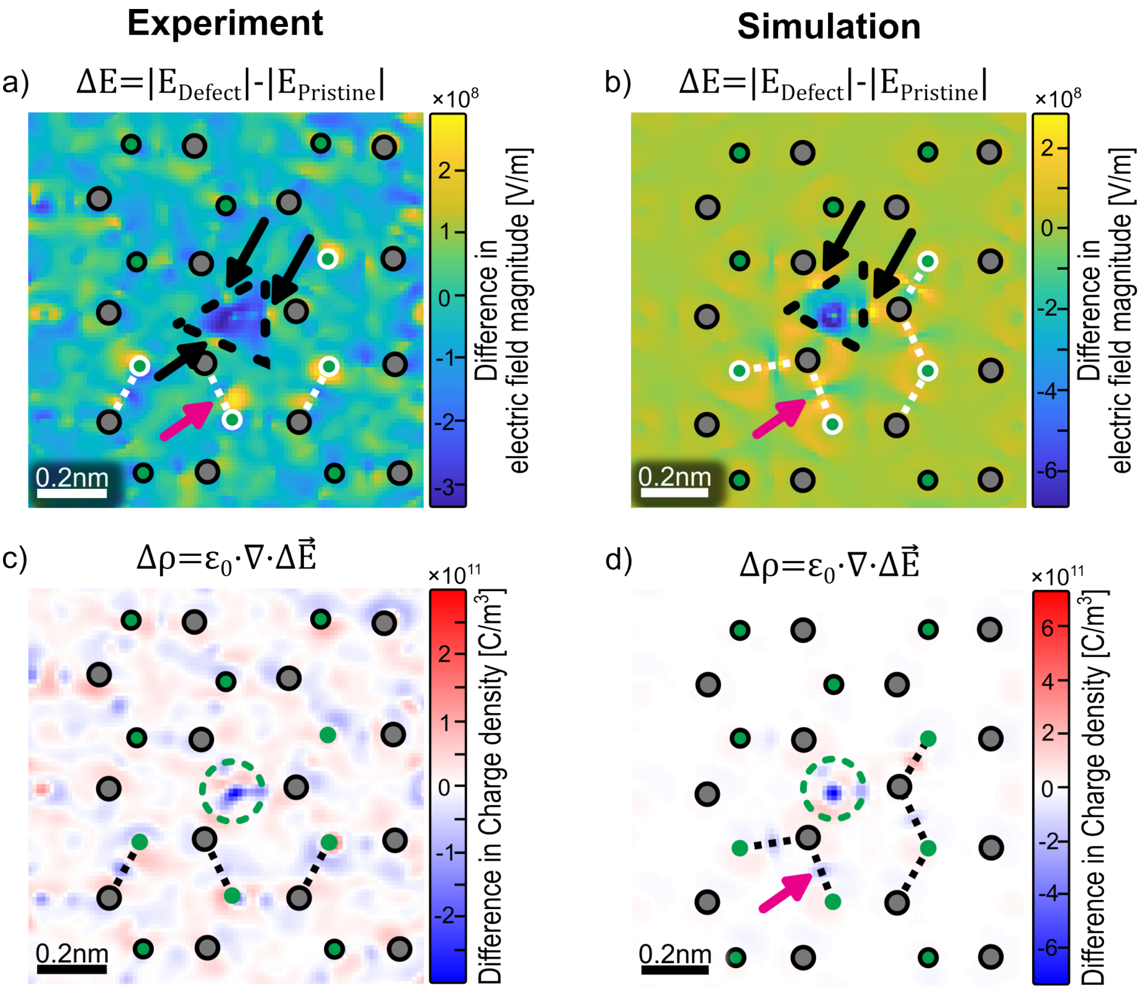

Figure 7.5: Difference maps of the electric field magnitude for a) the measurement and b) a corresponding multislice image simulation. c) and d) show the difference in charge density for the measurement and the simulation. The difference in charge density is calculated using Equation 2.13 and the difference in electric field $\Delta\vec{E}$. The atomic column positions are marked by green and grey dots for selenium and tungsten atomic columns, respectively. The single selenium vacancy is indicated by the green dashed circle in the charge density map.

the position of the defect site in the difference map of the electric field magnitude maps in Figure 7.5 a), the difference map shows a pronounced region with a triangular shape (marked by the black dashed triangle) which indicates a reduced electric field magnitude of the defect compared to the pristine lattice. Close to the three adjacent tungsten atomic columns an increased electric field of the defective area compared to the pristine is observed and highlighted by the three black arrows in Figure 7.5 a). Furthermore, the difference maps derived from the measurement show variations of the absolute difference in field magnitude even away from the defect. These arise due to lattice distortions and are possibly also influenced by the registration of the defective and pristine image. However, the observed difference in electric field distribution at the position of the defect is also visible in the difference maps of the corresponding multislice image simulations shown in Figure 7.5 b). Here the triangular shape is less pronounced (marked by the black dashed triangle) but still visible. Furthermore, due to the perfect alignment of the simulated images, the difference in the outer region of the image approaches zero as no lattice distortions are present and the registration of the two images is more accurate.

For the 12 nearest neighbours of the defect site the experimental atomic column positions are considered in the simulation to account for changes in the field distribution due to lattice distortion. Despite the local decrease in the electric field magnitude also two spots with higher electric field magnitude are observed in the simulation (marked by the black arrows). This contrasts the measurement, in which only two instead of three spots of positive difference (stronger field magnitude at the defect) are observed. This difference between simulation and measurement possibly arises due to an erroneous determined atomic position of the remaining selenium atom as the HAADF intensity is smeared out at the defect site and slightly elongated toward one of the tungsten atoms (Figure 7.1 a) and in Figure 9.11 in the Appendix without the coloured dots).

Furthermore, the difference map derived from the simulation shows a pronounced circular feature of reduced electric field magnitude within the triangular-shaped region. This feature is located directly at the position of the remaining single selenium atom. The indicated strong reduction in the electric field magnitude arises from the fact that close to the atomic column position the electric field magnitude is the highest and therefore the difference caused by the missing selenium is high. In addition, the missing atom also causes a change in the electric field magnitude which results in the triangular shaped area corresponding to a reduction of the electric field magnitude not only at the position of the atomic column but also in areas extending towards the adjacent atomic columns.

In addition to the changed electric field magnitude at the position of the defect site, the electric field distribution is also altered in the vicinity of the surrounding atomic columns. Especially in vicinity of the next selenium atomic columns in the bottom part of the difference map the electric field magnitude changes drastically. These selenium atomic columns are marked by a white edge colour in Figure 7.5 a) and b). For these selenium atomic columns, the difference in electric field magnitude changes along the connecting directions between the next selenium and tungsten atoms (whited dashed lines in Figure 7.5 a) and b). In the simulation, pronounced changes in the electric field magnitude are found along the connecting directions of the nearest selenium atoms and the tungsten atoms adjacent to the defect site. Around the atoms an enhanced electric field is observed which is indicated by the yellowish pixels, and along the connecting axis a strongly reduced field magnitude (blue pixels) is observed as exemplarily indicated by the pink arrows. These features in the electric field magnitude difference map are also observed in the measurement and arise due to the distorted lattice and the shift of the three tungsten atoms away from their lattice position in a pristine lattice. In the measurement, however, the peaks of difference are less distinct and separated but still visible, even though the measurement generally exhibits more variation of the difference in electric field magnitude due to distortions in the vicinity of the shown area (exemplarily marked by the pink arrow in Figure 7.5 a) and a non-optimal alignment of the atomic columns. As the features of the measurement as well as the corresponding simulation are very similar and the fact that the experimental atomic column position are assumed for the simulation with the independent atom model, these features do not arise due to charge redistribution but presumably due to the lattice distortion.

Figure 7.5 c) and d) show the corresponding difference maps for the charge density $\Delta\rho$ distribution which are calculated using the difference in electric field distribution $\Delta\vec{E}$ and not the difference of the individual charge density maps (to account for directional changes in the electric field distribution). In case of an equal charge density distribution between defective and pristine areas, the difference would contain only zero values corresponding to white pixels. Any change of the charge density distribution caused by the defect leads to a non-zero difference which represented by either red or blue pixels depending on the sign of the difference. Thus, the difference maps of the charge density can be interpreted as the defect-induced charge density. Overall, the difference map of the measurement shown in Figure 7.5 c) shows more changes in the defect-induced charge density distribution than the simulation presumably due to lattice distortions. However, significant changes in the vicinity of the defect site are observed for both. The two difference maps show a pronounced negative defect-induced charge density difference. This is particularly visible at the position of the vacancy site which is expected due to the missing selenium atom and the resulting less positive charge density at this position compared to a pristine selenium atomic column (Figure 7.3). This defect-induced negative charge difference is circular shaped for the simulations and elongated towards the neighbouring tungsten atoms for the measurement. The simulation shows two separated negative charge density differences at the top and right tungsten atomic columns which arise do to the reduced overlap of electric fields. In the measurement, these two local negative charge differences merge with the negative charge difference at the vacancy site and are thus not clearly separated. As the defect site misses an atomic nucleus the defect-induced negative charge density difference values are in good agreement with the observed impact on the charge density at the defect site shown in Figure 7.3 a) and therefore indeed indicate a reduced positive charge density compared to the pristine lattice. Furthermore, both charge density difference maps show a slightly positive difference for the surrounding region around the defect.

The difference in charge density observed in the vicinity of the selenium atomic columns marked by white edge colour in the corresponding difference map of the electric field magnitude are not an artefact but arise due to the shifted atomic column positions and the resulting shift of the positive charge density of the atomic nucleus. These atomic columns are indicated without any edge colour in the charge density difference maps in the simulation and the measurement. In the measurement, these features are not clearly visible and can not be distinguished between the distortions all over the area. A region of this less negative charge density compared to the pristine lattice is marked in both by the pink arrow in the difference map derived by the simulation.

Quantitatively, the influence of the shifted atomic column positions on the defect-induced difference in charge density is small compared to the influence of a missing atom in an atomic column. This is expected, as a shift in the atomic column position might slightly alter the overlap of electric fields, but the interaction with the electron beam is still dominated by the atomic nucleus. Thus, a missing atomic nucleus influences the actual charge density distribution derived using STEM-DPC, although the influence is localized to the defect site itself.

Although both types of difference maps are quantitatively derived and give absolute values of the difference between defective and pristine area, the interpretation of these absolute values is not straight-forward, but potentially indicates a significant change of the local specimen potential which could promote adatom trapping or optical recombinations. Therefore, the following chapter focuses on the quantitative interpretation of difference maps in electric field magnitude for three different point defects.

Section summary

- A missing selenium atom in a WSe_2 monolayer alters the electric field and charge density distribution. It leads to a reduced electric field and positive charge density at the defect site compared to a pristine selenium atomic column in a WSe_2 monolayer.
- Although no atomic relaxation of the lattice in the vicinity is expected, lattice distortions are observed and assigned to strain and specimen drift.
- The atomic electric field distribution is highly sensitive to lattice distortions.
- A single selenium vacancy does not influence the observed positive charge density directly at the neighbouring atomic columns. The position of the atomic nuclei dominate the observed charge density distribution.
- The spatial distribution of the difference in electric field magnitude between the defective area and a pristine area shows a triangular-shaped region with locally reduced electric field magnitude compared to the pristine lattice.
- Local variations in the electric field magnitude apart from the defect site arise from lattice distortions.
- The spatial distribution of the difference in charge density highlights that the charge density is mostly influenced by the position of the atomic nuclei and not by charge redistributions.

7.2 Comparison of different Point Defects in a WSe_2 Monolayer

Although the single selenium vacancy is the most prominent defect in a WSe_2 monolayer, as it exhibits the lowest formation energy, double selenium vacancies can also be observed, albeit they do not occur as frequently. Since for a selenium double vacancy, two selenium atoms are missing from the same atomic column, in a monolayer of WSe_2 this defect leads to a completely missing selenium atomic column. Thus, the influence on the electric field distribution is expected to be even stronger than for the single selenium vacancy.

Therefore, different point-like vacancies in a WSe_2 monolayer are investigated by STEM-DPC including a quantitative comparison of these defects and their impact on the local electric field distribution.

Figure 7.6 shows the STEM-DPC measurements of a single (first column) and a selenium double vacancy (middle column) as well as a double vacancy occupied with a substitutional atom (third column). The distinction between the empty double vacancy and the occupied double vacancy is part of the following discussion. The selenium single vacancy depicted in the first column is the same as discussed in the previous Chapter 7.1.

Figure 7.6 a-c) depicts the individual HAADF images of the three different defects with the atomic column positions and types marked by green and grey dots for selenium and tungsten, respectively. Each of these defects corresponds to an individual DPC measurement and therefore differences in the HAADF image contrast are possibly due to the manually adjusted gain and offset settings of the HAADF detector. It can also be recognized by the HAADF image contrast that the individual measurements were subject to different residual lens aberrations.

The HAADF image of the first double vacancy shown in Figure 7.6 b) show bright intensities at the atomic column positions which are slightly diagonally elongated (from the top left to the bottom right). In accordance with the influence of astigmatism described in Chapter 4.2, this elongation is due to residual two-fold astigmatism.

A similar behaviour is observed for the second double vacancy shown in Figure 7.6 c), where the bright image contrasts at the atomic columns are slightly elongated in a different direction: from top right to the bottom left. Still, for both double selenium vacancies, the defect is clearly identified by the lack of HAADF intensity in the centre of the shown HAADF images.

Vacancy-type defects might introduce a local change in the atomic column positions due to a structural relaxation close to the defect. Therefore, the atomic column positions identified by the HAADF images in Figure 7.6 a-c) are used to investigate possible changes in the atomic structure introduced by the different defect types. As all three measurements were prone to specimen drift, a drift correction is applied for the structural analysis but not shown in the DPC analysis as it might introduce artefacts in the electric field distribution due to the interpolation between the atomic column positions. The drift-corrected HAADF images used for the structural analysis are given in Figure 9.16 in the Appendix 9.9.

As previously discussed, the missing selenium atom does not significantly alter the W-to-W

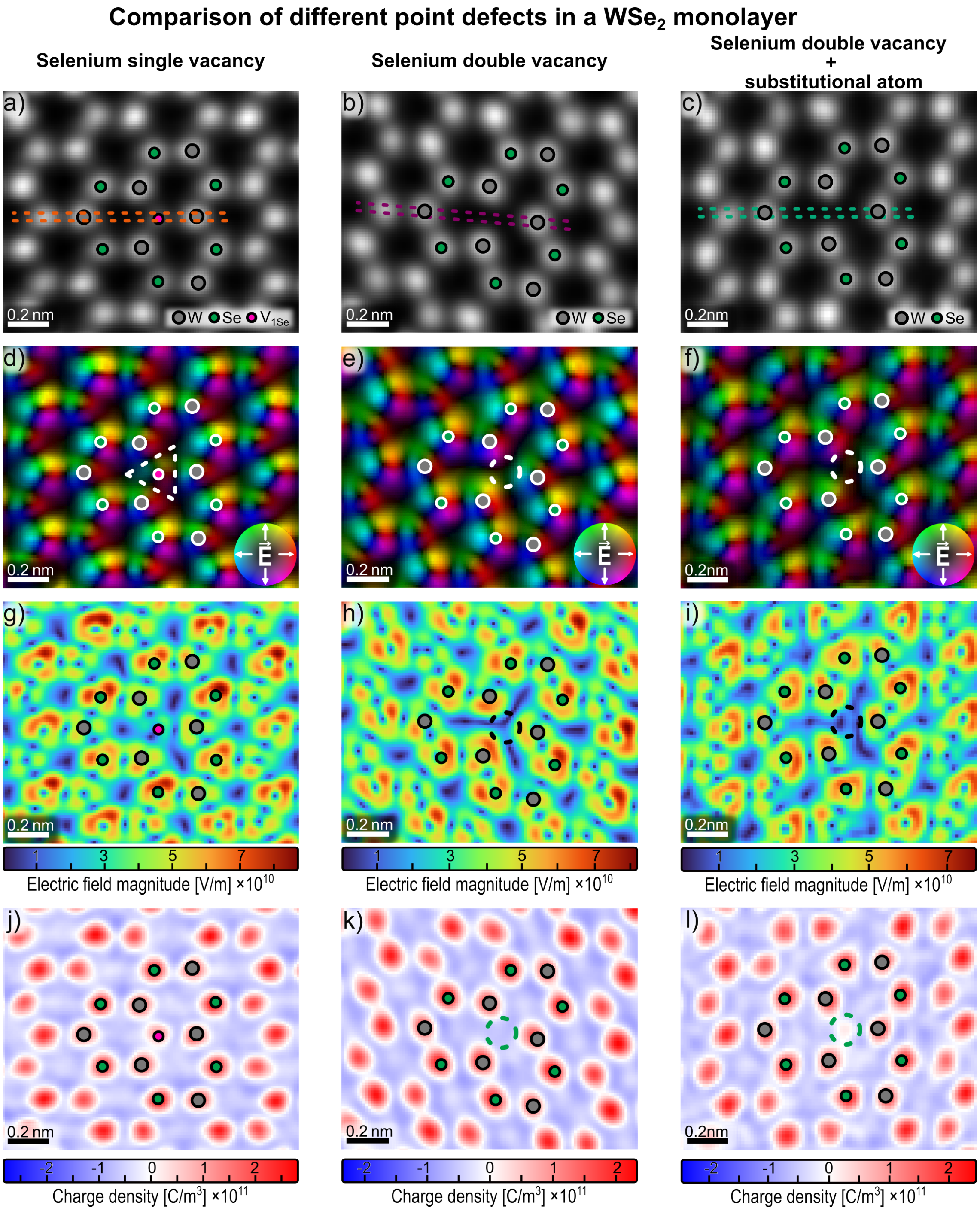
Comparison of different point defects in a WSe_2 monolayer

Selenium single vacancy

Selenium double vacancy

Selenium double vacancy + substitutional atom

Figure 7.6: Comparison of different point defects in a WSe_2 monolayer. From left to right three different point defects are displayed, namely a selenium single vacancy, a selenium double vacancy, and a selenium double vacancy with a residual substitutional atom present at the position of the missing atomic column. a-c) show the HAADF images for each point defect with the atomic column positions marked by green and grey dots for selenium and tungsten atomic columns, respectively. d-f) depict the corresponding colour coded DPC images and g-h) the electric field magnitude maps. j-l) display the derived charge density maps.

distance of the three adjacent tungsten atoms compared to the ideal distance in a defect-free lattice. Thus, an atomic relaxation of the atomic structure due to a single selenium vacancy is not observed.

In a comparable manner, the structural relaxation possibly introduced by the two double vacancies is investigated in the following. For both, the mean W-to-W distance of all tungsten atoms in the scan area is calculated and the W-to-W distances of the three tungsten atoms close to the defect site are determined.

For the first double vacancy shown in Figure 7.6 b), a mean W-to-W distance of the three tungsten atoms adjacent to the defect is determined to $\bar{d}^{\mathrm{V2Se}}_{\mathrm{W-W}} = (2.89 \pm 0.04)\,\text{Å}$. Thus, the distance of the three tungsten atoms close to the defects is reduced compared to the ideal distance ($a = 3.29\,\text{Å}$) in a pristine lattice, indicating an atomic relaxation of the three tungsten atoms towards the defect site. This observation is comparable to the structural relaxation predicted by DFT calculations of a missing selenium atomic column in a WSe_2 monolayer shown in Ref. [41, 228, 229]. The DFT calculations show that the full atomic relaxation reduces the W-to-W distance between the adjacent tungsten atoms even stronger, resulting in a mean distance of the three atoms of about $2.76\,\text{Å}$ [41]. Thus, the atomic relaxation observed for the selenium double vacancy shown in Figure 7.6 b) is less than theoretically predicted but still evident. Possible reasons for the reduced inwards relaxation of the neighbouring atoms is the migration of defects, especially under electron irradiation, which is a highly dynamic process [182, 230]. Since STEM images only take a snapshot of a current state, it might be possible that the defect was imaged during a migration process. Furthermore, also other defects in the vicinity might influence the structural relaxation of the tungsten atoms due to strain.

For the second selenium double vacancy shown in Figure 7.6 c), a comparable behaviour is observed with a reduced W-to-W distance of the three tungsten atoms close to the defects. The mean distance between these three atoms is determined to $\bar{d}^{\mathrm{V2Se+X}}_{\mathrm{W-W}} = (2.96 \pm 0.09)\,\text{Å}$, which is significantly less than the ideal distance in a pristine lattice. Thus, a structural relaxation is also observed for the second double vacancy. In the limits of the standard deviations, both double vacancies show a similar relaxation.

Based on the DFT calculations in Ref. [41], a reduced atomic relaxation as observed for both defects can also be introduced by additional atoms, such as oxygen atoms, filling up a selenium double vacancy. It is shown that, atoms inside the defect prevent a full atomic relaxation resulting in a mean distance between the three tungsten atoms close to the defect site of about $2.92\,\text{Å}$ [41]. Thus, the here shown selenium double vacancies are presumably occupied with light contamination atoms not visible in the HAADF signal. Since DPC imaging is more sensitive to heavy and light atoms than HAADF imaging, the following analysis of the electric field and charge density distribution gives a greater insight into possible residual atoms in the defect.

The colour-coded DPC images for the three different defects are depicted in Figure 7.6 d-f). Despite the presence of residual lens aberrations which were deduced from the HAADF images, the corresponding DPC images still show the expected rotational symmetric electric field distribution around each individual atomic column for each measurement.

The electric field distribution of the single selenium vacancy shows a rotational symmetric electric field distribution comparable to the reference colour wheel at the position of the defect site (marked by the white dashed triangle in Figure 7.6 d). For the selenium double vacancies, a similar field distribution at the position of the missing atomic column is not visible (marked by the white dashed circle in e) and f). This is expected as no selenium atom is present at the defect site meaning that the electrons of the electron beam can not be deflected towards the position of the missing atomic column. Instead, a local field minimum is observed with small electric field components originating from the adjacent tungsten atomic columns which are no longer suppressed in the direction towards the defect site by the selenium atomic column. However, if contamination atoms are present in the defect as indicated by the reduced atomic relaxation, a weak but still visible electric field distribution at the defect site is expected as atomic cores would be present. Thus, the electric field magnitude maps in Figure 7.6 h) and i) are analysed. The position of the missing selenium atomic column is marked by the black dashed circle in both images.

A reduced electric field magnitude due to the missing selenium atomic column is evident in the electric field magnitude maps for both double vacancies. Qualitatively, the reduction of the electric field magnitude is comparable to the field distributions observed in Ref. [35, 38]. Up to this point, no significant difference between the two selenium double vacancy shown in the middle column and the right column in Figure 7.6 has been addressed. Besides the different residual lens aberrations, which lead to slight distortion of the triangular shape of the atomic electric field distributions, both HAADF and DPC images of the two double vacancies look similar. The corresponding charge density distributions shown in Figure 7.6 k) and l) however reveal a significant difference between the two double vacancies. Both charge distributions show a delocalized negative charge density and positive charge density features localized at the position of the atomic columns. The selenium double vacancy is here marked by the green dashed circle for both defects. The charge density of the double vacancy shown in k) indicates a negative charge density at the position of the missing atomic column. This can be expected due to the fading of electric field features from the neighbouring atoms. In contrast to this, the charge density distribution of the defect shown in l) indicates a slightly positive charge density at the position of the missing atomic column. This is an unexpected finding for a presumed selenium double vacancy as a positive charge density indicates a positively charged atomic nucleus located within the defect, while the HAADF image shows no bright image contrast at the position of the defect site. Therefore, the positive charge density at the selenium double vacancy is presumably due to a substitutional atom at the defect. The presence of the substitutional atom could potentially also explain the observed W-to-W distances and the reduced atomic relaxation compared to the predicted relaxation of an empty double vacancy [41]. As this atom is not observed in the HAADF image it is presumably a low-Z atom.

To ensure that this positive charge density is not introduced by a combination of different lens aberrations or other experimental effects, all three defects are simulated using the experimental atomic column positions and ideal imaging conditions (Figure 9.12 in the Appendix). For the simulation of the selenium double vacancy which is filled with a substitutional atom, an oxygen atom is placed at the defect site of the lower selenium slice. For the simulation of the occupied selenium double vacancy, oxygen is chosen as a substitutional atom as it is among the most common atomic species present in the TEM column even under high vacuum conditions and can be in cooperated in 2D TMDs under electron irradiation and alter the defect formation process [231, 232]. Other possible atomic species, such as nitrogen or carbon, are not simulated here since the change in DPC signal is small for light atoms (between Z=6 and Z08) as shown in Chapter 4.4.1. The images from the multislice image simulation are given in the Appendix 9.8 and details on the simulation are compiled in Table 9.13 in the Appendix.

The HAADF and DPC images of the measurements and simulations, as well as the electric field magnitude maps of the three different defects are in good agreement. Furthermore, the charge density distributions of the simulations of an empty and a filled selenium double vacancy reflect the same behaviour as observed in the corresponding measurements (Appendix 9.8).

To analyse these three defects quantitatively, line profiles of the HAADF intensity and charge density are taken from the measurements and the simulations of all three defects. The line profiles are integrated over the regions marked by the orange, purple and green boxes indicated in the HAADF images in Figure 7.6 and Figure 9.12.

Figure 7.7 shows the integrated line profiles of the HAADF intensity and the charge density distribution for the measurements and the corresponding simulations. In addition to the three defects, an integrated line profile over a similar area of a nearby pristine monolayer is plotted as a reference. The HAADF line profiles for the three different defects from the measurements and the simulations are shown in Figure 7.7 a) and b), respectively. The spheres in all line profiles indicate the type of the atomic columns determined from the HAADF intensity. For the single selenium vacancy, the HAADF intensity is discussed in detail in the previous Chapter 7.1 and here only used for comparison (orange line). Comparing the HAADF line profiles of the assumed empty double selenium vacancies indicated by the purple line barely shows any HAADF intensity at the position of the defect in Figure 7.7 a). A slight increase in the HAADF intensity can be observed for the presumably filled double vacancy (green line). A local maximum of HAADF intensity is evident, which is shifted from the position of the defect site. This local maximum can partially be explained by the HAADF intensity of the neighbouring tungsten atomic columns extending into the line profile region due to atomic relaxation, probe size and generally thermal lattice vibrations which lead to a broadening of the atomic column intensity. This assumption is supported by the corresponding line profiles of the multislice image simulations. These line profiles in Figure 7.7 b) also show an almost identical HAADF intensity profile for both, the selenium double vacancy and the partially filled double vacancy. However, no minor increase in the HAADF intensity at the defect site is observed in the simulations. Since the simulations are conducted without taking any thermal vibrations into account, the observed minor intensity increase identified in the measurement can be due to the neighbouring atomic columns or a larger probe size in the measurements compared to the simulations. Thus, the HAADF image intensity is not suitable to further identify the origin of the

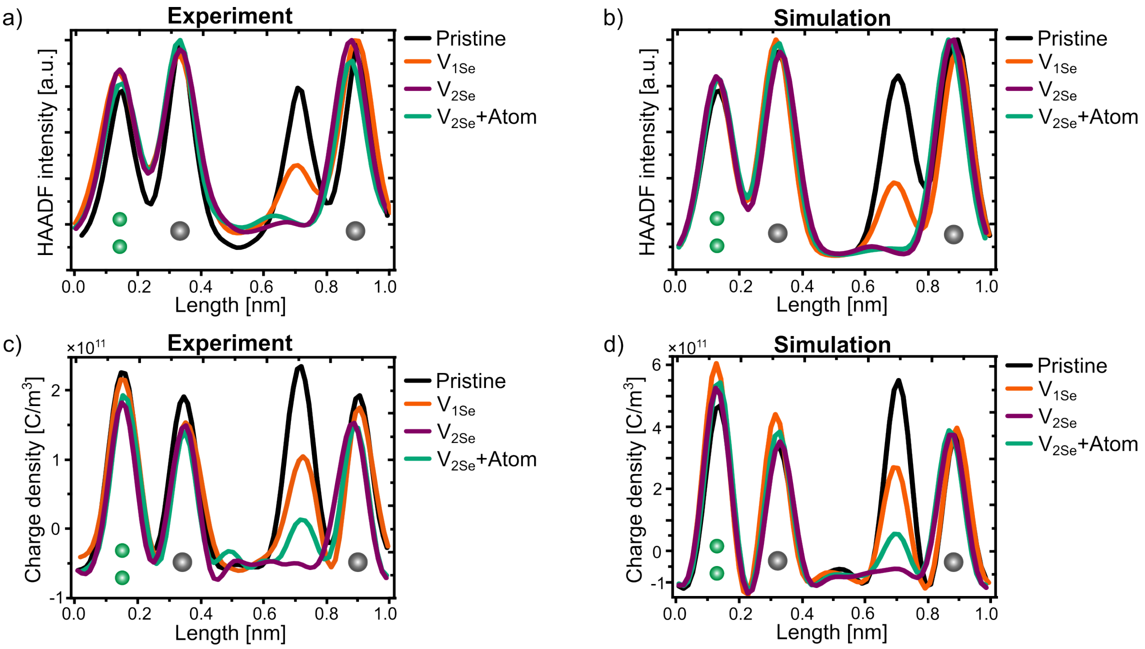

Figure 7.7: a) Line profiles of the normalized HAADF intensity integrated over the regions indicated by the dashed boxes in Figure 7.6 a-c) for the three observed vacancy-type defects and b) the HAADF line profiles of corresponding multislice image simulations shown in Figure 9.12. c) & d) Corresponding line profiles of the charge density for the same area as the HAADF line profiles. The black line corresponds to the line profile of a pristine lattice and is used as a reference. For the multislice image simulation of the selenium double vacancy with a substitutional atom, a single oxygen atom is placed at the position of the upper missing selenium atom.

observed positive charge density found in Figure 7.6 l) for the selenium double vacancy. Figure 7.7 c) and d) depict the integrated line profiles of the charge density distribution for the measurements and the simulations of the three defects and a pristine lattice. The charge density of a pristine lattice is represented by the black line showing the four peaks of positive charge density which correspond to the two W-Se dumbbells. The charge density line profile of the single selenium vacancy is given by the orange line and reveals a positive charge density at the defect site which is reduced by about 50 % compared to a pristine selenium atomic column. The line profile of the selenium double vacancy is given by the purple line which exhibits a plateau of only negative charge density values in the vicinity of defect site. The second selenium double vacancy is indicated by the green line and shows a small but significant peak in the charge density profile which implies the presence of a positive charge density at the defect site. The positive charge density at the position of the defect is lower than the positive charge density of the single selenium vacancy (orange line). Thus, a remaining selenium atom at the position of the defect can be excluded and the present atom presumably is of a lower atomic number than selenium.

These findings are in great agreement with the corresponding line profiles of the multislice image simulations shown in Figure 7.7 d). Based on charge density distribution, the two double vacancies can be identified as two different types of defects. The selenium double vacancy in the middle column of Figure 7.6 is presumably an empty selenium double vacancy, whereas the second selenium double vacancy shown in the right column of Figure 7.6 is presumably filled with a low-Z atom. The finding of the positive charge density at the defect site and the assumed presence of an additional low-Z atom is also in good agreement with the reduced structural relaxation observed by the atomic column positions in the HAADF image and the corresponding DFT calculations [41]. However, for the empty double vacancy a stronger atomic relaxation than observed is expected from the DFT calculations. Since no positive charge density is found at the defect site, the occupation of the defects is unlikely, however, defect migration and strain in the area might lead to the observed W-to-W distances.

It is shown that a detailed analysis of defects using DPC, and especially the derived charge density distribution, gives a greater insight into the defect structure and possible substitutional atoms can be detected, which are not evident by HAADF imaging.

Due to the non-monotonic Z-dependency of the DPC signal and its relation with the charge density (Chapter 4.4), a direct determination of the atomic species of the substitutional atom is not possible from the STEM-DPC signal or the charge density at the defect site. Still, comparing the charge density ratio of measurement and simulation should allow for an estimation as residual lens aberrations of the present atomic species. Therefore, to further analyse the filled double vacancy, the charge density ratios of the maximum positive charge density at the defect position and the next pristine selenium atomic column are calculated for both, the measurement and the simulation. The charge density ratio of the maximum charge at the defect position in reference to the maximum charge density of the neighbouring selenium atomic column is about 0.08 for the measurement and of about 0.1 for the simulation with an oxygen atom residual at the defect site. These low ratios can also be seen in the line profiles, indicating an order of magnitude lower charge density at the defect position compared to the maximum charge density at selenium atomic columns. The strongly reduced positive charge density at the defect site emphasises the presence of a low-Z atom. Furthermore, the calculated ratio from the simulation, which takes the presence of a single oxygen atom into account, is higher than the ratio calculated from the measurement. Thus, the charge density induced by the single oxygen atom might be too high and therefore an atom with a lower Z atom like nitrogen or carbon is probably present.

The analysis above highlights the sensitivity of STEM-DPC to image light atoms and the possibility to detect substitutional atoms which is exploited for the first time to estimate the atomic number of substitutional atoms.

As other STEM techniques such as energy-dispersive X-ray spectroscopy and electron energy-loss spectroscopy typically do not exhibit a sufficient sensitive for single atom detection and also cause ionisation damage resulting in a loss of the low-Z atom, phase-retrieval methods such as STEM-DPC as well as ptychography are the only techniques to detect single low-Z atoms. To investigate how these different defects locally influence the electric field distribution of the material, Figure 7.8 shows difference maps of the electric field magnitude. The difference maps $\Delta|\vec{E}(\vec{R})|$ are calculated by subtracting the electric field magnitude from a pristine area $|\vec{E}_{\text{Pristine}}(\vec{R})|$of the electric field magnitude of the defective area $|\vec{E}_{\text{Defect}}(\vec{R})|$ for each pixel $\vec{R}$. Prior to subtraction, the images are aligned using the non-rigid registration algorithm by A. B. Yankovich et al. [184] to exclude the influence of lattice distortions originating from the defect (Chapter 3.3). For a straightforward interpretation of these differences in the electric field magnitude, the relative values in reference to the electric field magnitude of the pristine area instead of the absolute difference values are calculated for each pixel. This calculation of the relative difference $\Delta|\vec{E}|/|\vec{E}_{\text{Pristine}}|$ can be interpreted as the relative change introduced by the defect. Negative values correspond to reduced electric field magnitudes of the defective area compared to a defect-free area. Positive values correspond to a higher electric field magnitudes observed in the electric field distribution of the defect area compared to the pristine area. For all difference maps, the same colorbar limits are used. It is important to note, that this colormap is clipped between -1 and +3 although the individual pixels in the six different maps peaked up to a relative difference of about 10. These pixels with high relative difference are located at the high symmetry points and arise due to a slight misalignment of the two images during the non-rigid registration. To enhance the visibility of the other features induced by the defect, the cut-off limit at a value of +3 is chosen. Additionally, it is the maximum value of the relative difference for the measured single selenium vacancy. Thus, the interpretation of these relative difference maps needs to be done carefully and the corresponding non-clipped relative difference maps and the absolute difference maps of the electric field distribution are given in the Appendix 9.8.1.

To illustrate the influence of the defect on the electric field distribution Figure 7.8 shows the clipped relative difference maps of the electric field magnitude for the three different defects discussed previously. The top row of Figure 7.8 depicts the relative difference maps of the measurements and the bottom row shows the corresponding difference maps of the multislice image simulations. Figure 7.8 a) and b) depict the relative difference maps for the single selenium vacancy discussed in Chapter 7.1. Instead of the absolute difference values shown in Figure 7.5 a) and b), here the relative difference maps enable a more intuitive interpretation of the changes in the distribution of the electric field magnitude induced by the defect. Negative values (blue pixels) correspond to a lower electric field magnitude in the defect image compared to the one of a pristine area. Positive values (yellow pixels) indicate a higher electric field magnitude in the field distribution of the defect area compared to the pristine area. The relative difference map at the position of the defect site shows a triangular region of reduced electric field magnitude comparable to the feature as already described in the absolute difference map in Figure 7.5 a). Compared to the pristine area, the relative change is about -0.94 for the pronounced tip of the triangle and only of about 0.5 for other regions of the triangle. This is in good agreement with the corresponding relative difference derived from the simulation of a single selenium vacancy which shows a comparable triangular-shaped region with decreased field magnitude. In contrast to the pronounced tip of the triangular-shaped feature in the measurement, the simulation exhibits a pronounced feature of negative difference at the lower left adjacent tungsten atom (white arrow in Figure 7.8 b). The decrease in electric field magnitude of the defect site at this position is about -0.81 and therefore smaller than the decrease observed in the measurement. In addition, the overall change of the triangular feature in the simulation is only of about 0.3.

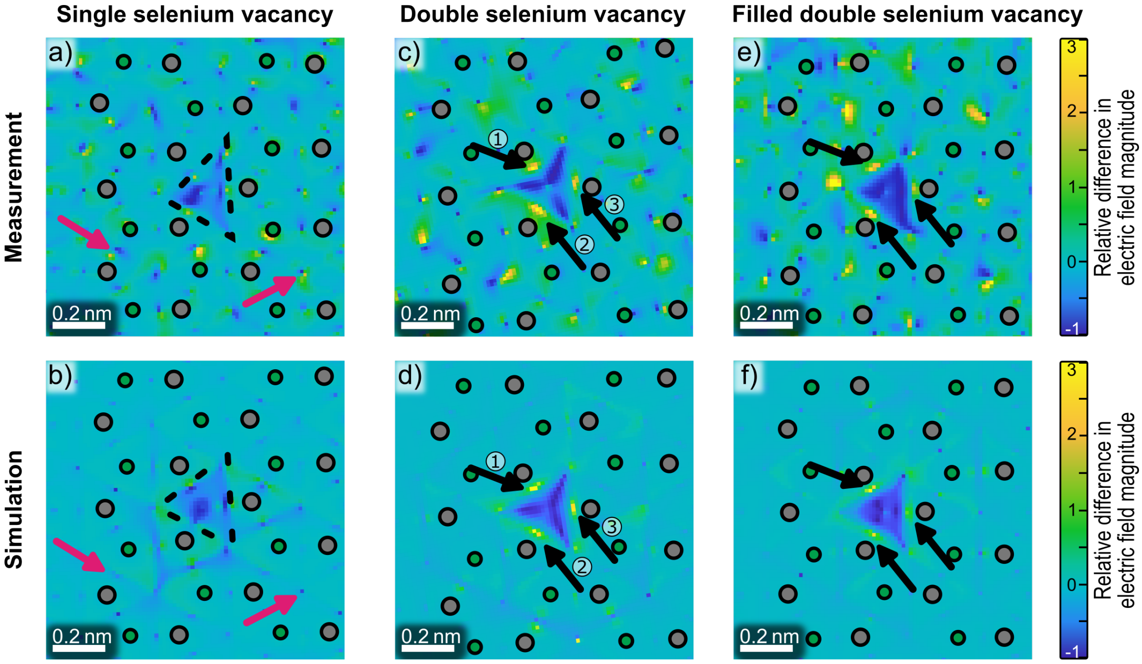

Figure 7.8: Relative difference maps of the electric field magnitude in the vicinity of the three point defects. The top row (a,c,e) shows the relative difference in the electric field magnitude for the measurement. The bottom row (b,d,f) shows the corresponding difference maps derived from the multislice image simulation of the three different defects. From left to right the relative difference in electric field magnitude are shown for a) and b) a single selenium vacancy, c) and d) an empty selenium double vacancy, and e) and f) a selenium double vacancy filled with a substitutional atom. The atomic column positions are marked by green and grey dots for selenium and tungsten atomic columns, respectively. To compare these six different images the colorbar is the same for all and shown on the left. The limits of the colorbar are set between -1 and +3. For more details the reader is referred to the main text.

Furthermore, the relative difference maps of the measurement and the simulation indicate a strong change in the electric field magnitude at high symmetry positions such as the centre of hexagonal W-Se rings or the middle between two atomic column positions. These positions are exemplarily marked by the pink arrows in Figure 7.8 a) and b). Although the simulation purely indicates decreased electric field magnitudes, the measurement often exhibits pairs of increased and decreased electric field magnitudes at these positions. As these features presumably arise due to the non-rigid registration and are not introduced by the presence of the selenium vacancy itself. Due to lattice and scan distortions in the measured electric field distribution, these features are enhanced in the measurement compared to the simulation, still, they are clearly visible also in the simulation.
Figure 7.8 c) and d) depict the relative difference maps of the empty selenium double vacancy for the measurement and simulation, respectively. In both, a decrease in the electric field magnitude at the defect position is observed. However, in contrast to the single selenium vacancy this region of decreased field magnitude is not triangular-shaped but exhibits a rotor-like shape with its tips pointing to areas between the three adjacent tungsten atoms. At the position of the missing selenium atomic columns, a significantly reduced relative electric field magnitude difference is observed. This is due to the fact that

an electric field can not be measured at the exact position of the atomic columns as the present electric field components at such positions are ideally only parallel to the incident electron beam direction. The rotor-like feature itself shows three pronounced regions with strongly reduced electric field magnitude of the defective image compared to a pristine area. A comparable feature was also observed in literature for a missing selenium atomic columns in a WSe_2 trilayer [41] and for a missing boron atomic column in few-layers h-BN [35]. The rotor-like feature arises due to the electric field of the adjacent three tungsten atoms which extends into the defect region as no opposing electric field is present anymore due to the missing selenium atomic column. Within this rotor-like region, the electric field magnitude of the defect area is reduced by up to 99% compared to the field magnitude of the pristine area for the simulation and up to about 96% for the measurement. However, these values peak close to the tips of the three rotors.

In the vicinity of the three adjacent atomic columns, areas with a local increase in the electric field magnitude are found. For the measurement and the simulation, the three spots with increased electric field magnitude are marked by black arrows numbered with 1, 2, and 3. In the measurement, the three spots do not indicate an equal increase in the electric field magnitude introduced by the defect but the spot labelled with the number 3 has the smallest impact with a relative increase of about 2.2. The other two spots labelled with number 1 and 2 have a relative increase of 6.3 and of 5.3, respectively. The three spots are similarly observed in the corresponding simulation. There the three spots show a local increase in the electric field magnitude of 4.8, 5.8 and 2.7 for the three spots labelled with 1,2 and 3, respectively. Thus, simulation and measurement are in good agreement. As the multislice image simulation was done using the experimental atomic column positions for the 12 nearest neighbours of the defect two findings can be made about the observed features in the change of the electric field magnitude.

First, as the simulation was done using the isolated atom mode (IAM), no charge redistributions are included. Since the simulation resembles, even quantitatively, the same features as observed in the measurement, these features only arise due to the missing atom and the slightly distorted lattice structure, and not due to redistribution effects.

Second, it is noteworthy that the positions of the defect-induced strongly localized increase in electric field magnitude are almost halfway between the selenium atom and the adjacent tungsten atoms in a pristine lattice. For a pristine lattice, a local field minimum is typically observed due to the overlap of opposing electric field components at these positions. However, these local field minima are reduced as the opposing field from the selenium atoms is missing. Thus, the interpretation needs to be done with caution. The electric field close to the three neighbouring tungsten atoms close to the defect is indeed higher compared to a pristine lattice but only because it is drastically reduced in the pristine lattice due to the overlap of fields. In addition, this is influenced by the specific atomic column positions and therefore depends on the distortion of the lattice. Thus, the change in the electric field magnitude due to a missing atomic column is strongly influenced by the position of the adjacent atomic columns.

Figure 7.8 e) and f) depict the relative difference maps of the selenium double vacancy, which is filled with a substitutional atom. Compared to a genuine selenium double vacancy, the relative difference at the defect site of the filled selenium double vacancy is different. This is unexpected as the low-Z atom with a previously estimated atomic number of Z=8 is expected to have only minor influence compared to high-Z atoms of WSe_2. However, the difference in the features observed in the relative difference maps between the two defects is apparent. Instead of the rotor-like feature of a decreased electric field magnitude which was observed for the empty double vacancy, the filled double vacancy shows a more triangular-shaped distribution of decreased electric field of the defective are compared to the pristine area. The shape is in good agreement with the simulation although it is slightly distorted in the measurement. The shape is comparable to the one observed for the single selenium vacancy, however, the relative difference is more reduced for the filled double vacancy than for the single vacancy. This highlights that the present low-Z atoms does not alter the electric field distribution as strong as a remaining selenium atom. For the measurement, the relative difference indicates a reduction in electric field magnitude of 94 % and the simulations exhibits a reduction due to the defect of about 98 % compared to the field magnitude of a pristine lattice. Here again, the relative difference map of the measurement is in great agreement with one of the corresponding multislice image simulation using the isolated atom model.

Furthermore, three spots with a positive relative difference are found in the vicinity of the three nearby tungsten atoms (indicated by the black arrows in Figure 7.8 e) and f)). Likewise to the empty double vacancy this higher electric field magnitude observed in the defective area are due to the missing opposing field from the selenium atomic column. In case of the filled double vacancy, these three spots are less pronounced and exhibit a lower relative difference than observed for the empty double vacancy.

Comparing both selenium double vacancies reveals that although the shape of the induced changes in the electric field magnitude differ between the empty and the filled double vacancy, the relative differences are similar between both. Thus, the additional substitutional atom, which is a single oxygen atom in case of the simulation, leads to small changes in the field distribution surrounding the defect. Although the observation of these changes dependent on the illumination conditions (i. e. defocus), the low-Z atom is not expected introduce an electric field comparable to the electric fields of a single selenium atom. Still, the presence of a single low-Z atom significantly impacts the electric field distribution induced by the defect and a triangular feature of field magnitude reduction is observed instead of a rotor-like feature.

Section summary

- Different point defects introduce structural distortions observable as a change in the tungsten-to-tungsten distance close to the selenium single and double vacancies. Strain, specimen drift, and other defects in the vicinity make it difficult to investigate small changes in the atomic column positions.

- The atomic electric field distribution of an empty selenium double vacancy and a selenium double vacancy filled with substitutional low-Z atom shows a similar distribution despite the additional atom.
- In contrast, the charge density distribution clearly reveals a positive charge density at the defect site for the presumably occupied double vacancy. Thus, the charge density enables the visualization of light atoms in the matrix of high-z atoms, which are not visible in the HAADF image.
- Although a direct determination of the atomic species of the residual atom is not possible from the electric field or charge density distributions due to the non-monotonic behaviour of the DPC signal with the atomic number, an estimation is possible by calculating the ratio of positive charge density between the defect site and a nearby pristine selenium atomic column. In comparison with multislice image simulations of a selenium double vacancy occupied with an oxygen atom, the low-Z atom present in the measurement presumably exhibits an atomic number of about $Z=8$.
- Difference maps of the electric field magnitude reveal characteristic changes in the electric field magnitude introduced by the different defects. Each type of defect introduces a region with locally reduced electric field compared to the pristine lattice and also regions which locally enhanced electric field whose shape is characteristic to the type of defect.
- These changes are not introduced by charge redistributions but due to the missing atomic field of the selenium atoms and the introduced lattice distortions.

7.3 Comparison with DFT Calculations

The previous discussion on the influence of different types of defects on the local electric field distribution illustrates the capability of STEM-DPC imaging to measure changes in the atomic field distribution. Although a direct quantitative interpretation of DPC images is difficult due to the non-monotonic behaviour of the dynamic beam deflection in dependence of the atomic number, stacking distance and the number of atoms (Chapter 4.4) as well as the detector anisotropy and residual lens aberrations, the impact of defects on the charge distribution requires careful simulations for a correct interpretation. Still, as the previous chapter has shown, a local change in field distribution originating from the presence of defects is clearly measurable.

To further investigate whether the triangular-shaped change in field distribution observed for point defects is an expected observation, a DFT calculation of the charge density distribution introduced by a double vacancy in a WSe_2 monolayer is analysed. Parts of the following results are already published in Ref. [41] in the context of a WSe_2 trilayer, however, the discussion here is focussed on a selenium double vacancy in a WSe_2 monolayer. In addition to the already discussed atomic relaxation introduced by a missing selenium atomic column in a WSe_2 monolayer, the change in the electron density distribution due to a selenium double vacancy is investigated by first-principles calculations using the density functional theory (DFT). Detailed information on the parameter for the DFT calculations are adapted from Ref. [41] and given in Appendix 9.11.

For comparison, the absolute difference in charge density is displayed in Figure 7.9 a) and b) for the measurement and simulation, respectively. The difference maps are calculated from the difference in electric field distribution for a selenium double vacancy in a WSe_2 monolayer. The DFT calculation procedure is given in Chapter 9.11.2.

The atomic column positions of the defective area are indicated by the green and grey dots for selenium and tungsten atomic columns, respectively. The difference in charge density distribution between a pristine area and an area containing a selenium double vacancy exhibits a negative charge density difference (blue pixels) at the position of the defect site for the measurement and the simulation (Figure 7.9 a) and b). These negative difference values indicate a less positive charge density in the defective area compared to the pristine area. This is expected, since two positively charged selenium atomic nuclei are missing at the defect site, i. e. there is no positive charge at this position in the charge density map. The negative region at the defect site is surrounded by a positive charge density difference facing the adjacent tungsten atoms, indicating a higher positive charge density at these regions in the defective area than in the pristine area. This is observed in measurement and simulation, and dominantly arises due to missing overlap between opposing electric fields caused by the missing atomic column. This means that the fields of the adjacent tungsten atomic columns extend slightly further into the defect area as they are not compensated by a present selenium atom. Therefore, it results in a slower change rate of the electric fields impacting the calculated charge density difference due to the weakened divergence of the field distribution.

In addition, both difference maps show variations in the charge density in the surrounding

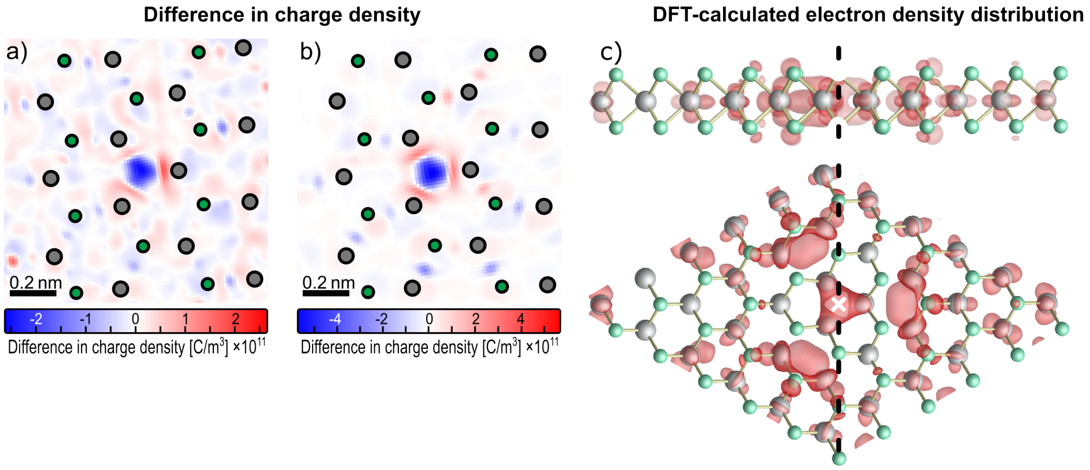

Figure 7.9: a) and b) Charge density distribution derived from the difference in electric field distribution between the defective area with a selenium double vacancy and a nearby pristine area for the measurement and simulation, respectively. The selenium atomic columns are marked by green dots and the tungsten atomic columns are marked by grey dots. c) Electron charge distribution introduced by the missing selenium atomic column (marked by the white cross) derived using DFT calculations.

area. As the experimental atomic column positions are used for the simulation, these variations mostly arise due to the lattice distortion and are dominated by the position of the atomic nuclei. For the measurement, contaminations might also introduce fluctuations in the observed charge density distribution, although they are not visible in the corresponding HAADF image (shown in Figure 7.6 b).

In the following, a further analysis of the triangular-shaped negative difference at the defect position is conducted. The initial charge density map shown in Figure 7.6 k) shows a slightly negative region at the defect site. For the calculation of the difference map, the positive charge density of a selenium atomic column in the pristine reference is subtracted from this slightly negative defective region which introduces increased negative values. To investigate the introduced changes beyond the missing atomic column, a comparison between the minimum values in the difference of charge density at the defect site and the maximum of positive charge density for selenium atomic columns in the pristine area is done.

For the measurement, the charge density difference map exhibits a local minimum of $(-2.5 \pm 0.1) \cdot 10^{11}\,\mathrm{C/m^3}$ at the defect. The maximum positive charge density of selenium atomic columns, given by the charge density map in Figure 7.6 k), exhibits a mean value of $(+2.1 \pm 0.2) \cdot 10^{11}\,\mathrm{C/m^3}$ at the selenium atomic column positions. Thus, the difference in charge density is in the order of magnitude as the positive charge density of a pristine selenium atomic column. But a slightly more negative difference value is observed which can not be explained by image noise or contamination-induced signal fluctuations as standard deviation of the calculated mean value of the positive charge density at selenium atomic columns is too small.

For the simulation, the local minimum in the difference map of charge density is $(-5.6 \pm 0.2) \cdot 10^{11}\,\mathrm{C/m^3}$ and the maximum positive charge density at selenium atomic columns averaged of the selenium atomic columns in the scan area is $(+6.0 \pm 0.1) \cdot 10^{11}\,\mathrm{C/m^3}$. For the simulation, the defect introduces a change in charge density which is less than the change introduced by a missing selenium atomic column. As the experimental atomic column positions are used for the simulation, atomic relaxation or lattice distortion do not cause the deviation between simulation and measurement. Also, the simulation was done using the IAM-based atomic potentials, which neglect any charge redistributions due to bonding. This could potentially explain the differently observed impact of defects in the measurement and the simulation and potentially indicates a redistribution in the electron charge distribution due to the missing selenium atomic column. However, it is to note that it is difficult to unambiguously relate the higher values of negative charge density observed at the defect site to possible electron redistribution, since the derived charge density distributions are strongly affected by the finite and typically imperfect electron probe, the detector's anisotropy, the actual lateral and vertical positions of the atomic nuclei, which are additionally impacted by phonons and dynamics of the defect formation process, as well as a non-perfect image registration of the two areas used for the calculation of the difference maps.

To get a detailed insight into the actual changes in charge density distribution introduced by the defect, Figure 7.9 c) shows the electron charge distribution (indicated by the red colour) of a WSe_2 monolayer with a selenium double vacancy (marked by the white cross) derived by first-principles calculations using the DFT approach. The atomic structure of the defective WSe_2 monolayer is shown in side and top view. The full atomic relaxation is considered for the six tungsten and six selenium atoms close to the double vacancy and is indicated by the missing lines marking the missing covalent bonds.

The red colour shows the electron charge distribution, corresponding to states introduced by the defect. Contributions from the pristine atomic lattice are therefore not indicated.

The DFT-calculated electron charge distribution related to the defect level shows a triangular-shaped regions with pronounced electron charge at the position of the defect site (marked by the white cross in Figure 7.9 c) extending towards the three nearest tungsten atoms. Furthermore, for the subsequent atomic neighbours, crescent-shaped accumulations of electronic charge are observed. Although this crescent-shaped features are not observed in the difference maps of charge density derived by STEM-DPC, the triangular-shaped region with a large charge accumulation at the defect site, seen in the DFT-calculated distribution, agrees with the observed negative charge difference at the position of the defect in the DPC difference maps.

Thus, the red area can be interpreted as the charge density distribution introduced by the defect. A direct comparison between this electron charge distribution derived by DFT and the difference in charge distribution derived by DPC is, however, not possible due to the different approaches of the two techniques. Still, the DFT-derived electron distribution can give an indication on the observed defect-induced changes in the DPC-derived charge density.

It is further to note, that the electron charge distribution is calculated considering a full atomic relaxation. This leads to an inward relaxation of the three adjacent tungsten atoms by about 15 % resulting in a tungsten-to-tungsten distance of the three tungsten atoms of about 2.76 Å compared to the ideal distance of 3.29 Å in pristine WSe_2 [41]. However, the selenium double vacancy examined here does not exhibit a similar relaxation (Chapter 7.2). Since the triangular-shaped region of electron charge density derived by DFT is robust and observed even in presence of other defects such as single vacancies (not shown here but in Ref. [41]), it is not expected that the different states of atomic relaxation strongly alter the distribution [41]. Thus, the here shown electron charge distribution observed by the fully relaxed DFT calculation is in good agreement with the difference in charge density, both showing a triangular-shaped region with significant negative charge density at the defect site. In addition, the electron charge distribution derived by DFT calculations might explain the strongly negative values in the difference map for the experimentally observed charge density distribution which indicates more a negative charge density than only a missing atomic column. However, this is can not be proofed by the here shown simulations and DFT calculations, as the DPC images do not show the electron charge introduced by the defect but a net charge density convolved with the imperfect electron probe. Furthermore, the DPC measurements are strongly influenced by the exact position of the atomic nuclei, the projection of the atomic structure and the anisotropy of the segmented detector as well as specimen drift and scan noise. Thus, the quantitative measurement of the electron charge distribution is impeded but the shown difference map give an insight into pronounced changes in the net charge distribution including the influence of atomic relaxation [28, 42].

Section summary

- The difference in charge density between a defective are with a selenium double vacancy and a pristine area in a WSe_2 monolayer exhibits a region with pronounced negative values for the measurement and the simulation. The measured and simulated difference maps are obtained using the experimental atomic column positions to exclude atomic relaxation induced influence on the difference maps.

- Quantitatively, the observed changes in the charge density distributions deviate between the measurement and the IAM-based simulation which indicate a pronounced charge redistribution due to the presence of a selenium double vacancy.

- An additional DFT-calculated electron charge distribution induced by the selenium double vacancy shows a feature at the defect site which is comparable to the feature observed in the DPC-derived difference map, indicating that the triangular-shaped region with reduced charge density can be presumably related to the charge redistribution.

Chapter 8

Conclusion and Outlook

In this thesis, the atomic electric field and charge density distributions in 2D transition metal dichalcogenides are investigated by differential phase contrast (DPC) imaging in scanning transmission electron microscopy (STEM). In a high-resolution DPC measurement of the atomic electric fields in a WSe_2 monolayer acquired with a segmented detector, an unexpected ratio in the atomic fields of the two different atomic columns was observed. A higher electric field magnitude as well as positive charge density were observed at the lower-Z selenium atomic columns compared to the higher-Z tungsten atomic columns. Since this finding contrasts the expected linear relationship of DPC imaging with the projected atomic number of the atomic columns, this thesis aims to find a possible explanation. As DPC imaging is sensitive to various microscope and specimen-related parameters, the first part of this thesis gave a detailed analysis on parameters including lens aberrations, detector configurations and the stacking of atoms using multislice image simulations.

Since lens aberrations are omnipresent in (S)TEM imaging, multislice image simulations of various combinations of lens aberrations are performed for a WSe_2 monolayer to investigate their influence on the atomic electric field and charge density distributions. It is shown, that all simulated combinations of lens aberrations have a significant influence on the shape and magnitude of atomic electric field distributions. With focus on the unexpected charge density ratio, a quantitative analysis of the impact of lens aberrations on the charge density distribution is done by comparing the positive charge densities at the selenium and tungsten atomic columns. It is evident that different combinations of lens aberrations, which are assumed to be in a reasonable range of magnitudes typically present in daily microscopy work, do not lead to an inversion of the charge density ratio between these atomic columns. Hence, these simulations demonstrate that the unexpected charge density ratio observed in a WSe_2 monolayer is not caused by lens aberrations. As this analysis provides a detailed overview how different lens aberrations and their combinations alter the measurable atomic electric field distributions, it facilitates detection and correction of them already during the measurement. In addition, it also enables to readily detect residual lens aberrations in DPC images of other 2D materials with comparable structural symmetry.

Furthermore, the influence of the limited number of segments and the detector anisotropy is investigated. Since the limited number of segments of the segmented detector results only in an approximation of the atomic field distribution which additionally is influenced by the detector anisotropy, the influence of the segmented detector is analysed by multislice image simulations of a 4D-STEM data set. It is shown that the different detector configurations of an eight-fold segmented detector introduce artefacts in the derived field and charge density distributions, e. g. positive charge density at interatomic pixels when using only the inner layer of segments. The anisotropy of the segmented detector strongly influences the measurable atomic field distribution, i. g. it locally enhances the electric field magnitude close to the atomic columns by up to 15 % compared to the field magnitudes derived from a pixelated detector. Comparing the obtainable electric field and charge density distributions derived by a segmented detector with the ones obtained from a pixelated detector reveals that the use of all detector segments allows for optimum quantitative measurements which exhibit the highest similarity to the ideal CoM-based images.

In addition, the orientation of the convergent beam electron diffraction (CBED) pattern on the detector influences the obtainable DPC image due to the symmetry of the CBED pattern in combinations with the anisotropy of the segmented detector. By rotating the segmented detector, the way how the CBED intensity is captured by the segments is changed and the introduced artefacts are altered. For the first time, the influence of the detector rotation is experimentally investigated for a WSe_2 monolayer. It is demonstrated that the rotation of the detector leads to a rotation of the position of the local field maxima artificially introduced by the detector anisotropy around the atomic column positions. Due to the symmetry of the eight-fold segmented detector and the CBED pattern of WSe_2, the impact is reduced for certain detector rotations, i. e. multiple of 30° with respect to the directions of the W-Se dumbbells. These results show that the segmented detector introduces non-negligible artefacts in the atomic electric field distribution, especially close top the atomic column positions. With the shown experimental measurements it is demonstrated that contributions of the detector anisotropy are non-negligible and can be introduced changes comparable to the influence of lens aberrations. Since the influence of the detector anisotropy depends on the symmetry of the CBED pattern and therefore on the specimen crystal structure, the influence of the detector anisotropy appears different for other materials. These results are of great importance also for other researchers as they can be adapted for a correct interpretation of features in the electric field distribution obtained by DPC measurements of other 2D TMDs with comparable symmetry.

In this thesis, it is investigated how the incident electron beam interacts with one, two and more atoms stacked on top of each other using multislice image simulations. Since the simulations are conducted for different atomic numbers, numbers of atoms per atomic column as well as vertical distances between the atoms, a multitude of different aspects influencing the DPC signal are revealed. First, the influence of the atomic number on the measurable DPC signal and the charge density is analysed. It is shown that the DPC signal does not increase linearly with increasing atomic number, which makes it difficult to directly determine or distinguish atomic species based on the DPC signal. This finding contrast the theory where a linear imaging technique is described. Instead, the mean DPC signal shows a proportionality with $Z^{0.61}$ which is comparable to the Z-dependency of conventional bright-field imaging. Furthermore, the analysis of the influence of the atomic number shows that the measured positive charge density of two atoms is less than twice the charge density of one atom for Z=1–87 highlighting the non-linearity. In addition, the impact of the vertical distance between atoms changing the beam propagation is shown by corresponding multislice image simulations. It is found that the distance between two atoms non-linearly alters the beam deflection. Although the distance of atoms in a crystal can not be changed intentionally, this finding has a great impact on the quantitative analysis when defects are present in an atomic column as any changes introduced by the defect, e. g. a missing atom, are also affected by the changed distance of the remaining atoms.

Furthermore, the influence of the number of atoms within an atomic column is investigated for selenium and tungsten atomic columns with one to six atoms per column, respectively. For increasing number of atoms the increase in the DPC signal becomes non-linear indicating the break-down of the weak-phase object approximation (WPOA) necessary for quantitative DPC imaging. These results show that quantitative DPC imaging is reasonable for up to four selenium atoms or for two tungsten atoms stacked on top of each other, respectively. It indicates that 2D materials do not inherently fulfil the requirements for quantitative DPC imaging, as the WPOA might not hold even for bilayer of TMDs. It is noteworthy, that this will depend on the atomic number of the atoms possibly facilitating correct quantitative analysis of small Z TMDs.

To further investigate the unexpected charge density in a WSe_2 monolayer, the electron beam propagation in the vicinity of a selenium and a tungsten atomic column is investigated by multislice image simulations. This is achieved by the calculation of the probe intensity distribution after the interaction with one to six selenium or tungsten atoms. From the evolution of the probe intensity distribution in the vicinity of an atomic column it is found that a refocussing action from the atomic potentials occurs and results in the formation of a global intensity maximum with a FWHM smaller than the incident electron probe. This leads to a confinement of probe intensity and a global maximum with an increased intensity of about 150 % after the interaction with four selenium or two tungsten atoms. Thus, following atoms are probed with a smaller electron probe of greater intensity density than the first atoms. For small specimen thicknesses with only a few atoms stacked on top of each other, it can therefore be deduced that the usually assumed broadening of the electron probe is prevented by the atomic potentials, and instead a refocussing of the electron beam takes place. Thus, even for only a few atoms in an atomic column, the atoms are not probed by the same incident electron probe. The contribution of subsequent atoms to the DPC signal of the atomic column will be altered by the refocussing of the electron probe. This is an important finding which needs to be considered when aiming to measure bonding effects, which is currently beyond the capabilities of STEM-DPC with segmented detectors.

Finalising the simulative investigations, the atomic potentials and their projection are analysed using the IAM- and DFT-based calculations. It is shown that the mean potential non-linearly depends on the atomic number. Its behaviour is comparable to the mean beam deflection, still, increasing with increasing atomic number. Thus, for sufficiently high spatial resolution, STEM-DPC resembles the atomic potential. Furthermore, it is shown that the projected potential of the atoms , which is the ideal potential landscape the electron beam "sees" in the multislice algorithm, scales linearly with the number of atoms stacked on top of each other. This contrasts with the obtainable DPC signal indicating that the beam propagation strongly influences the measurable DPC signal and diminishes the measured atomic field magnitude and charge density for two vertically stacked atoms.

With the simulative findings, STEM-DPC measurements on mechanically exfoliated MoS_2 monolayer are quantitatively analysed and compared to the one of a WSe_2 monolayer. The electric field distribution of MoS_2 is similar to the atomic field distribution observed in a WSe_2 monolayer with reduced electric field magnitudes. the latter is expected due to the lower Z of MoS_2. Here again, it is found that the lower-Z sulphur atomic column exhibits a higher electric field magnitude and also a higher positive charge density compared to the higher-Z molybdenum atoms. This finding contrasts the projected atomic potentials of sulphur and molybdenum and can not be explained by the atomic potentials or lens aberrations as revealed by the detailed simulative study in the first part of this thesis. It can be deduced that the unexpected behaviour in the atomic field distribution in 2D materials is not only determined by the atomic potentials but is also strongly influenced by the beam propagation and thus also by the vertical distance between the atoms.

The first parts of this thesis cover a variety of different aspects of DPC imaging, which are of great importance for the correct interpretation and quantitative analysis of atomic electric fields and charge density distributions. The influence of microscope and specimen related parameters are investigated in great detail and the limitations using a segmented detector are discussed. The results facilitate a correct interpretation of atomic field distributions derived with a segmented detector and, in case of lens aberrations, and dynamic effects, also holds for other types of detectors. Concluding the first part, the main sources of artefacts in the derived electric field distribution can be summed up to an imperfect incident electron probe, the anisotropy of the segmented detector and the beam propagation of the electron beam in the specimen.

Although, segmented detectors still outperform pixelated detectors in terms of acquisition speed, pixelated detector exhibit a mostly isotropic characteristic. Therefore, pixelated detectors show minimal artefacts due to the high reciprocal space resolution. Furthermore, when acquiring the CBED pattern at each position of the scan with a pixelated detector, electron ptychography can be applied, which is a technique that allows to separately calculate the electron probe and specimen potential. By this, the influence of lens aberrations and the diffraction-limited the size of the probe can be minimized revealing the atomic potentials in the specimen. In addition, using ptychography in combination with an inverse multislice approach even enables to reconstruct the propagation of the electron probe inside the specimen. Although this topic is currently focus of research, it still lacks of quantitative accuracy, but demonstrates significant potential for the future.

With the findings from the simulative studies of this thesis, the application of quantitative DPC imaging is shown in the second part of this thesis. Different stacking configurations, namely AA' and AB, of a WSe_2 bilayer are investigated and their influence on the DPC signal are revealed for the first time. For the investigation of the obtained electric field distribution, difference maps were calculated by subtracting the derived wave vector magnitude maps of a monolayer from the wave vector magnitude map of the bilayer in the respective stacking configuration. For the AA'-stacked bilayer it is shown by the difference map that the electric field distribution behaves like the electric field distribution of two individual monolayers stacked in an antiparallel way. Only the slightly reduced values, which are in agreement with the observed trend for increasing number of atoms within an atomic column, indicate the influence of the beam propagation along the mixed-type atomic columns. For the AB'-stacked bilayer, the influence of the stacking is more pronounced. It is shown that the individual pure selenium or tungsten atomic columns show the same behaviour as in a monolayer, although they are in different layers along the beam propagation direction. However, as one atomic column occupies the centre of the hexagonal WSe_2 rings in projection due to the AB' stacking, the reduced lateral distances between the atomic columns influence the beam propagation which is indicated by the difference map.

Moreover, a twisted WSe_2 bilayer possessing a gradual change in stacking configuration is investigated. It is evident, that the derived atomic electric field distribution is highly determined by the vertical stacking of atoms. For the high symmetry stacking configurations, high electric field magnitudes are found whereas even slight changes in the stacking configuration, and thus changes in the projection of atomic potentials, due to the rotation of the two layers reduce the observable field magnitudes. Furthermore, no long-range electric field introduced by the Moiré potential is measurable by STEM-DPC and the acquisition parameters used. Although variations of the electric field in the different stacking regions are present, no directionality over the length of the Moiré wavelength is observed. These findings support the simulative studies in the first part of the thesis, where the influence of the specific stacking of atoms and the change in the beam propagation were shown to dominate the DPC signal.

Finally, measurements of the electric field distribution for different point defects in a WSe_2 monolayer were performed to investigate changes in the field distribution introduced by these defects. For a selenium single vacancy, an empty selenium double vacancy and a selenium double vacancy occupied with a substitutional atom, the electric field distributions derived by DPC measurements are compared and additionally supplemented by corresponding multislice image simulations. To access changes in the field distribution introduced by the defect, differences between the defective area and a nearby pristine area are calculated. These difference maps reveal characteristic changes in the electric field distributions with regions with locally reduced field magnitudes compared to the pristine lattice, and even regions with locally enhanced electric field magnitudes whose shape depends on the specific type of defect. Even substitutional low-Z atoms are identified by the charge density and the change in the field distribution. The substitutional low-Z atom is not visible in the HAADF image. Still, it is noteworthy that these changes are not solely introduced by the missing atoms itself but are also altered by the introduced lattice distortions in the vicinity of the defect leading to changes in the atomic column positions and a superposition of influences. The characteristic change in the electric field distribution is sufficiently significant to detect and distinguish different defects based on the local electric field distribution even enabling to detect residual light atoms in the defects.

In conclusion, this thesis contributes to the detailed understanding of the atomic electric field and charge density distribution in 2D materials derived by DPC imaging. With focus on features in the field distribution introduced by microscope and specimen, completing investigations for the correct interpretation of atomically resolved DPC images are given highlighting the capabilities of STEM-DPC to access not only the atomic structure but also the atomic electric field distribution.

Chapter 9

Appendix

9.1 Contrast Transfer Function of segmented Detectors

The (phase) contrast transfer function describes the transfer of information for (phase retrieval) imaging techniques in the (S)TEM. The CTF depends on the detector response function, the probe parameters given by the aperture function and the lens aberration function as indicated by Equation 2.16. In conventional (S)TEM imaging techniques, the CTF is mostly used to describe how lens aberrations modulate the phase information in the image. For the phase-retriveal methods such as STEM-DPC, segmented detectors rather than the conventional circular- or ring-shaped detectors are used which alter the detector response function depending on the number of rings and segments as well as their extension and orientation. Detailed investigations on the various CTF for different detector configurations can be reviewed elsewhere [28, 86, 88]. Bekkevold et al. give an interactive python script which calculates and illustrates the CTF depending on various detector parameters [88]. The CTF shown Chapter 2.5 is adapted from their work and python scripting. Thus, the reader is referred to Ref. [88] for details on the calculation of the CTF. In the following, the parameters used for the CTF shown in Figure 2.6 are briefly discussed. Since the CTF depends on various parameters such as lens aberrations and probe parameters e. g. convergence angle, a variety of different CTFs exist for the same detector. Figure 2.6 aims to show the CTF comparable to the CTF of the DPC measurements. As the residual lens aberrations during the measurements are not known, the CTF is calculated for a defocus of zero and no other lens aberrations. Furthermore, the CTF is calculated for a semi-convergence angle of 30 mrad an an acceleration voltage of 80 keV resembling the experimental probe conditions. Moreover, an eight-fold segmented detector consisting of two rings with four segments each is assumed for the calculation. The extension of the detector in reference to the bright-field disk is adjusted by the probe parameters so that the bright-filed disk illuminates about half of the outer layer (Figure 3.2 a). The detector is at a detector rotation of zero degree which corresponds to the detector arrangement similar to the one indicated in Figure 3.2 a). Table 9.1 gives the parameters used for the calculation of the CTF. It is to note, that the CTF calculated using the python script given by Ref. [88] uses the iCoM signal of a segmented detector which is the integrated DPC signal. Since both signals can be obtained by the same segmented detetor and only differ in the calculation of the signal, it is not expected that the different signals qualitatively lead to different CTFs as it will be dominated by the segmentation and extension of the detector. However, the use of the iCoM instead of the DPC signal presumably alters the CTF qualitatively. Since the CTF is only used in this work to qualitatively illustrate the anisotropic behaviour of the segmented detector, the calculation of the CTF is done using the iCoM signal as described by Ref. [88].

Wavelength [Å]	0.041757
q_{max} [Å^{-1}]	1.44
q_{probe} [Å^{-1}]	0.72
Real space sampling [[Å]	0.35
Reciprocal space sampling [Å^{-1}]	0.03
Scan step size [pixels]	1
Lens aberrations	no
Detector inner collection angle [q_{probe}]	0
Detector outer collection angle [q_{probe}]	1.2
Number of annular segments	4
Number of radial rings	2
Detector rotation [°]	0
Sampling	150
Scan grid	150

Table 9.1: Parameters for the calculation of the CTF of an eight-fold segmented detector using the python script given by Ref. [88].

9.2 Drift Correction of high-resolution STEM Images

Among the different sources of image distortions is the specimen drift, which is especially for high-resolution imaging challenging and results from mechanical or thermal instabilities of the specimen holder. These instabilities lead to a drift of the specimen in x-, y- and z-direction and is typically difficult to avoid. Since STEM images are acquired in a serial manner, pixel by pixel and line by line, the scan exhibits a so-called fast-scan axis and a slow-scan axis which are differently influenced by specimen drift. The fast-scan axis is the axis which is scanned pixel-by-pixel whereas the slow-scan axis is defined as the axes which is then built up row-by-row. The fast-scan axis of the image is typically less prone to specimen drift due to the high scan speed of the pixels. In contrast to this, the slow-scan axis which is built up by lines of the scan is slower and therefore more strongly influenced by specimen drift, which leads to shift of the image features between the scan lines. It is possible to reduce the influence of specimen drift on the resulting image by using a high acquisition speed, however, this is not always feasible. As DPC measurements of 2D materials exhibit a lot of image noise, a reduction in dwell time is not suggested and the drift is corrected in a post-processing step. Thus, the procedure for the drift correction is explained in the following using high-resolution HAADF images of a WSe_2 monolayer in [0001] zone-axis orientation.

The drift correction is done using the high-resolution HAADF image. Figure 9.1 shows the as-measured HAADF image with atomic column positions exemplarily marked by the cyan dots. The fast-scan axis is in x-direction and the slow-scan axis is the y-direction as indicated in Figure 9.1. In a first step, the small values of scan rotation are corrected by aligning the rows of atomic columns with the scan direction using an image rotation. By manually drawing a line over the atomic column position in the image (red solid line), the angle between with the x-direction of the image is determined. Then, the image is rotated by this angle to align the crystallographic direction with the x-direction and cropped to the maximum possible image area after image rotation. As indicated in the shown corrected HAADF image in Figure 9.1, the rows of atomic columns are parallel to the x-direction of the image (dashed red line).

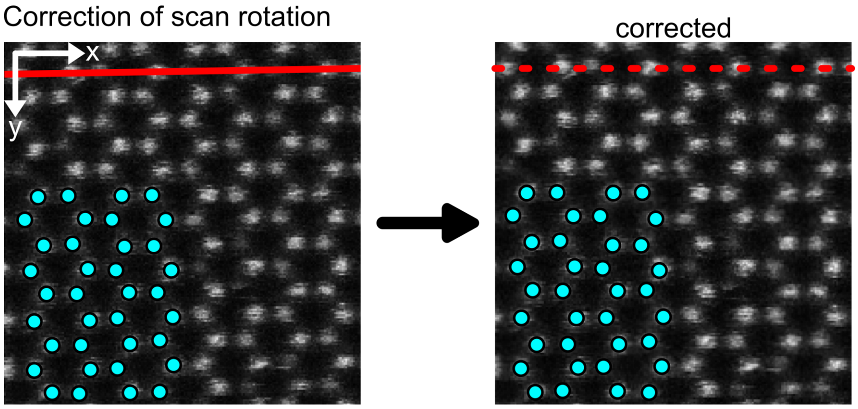

Figure 9.1: Correction of the scan rotation. HAADF image of a WSe_2 monolayer in [0001] zone-axis orientation.

In a second step, the influence of the horizontal shear due to specimen drift is corrected by the alignment of the scan lines in vertical direction. This is done by manually drawing a straight line across a vertical line of atomic columns as indicated by the blue line in Figure 9.2. The image is geometrically transformed to correct for the horizontal shear by an image warping to align the scan lines of the slow-scan axis. The image features (e. g. atomic columns) are aligned in the y-direction of the image. The last step for the correction of specimen drift is a correction of the compression or elongation of image features due to the movement of the specimen during image acquisition. For this, a straight vertical line and a straight horizontal line are manually drawn in the image over a known distance. In the case of high-resolution images with a known structure, both lines span over several atomic columns but start and end on the centre of an atomic column as indicated in Figure 9.3 by the green and yellow lines. Since the specimen drift leads to an artificial compression or elongation of the atomic structure, the atomic distances are typically incorrect in one direction, most probably in direction of the slow-scan axis. Thus, the pixels along this direction need to be repositioned by a certain amount, which is determined by the known atomic structure and ratio between the green and yellow line. From the ratio between the green and yellow line a factor is calculated to correct the incorrect distances in accordance to the ideal ratio. Then, the position of the pixels is readjusted by this factor along the slow-scan axis and an interpolation between the pixels is done. Finally, the image is cropped to the largest possible square. By this procedure, the influence of the specimen drift is reduced and the image features are now aligned and corrected for compression or elongation in the direction of the slow-scan axis.

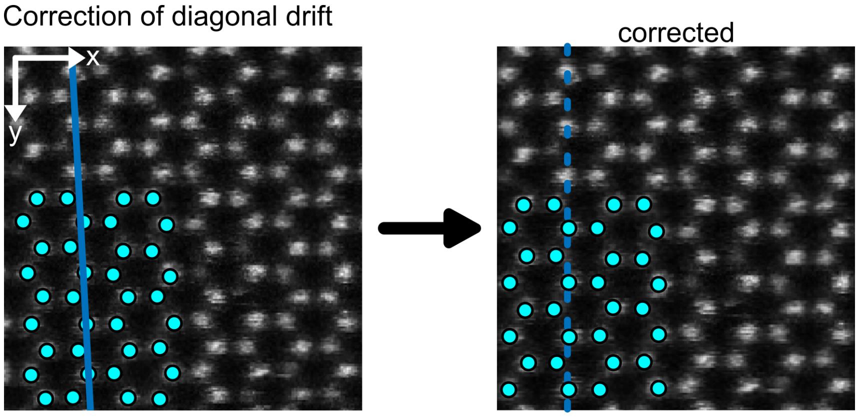

Figure 9.2: Correction of the diagonal drift. HAADF image of a WSe_2 monolayer in [0001] zone-axis orientation.

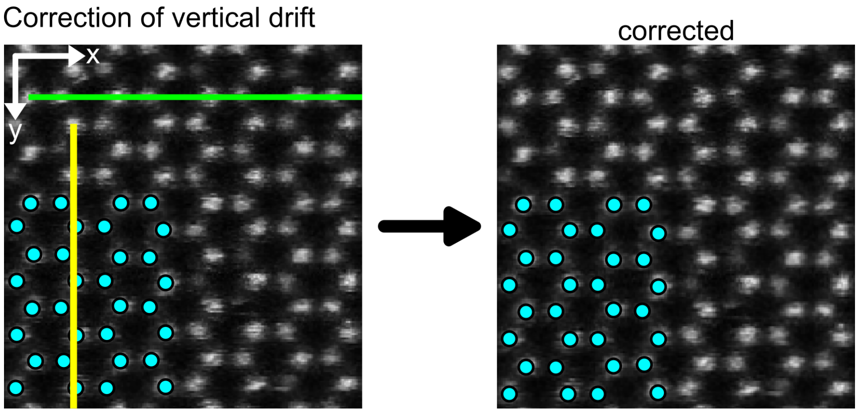

Figure 9.3: Correction of the compression or elongation of image features in one direction due to the specimen drift. HAADF image of a WSe_2 monolayer in [0001] zone-axis orientation.

9.3 Influence of the Detector Rotation

The following Figures 9.4 and 9.5 show the individual DPC images, electric field magnitude as well as charge density maps for the different detector rotations quantitatively analysed in Chapter 4.3.2. Changes in the electric field distribution are difficult to observed by eye, especially for the DPC images, but become apparent when directly comparing the electric field magnitude or charge density map. From the electric field magnitude maps a rotation of the local maxima close to the atomic columns for increasing detector rotation can be observed. For the charge density distribution, the rotation of the detector does not significantly alter the positive charge density at the atomic columns but the negative charge density surrounding the atomic columns. This is in particular visible along the connecting direction between to atomic columns. In dependence on the detector rotation, the neutral charge distribution between the atomic columns is more or less pronounced. For a detector rotation of 0°, the region of neutral charge density is pronounced at the two o'clock and eight o'clock positions. For a detector rotation of 20°, the region of neutral charge density is pronounced at the two o'clock and eight o'clock positions four o'clock and ten o'clock positions.

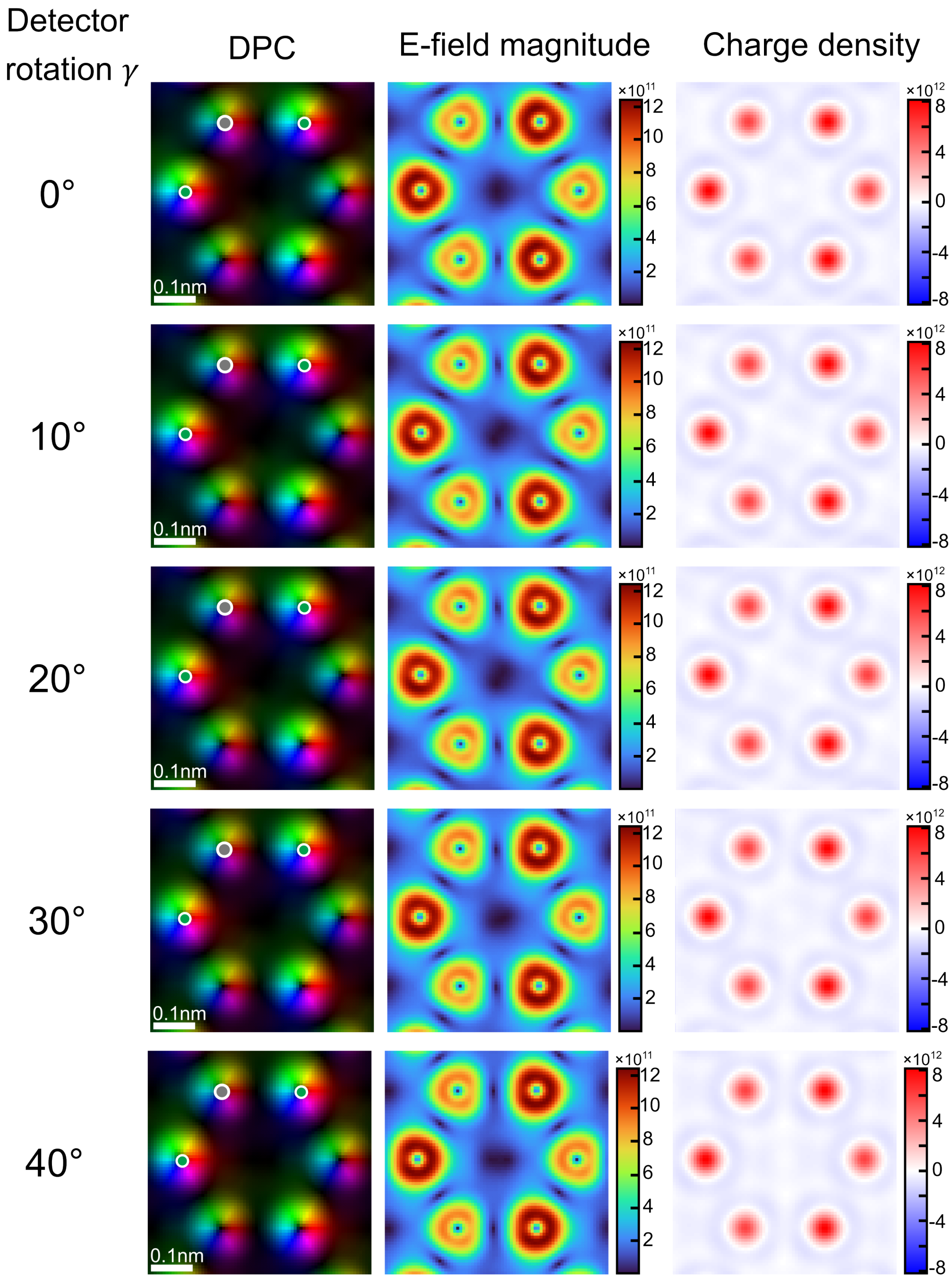

Figure 9.4: DPC images as well as the electric field magnitude and charge density maps for different detector rotations. The electric field magnitude is given in unit of V/m and the charge density is given in units of C/m^3.

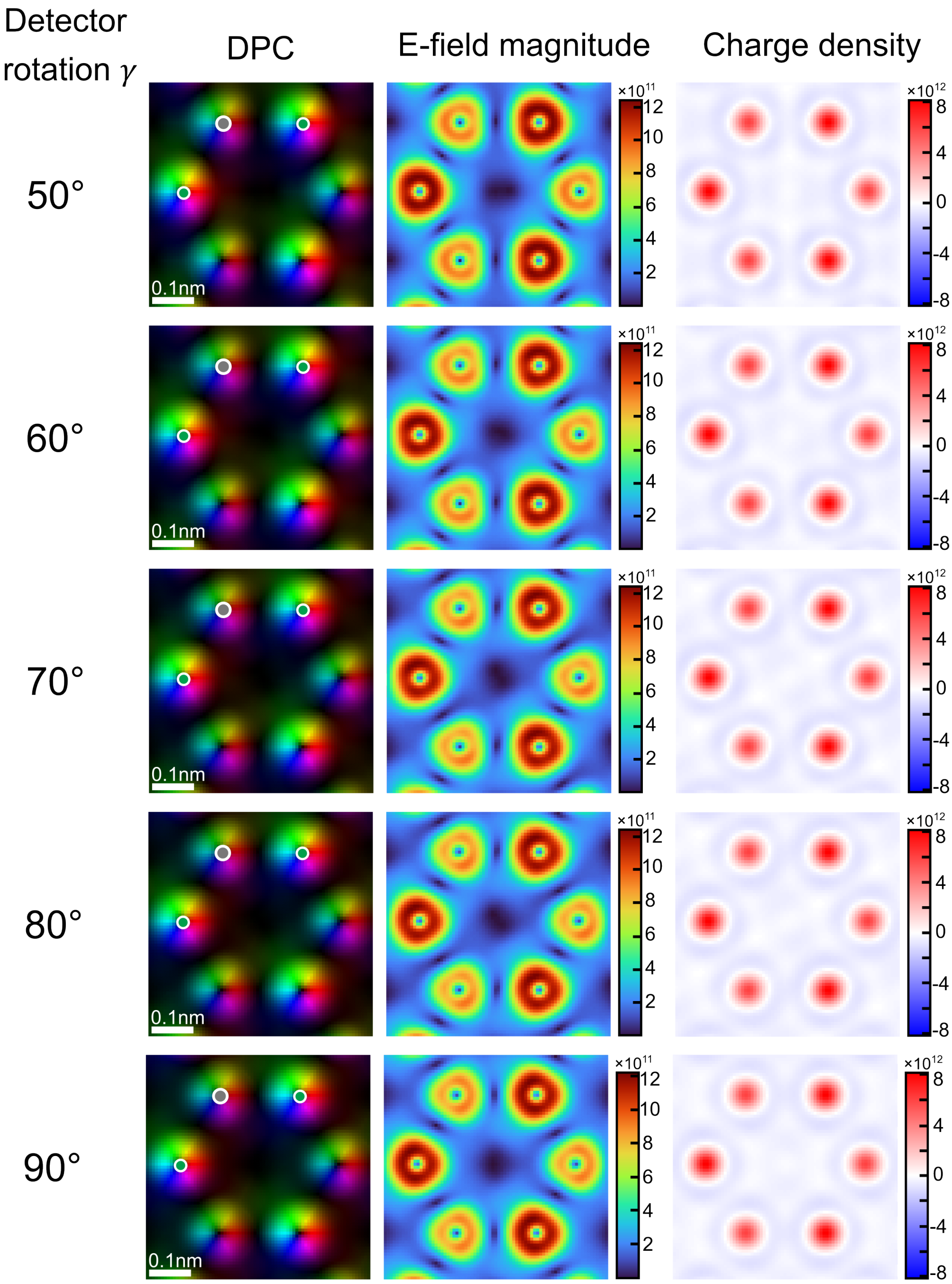

Figure 9.5: DPC images as well as the electric field magnitude and charge density maps for different detector rotations. The electric field magnitude is given in unit of V/m and the charge density is given in units of C/m^3.

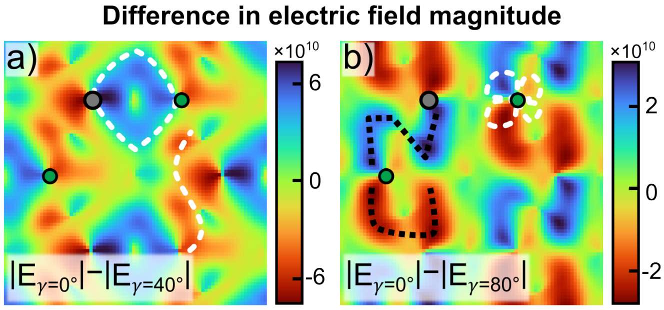

Figure 9.6: Difference map calculated for a detector rotation of a) 40° and b) 80° in reference to a non-rotated detector.

The here shown DPC images are simulated using an ideal probe, however, this assumption is feasibly to phenomenological investigate the influence of the detector, but it does not represent experimental imaging conditions. To investigate the influence of a finite probe size, a Gaussian blurring with a FWHM of 70 pm is applied to the DPC images of the different detector rotations. The blurring of about 70 pm is chosen as it reflects the experimental imaging conditions the best. To map the change in electric field distribution out difference maps the same way as described in Chapter 4.3.2 are calculated and depicted in Figure 9.6. Figure 9.6 a) shows the difference map calculated by the subtraction of the electric field magnitude map obtained using a segmented detector rotated by 40° and a non-rotated detector.

In comparison to the difference maps calculated using an ideal electron probe, detailed features in the difference map vanish. However, the pronounced changes described in Chapter 4.3.2 are still visible, even thought the exact shape slightly changed. The reduced electric field between the two atoms of a WSe_2 dumbbell is not cross-shaped anymore, but is more extended and elliptically formed. The described s-shaped line with a higher electric field magnitude is less pronounced than for an ideal electron probe but still visible. Overall, the same features are identified described in Chapter 4.3.2. For a detector rotation of 80°, the blurring leads to differently shaped features, as the weak features identified as trefoil feature almost vanished. The most pronounced features in the difference map shown in Figure 9.6 b) are alternating N-shaped regions with higher electric field magnitude between the diagonal connecting axes of Se and W atomic columns and u-shaped regions with lower electric field magnitude in the other direction. The maximum relative change observed for both difference maps is of about 11% for a detector rotation of 40° and of about 5% for a detector rotation of 80°.

9.4 Influence of the Number of Atoms

The maximum beam deflection in dependence of the number of atoms stacked on top of each other in an equidistant way is elaborated in Chapter 4.4.3. Here, supporting information on the fitting of linear regressions for an increasing number of atoms is given. Figure 9.7 depict the maximum beam deflection in dependence of the number of selenium and tungsten atoms stacked on top of each other in beam propagation direction. To analyse the regime, which exhibits a linear increase in maximum beam deflection with increasing number of atoms, multiple linear regressions with the function $f(x) = a + b \cdot x$ are used. Starting with a linear region limited to two atoms, the number of contributing data points is step-wise increased and for each step a linear regression is fitted to the respective part of the data. This is done until the R^2-value of the current linear regression drops below 0.99, indicating an increasing deviation from the linear trend. Figure 9.7 a) shows the maximum beam deflection for a selenium atomic column in dependence of the number of atoms. Four different linear regressions are used to analyse the linear trend. For the smallest number of atoms within an atomic column, the linear regression (green solid line) trivially results in an R^2-value of one, since two data point always fulfil a linear trend. Taking an additional atom in to account, the match of the data points with the linear regression (blue dashed line) are still high leading to an R^2-value of approximately one. With further increasing number of atoms the linear regressions for four (pink dashed line) and five (orange dashed line) atoms indicate a degradation of the linear behaviour by a reduction in the R^2-values. Thus, with increasing number of atoms within a selenium atomic column the maximum beam deflection behaves linearly up to four selenium atoms. With additional atoms, the deviation from a linear relationship of the maximum beam deflection with the number of atoms increases.

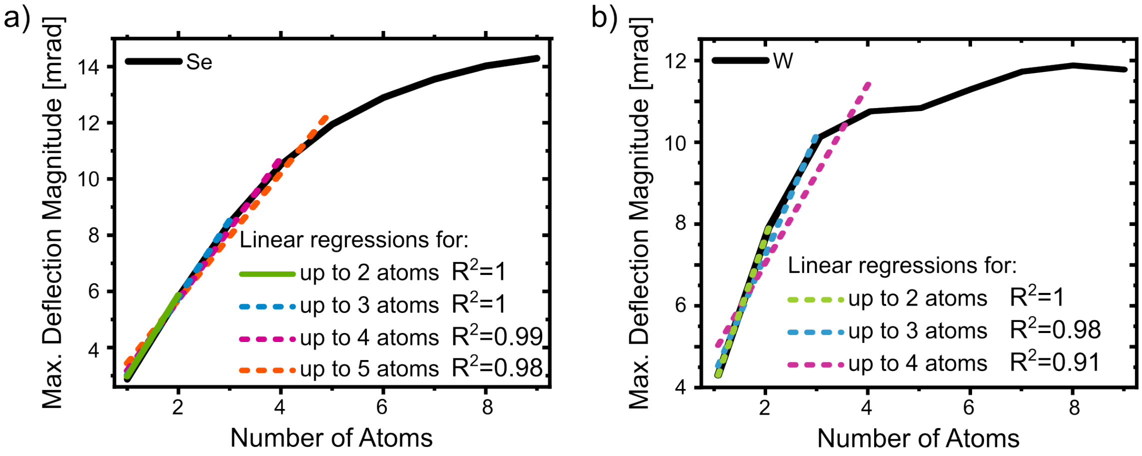

Figure 9.7: a) Maximum beam deflection with increasing number of selenium atoms stacked on top of each other (black curve). b) Maximum beam deflection with increasing number of tungsten atoms stacked on top of each other (black curve). Linear regressions are used to investigate the linearity of the increase in dependence of the number of atoms and are indicated by the coloured (dashed) lines. The R^2-values are given for each linear regression.

A similar analysis done for the tungsten atomic column. Again, linear regressions are used to step-wise analyse the linear relationship of the maximum beam deflection to the number of atoms in an atomic column. Here again, the first regression for two tungsten atoms shows a perfect agreement indicated by the R^2-value of one (green dashed line in Figure 9.7 b). For more than two tungsten atoms, the deviation from a linear regression becomes significant indicated by the drop in R^2-values as indicated by the two more linear regressions for three and four tungsten atoms (blue and pink dashed lines). Thus, the maximum beam deflection is only linear for up to two tungsten atoms and a strong decrease is observed for increasing number of atoms.

9.5 Influence of the non-rigid Registration Algorithm on STEM-DPC Images of a contaminated WSe_2 Monolayer

It is shown in Chapter 4.5, that contaminations of low-Z atoms are typically barely visible in HAADF images but strongly influence DPC images. Although, a clean and contamination-free specimen would be preferential for the investigation of the atomic electric fields by STEM-DPC, the polymer-based transfer process to the TEM grids usually leads to residual atoms on the surface of the 2D material. Figure 9.8 shows a direct comparison of the influence of different amount of amorphous carbon contamination on simulated HAADF and DPC images. The multislice image simulations were done using the diamond unit cell and by randomly displacing the atoms by half the bond length as described in Chapter 4.5. The simulation parameters are given in Table 9.10. Due to the HAADF detector settings used and the high-Z atoms of the WSe_2 monolayer, the contamination atoms are not visible in the HAADF images even for increasing amount of carbon contamination (middle column from left to right). But the influence of the additional atoms is visible in the corresponding DPC images. The simulated contamination-free DPC image (bottom left) clearly shows the rotational symmetric electric field distribution around the individual atomic columns which exhibit a slightly triangular shape due to the overlap of opposing field components from neighbouring atomic columns. With one unit cell of amorphous carbon contamination, the individual atomic electric fields are still visible but strongly reduced in their magnitude which can be identified by the reduced colour saturation. Furthermore, the rotational electric field distributions around tungsten and selenium atomic columns are slightly distorted (exemplarily marked by a white arrow) and rotational electric fields can be found in the hollow space of W-Se rings (exemplarily marked by the white dashed circle). With increasing number of unit cells of amorphous carbon below the WSe2 monolayer, these distortions of the atomic fields of selenium and tungsten atomic columns get more pronounced. For three unit cells below the specimen, the rotational symmetry field around the individual selenium or tungsten atomic columns are strongly distorted and do not exhibit the triangular shape anymore. Thus, even three unit cells of amorphous carbon which correspond to a thickness of only about 1.2 nm leads to strong distortions in the electric field distribution derived by STEM-DPC hindering a correct quantitative analysis. Even a single unit cell leads to visible changes in the electric field distribution. Thus, a contamination-free specimen is of great importance for the quantitative correct interpretation of DPC images. A method to reduce the influence of contamination is the non-rigid registration of several images as the registration leads to an averaging of the individual images and thus reduces the contribution of randomly ordered atoms. To investigate the influence of the non-rigid registration algorithm on the resulting electric field distribution, different numbers of simulated images are registered and compared to the simulation of a contamination-free WSe_2 monolayer. Since the influence of contamination increases with the amount of contamination below the specimen, this analysis is done for the multislice image simulation of three unit cells amorphous carbon below a WSe_2 monolayer as shown in Figure 9.8 d). The non-rigid registration procedures are all done with a threshold of 0.75 and for the same

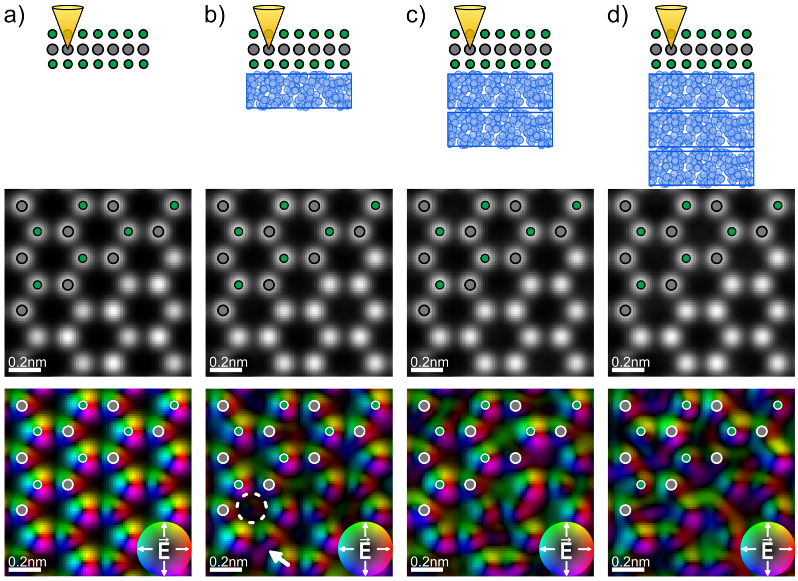

Figure 9.8: Multislice image simulations of a WSe_2 monolayer a) without contamination, b) with one unit cell amorphous carbon, c) with two unit cells amorphous carbon, and d) with three unit cells amorphous carbon. As indicated by the sketches in the first row, the amorphous carbon contamination (indicated by the blue spheres) is in beam propagation direction below the WSe_2 monolayer and the defocus is fixed to the tungsten atomic plane. The middle row shows the HAADF images and the bottom row shows the corresponding DPC images. The atomic column positions of selenium and tungsten atomic columns are marked by green and grey dots, respectively.

image area but with increasing number of images which contribute to the registration process. The quality of the resulting image after the non-rigid registration procedure is determined by the similarity with the DPC image of a simulated contamination-free WSe_2 monolayer via the cross-correlation coefficient. Figure 9.9 shows the calculated cross-correlation coefficients of the DPC signal in dependence of the number of registered images. It is evident from the plot, that with increasing number of images used for the non-rigid registration the cross-correlation coefficient increases. For the DPC image without any image registration, the similarity to the DPC image of a clean WSe_2 monolayer is low as indicated by the low cross-correlation coefficient of about 0.22 (marked by the cyan edge colour in Figure 9.9). This can be explained by two contributions. On the one hand, the three unit cells of carbon contamination below the WSe_2 monolayer strongly reduce the measurable DPC magnitudes compared to the derived DPC magnitudes of a contamination-free specimen. This can also be clearly seen in the DPC images in Figure 9.8 a) and d) where the colour saturation, and thereby the field magnitude, is strongly reduced when carbon contamination is present. Thus, the DPC image of the contaminated specimen deviates quantitatively from the DPC image of a clean specimen. On the other hand, also the distribution of the electric field in the DPC image of a contaminated WSe_2 monolayer is changed compared to a clean specimen. As the randomly distributed contamination atoms below the WSe_2 monolayer introduce additional atomic fields at positions where no field is expected from the WSe_2 monolayer, the DPC image of the specimen with contamination deviates also qualitatively from the one of a contamination-free specimen. Thus, the cross-correlation coefficient is

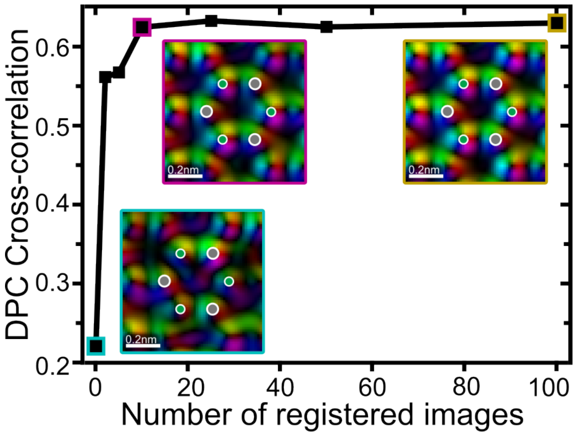

Figure 9.9: Cross-correlation coefficient of the DPC images in dependence of the number of images used for the non-rigid registration process. The reference for the calculation of the cross-correlation coefficient is the multislice image simulation of a contamination-free WSe_2 monolayer. The DPC cross-correlation coefficient for each image is calculated by the sum of the cross-correlation coefficient of the direction and the cross-correlation coefficient of the magnitude.

further reduced.

Figure 9.9 shows that with the non-rigid registration procedure the similarity with a contamination-free specimen can be increased as indicated by the increasing cross-correlation coefficient in dependence of the number of registered images. Even for only two registered images, the cross-correlation coefficient increases up to 0.56 and for 10 registered images it further increases to 0.63 (marked by the pink edge colour in Figure 9.9). The DPC image with the pink frame shows the corresponding DPC image after the non-rigid registration of 10 images. In contrast to the unregistered DPC image indicated by the inset with the cyan frame, the additional electric fields of the contamination atoms are not visible after the registration of 10 images. Thus, the non-rigid registration restores the qualitative field distribution due to the calculation of the pixel mean values for all pixel of the registered images. However, this is only possible as the contamination is amorphous and thus the averaging of registered pixels leads to reduction of the influence of the randomly distributed contamination atoms. A further increase in the number of registered images up to 100 does not significantly improve the similarity and the cross-correlation coefficient remains at 0.63 (marked by the data point with a yellow edge colour and the DPC image with a yellow frame). This can be explained by the two contributions, namely the qualitative and quantitative contribution to the DPC cross-correlation. After the image registration with a few tens or hundreds of images, the obtained DPC image exhibits a high qualitative similarity with the contamination-free DPC image, but the quantitative values can not be restored by the image registration as the field magnitudes are inherently reduced due to the contamination. Thus, the non-rigid registration algorithm is a suitable tool to reduce the influence of amorphous contamination in DPC measurements while maintaining the spatial resolution.

9.6 Visible Light Microscopy Image of 2D-MoS_2 Flakes

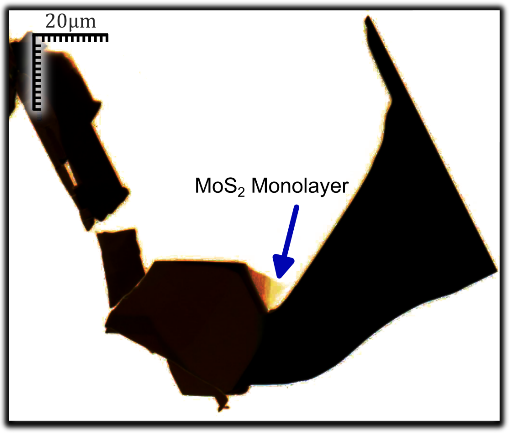

Figure 9.10: Visible light microscopy image of the mechanically exfoliated MoS_2 flake on PDMS obtained by a confocal laser scanning microscope (LEXT OLS5100 Microscope). The colour is inverted for a better visibility of the monolayer region (indicated by the blue arrow).

9.7 STEM-DPC investigations of a Selenium Single Vacancy in a WSe_2 Monolayer

Figure 9.11 shows the STEM-DPC images of a selenium single vacancy in a WSe_2 monolayer. The images are the same as discussed in Chapter 7.1 but here shown without the dots marking the atomic column positions to enable a better comparison of contrast between atomic columns.

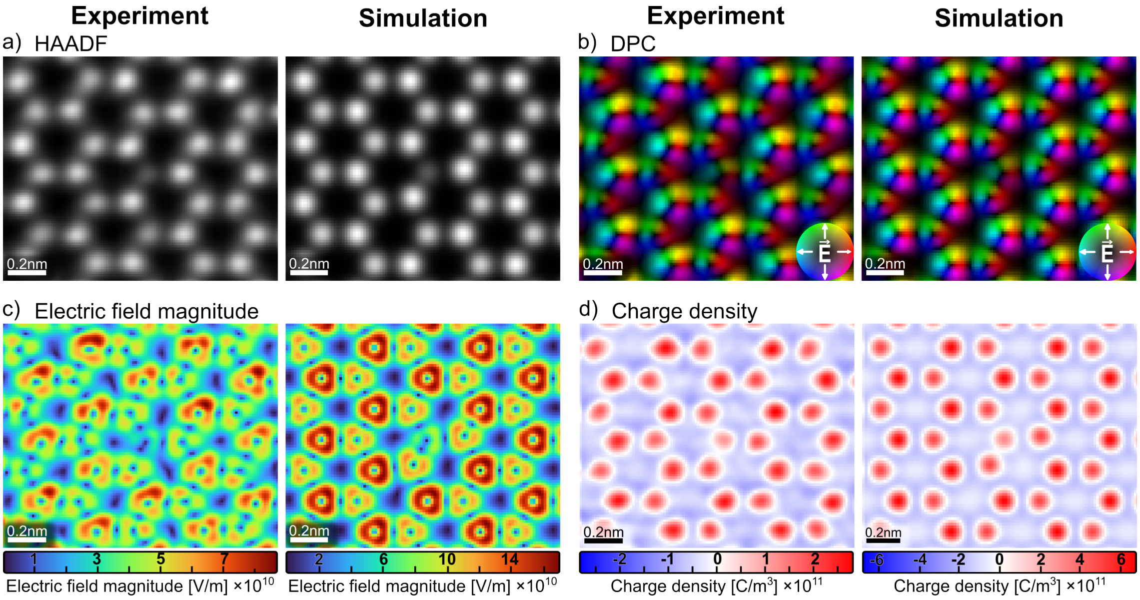

Figure 9.11: STEM-DPC investigation of a selenium single vacancy with the experimental images on the left and the images from a corresponding multislice image simulation on the right. From top to bottom: a) HAADF images and b) colour-coded DPC images as well as c) electric field magnitude maps and d) the charge density maps.

9.8 Multislice Image Simulations of Point Defects in a WSe_2 Monolayer

In Chapter 7.2, different point defects, such as a selenium single and a selenium double vacancy as well as a selenium double vacancy occupied with a substitutional atom, are investigated by STEM-DPC and compared with multislice image simulations. Figure 9.12 shows the corresponding multislice image simulations of these three defects (from left to right). For each defect type, the HAADF and DPC images as well as the electric field magnitude and charge density maps are shown from top to bottom. Details on the simulation parameters are given in Table 9.13. For the multislice image simulations, the experimental atomic column positions of the twelve nearest atomic columns of the defect site are used.

Figure 9.13 shows the integrated line profiles of the HAADF intensity and charge density for the three different point defects. The line profiles are integrated over the regions indicated by the coloured boxes in the corresponding HAADF images shown in Figure 9.12 a-c). A line profile of a pristine lattice over a similar area and integration width is added as a reference but the images are not shown here.

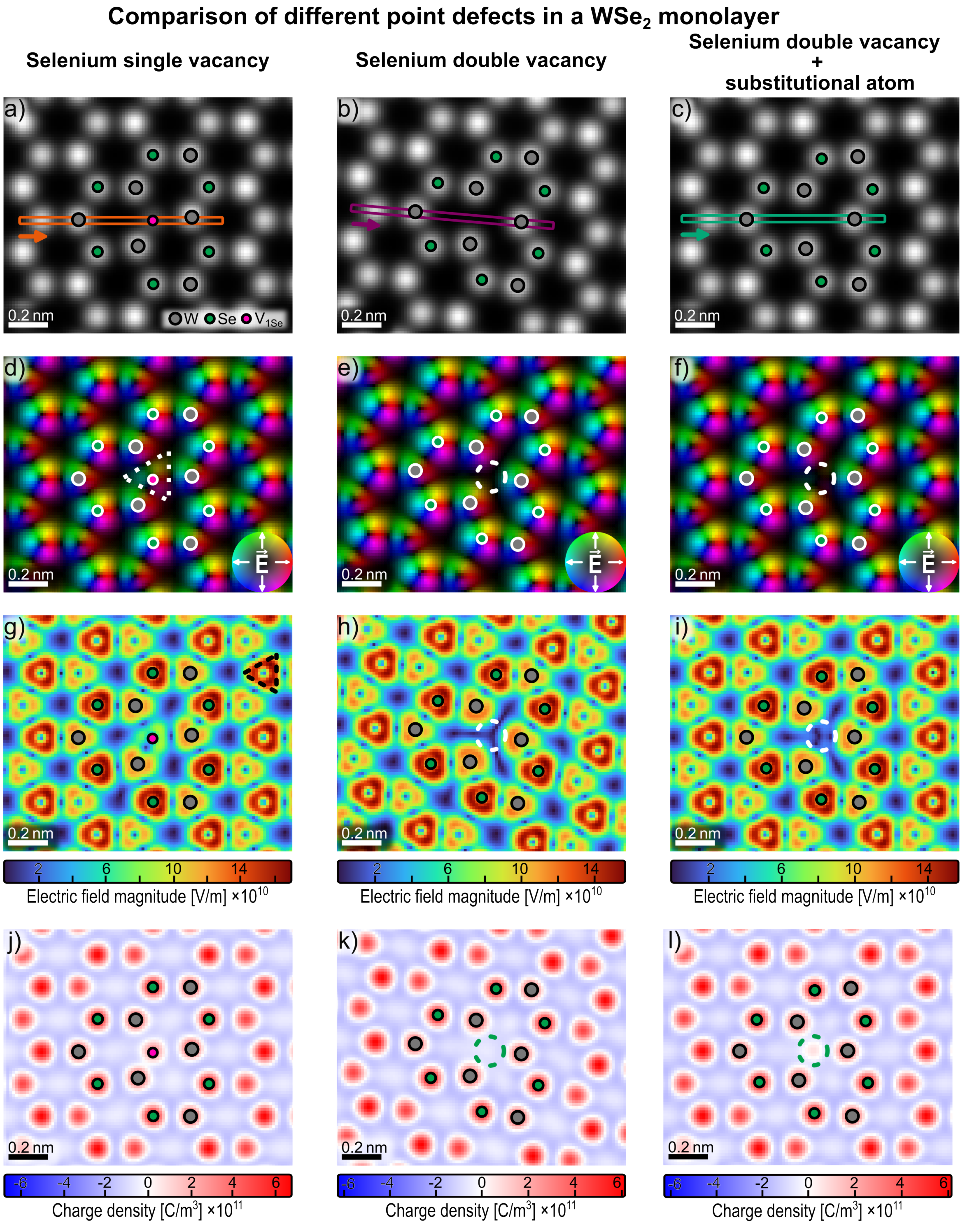

Figure 9.12: Multislice image simulation of different point defects in a WSe$_2$ monolayer. From left to right three different point defects are displayed, namely a single selenium vacancy, a selenium double vacancy, and a selenium double vacancy with a residual substitutional atom present within the missing atomic column. a-c) show the HAADF images for each point defect with the atomic column positions marked by green and grey dots for selenium and tungsten atomic columns, respectively. d-f) depict the corresponding colour-coded DPC images and g-h) the electric field magnitude maps. j-l) display the derived charge density maps.

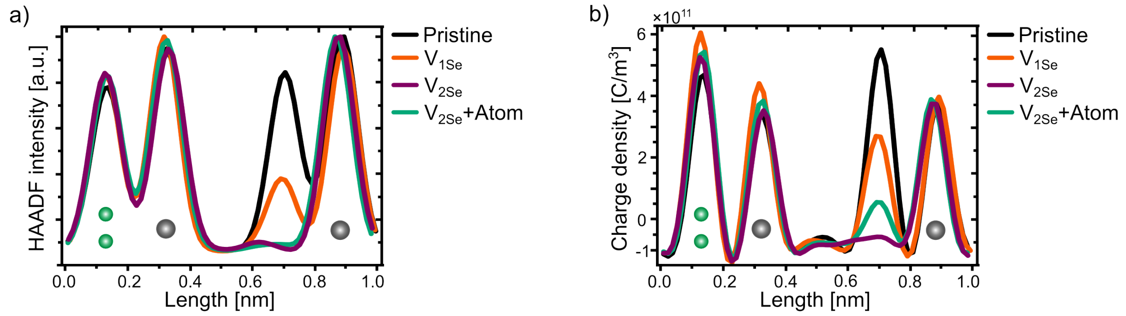

Figure 9.13: a) Line profiles of the normalized HAADF intensity integrated over the regions indicated by the dashed boxes in Figure 9.12 a-c) for the three observed vacancy-type defects. b) Corresponding line profiles of the charge density for the same area as the HAADF line profiles. The black line corresponds to the line profile of a pristine lattice and is used as a reference.

9.8.1 Difference Maps of the Electric Field Magnitude of different Point Defects in a WSe_2 Monolayer

Figure 9.14 shows the difference maps of the three different point defects in a WSe_2 monolayer discussed in Chapter 7.2. The difference maps of the electric field magnitude are calculated by the pixel-wise subtraction of the electric field magnitude map of a monolayer area from the electric field magnitude map of the defective area. The calculated difference of each pixel is divided by the pixel value of the monolayer area to obtain a relative difference. Thus, the electric field magnitude difference maps shown in Figure 9.14 for the measurements (top row) and the simulations (bottom row) show the relative difference of the electric field magnitude of the defective area compared to a pristine monolayer area. For the selenium single vacancy, the difference maps from the measurement and the simulation show a triangular region with negative relative difference at the defect site (marked by the black dashed triangle in Figure 9.14 a) and b) indicating a reduced electric field magnitude at defects compared to a pristine monolayer. Both difference maps additionally show variations in the difference maps especially at high-symmetry points of the crystal lattice e. g. along the connecting axis of two neighbouring atomic columns and in the hexagonal W-Se rings.

Quantitatively, the measurement and the simulation exhibit comparable negative relative differences at the position of the defect in the range of 80–96 % at the tips of the triangular shaped feature. Positive relative difference values are observed at the high-symmetry positions of the lattice for the measurement in Figure 9.14 a) as well as close to the three tungsten atomic at the defect site. For the simulation, only the three positive difference values close to the defects are visible. The positive relative difference values are higher for

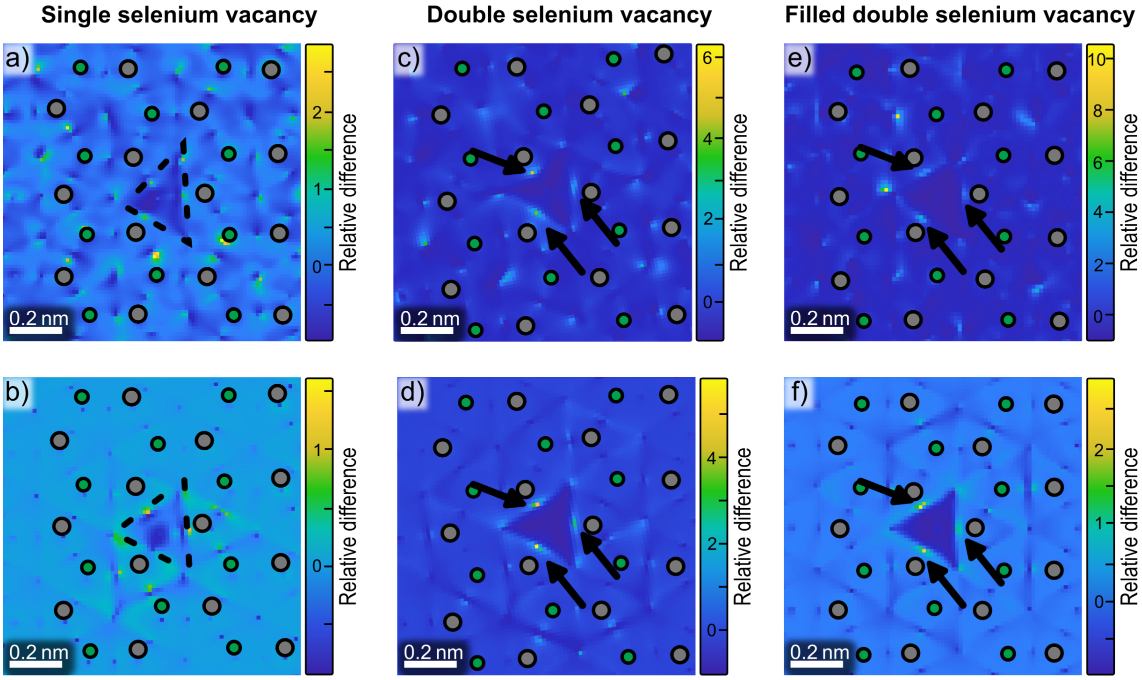

Figure 9.14: Difference maps of the electric field magnitude for the three different point defects in relative values.

the measurement than for the simulation which is presumable caused by variations in the electric field magnitude due to lattice distortions and a misalignment of the defective are with the monolayer area.

Figure 9.14 c) and d) depict the relative difference maps for the selenium double vacancy calculated for the measurement and the simulation, respectively. Both difference maps show again a triangular-shaped region with slightly negative difference values. Close to the three adjacent tungsten atoms, three spots with positive difference are observed and highlighted by the three black arrows. The difference map of the measurements exhibits higher positive difference values than the simulation.

Figure 9.14 e) and f) depict the difference map for a selenium double vacancy with a substitutional atom at the defect site. Due to the alignment of the defective and pristine image area and the variations in the electric field distribution, the high-symmetry areas exhibit high positive values which peak up to a relative difference of 10 whereas the negative difference at the defect site is also in the range of 77–96 %. Thus, the triangular feature is barely visible for the difference map of the measurement. The triangular region with negative difference is clearly visible for the difference map of the simulation shown in Figure 9.14. Figure 9.15 shows the corresponding difference maps in absolute values of the electric field magnitude.

a) Single selenium vacancy b) Double selenium vacancy c) Filled double selenium vacancy

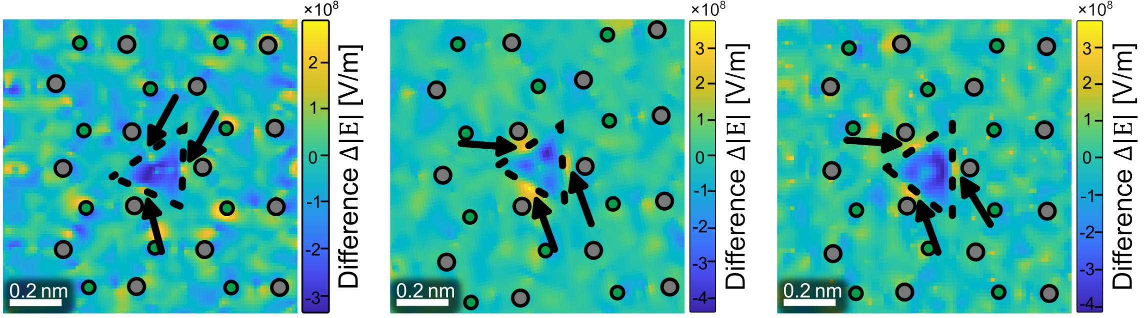

d) Single selenium vacancy e) Double selenium vacancy f) Filled double selenium vacancy

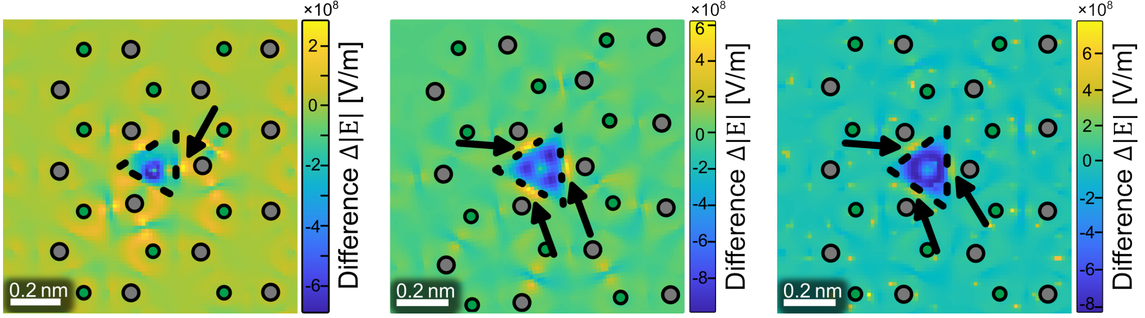

Figure 9.15: Difference maps of the electric field magnitude of the three point defects in absolute values.

9.9 Drift-corrected HAADF Images of three different Point Defects in a WSe_2 Monolayer

Figure 9.16 shows the HAADF images of the three different point defects shown in Chapter 7.2 used for the analysis of structural relaxation. Thus, the images are drift-corrected by procedure described in Chapter 9.2 in the Appendix. For each defect, the distance to the three nearest tungsten atoms are measured and marked by in the respective HAADF image.

The W-to-W distances for the selenium single vacancy shown in Figure 9.16 a) is not strongly altered by the single missing selenium atom and exhibits a mean value of the W-to-W distance of the three nearest neighbours of $d^{\text{mean}}_{W-W} = (3.1 \pm 0.1)\,\text{Å}$ compared to the ideal W-to-W distance of a pristine lattice of $a = 3.29\,\text{Å}$. Thus, no structural relaxation is observed for a selenium single vacancy.

For a selenium double vacancy, the mean W-to-W distance of the three tungsten atoms adjacent to the defect exhibit a mean distance of $\bar{d}_{\mathrm{W-W}} = (2.9 \pm 0.1)\,\text{Å}$, indicating a more pronounced structural relaxation for the neighbouring atomic columns.

The third defect under investigation with a substitutional atom in a selenium double vacancy exhibits a mean W-to-W distance of the neighbouring tungsten atoms of $\bar{d}_{\mathrm{W-W}} = (3.0 \pm 0.1)\,\text{Å}$.

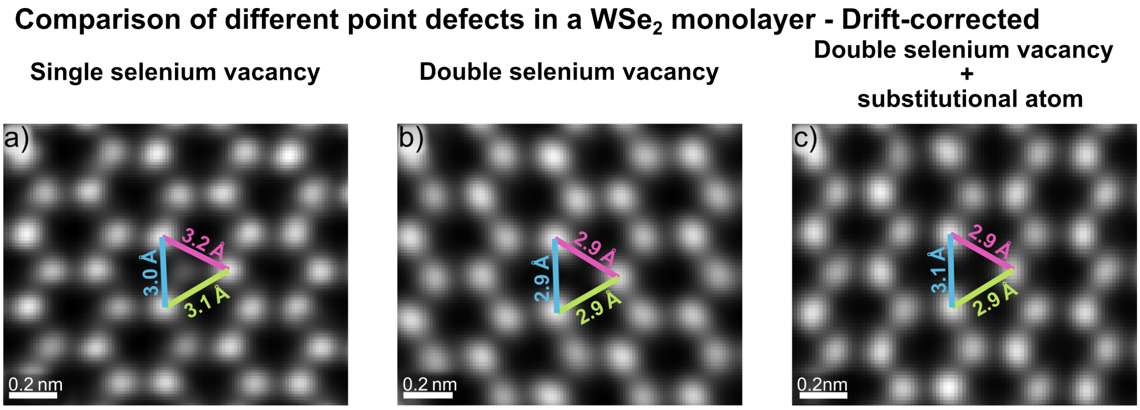

Figure 9.16: The drift-corrected HAADF images for the three different point defects, namely a) selenium single vacancy, b) selenium double vacancy, and c) selenium double vacancy with substitutional atom. The distances between the three adjacent tungsten atomic columns are indicated by the lines.

9.10 Determination of the Number of Layers by HAADF Imaging

The determination of the thickness of 2D TMDs in terms of the number of layers in the TEM is not trivial, although the TEM offers a variety of techniques to access the specimen thickness. One of the most common techniques in TEM for the determination of the specimen thickness is electron energy-loss spectroscopy (EELS). However, for the standard log-ratio technique shown by Malis et al., the thickness can be determined with an accuracy of 10 % in a thickness range between 10–200 nm [233, 234]. For 2D materials, EELS measurements result in an overestimation of the number of layers as shown by Köster et al. [215]. It is shown, that most of the TEM techniques for the thickness determination of 2D materials are not suitable to reliably measure the number of layers of 2D TMDs [215]. Due to the lack of reliable techniques for the determination of the number of layers of a TMD flake, the HAADF image intensity is used for a thickness estimation. For thin specimens, the HAADF image intensity scales with the number of atoms in the atomic column, which enable the counting of the number of layers [235, 236]. It is important to note that this approach gives only in estimation of the number of layers as experimental detector settings, such as brightness and contrast, as well as the detector quantum efficiency and the non-linear detector output, influence the measured signal [72, 237]. For a quantitative HAADF analysis in terms of atom counting, a calibration of the detector signal and an appropriate model, which includes the influence of dynamical diffraction effects and thermal diffuse scattering, are necessary [238].

In the following, the distinction between mono- and bilayer of WSe_2 are done by the HAADF image intensity under the assumption of an approximately linear increase in the HAADF intensity for the small number of layers. Since the WSe_2 samples were purchased from *2DSemiconductor* (Arizona, United States) as CVD-grown monolayers transferred to the TEM grid, the monolayer is clearly identified. Due to nucleation sites from the growth process, small multilayer regions formed on the monolayer and are visible by the higher HAADF image intensity.

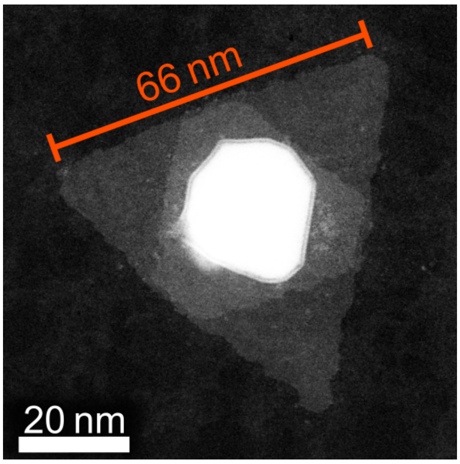

Figure 9.17: HAADF image of a growth nucleation site on the WSe_2 monolayer.

Figure 9.17 exemplarily shows a nucleation site on a WSe_2 monolayer with higher number of layers visible by the increasing HAADF image intensity. The lateral dimensions of these nucleation sites on the WSe_2 monolayer are in the range of several tens of nanometres. From the step-wise increase in the HAADF image intensity the number of layers can be determined by calculating the quotient of the multilayer HAADF image intensity and the HAADF intensity of the monolayer [236]. This estimation of the thickness of the TMD layers is suitable for a few layers, however, for the central part of the nucleation site the

HAADF signal is within the non-linear detector output due to the detector saturation [237]. In the present work, the HAADF signal is only used to distinguish between mono- and bilayers.

AA' Stacking Configuration of a WSe_2 Bilayer

Figure 9.18 a) shows a high-resolution HAADF image of an interface region between a WSe_2 mono- and bilayer. The shown area has a dimension of about $9 \times 9\,\mathrm{nm}^2$. Two regions with highly different HAADF image intensity can be identified. The upper part of the image exhibits a low HAADF image intensity, still atomic columns with alternating high and dim intensity are visible. This part corresponds to the WSe_2 monolayer. For the determination of the number of layers in the lower part of the HAADF image with an overall higher HAADF intensity, an integrated line profile is taken from the region marked by the blue box in the HAADF image. The line profile is aligned perpendicular to the interface between the two regions and plotted in Figure 9.18 b). The line profile shows a step-like behaviour of the HAADF intensity superimposed with fast oscillations in the HAADF signal. The step-like drop in HAADF intensity indicates the two different regions with different number of layers leading to a drop in the average HAADF intensity within the two regions (separated by the blue dashed line). The fast oscillations arise due to the atomic columns and oscillate around a mean HAADF signal which is different for the two regions. To access the step-wise drop in the mean HAADF image intensity due to the difference in the number of layers for the upper and bottom part of the HAADF image, a sigmoidal fit is used (red line). The function is defined by $f(x) = I_2 + (I_1 - I_2)/(1 + \exp((x - x_0)/\mathrm{d}x))$, where $I_{1,2}$ are the initial and final constant values for the s-shape. x_0 is the function's midpoint at which the derivative of the function exhibits its maximum. Based on the derived parameters of the fit function, the average HAADF intensity levels I_1 and I_2 for the two different regions are given and a quotient between the region with unknown thickness (bottom part in the

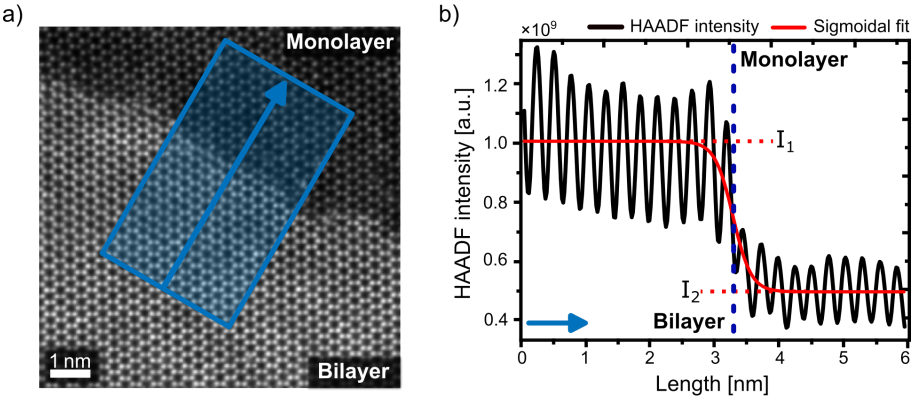

Figure 9.18: a) HAADF image of the interface region of a WSe_2 monolayer and a WSe_2 bilayer in AA' stacking configuration. b) Integrated line profile of the HAADF signal derived from the region marked by the blue box in a). The different intensity levels are determined using a sigmoidal fit indicated by the red line. From the fit, the HAADF intensity levels $I_1 = (1.01 \pm 0.02) \cdot 10^9$ and $I_2 = (4.94 \pm 0.13) \cdot 10^8$ are derived. The intensity is given in a. u.

HAADF image) and the known monolayer region (upper part in the HAADF image) is calculated by $R = \frac{I_1}{I_2}$. The ratio is $R_{\mathrm{AA'}} = 2.03$ with a relative error of 1.3 %. The bright region in the bottom of the HAADF image shows an average HAADF image intensity which is twice the HAADF image intensity of the know monolayer region. Therefore, this region can be identified as a bilayer region, here in AA' stacking configuration.

AB Stacking Configuration of a WSe$_2$ Bilayer

The analysis of the number of layer of WSe$_2$ for the AB stacking configuration is done in the same manner as described for the AA' stacking configuration. Figure 9.19 a) shows the HAADF image of an interface region between the know monolayer region (on the right) and a multilayer region in AB stacking configuration with unknown number of layers (on the left in the HAADF image). An integrated line profile of the HAADF image intensity is used to analyse the stepwise increase in the HAADF image contrast in dependence of the number of layer. The HAADF line profile shown in Figure 9.19 b) depicts the oscillating behaviour of the HAADF signal due to the arrangement of the atomic columns even for the integrated line profile and indicates an overall drop in HAADF intensity from left to right. The fit, indicated by the red line, gives the average HAADF image intensity for the two regions which are determined to $I_1 = (1.82 \pm 0.02) \cdot 10^9$ and $I_2 = (9.85 \pm 0.17) \cdot 10^8$. The ratio in HAADF image intensity between the two regions is $R_{\mathrm{AB}} = 1.9$ with an relative error of 1.1 %. The ratio indicates that the HAADF intensity on the left is twice the HAADF intensity of the monolayer on the right. Thus, on the left side of the HAADF image a WSe$_2$ bilayer in AB stacking configuration is observed.

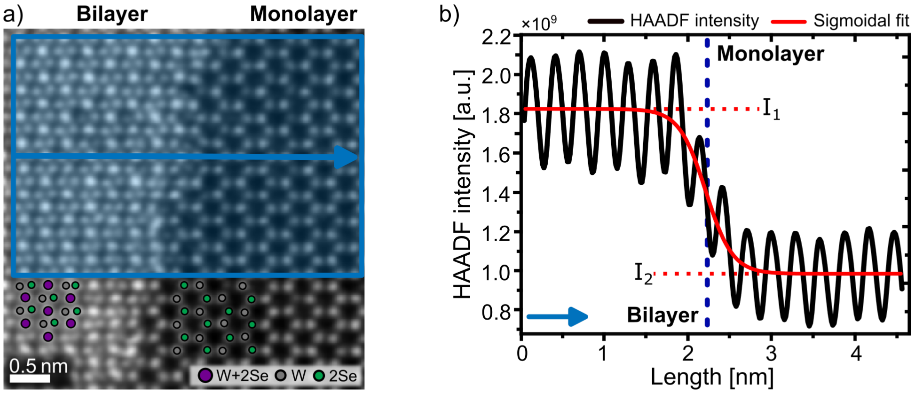

Figure 9.19: a) HAADF image of the interface region of a WSe$_2$ monolayer and a WSe$_2$ bilayer in AB stacking configuration. b) Integrated line profile of the HAADF signal derived from the region marked by the blue box in a). The different intensity levels are determined using a sigmoidal fit indicated by the red line. From the fit the HAADF intensity levels $I_1 = (1.01 \pm 0.02) \cdot 10^9$ and $I_2 = (4.94 \pm 0.13) \cdot 10^8$ are derived. The intensity is given in a. u.

Twisted Stacking of a WSe_2 Bilayer

Figure 9.20 a) depicts an HAADF image of an interface between a known monolayer region (upper part) and a twisted multilayer region (bottom part). In a comparable manner as described for the AA' and AB stacking configurations, the number of layers for the twisted region is estimated by the HAADF signal. Figure 9.20 b) shows the corresponding line profile integrated over the region marked by the blue box in the HAADF image. Again, a drop in HAADF intensity is observed when passing over the interface towards the monolayer region (marked by the blue dashed line). The ratio between the average HAADF intensity levels for the two regions is $R_{\mathrm{Moire}} = 2.3$ with a relative error of $1\,\%$. Thus, the Moiré superlattice shows almost twice the HAADF intensity than a WSe_2 monolayer and is therefore identified as a bilayer.

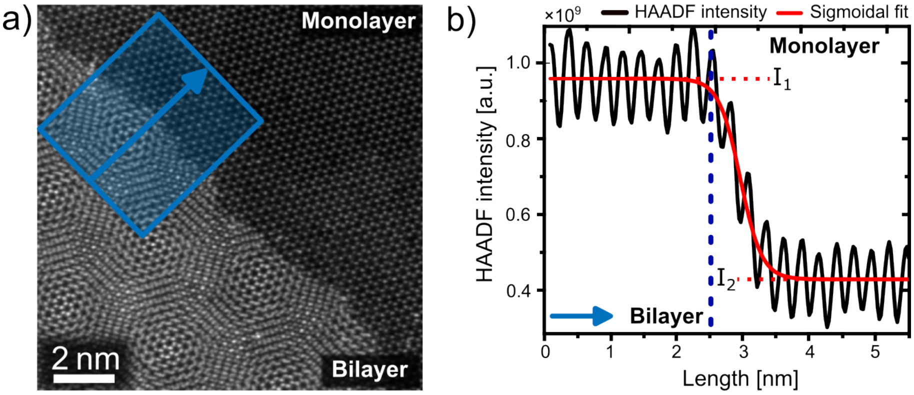

Figure 9.20: a) HAADF image of the interface region of a WSe_2 monolayer and a twisted WSe_2 bilayer. b) Integrated line profile of the HAADF signal derived from the region marked by the blue box in a). The different intensity levels are determined using a sigmoidal fit indicated by the red line. From the fit the HAADF intensity levels $I_1 = (9.59 \pm 0.08) \cdot 10^8$ and $I_2 = (4.27 \pm 0.08) \cdot 10^8$ are derived. The intensity is given in a. u.

9.11 Simulation Parameters

9.11.1 Multislice Image Simulations

The following tables list the simulation parameters used for the different multislice image simulations shown within this work. Unless otherwise mentioned, all simulations are done using an acceleration voltage of 80 keV and a convergence semi-angle of 30 mrad. The segmented detector was simulated using the inner detection angle of β_{inner}=18.2 mrad and an outer detection angle of β_{outer}=36.1 mrad as well as a detector rotation of 0°. The calibration type is indicated either as signal-based or k-space calibrated in accordance to the two different calibrations given in Chapter 3.3). Most of the simulations are done without the frozen lattice approach, thus, the scan repetition is one. If thermal vibration is included in the simulation, the scan repetition is given and the number of variations of atomic configurations per slice is indicated in brackets. Independent on the convention in the two different simulation programs an overfocus is here given with positive defocus values and an under focus is given by negative values.

Figure	2.3, 2.7, 3.3
Simulation software	Dr. Probe [63]
Specimen	$SrTiO_3$ [001]
Unit cell size (x,y,z)	0.39 nm × 0.39 nm × 0.39 nm
Unit cell repetitions (x,y,z)	10 × 10 × 1
Supercell discretization	576 × 576
Number of slices along z-direction	2
Fixed absorption parameter	0.1
Pixel size	0.008 nm
Defocus	0 nm
Other lens aberrations	no
Detector rotation	0°
Image post-processing	
Calibration type	signal-based
Detector configuration	Layer 2
Gaussian blurring (FWHM)	-
Specimen thickness	0.39 nm

Table 9.2: Simulation parameters for the multislice image simulation of STO in [001] zone-axis orientation.

Figure	4.1
Simulation software	abTEM [89]
Specimen	WSe$_2$ [0001] monolayer
Unit cell size (x,y,z)	0.329 nm × 0.571 nm × 0.649 nm
Unit cell repetitions (x,y,z)	21 × 12 × 1
Supercell discretization	1380 × 1380
Slice thickness along z-direction	0.1 nm
Fixed absorption parameter	0
Pixel size	0.01456 nm
Defocus	0 nm
Other lens aberrations	no
Detector rotation	0°
Image post-processing	
Calibration type	k-space
Detector configuration	both layers
Gaussian blurring (FWHM)	75 pm
Specimen thickness	0.649 nm

Table 9.3: Simulation parameters for the multislice image simulation of a WSe$_2$ monolayer.

Figure	4.2, 4.3, 4.4	4.5
Simulation software	Dr. Probe [63]	
Specimen	WSe$_2$ [0001] monolayer	
Unit cell size (x,y,z)	0.329 nm × 0.571 nm × 0.649 nm	
Unit cell repetitions(x,y,z)	21 × 12 × 1	
Supercell discretization	960 × 960	
Number of slices along z-direction	3	
Frozen Lattice Configurations	50	
Scan repetitions	10	
Thermal vibration parameter	B(Se)=0.27 Å B(W)=0.33 Å	
Fixed absorption parameter	0.1	
Pixel size	0.00919 nm	
Defocus	-	0 nm
Other lens aberrations	A1x=-3:1:3 nm f=-3:1:3 nm	A1x=-1:1:1 nm A2y=-100:50:100 nm
Detector rotation	0°	
Image post-processing		
Calibration type	k-space	
Detector configuration	both layers	
Gaussian blurring (FWHM)	85 pm	
Specimen thickness	0.649 nm	

Table 9.4: Simulation parameters for multislice image simulations of 2-fold astigmatism and defocus.

Figure	4.7, 4.8, 4.10, 4.11, 4.12 9.4, 9.5
Simulation software	Dr. Probe [63]
Specimen	WSe$_2$ [0001] monolayer
Unit cell size (x,y,z)	0.329 nm × 0.571 nm × 0.649 nm
Unit cell repetitions (x,y,z)	21 × 12 × 1
Supercell discretization	960 × 960
Number of slices along z-direction	3
Thermal vibration parameter	0
Fixed absorption parameter	0.1
Real Space Sampling	70 × 70
Pixel size	0.00714 nm
Defocus	0 nm
Other lens aberrations	no
Room-angle per pixel	0.612 mrad/px
Detector rotation	between 0° and 90° in steps of 10°
Calibration type	k-space calibrated by gCoM
Detector configuration	Layer 1, Layer 2, both layers, CoM
Specimen thickness	0.649 nm

Table 9.5: Simulation parameters for the 4D-STEM data set.

Figure	4.13, 4.14, 4.20	
Simulation software	abTEM [89]	
Specimen	single atom with Z=1–57 and Z=72–86	two atoms with Z=1–57 and Z=72–86
Unit cell size (x,y,z)	3 nm × 3 nm × 0.6 nm	
Unit cell repetitions(x,y,z)	1× 1 × 1	1 × 1 × 2
Supercell discretization	600 × 600	
Number of slices along z-direction	1	2
Scan repetitions	10	
Fixed absorption parameter	0	
Pixel size	0.005 nm	
Defocus	-0.3 nm	-0.3 nm
Other lens aberrations	no	no
Detector rotation	0°	
Calibration type	k-space	
Detector configuration	both layers	
Specimen thickness	0.6 nm	1.2 nm

Table 9.6: Simulation parameters for multislice image simulations of single and multiple atoms.

Figure	4.15
Simulation software	abTEM [89]
Specimen	two selenium or tungsten atoms
Unit cell size (x,y,z)	3 nm × 3 nm × 0.1–2.4 nm
Unit cell repetitions(x,y,z)	1× 1 × 2
Supercell discretization	600 × 600
Number of slices along z-direction	2
Fixed absorption parameter	0
Pixel size	0.005 nm
Defocus	-(unit cell thickness in z-direction)
Other lens aberrations	no
Detector rotation	0°
Calibration type	k-space
Detector configuration	both layers
Specimen thickness	twice the distance

Table 9.7: Simulation parameters for multislice image simulations of two tungsten and selenium atoms with a variable vertical distance between the atoms. The distance is varied between 0.1 nm and 2.4 nm in steps of 0.1 nm. The focus set to the middle plane between the two atoms and therefore depends on the distance between the atoms.

Figure	4.16
Simulation software	abTEM [89]
Specimen	Selenium and tungsten atomic column with variable number of atoms between 1 and 6
Unit cell size (x,y,z)	3 nm × 3 nm × 0.6 nm
Unit cell repetitions(x,y,z)	1× 1 × 1–6
Supercell discretization	600 × 600
Number of slices along z-direction	1–6
Fixed absorption parameter	0
Pixel size	0.005 nm
Defocus	mid plane in the atomic column
Other lens aberrations	no
Detector rotation	0°
Calibration type	k-space
Detector configuration	both layers
Specimen thickness	0.6 nm times the number of atoms

Table 9.8: Simulation parameters for multislice image simulations of the influence of the number of atoms within an atomic column. The distance is between the atoms is fixed to 0.6 nm but the number of selenium or tungsten atoms in the atomic column is varied from one to six atoms.

Figure	4.17, 4.18
Simulation software	Dr. Probe [63]
Specimen	Selenium and tungsten atomic column with 6 atoms
Unit cell size (x,y,z)	3 nm × 3 nm × 0.6 nm
Unit cell repetitions(x,y,z)	1× 1 × 6
Supercell discretization	432 × 432
Number of slices along z-direction	6
Fixed absorption parameter	0.1
Pixel size	0.01 nm
Defocus	0 nm
Other lens aberrations	no
Specimen thickness	3.6 nm

Table 9.9: Simulation parameters for multislice image simulations of the beam propagation along an atomic column. After each interaction with an atom, the 2D real space probe intensity distribution is derived, meaning after each slice.

Figure	4.23, 4.24, 9.8
Simulation software	abTEM [89]
Specimen	WSe_2 [0001] monolayer with amorphous carbon
Unit cell size (x,y,z)	0.329 nm × 0.571 nm × 0.649 nm 0.356 nm × 0.356 nm × 0.356 nm
Unit cell repetitions(x,y,z)	21× 12 × 1 8× 8 × 0–3
Supercell discretization	1380 × 1380
Number of slices along z-direction	3–18
Fixed absorption parameter	0
Pixel size	0.01456 nm
Defocus	set to tungsten atomic plane
Other lens aberrations	no
Detector rotation	0°
Image post-processing	
Calibration type	k-space
Detector configuration	both layers
Gaussian blurring (FWHM)	80 pm
Specimen thickness	0.649 nm – 1.2 nm

Table 9.10: Simulation parameters for multislice image simulations of a WSe_2 monolayer with amorphous carbon on top or below the monolayer. The amount of carbon is varied between 0 and 3 unit cells and placed either above or below the WSe_2 monolayer along the beam propagation direction. As the thickness of the specimen changes the defocus is for each simulation set to the tungsten atomic plane in the WSe_2 monolayer.

Figure	6.3, 9.21
Simulation software	abTEM [89]
Specimen	WSe_2 [0001] monolayer and bilayer in AA' stacking configuration
Unit cell size (x,y,z)	0.329 nm × 0.571 nm × 0.649 nm
Unit cell repetitions(x,y,z)	21× 12 × 1
Supercell discretization	1380 × 1380
Number of slices along z-direction	6 and 13
Fixed absorption parameter	0
Pixel size	0.01456 nm
Defocus	0 nm
Other lens aberrations	no
Detector rotation	0°
Image post-processing	
Calibration type	k-space
Detector configuration	both layers
Gaussian blurring (FWHM)	80 pm
Specimen thickness	0.649 nm and 1.29 nm

Table 9.11: Simulation parameters for multislice image simulations of a WSe_2 bilayer in AA' Stacking configuration.

Figure	6.7, 9.21
Simulation software	abTEM [89]
Specimen	WSe_2 [0001] monolayer and bilayer in AB stacking configuration
Unit cell size (x,y,z)	0.329 nm × 0.571 nm × 0.649 nm
Unit cell repetitions(x,y,z)	21× 12 × 1
Supercell discretization	1380 × 1380
Number of slices along z-direction	6 and 13
Fixed absorption parameter	0
Pixel size	0.01456 nm
Defocus	0 nm
Other lens aberrations	no
Detector rotation	0°
Image post-processing	
Calibration type	k-space
Detector configuration	both layers
Gaussian blurring (FWHM)	80 pm
Specimen thickness	0.649 nm and 1.29 nm

Table 9.12: Simulation parameters for multislice image simulations of a WSe_2 bilayer in AB Stacking configuration.

Figure	7.1, 7.2, 7.3, 7.4, 7.5, 7.9	9.12	9.12
Simulation software	abTEM [89]		
Specimen	WSe_2 [0001] monolayer		
Defect type	V_{1Se}	V_{2Se}	V_{2Se}+O atom
Unit cell size (x,y,z)	0.329 nm × 0.571 nm × 0.649 nm		
Unit cell repetitions(x,y,z)	21× 12 × 1		
Supercell discretization	1380 × 1380		
Number of slices along z-direction	6		
Fixed absorption parameter	0		
Pixel size	0.01456 nm		
Defocus	0 nm		
Other lens aberrations	no		
Detector rotation	0°		
Image post-processing			
Calibration type	k-space		
Detector configuration	both layers		
Gaussian blurring (FWHM)	95 pm		
Specimen thickness	0.649 nm		

Table 9.13: Simulation parameters for multislice image simulations of a WSe_2 monolayer with different types of defects, namely single selenium vacancy (V_{1Se}), double selenium vacancy (V_{2Se}), and a selenium double vacancy with a substitutional oxygen atom (V_{2Se}+O atom) .

Figure	5.1
Simulation software	abTEM [89]
Specimen	MoS2 [0001] monolayer
Unit cell size (x,y,z)	0.316 nm × 0.548 nm × 0.649 nm
Unit cell repetitions(x,y,z)	15× 8 × 1
Supercell discretization	950 × 950
Number of slices along z-direction	6
Fixed absorption parameter	0
Pixel size	0.0203 nm
Defocus	0 nm
Other lens aberrations	no
Detector rotation	0°
Image post-processing	
Calibration type	k-space
Detector configuration	both layers
Gaussian blurring (FWHM)	90 pm
Specimen thickness	0.67 nm

Table 9.14: Simulation parameters for multislice image simulations of a WSe_2 bilayer in AB Stacking configuration.

9.11.2 DFT Calculations of the Electron Charge Distribution for a Selenium Double Vacancy

The DFT calculations of the selenium double vacancy in a WSe_2 monolayer are already published in Ref. [41] and therefore only summarized briefly here for the sake of completeness. The first-principle calculations and the modelling of the WSe_2 structure with a missing selenium atomic column was conducted using the Quantum ESPRESSO package and periodic boundary conditions (PBC) for a 6×6 supercell [239, 240]. The Brillouin zone was samples by a shifted equidistant 3×3 k-point set. Many-particle effects are considered using the semi-local Perdew-Burke-Ernzerhof (PBE) exchange-correlation functional [241]. In addition, fully-relativistic two-components calculations are included to investigate the influence of spin-orbit coupling (SOC) [242].

9.12 Details on Image Post-Processing of experimental Data

The experimental HAADF and DPC images are post-processed using an in-house built software (*DPCToolbox*) [84]. The different steps of image post-processing for the different images shown in this thesis are given below in Table 9.12, 9.12, and 9.12. Depending on the structure images, the post-processing includes either a non-rigid registration process or a gaussian denoising to reduce the image noise. The latter is used when defects are analysed as the non-rigid registration process is only suitable for the registration of similar image features. Furthermore, a correction of the rotation of the electric field is done for each image to account for the basic and scan rotation and also if needed for the detector rotation (Chapter 3.3).

Figure	4.1	4.12	4.23
Pixel size	0.013 nm	0.019 nm	0.013 nm
Drift correction	yes	no	no
Gaussian denoising (FWHM)	-	-	60 pm
Non-rigid registration			-
Threshold value	0.7	0.75	
Number of images	300	200	
Iterations	600,300,100	600,300,100	
Field-smoothing value	1	1	
Scan rotation	0°	0°	3°
Detector Rotation	0°	0°, 20° and 40°	0°
Detector Configuration	both layers	Layer 2	both layers
Specimen thickness	0.649 nm	0.649 nm	0.649 nm

Figure	6.1	6.5	6.8, 6.9
Pixel size	0.013 nm	0.019 nm	0.018 nm
Drift correction	yes	yes	no
Gaussian denoising (FWHM)	-	-	70 pm
Non-rigid registration			-
Threshold value	0.8	0.65	
Number of images	300	300	
Iterations	600,300,100	600,300,100	
Field-smoothing value	1	1	
Scan rotation	357°	349°	0°
Detector Rotation	0°	0°	0°
Detector Configuration	both layers	both layers	both layers
Specimen thickness	1.297 nm	1.297 nm	1.297 nm

Figure	7.1, 7.2, 7.3, 7.6 a),d),g),j)	7.6 b),e),h),k)	7.6 c),f),i),l)	5.1
Pixel size	0.013 nm	0.013 nm	0.015 nm	0.020 nm
Drift correction	no	no	yes	yes
Gaussian denoising (FWHM)	70 pm	70 pm	70 pm	-
Non-rigid registration	-	-	-	
Threshold value				0.8
Number of images				300
Iterations				600,300,100
Field-smoothing value				1
Scan rotation	10°	14°	108°	344°
Detector Rotation	0°	0°	0°	0°
Detector Configuration	both layers	both layers	both layers	both layers
Specimen thickness	0.649 nm	0.649 nm	0.649 nm	0.67 nm

9.13 Multislice Image Simulation of different Stacking Configurations

a) **AB Stacking**

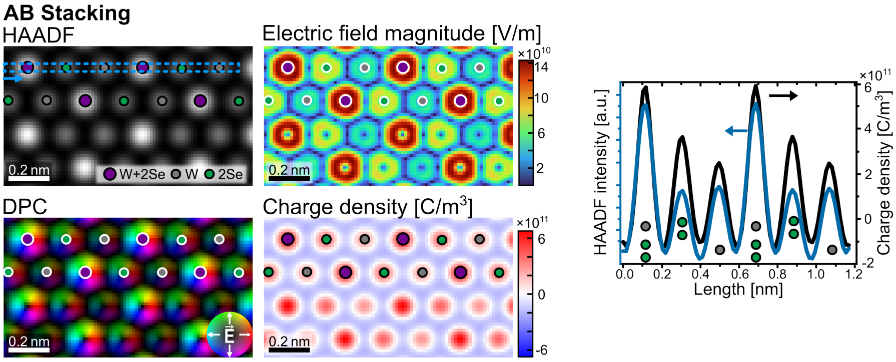

b) **AB' Stacking**

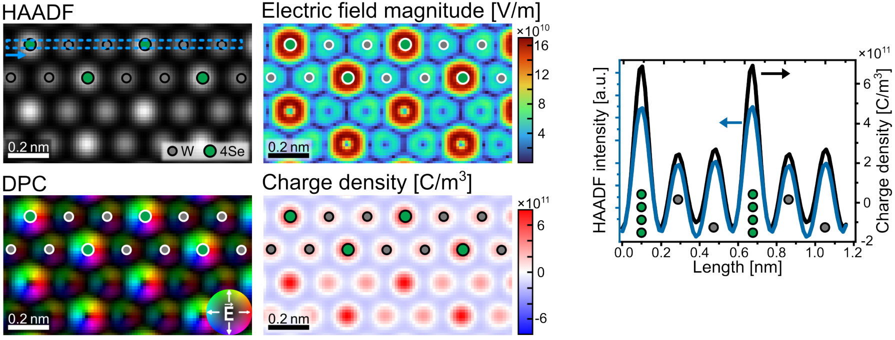

c) **A'B Stacking**

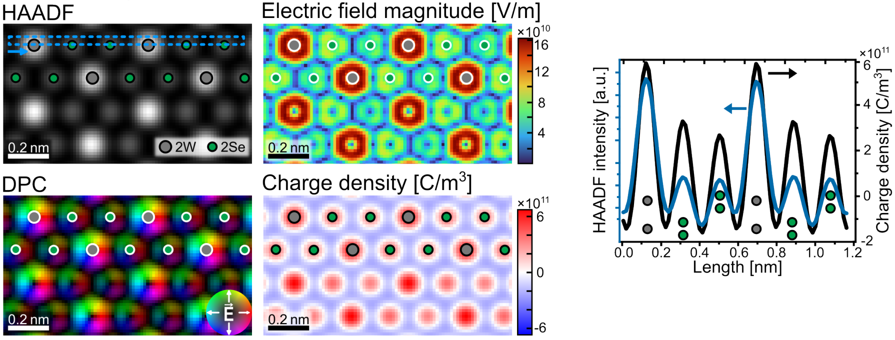

Figure 9.21: Simulative comparison of different bilayer stacking configurations of WSe_2. a)-c) show the simulated images for the three different stacking configurations, namely AB, AB', and A'B stacking. For each stacking configuration the HAADF and DPC image as well as the electric field magnitude and charge density maps are shown. The atomic column positions are marked by dots and the atomic species of the column is indicated by different colours and explained by the inserted legend. The three HAADF intensity and charge density line profiles for each stacking are integrated over the region indicated by the dashed box in the respective HAADF image.

9.14 Multislice image simulation of different Combinations of Lens Aberrations for a WSe_2 Monolayer

Figure	9.22,	9.23,	9.24	9.25	9.26
Simulation software	Dr. Probe [63]				
Specimen	WSe_2 [0001] monolayer				
Unit cell size (x,y,z)	0.329 nm × 0.571 nm × 0.649 nm				
Unit cell repetitions(x,y,z)	21 × 12 × 1				
Supercell discretization	960 × 960				
Number of slices along z-direction	3				
Frozen Lattice Configurations	50				
Scan repetitions	10				
Thermal vibration parameter	B(Se)=0.27 Å B(W)=0.33 Å				
Fixed absorption parameter	0.1				
Pixel size	0.00919 nm				
Defocus	0 nm	-	0 nm	0 nm	-
Other lens aberrations [nm]	A1x=-3:1:3 A1y=-3:1:3	A1x=-3:1:3 f=-3:1:3	A1x=-4:1:4 A2y=-200:50:200	B2=-100:20:100 A1x=-2:1:2	A2x=-200:40:200 f=-2:1:2
Detector rotation	0°				
Image post-processing					
Calibration type	k-space				
Detector configuration	both layers				
Gaussian blurring (FWHM)	85 pm				
Specimen thickness	0.649 nm				

Table 9.15: Simulation parameters for multislice image simulations of various different combinations of lens aberrations for a WSe_2 monolayer.

Figure	9.27	9.28	9.29	9.30	9.31
Simulation software	Dr. Probe [63]				
Specimen	WSe_2 [0001] monolayer				
Unit cell size (x,y,z)	0.329 nm × 0.571 nm × 0.649 nm				
Unit cell repetitions(x,y,z)	21× 12 × 1				
Supercell discretization	960 × 960				
Number of slices along z-direction	3				
Frozen Lattice Configurations	50				
Scan repetitions	10				
Thermal vibration parameter	B(Se)=0.27 Å B(W)=0.33 Å				
Fixed absorption parameter	0.1				
Pixel size	0.00919 nm				
Defocus	0 nm				
Other lens aberrations	A2x=-150:50:150 A2y=-150:50:150	-	S3x=-3:0.6:3 µm f=-2:1:2 nm	S3x=-3:0.6:3 µm S3y=-3:0.6:3 µm	C5=-5:1:5 µm f=-2:1:2 nm
Specimen tilt	0 mrad	tilt x=-45:15:45 mrad tilt y=-45:15:45 mrad	0 mrad	0 mrad	0 mrad
Detector rotation	0°				
Image post-processing					
Calibration type	k-space				
Detector configuration	both layers				
Gaussian blurring (FWHM)	85 pm				
Specimen thickness	0.649 nm				

Table 9.16: Simulation parameters for multislice image simulations of a WSe_2 monolayer for different tilt angles in x- and y-direction and different combinations of lens aberrations.

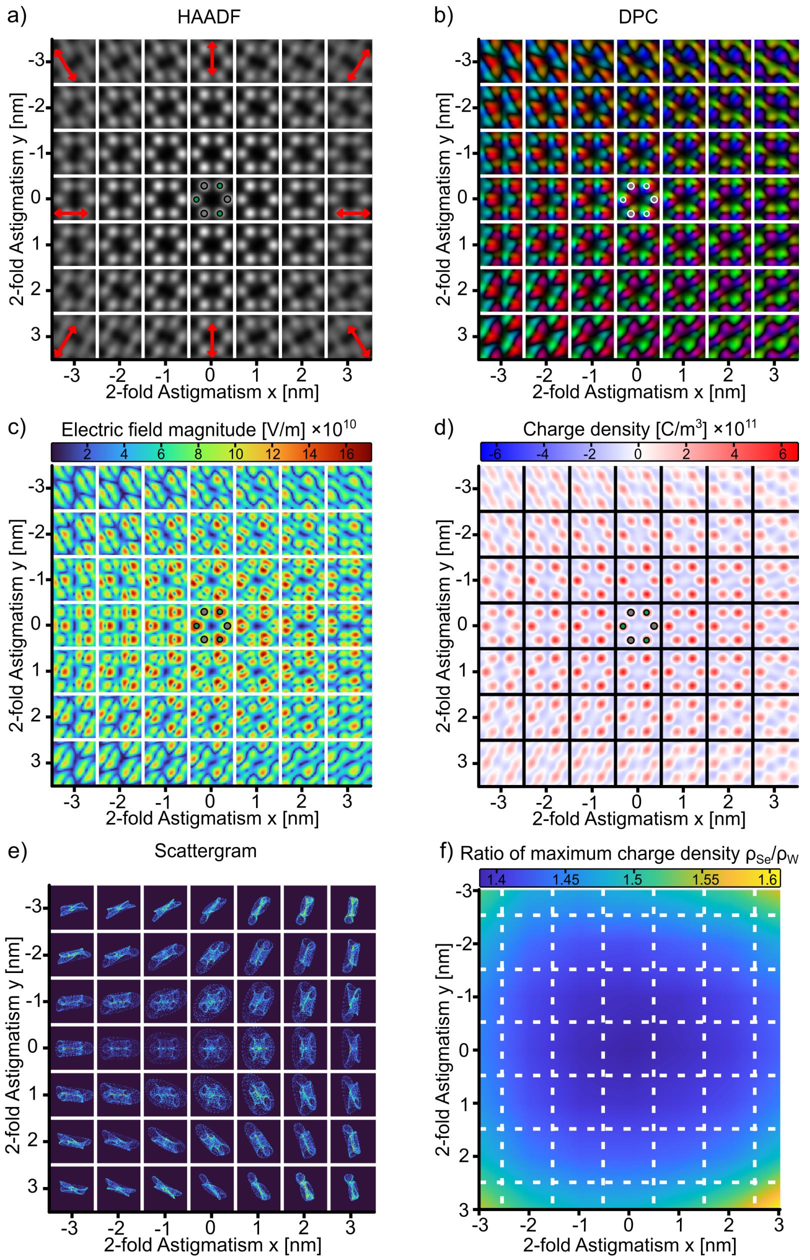

Figure 9.22: Multislice image simulation of different combinations of 2-fold astigmatism in x- and y-direction for a WSe_2 monolayer in [0001] zone-axis orientation. a) HAADF and b) normalized DPC images as well as c) the electric field magnitude maps and d) the charge density maps. The DPC images are individually normalized for a better visibility of colours. Thus, reductions in field magnitude can not be compared between the DPC images. e) Scattergrams with normalized intensity for each simulated DPC image. f) Map of the charge density ratio between the maximum positive charge density at selenium atomic columns and the maximum positive charge density at tungsten atomic columns.

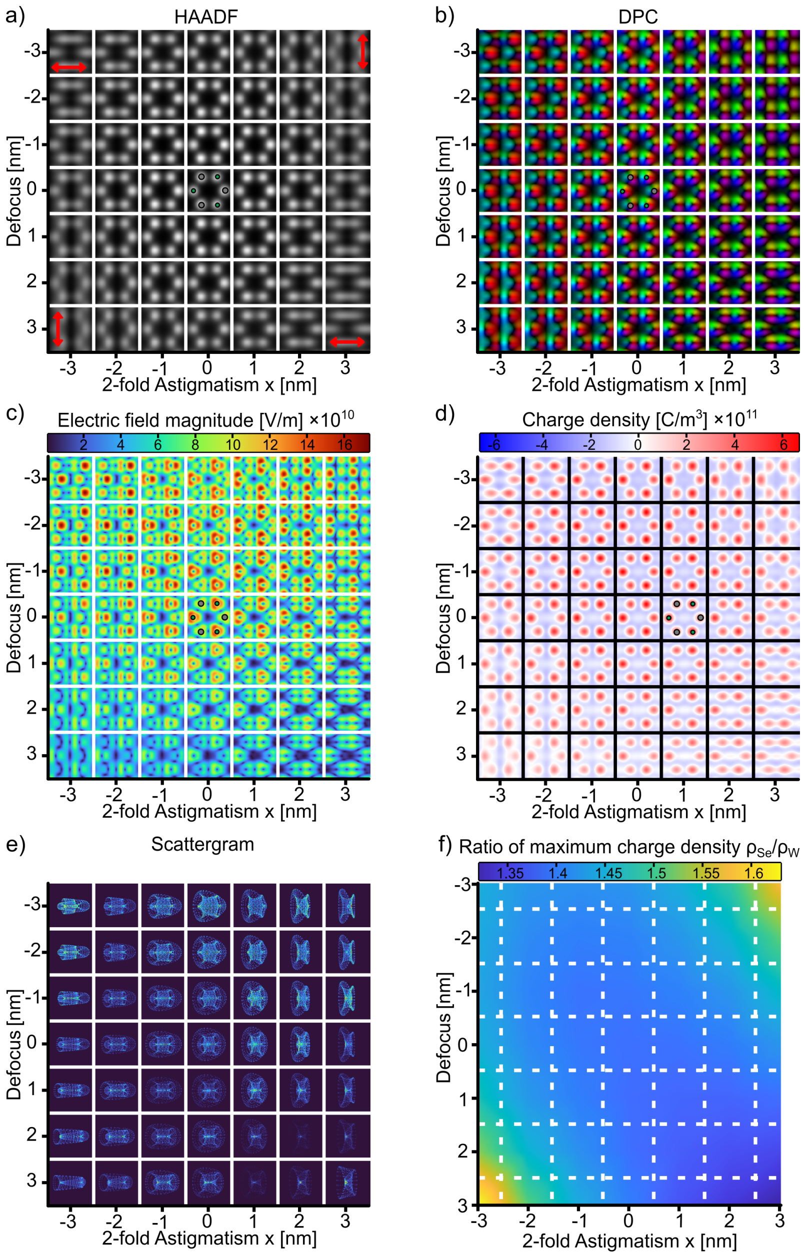

Figure 9.23: Multislice image simulation of different combinations of 2-fold astigmatism in x-direction and defocus for a WSe_2 monolayer in [0001] zone-axis orientation. a) HAADF and b) normalized DPC images as well as c) the electric field magnitude maps and d) the charge density maps. The DPC images are individually normalized for a better visibility of colours. Thus, reductions in field magnitude can not be compared between the DPC images. e) Scattergrams with normalized intensity for each simulated DPC image. f) Map of the charge density ratio between the maximum positive charge density at selenium atomic columns and the maximum positive charge density at tungsten atomic columns.

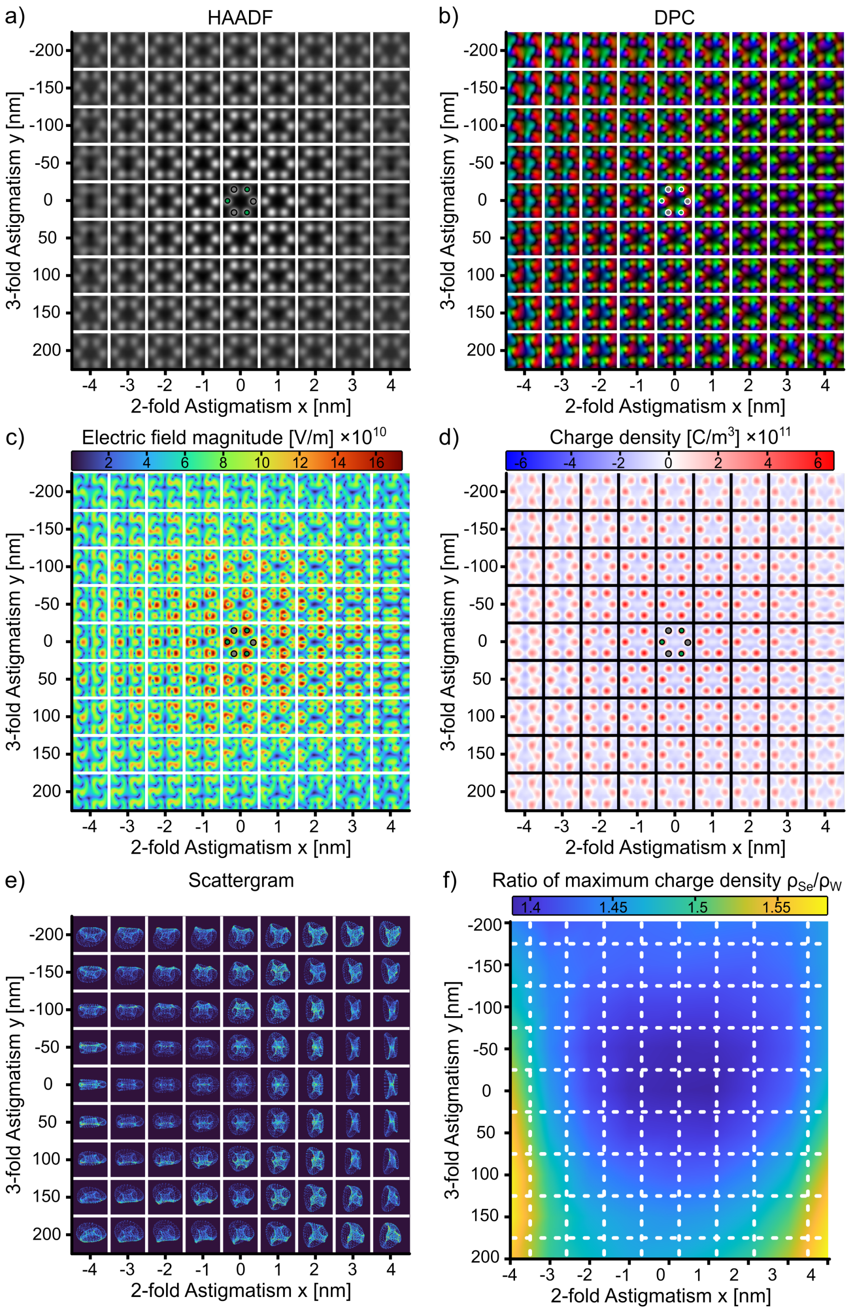

Figure 9.24: Multislice image simulation of different combinations of 2-fold astigmatism in x-direction and 3-fold astigmatism in y-direction for a WSe_2 monolayer in [0001] zone-axis orientation. a) HAADF and b) normalized DPC images as well as c) the electric field magnitude maps and d) the charge density maps. The DPC images are individually normalized for a better visibility of colours. Thus, reductions in field magnitude can not be compared between the DPC images. e) Scattergrams with normalized intensity for each simulated DPC image. f) Map of the charge density ratio between the maximum positive charge density at selenium atomic columns and the maximum positive charge density at tungsten atomic columns.

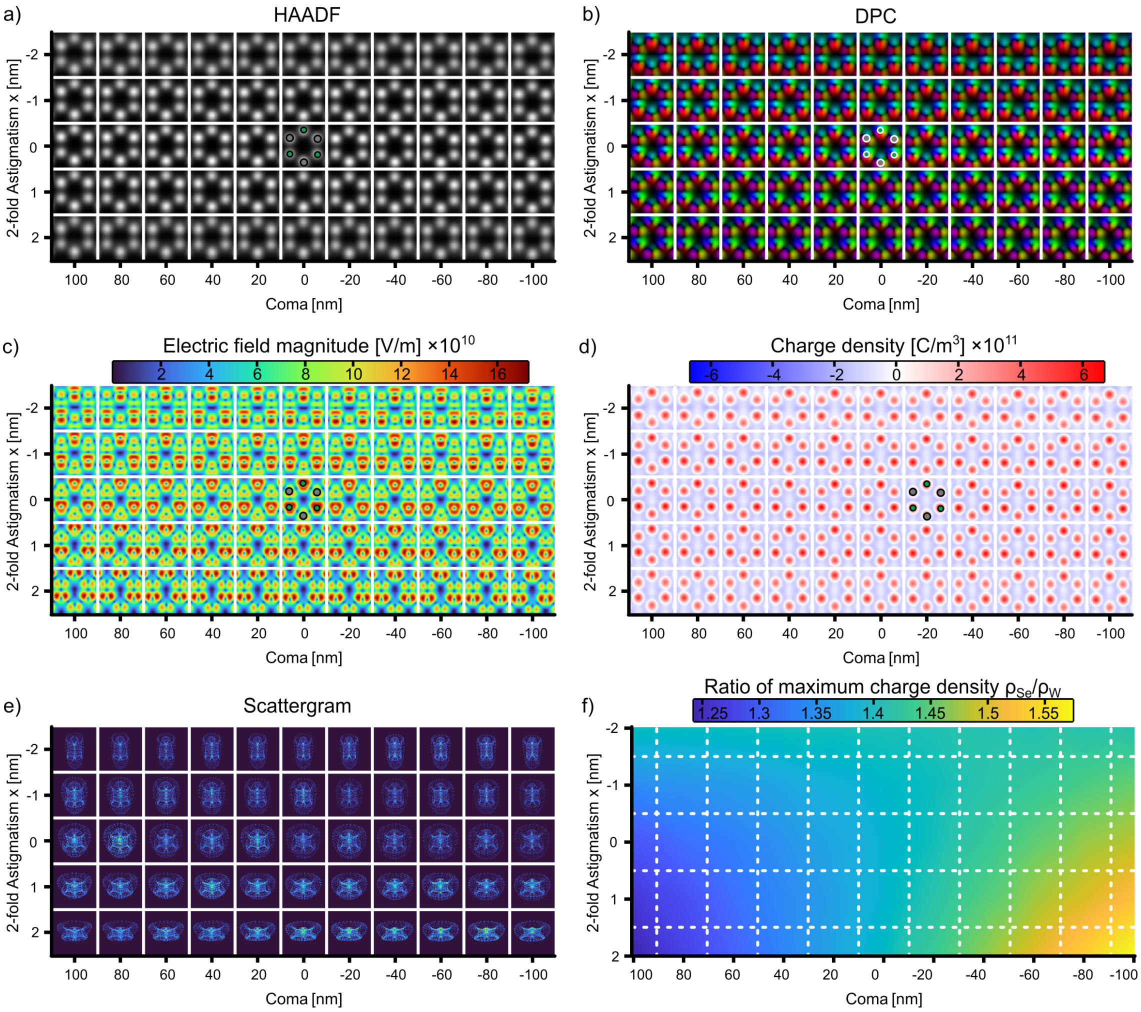

Figure 9.25: Multislice image simulation of different combinations of axial coma and 2-fold astigmatism in x-direction for a WSe_2 monolayer in [0001] zone-axis orientation. a) HAADF and b) normalized DPC images as well as c) the electric field magnitude maps and d) the charge density maps. The DPC images are individually normalized for a better visibility of colours. Thus, reductions in field magnitude can not be compared between the DPC images. e) Scattergrams with normalized intensity for each simulated DPC image. f) Map of the charge density ratio between the maximum positive charge density at selenium atomic columns and the maximum positive charge density at tungsten atomic columns.

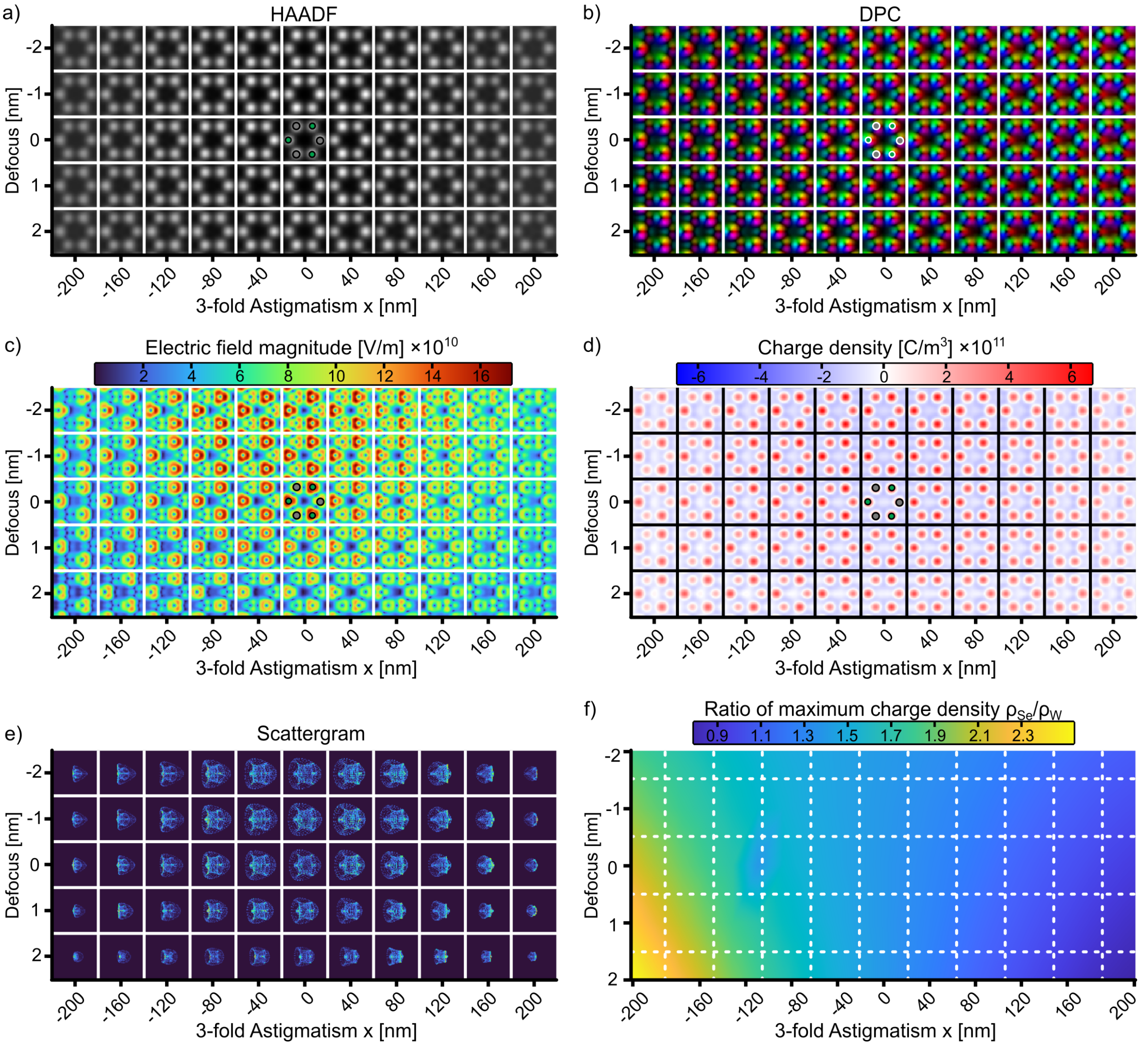

Figure 9.26: Multislice image simulation of different combinations of 3-fold astigmatism in x-direction and defocus for a WSe_2 monolayer in [0001] zone-axis orientation. a) HAADF and b) normalized DPC images as well as c) the electric field magnitude maps and d) the charge density maps. The DPC images are individually normalized for a better visibility of colours. Thus, reductions in field magnitude can not be compared between the DPC images. e) Scattergrams with normalized intensity for each simulated DPC image. f) Map of the charge density ratio between the maximum positive charge density at selenium atomic columns and the maximum positive charge density at tungsten atomic columns.

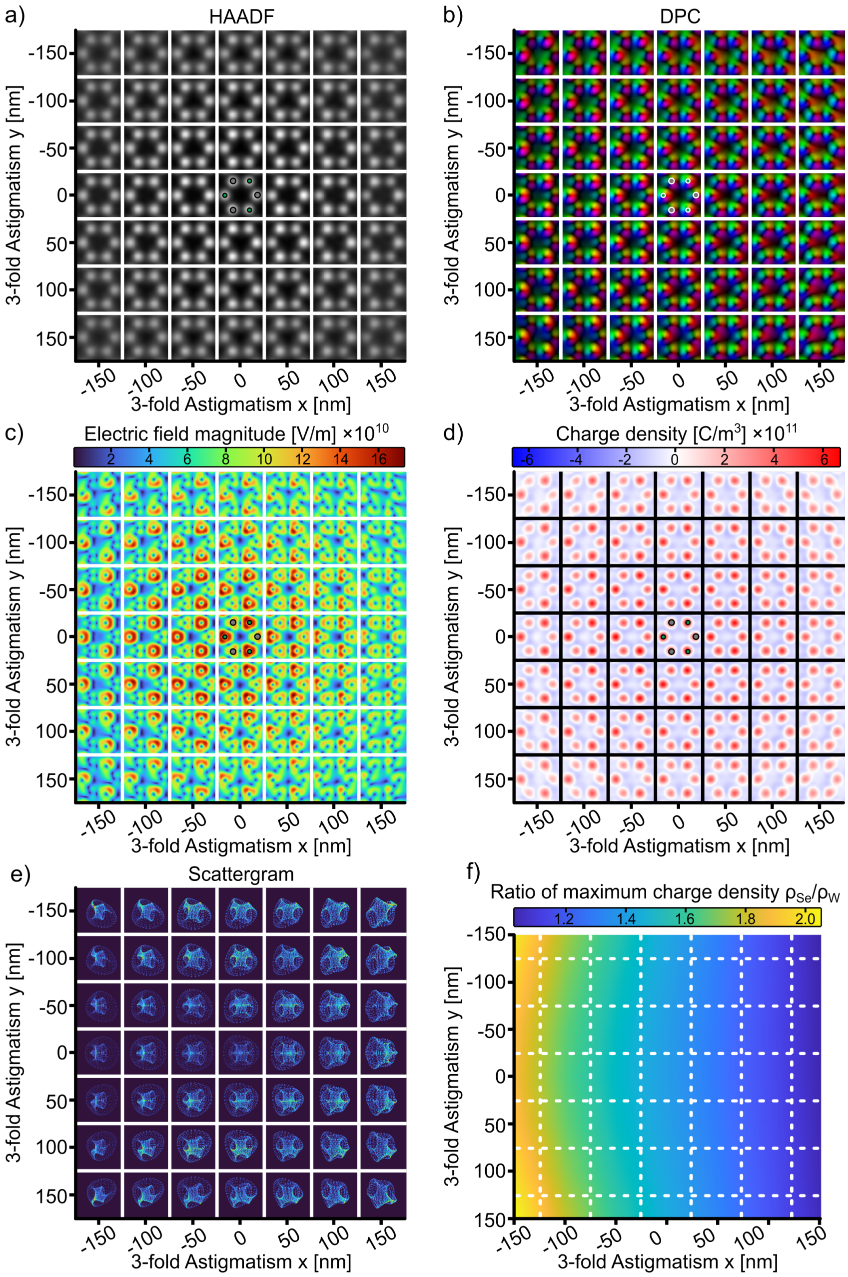

Figure 9.27: Multislice image simulation of different combinations of 3-fold astigmatism in x- and y-direction for a WSe_2 monolayer in [0001] zone-axis orientation. a) HAADF and b) normalized DPC images as well as c) the electric field magnitude maps and d) the charge density maps. The DPC images are individually normalized for a better visibility of colours. Thus, reductions in field magnitude can not be compared between the DPC images. e) Scattergrams with normalized intensity for each simulated DPC image. f) Map of the charge density ratio between the maximum positive charge density at selenium atomic columns and the maximum positive charge density at tungsten atomic columns.

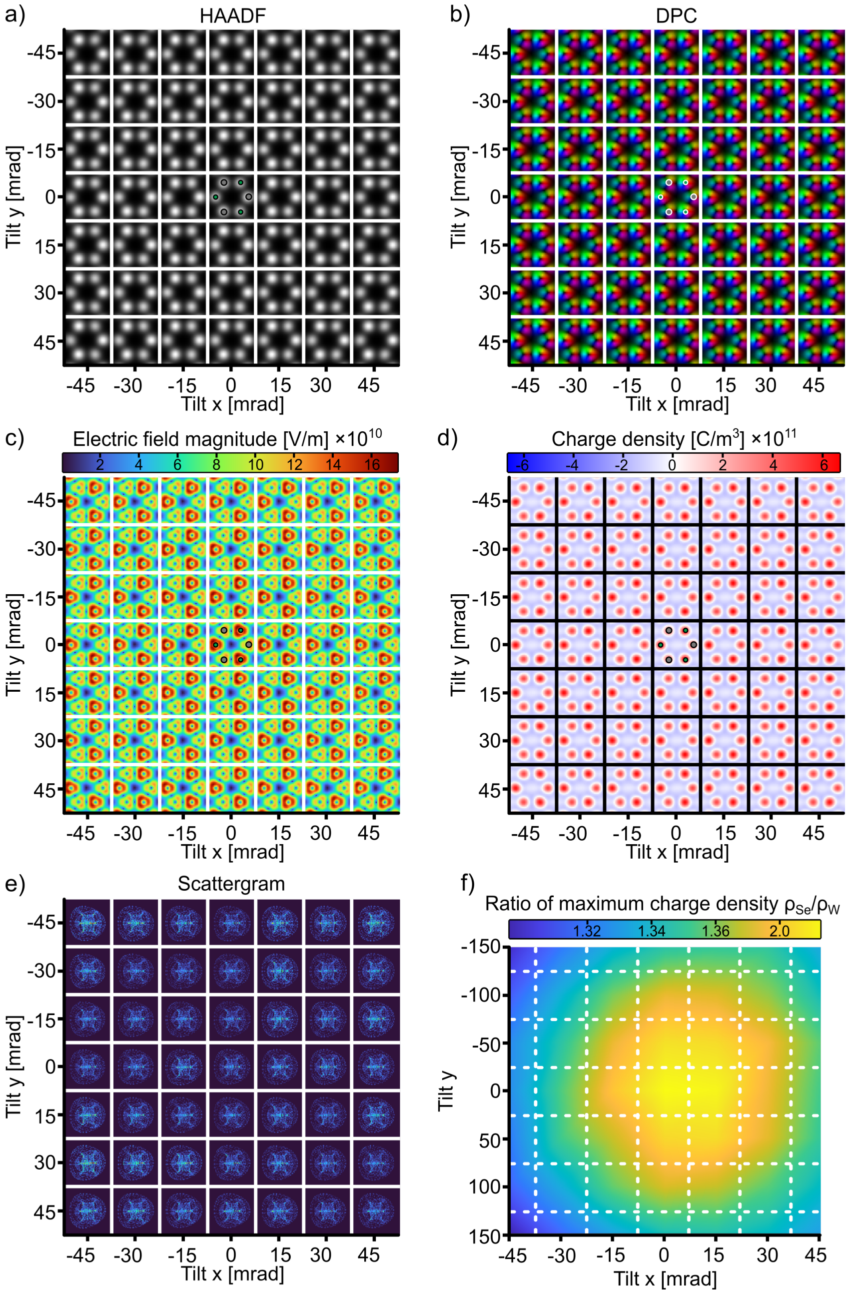

Figure 9.28: Multislice image simulation of different tilt angle in x- and y-direction for a WSe_2 monolayer in [0001] zone-axis orientation. a) HAADF and b) normalized DPC images as well as c) the electric field magnitude maps and d) the charge density maps. The DPC images are individually normalized for a better visibility of colours. Thus, reductions in field magnitude can not be compared between the DPC images. e) Scattergrams with normalized intensity for each simulated DPC image. f) Map of the charge density ratio between the maximum positive charge density at selenium atomic columns and the maximum positive charge density at tungsten atomic columns.

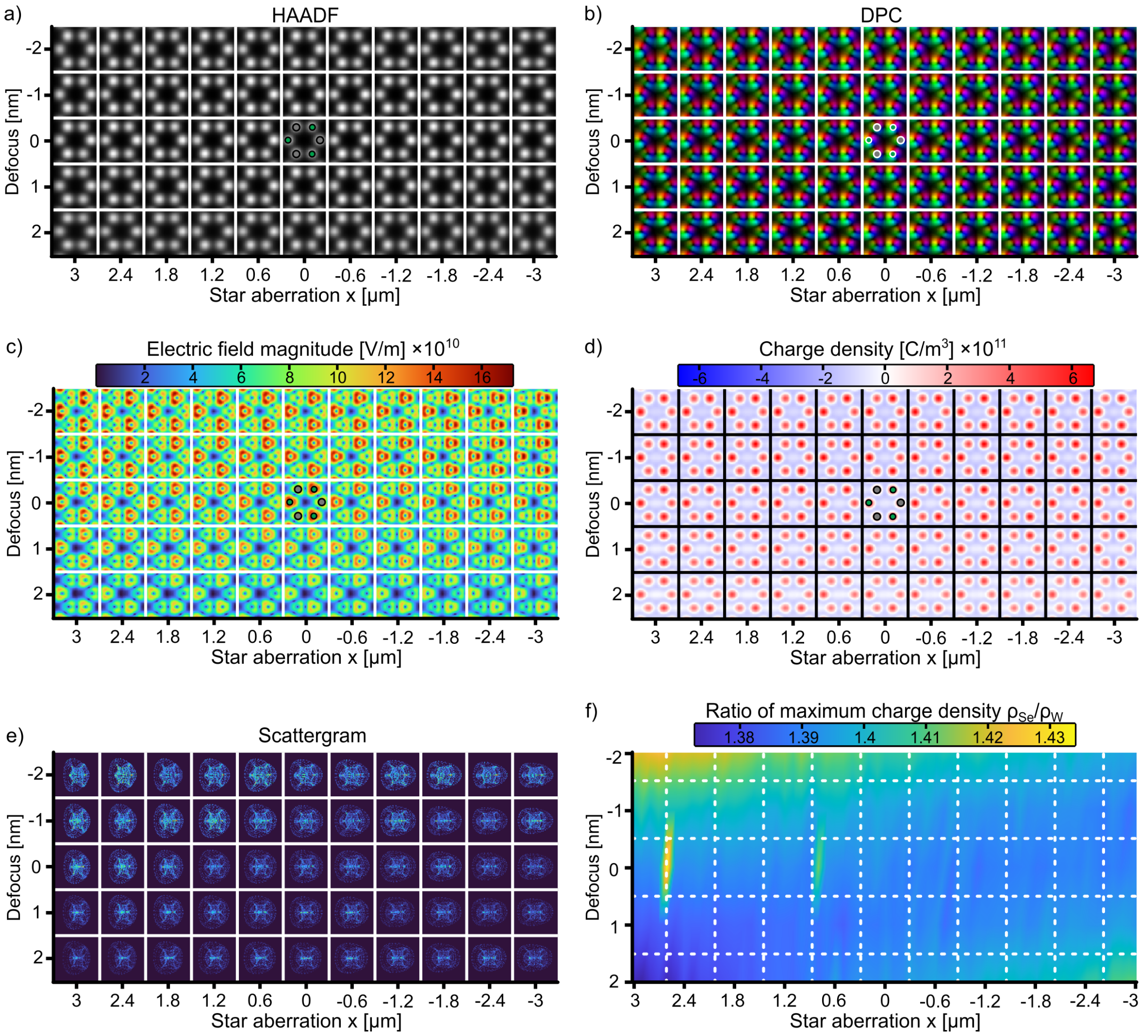

Figure 9.29: Multislice image simulation of different combinations of star aberration in x- and defocus for a WSe_2 monolayer in [0001] zone-axis orientation. a) HAADF and b) normalized DPC images as well as c) the electric field magnitude maps and d) the charge density maps. The DPC images are individually normalized for a better visibility of colours. Thus, reductions in field magnitude can not be compared between the DPC images. e) Scattergrams with normalized intensity for each simulated DPC image. f) Map of the charge density ratio between the maximum positive charge density at selenium atomic columns and the maximum positive charge density at tungsten atomic columns.

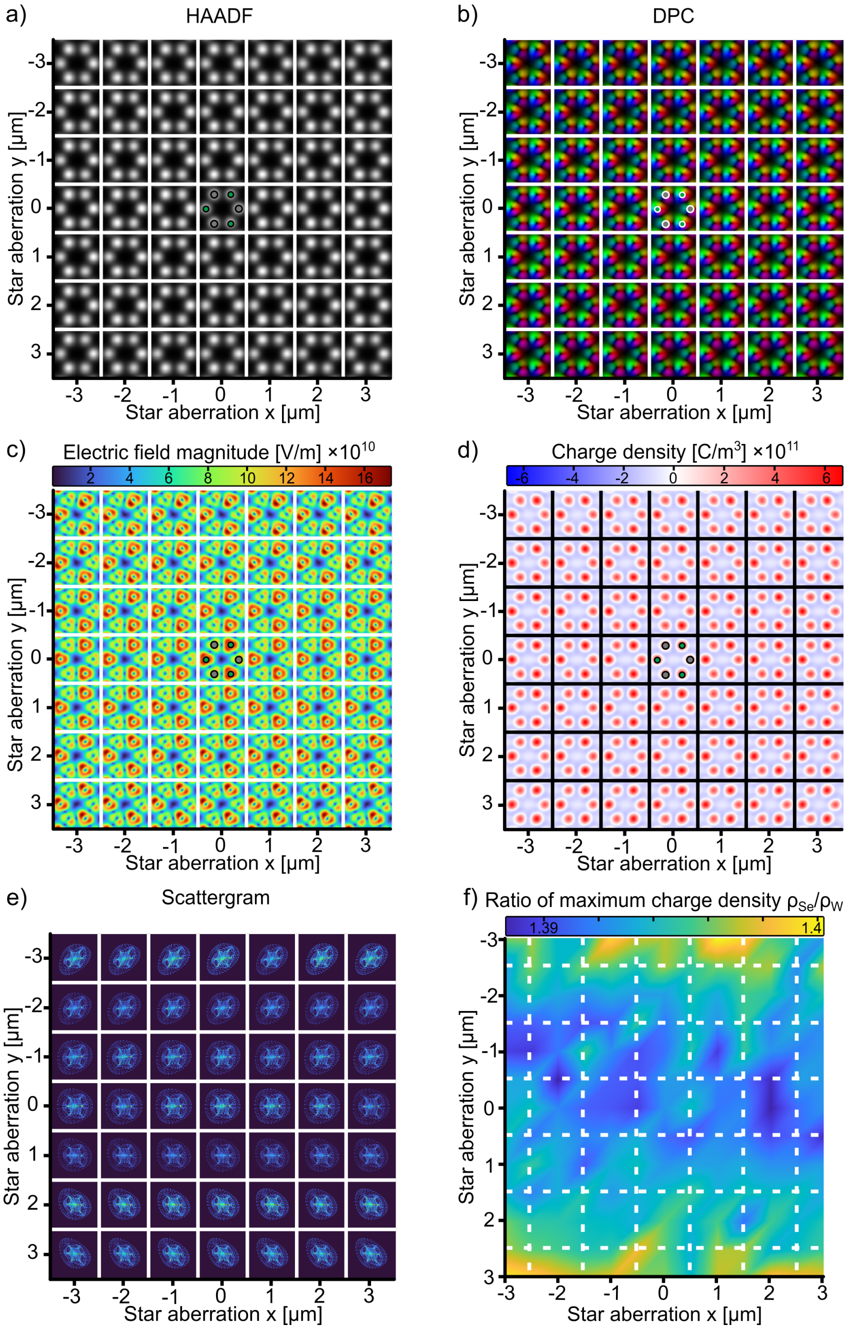

Figure 9.30: Multislice image simulation of different combinations of star aberration in x- and y-direction for a WSe_2 monolayer in [0001] zone-axis orientation. a) HAADF and b) normalized DPC images as well as c) the electric field magnitude maps and d) the charge density maps. The DPC images are individually normalized for a better visibility of colours. Thus, reductions in field magnitude can not be compared between the DPC images. e) Scattergrams with normalized intensity for each simulated DPC image. f) Map of the charge density ratio between the maximum positive charge density at selenium atomic columns and the maximum positive charge density at tungsten atomic columns.

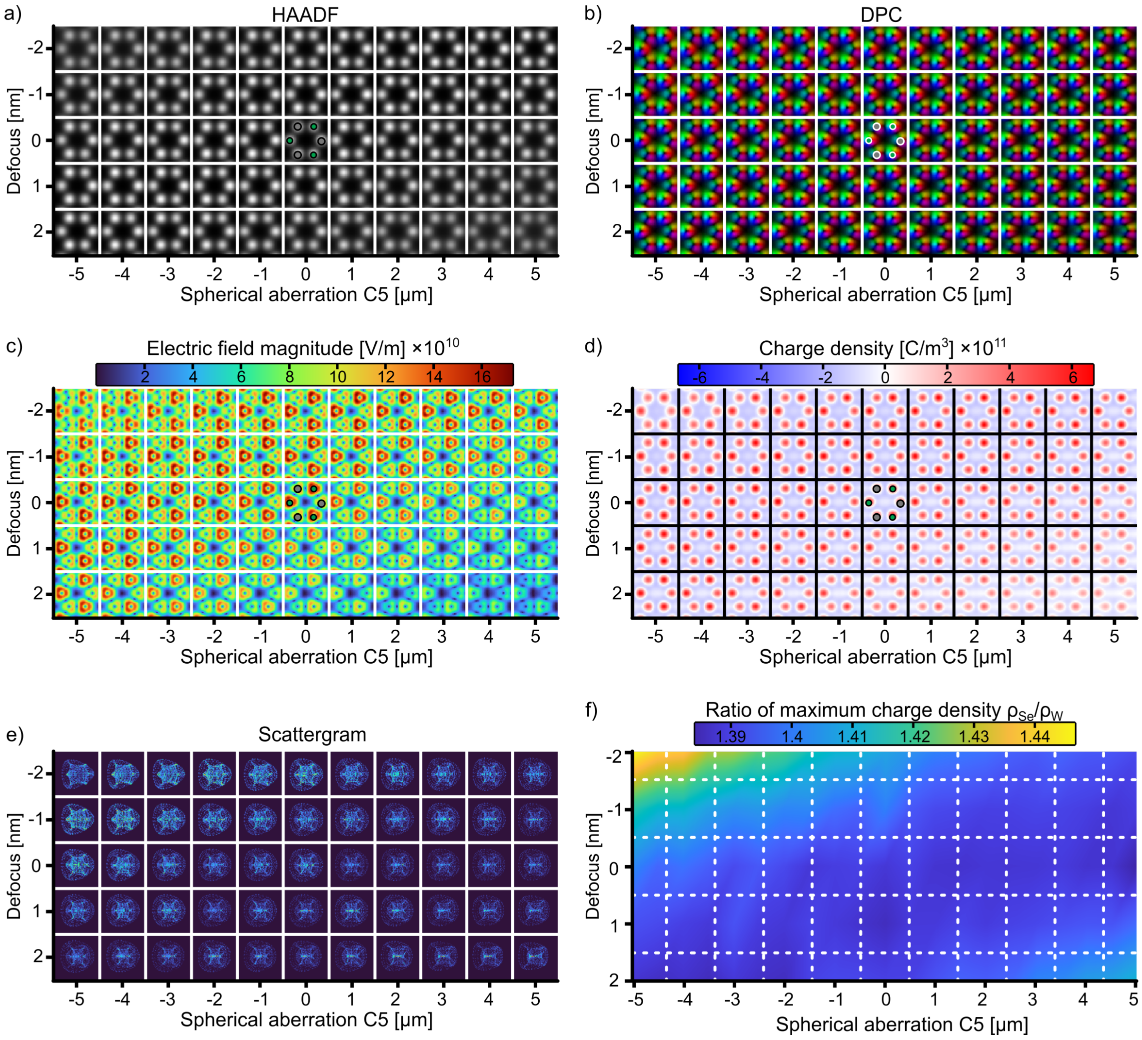

Figure 9.31: Multislice image simulation of different combinations of spherical aberration and defocus for a WSe_2 monolayer in [0001] zone-axis orientation. a) HAADF and b) normalized DPC images as well as c) the electric field magnitude maps and d) the charge density maps. The DPC images are individually normalized for a better visibility of colours. Thus, reductions in field magnitude can not be compared between the DPC images. e) Scattergrams with normalized intensity for each simulated DPC image. f) Map of the charge density ratio between the maximum positive charge density at selenium atomic columns and the maximum positive charge density at tungsten atomic columns.

References

[1] N. Dekker and H. De Lang, *Optik* **41**, 452–456, (1974).

[2] H. Rose, *Ultramicroscopy* **2**, 251–267, (1976), DOI: 10.1016/S0304-3991(76)91538-2.

[3] H. Rose, *Optik* **39**, 416–436, (1974).

[4] K. Müller, F. F. Krause, A. Béché, M. Schowalter, V. Galioit, S. Löffler, J. Verbeeck, J. Zweck, P. Schattschneider, and A. Rosenauer, *Nature Communications* **5**, 5653, (2014), DOI: 10.1038/ncomms6653.

[5] R. Close, Z. Chen, N. Shibata, and S. Findlay, *Ultramicroscopy* **159**, 124–137, (2015), DOI: 10.1016/j.ultramic.2015.09.002.

[6] I. Lazić, E. G. Bosch, and S. Lazar, *Ultramicroscopy* **160**, 265–280, (2016), DOI: 10.1016/j.ultramic.2015.10.011.

[7] K. Müller-Caspary, F. F. Krause, T. Grieb, S. Löffler, M. Schowalter, A. Béché, V. Galioit, D. Marquardt, J. Zweck, P. Schattschneider, J. Verbeeck, and A. Rosenauer, *Ultramicroscopy* **178**, 62–80, (2017), DOI: 10.1016/j.ultramic.2016.05.004.

[8] N. Shibata, T. Seki, G. Sánchez-Santolino, S. D. Findlay, Y. Kohno, T. Matsumoto, R. Ishikawa, and Y. Ikuhara, *Nature Communications* **8**, 15631, (2017), DOI: 10.1038/ncomms15631.

[9] D. Jannis, C. Hofer, C. Gao, X. Xie, A. Béché, T. Pennycook, and J. Verbeeck, *Ultramicroscopy* **233**, 113423, (2022), DOI: 10.1016/j.ultramic.2021.113423.

[10] D. G. Stroppa, M. Meffert, C. Hoermann, P. Zambon, D. Bachevskaya, H. Remigy, C. Schulze-Briese, and L. Piazza, *Microscopy Today* **31**, 10–14, (2023), DOI: 10.1093/mictod/qaad005.

[11] J. M. Bekkevold, J. J. P. Peters, R. Ishikawa, N. Shibata, and L. Jones, *Microscopy and Microanalysis* **30**, 878–888, (2024), DOI: 10.1093/mam/ozae082.

[12] N. Shibata, S. D. Findlay, H. Sasaki, T. Matsumoto, H. Sawada, Y. Kohno, S. Otomo, R. Minato, and Y. Ikuhara, *Scientific Reports* **5**, 10040, (2015), DOI: 10.1038/srep10040.

[13] H. G. Brown, N. Shibata, H. Sasaki, T. C. Petersen, D. M. Paganin, M. J. Morgan, and S. D. Findlay, *Ultramicroscopy* **182**, 169–178, (2017), DOI: 10.1016/j.ultramic.2017.07.002.

[14] L. Clark, H. G. Brown, D. M. Paganin, M. J. Morgan, T. Matsumoto, N. Shibata, T. C. Petersen, and S. D. Findlay, *Physical Review A* **97**, 043843, (2018), DOI: 10.1103/PhysRevA.97.043843.

[15] A. Beyer, M. S. Munde, S. Firoozabadi, D. Heimes, T. Grieb, A. Rosenauer, K. Müller-Caspary, and K. Volz, *Nano Letters* **21**, 2018–2025, (2021), DOI: 10.1021/acs.nanolett.0c04544.

[16] M. Lohr, R. Schregle, M. Jetter, C. Wächter, T. Wunderer, F. Scholz, and J. Zweck, *Ultramicroscopy* **117**, 7–14, (2012), DOI: 10.1016/j.ultramic.2012.03.020.

[17] C. Mahr, T. Grieb, F. F. Krause, M. Schowalter, and A. Rosenauer, *Ultramicroscopy* **236**, 113503, (2022), DOI: 10.1016/j.ultramic.2022.113503.

[18] J. N. Chapman, P. E. Batson, E. M. Waddell, and R. P. Ferrier, *Ultramicroscopy* **3**, 203–214, (1978), DOI: 10.1016/S0304-3991(78)80027-8.

[19] M. Krajnak, D. McGrouther, D. Maneuski, V. O. Shea, and S. McVitie, *Ultramicroscopy* **165**, 42–50, (2016), DOI: 10.1016/j.ultramic.2016.03.006.

[20] T. Matsumoto, Y.-G. So, Y. Kohno, H. Sawada, Y. Ikuhara, and N. Shibata, *Science Advances* **2**, e1501280, (2016), DOI: 10.1126/sciadv.1501280.

[21] D. McGrouther, R. J. Lamb, M. Krajnak, S. McFadzean, S. McVitie, R. L. Stamps, A. O. Leonov, A. N. Bogdanov, and Y. Togawa, *New Journal of Physics* **18**, 095004, (2016), DOI: 10.1088/1367-2630/18/9/095004.

[22] H. Sawada, T. Sannomiya, F. Hosokawa, T. Nakamichi, T. Kaneyama, T. Tomita, Y. Kondo, T. Tanaka, Y. Oshima, Y. Tanishiro, and K. Takayanagi, *Ultramicroscopy* **108**, 1467–1475, (2008), DOI: 10.1016/j.ultramic.2008.04.095.

[23] R. Erni, M. D. Rossell, C. Kisielowski, and U. Dahmen, *Physical Review Letters* **102**, 096101, (2009), DOI: 10.1103/PhysRevLett.102.096101.

[24] N. Shibata, S. D. Findlay, Y. Kohno, H. Sawada, Y. Kondo, and Y. Ikuhara, *Nature Physics* **8**, 611–615, (2012), DOI: 10.1038/nphys2337.

[25] G. Sánchez-Santolino, N. R. Lugg, T. Seki, R. Ishikawa, S. D. Findlay, Y. Kohno, Y. Kanitani, S. Tanaka, S. Tomiya, Y. Ikuhara, and N. Shibata, *ACS Nano* **12**, 8875–8881, (2018), DOI: 10.1021/acsnano.8b03712.

[26] J. Bürger, T. Riedl, and J. K. Lindner, *Ultramicroscopy* **219**, 113118, (2020), DOI: 10.1016/j.ultramic.2020.113118.

[27] K. Müller-Caspary, M. Duchamp, M. Rösner, V. Migunov, F. Winkler, H. Yang, M. Huth, R. Ritz, M. Simson, S. Ihle, H. Soltau, T. Wehling, R. E. Dunin-Borkowski, S. Van Aert, and A. Rosenauer, *Physical Review B* **98**, 121408, (2018), DOI: 10.1103/PhysRevB.98.121408.

[28] K. Müller-Caspary, F. F. Krause, F. Winkler, A. Béché, J. Verbeeck, S. Van Aert, and A. Rosenauer, *Ultramicroscopy* **203**, 95–104, (2019), DOI: 10.1016/j.ultramic.2018.12.018.

[29] E. Yücelen, I. Lazić, and E. G. T. Bosch, *Scientific Reports* **8**, 2676, (2018), DOI: 10.1038/s41598-018-20377-2.

[30] Y. Hao, A. De Backer, S. D. Findlay, and S. Van Aert, *Ultramicroscopy* **268**, 114066, (2025), DOI: 10.1016/j.ultramic.2024.114066.

[31] J. S. Ponraj, Z.-Q. Xu, S. C. Dhanabalan, H. Mu, Y. Wang, J. Yuan, P. Li, S. Thakur, M. Ashrafi, K. Mccoubrey, Y. Zhang, S. Li, H. Zhang, and Q. Bao, *Nanotechnology* **27**, 462001, (2016), DOI: 10.1088/0957-4484/27/46/462001.

[32] K. F. Mak and J. Shan, *Nature Photonics* **10**, 216–226, (2016), DOI: 10.1038/nphoton.2015.282.

[33] M. Bernardi, C. Ataca, M. Palummo, and J. C. Grossman, *Nanophotonics* **6**, 479–493, (2017), DOI: 10.1515/nanoph-2015-0030.

[34] R. Ishikawa, S. D. Findlay, T. Seki, G. Sánchez-Santolino, Y. Kohno, Y. Ikuhara, and N. Shibata, *Nature Communications* **9**, 3878, (2018), DOI: 10.1038/s41467-018-06387-8.

[35] O. Cretu, A. Ishizuka, K. Yanagisawa, K. Ishizuka, and K. Kimoto, *ACS Nano* **15**, 5316–5321, (2021), DOI: 10.1021/acsnano.0c10849.

[36] A. A. Murthy, S. M. Ribet, T. K. Stanev, P. Liu, K. Watanabe, T. Taniguchi, N. P. Stern, R. d. Reis, and V. P. Dravid, *Nano Letters* **21**, 7131–7137, (2021), DOI: 10.1021/acs.nanolett.1c01636.

[37] S. Fang, Y. Wen, C. S. Allen, C. Ophus, G. G. D. Han, A. I. Kirkland, E. Kaxiras, and J. H. Warner, *Nature Communications* **10**, 1127, (2019), DOI: 10.1038/s41467-019-08904-9.

[38] S. Calderon V, R. V. Ferreira, D. Taneja, R. Jayanth, L. Zhou, R. M. Ribeiro, D. Akinwande, and P. J. Ferreira, *Nano Letters* **21**, 10157–10164, (2021), DOI: 10.1021/acs.nanolett.1c02334.

[39] S. de Graaf, M. Ahmadi, I. Lazić, E. G. T. Bosch, and B. J. Kooi, *Nanoscale* **13**, 20683–20691, (2021), DOI: 10.1039/D1NR06614E.

[40] D. Dosenovic, S. Dechamps, K. Sharma, J.-L. Rouviere, Y. Lu, M. I. den Hertog, L. Genovese, S. M.-M. Dubois, J.-C. Charlier, M. Jamet, A. Marty, and H. Okuno, *ACS Nano* **18**, 23354–23364, (2024), DOI: 10.1021/acsnano.4c06561.

[41] M. Groll, J. Bürger, I. Caltzidis, K. D. Jöns, W. G. Schmidt, U. Gerstmann, and J. K. N. Lindner, *Small* **20**, 2311635, (2024), DOI: 10.1002/smll.202311635.

[42] J. Martis, S. Susarla, A. Rayabharam, C. Su, T. Paule, P. Pelz, C. Huff, X. Xu, H.-K. Li, M. Jaikissoon, V. Chen, E. Pop, K. Saraswat, A. Zettl, N. R. Aluru, R. Ramesh, P. Ercius, and A. Majumdar, *Nature communications* **14**, 4363, (2023), DOI: 10.1038/s41467-023-39304-9.

[43] S. Tongay, J. Suh, C. Ataca, W. Fan, A. Luce, J. S. Kang, J. Liu, C. Ko, R. Raghunathanan, J. Zhou, F. Ogletree, J. Li, J. C. Grossman, and J. Wu, *Scientific Reports* **3**, 2657, (2013), DOI: 10.1038/srep02657.

[44] P. Tonndorf, R. Schmidt, R. Schneider, J. Kern, M. Buscema, G. A. Steele, A. Castellanos-Gomez, H. S. J. Van Der Zant, S. Michaelis De Vasconcellos, and R. Bratschitsch, *Optica* **2**, 347, (2015), DOI: 10.1364/OPTICA.2.000347.

[45] L. de Broglie, *Nobel Lecture*, (1929).

[46] N. D. Browning, M. F. Chisholm, and S. J. Pennycook, *Nature* **366**, 143–146, (1993), DOI: 10.1038/366143a0.

[47] R. F. Egerton, *Reports on Progress in Physics* **72**, 016502, (2009), DOI: 10.1088/0034-4885/72/1/016502.

[48] D. B. Williams and C. B. Carter, *Transmission electron microscopy : a textbook for materials science*, 2. ed. Springer New York, (2009), ISBN: 9780387765006.

[49] O. Scherzer, *Journal of Applied Physics* **20**, 20–29, (1949), DOI: 10.1063/1.1698233.

[50] M. Haider, H. Rose, S. Uhlemann, E. Schwan, B. Kabius, and K. Urban, *Ultramicroscopy* **75**, 53–60, (1998), DOI: 10.1016/S0304-3991(98)00048-5.

[51] E. M. James and N. D. Browning, *Ultramicroscopy* **78**, 125–139, (1999), DOI: 10.1016/S0304-3991(99)00018-2.

[52] M. Haider, S. Uhlemann, and J. Zach, *Ultramicroscopy* **81**, 163–175, (2000), DOI: 10.1016/S0304-3991(99)00194-1.

[53] A. J. Freeman, *Acta Crystallographica* **12**, 261–271, (1959), DOI: 10.1107/S0365110X59000834.

[54] D. T. Cromer and J. T. Waber, *Acta Crystallographica* **18**, 104–109, (1965), DOI: 10.1107/S0365110X6500018X.

[55] P. A. Doyle and P. S. Turner, *Acta Crystallographica Section A* **24**, 390–397, (1968), DOI: 10.1107/S0567739468000756.

[56] L.-M. Peng, *Micron* **30**, 625–648, (1999), DOI: 10.1016/S0968-4328(99)00033-5.

[57] J. A. Ibers, *Acta Crystallographica* **11**, 178–183, (1958), DOI: 10.1107/S0365110X58000475.

[58] P. J. Brown, A. G. Fox, E. N. Maslen, M. A. O'Keefe, and B. T. M. Willis, *International Tables for Crystallography* **C**, 554–595, (2006), DOI: 10.1107/97809553602060000600.

[59] C. Colliex, J. M. Cowley, S. L. Dudarev, M. Fink, J. Gjùnnes, R. Hilderbrandt, A. Howie, D. F. Lynch, L. M. Peng, G. Ren, A. W. Ross, V. H. S. Jr, J. C. H. Spence, J. W. Steeds, J. Wang, M. J. Whelan, and B. B. Zvyagin, "4.3. Electron diffraction," in *International Tables for Crystallography.* (2006), pages 259–429.

[60] B. Fultz and J. M. Howe, *Transmission Electron Microscopy and Diffractometry of Materials*, Third Edition. Berlin, Heidelberg : Springer-Verlag Berlin Heidelberg, (2008). DOI: 10.1007/978-3-540-73886-2.

[61] N. D. Browning, D. J. Wallis, P. D. Nellist, and S. J. Pennycook, *Micron* **28**, 333–348, (1997), DOI: 10.1016/S0968-4328(97)00033-4.

[62] R. Egerton, *Electron Energy-Loss Spectroscopy in the Electron Microscope*. Boston, MA: Springer US, (2011). DOI: 10.1007/978-1-4419-9583-4.

[63] J. Barthel, *Ultramicroscopy* **193**, 1–11, (2018), DOI: url{10.1016/j.ultramic.2018.06.003}.

[64] P. D. Nellist, "The Principles of STEM Imaging," in *Scanning Transmission Electron Microscopy: Imaging and Analysis*, S. J. Pennycook, Ed. New York, NY: Springer New York, (2011), pages 91–115. DOI: 10.1007/978-1-4419-7200-2_2.

[65] O. Krivanek, N. Dellby, and A. Lupini, *Ultramicroscopy* **78**, 1–11, (1999), DOI: 10.1016/S0304-3991(99)00013-3.

[66] E. G. Bosch and I. Lazić, *Ultramicroscopy* **156**, 59–72, (2015), DOI: 10.1016/j.ultramic.2015.02.004.

[67] E. J. Kirkland, *Advanced Computing in Electron Microscopy*. Springer US, (2010), ISBN: 978-1-4419-6533-2. DOI: 10.1007/978-1-4419-6533-2.

[68] S. J. Pennycook, "Scanning Transmission Electron Microscopy: Z-Contrast Imaging," in *Characterization of Materials*, John Wiley & Sons, Ltd, (2012), pages 1–29, ISBN: 978-0-471-26696-9. DOI: 10.1002/0471266965.com083.pub2.

[69] A. V. Crewe, J. Wall, and J. Langmore, *Science* **168**, 1338–1340, (1970), DOI: 10.1126/science.168.3937.1338.

[70] S. Pennycook, B. Rafferty, and P. Nellist, *Microscopy and Microanalysis* **6**, 343–352, (2000), DOI: 10.1007/s100050010045.

[71] M. De La Mata and S. I. Molina, *Nanomaterials* **12**, 337, (2022), DOI: 10.3390/nano12030337.

[72] S. Yamashita, J. Kikkawa, K. Yanagisawa, T. Nagai, K. Ishizuka, and K. Kimoto, *Scientific Reports* **8**, 12325, (2018), DOI: 10.1038/s41598-018-30941-5.

[73] M. Vulović, L. M. Voortman, L. J. Van Vliet, and B. Rieger, *Ultramicroscopy* **136**, 61–66, (2014), DOI: 10.1016/j.ultramic.2013.08.002.

[74] T. Seki, K. Khare, Y. O. Murakami, S. Toyama, G. Sánchez-Santolino, H. Sasaki, S. D. Findlay, T. C. Petersen, Y. Ikuhara, and N. Shibata, *Ultramicroscopy* **240**, 113580, (2022), DOI: 10.1016/j.ultramic.2022.113580.

[75] J. Madsen, T. J. Pennycook, and T. Susi, *Ultramicroscopy* **231**, 113253, (2021), DOI: 10.1016/j.ultramic.2021.113253.

[76] S. McVitie, D. McGrouther, S. McFadzean, D. MacLaren, K. O'Shea, and M. Benitez, *Ultramicroscopy* **152**, 57–62, (2015), DOI: 10.1016/j.ultramic.2015.01.003.

[77] J. Zweck, F. Schwarzhuber, J. Wild, and V. Galioit, *Ultramicroscopy* **168**, 53–64, (2016), DOI: 10.1016/j.ultramic.2016.05.007.

[78] F. Schwarzhuber, P. Melzl, and J. Zweck, *Ultramicroscopy* **177**, 97–105, (2017), DOI: 10.1016/j.ultramic.2017.02.005.

[79] N. Shibata, *Journal of the Ceramic Society of Japan* **127**, 708–714, (2019), DOI: 10.2109/jcersj2.19118.

[80] T. Seki, Y. Ikuhara, and N. Shibata, *Microscopy* **70**, 148–160, (2021), DOI: 10.1093/jmicro/dfaa065.

[81] L. Reimer, *Transmission Electron Microscopy: Physics of Image Formation and Microanalysis.* Springer, (2013), ISBN: 978-3-662-13553-2.

[82] A. Edström, A. Lubk, and J. Rusz, *Physical Review B* **99**, 174428, (2019), DOI: 10.1103/PhysRevB.99.174428.

[83] Z. Li, J. Biskupek, U. Kaiser, and H. Rose, *Microscopy and Microanalysis* **28**, 611–621, (2022), DOI: 10.1017/S1431927622000289.

[84] J. Bürger, "Contributions to differential phase contrast imaging," Dissertation, Universität Paderborn, (2024).

[85] T. J. Pennycook, A. R. Lupini, H. Yang, M. F. Murfitt, L. Jones, and P. D. Nellist, *Ultramicroscopy* **151**, 160–167, (2015), DOI: 10.1016/j.ultramic.2014.09.013.

[86] T. Seki, G. Sánchez-Santolino, R. Ishikawa, S. D. Findlay, Y. Ikuhara, and N. Shibata, *Ultramicroscopy* **182**, 258–263, (2017), DOI: 10.1016/j.ultramic.2017.07.013.

[87] H. Yang, T. J. Pennycook, and P. D. Nellist, *Ultramicroscopy* **151**, 232–239, (2015), DOI: 10.1016/j.ultramic.2014.10.013.

[88] J. M. Bekkevold, S. M. Ribet, M. C. Scott, L. Jones, C. Ophus, and G. Varnavides, *Elemental Microscopy*, (2025), DOI: 10.69761/ehch7395.

[89] J. Madsen and T. Susi, *The abTEM code: Transmission electron microscopy from first principles*, (2021). DOI: 10.12688/openreseurope.13015.2.

[90] M. Kulik and P. M. Dominiak, *Computational and Structural Biotechnology Journal* **20**, 6237–6243, (2022), DOI: 10.1016/j.csbj.2022.10.018.

[91] P. Hohenberg and W. Kohn, *Physical Review* **136**, 864–871, (1964), DOI: 10.1103/PhysRev.136.B864.

[92] W. Kohn, *Nobel Lecture*, (1999), DOI: 10.1103/RevModPhys.71.1253.

[93] W. Kohn and L. J. Sham, *Physical Review* **140**, 1133–1138, (1965), DOI: 10.1103/PhysRev.140.A1133.

[94] E. Engel and R. M. Dreizler, *Density Functional Theory: An Advanced Course* (Theoretical and Mathematical Physics). Berlin, Heidelberg: Springer, (2011). DOI: 10.1007/978-3-642-14090-7.

[95] P. E. Blöchl, *Physical Review B* **50**, 17953–17979, (1994), DOI: 10.1103/PhysRevB.50.17953.

[96] C. Rostgaard, *The Projector Augmented-wave Method*, (2009). DOI: 10.48550/arXiv.0910.1921.

[97] K. S. Novoselov, A. K. Geim, S. V. Morozov, D. Jiang, Y. Zhang, S. V. Dubonos, I. V. Grigorieva, and A. A. Firsov, *Science* **306**, 666–669, (2004), DOI: 10.1126/science.1102896.

[98] K. S. Novoselov, D. Jiang, F. Schedin, T. J. Booth, V. V. Khotkevich, S. V. Morozov, and A. K. Geim, *Proceedings of the National Academy of Sciences* **102**, 10451–10453, (2005), DOI: 10.1073/pnas.0502848102.

[99] A. K. Geim and K. S. Novoselov, *Nature Materials* **6**, 183–191, (2007), DOI: 10.1038/nmat1849.

[100] N. Alem, R. Erni, C. Kisielowski, M. D. Rossell, W. Gannett, and A. Zettl, *Physical Review B* **80**, 155425, (2009), DOI: 10.1103/PhysRevB.80.155425.

[101] Q. H. Wang, K. Kalantar-Zadeh, A. Kis, J. N. Coleman, and M. S. Strano, *Nature nanotechnology* **7**, 699–712, (2012), DOI: 10.1038/nnano.2012.193.

[102] J. Gusakova, X. Wang, L. L. Shiau, A. Krivosheeva, V. Shaposhnikov, V. Borisenko, V. Gusakov, and B. K. Tay, *physica status solidi (a)* **214**, 1700218, (2017), DOI: 10.1002/pssa.201700218.

[103] T. Li and G. Galli, *The Journal of Physical Chemistry C* **111**, 16192–16196, (2007), DOI: 10.1021/jp075424v.

[104] S. Lebègue and O. Eriksson, *Physical Review B* **79**, 115409, (2009), DOI: 10.1103/PhysRevB.79.115409.

[105] A. Splendiani, L. Sun, Y. Zhang, T. Li, J. Kim, C.-Y. Chim, G. Galli, and F. Wang, *Nano Letters* **10**, 1271–1275, (2010), DOI: 10.1021/nl903868w.

[106] M. Chhowalla, H. S. Shin, G. Eda, L.-J. Li, K. P. Loh, and H. Zhang, *Nature Chemistry* **5**, 263–275, (2013), DOI: 10.1038/nchem.1589.

[107] A. K. Geim and I. V. Grigorieva, *Nature* **499**, 419–425, (2013), DOI: 10.1038/nature12385.

[108] K. S. Novoselov, A. Mishchenko, A. Carvalho, and A. H. Castro Neto, *Science* **353**, aac9439, (2016), DOI: 10.1126/science.aac9439.

[109] W. S. Yun, S. W. Han, S. C. Hong, I. G. Kim, and J. D. Lee, *Physical Review B* **85**, 033305, (2012), DOI: 10.1103/PhysRevB.85.033305.

[110] P. Johari and V. B. Shenoy, *ACS Nano* **6**, 5449–5456, (2012), DOI: 10.1021/nn301320r.

[111] S. Kumar, A. Kaczmarczyk, and B. D. Gerardot, *Nano Letters* **15**, 7567–7573, (2015), DOI: 10.1021/acs.nanolett.5b03312.

[112] W.-F. Li, C. Fang, and M. A. Van Huis, *Physical Review B* **94**, 195425, (2016), DOI: 10.1103/PhysRevB.94.195425.

[113] B. Radisavljevic, A. Radenovic, J. Brivio, V. Giacometti, and A. Kis, *Nature Nanotechnology* **6**, 147–150, (2011), DOI: 10.1038/nnano.2010.279.

[114] Y. Yoon, K. Ganapathi, and S. Salahuddin, *Nano Letters* **11**, 3768–3773, (2011), DOI: 10.1021/nl2018178.

[115] B. Radisavljevic and A. Kis, *Nature Materials* **12**, 815–820, (2013), DOI: 10.1038/nmat3687.

[116] O. Lopez-Sanchez, D. Lembke, M. Kayci, A. Radenovic, and A. Kis, *Nature Nanotechnology* **8**, 497–501, (2013), DOI: 10.1038/nnano.2013.100.

[117] D. Lembke, S. Bertolazzi, and A. Kis, *Accounts of Chemical Research* **48**, 100–110, (2015), DOI: 10.1021/ar500274q.

[118] A. Sebastian, R. Pendurthi, T. H. Choudhury, J. M. Redwing, and S. Das, *Nature Communications* **12**, 693, (2021), DOI: 10.1038/s41467-020-20732-w.

[119] P. Villars and K. Cenzual, Eds., *WSe2 Crystal Structure: Datasheet from "PAULING FILE Multinaries Edition – 2022" in SpringerMaterials*. [Online]. Available: `https://materials.springer.com/isp/crystallographic/docs/sd_0532311`.

[120] M. Traving, M. Boehme, L. Kipp, M. Skibowski, F. Starrost, E. E. Krasovskii, A. Perlov, and W. Schattke, *Physical Review B* **55**, 10392–10399, (1997), DOI: 10.1103/PhysRevB.55.10392.

[121] D. Voß, P. Krüger, A. Mazur, and J. Pollmann, *Physical Review B* **60**, 14311–14317, (1999), DOI: 10.1103/PhysRevB.60.14311.

[122] T. Jiang, H. Liu, D. Huang, S. Zhang, Y. Li, X. Gong, Y.-R. Shen, W.-T. Liu, and S. Wu, *Nature Nanotechnology* **9**, 825–829, (2014), DOI: 10.1038/nnano.2014.176.

[123] M. Xia, B. Li, K. Yin, G. Capellini, G. Niu, Y. Gong, W. Zhou, P. M. Ajayan, and Y.-H. Xie, *ACS nano* **9**, 12246–12254, (2015), DOI: 10.1021/acsnano.5b05474.

[124] Y.-M. He, G. Clark, J. R. Schaibley, Y. He, M.-C. Chen, Y.-J. Wei, X. Ding, Q. Zhang, W. Yao, X. Xu, C.-Y. Lu, and J.-W. Pan, *Nature Nanotechnology* **10**, 497–502, (2015), DOI: 10.1038/nnano.2015.75.

[125] W. Li, T. Wang, X. Dai, X. Wang, C. Zhai, Y. Ma, and S. Chang, *Solid State Communications* **225**, 32–37, (2016), DOI: 10.1016/j.ssc.2015.10.013.

[126] A. Mahmoudi, M. Bouaziz, D. Romanin, M. Pala, A. Thieffry, T. Brulé, J. Chaste, F. Oehler, and A. Ouerghi, *Physical Review B* **110**, 165418, (2024), DOI: 10.1103/PhysRevB.110.165418.

[127] Z. Li, J. Förste, K. Watanabe, T. Taniguchi, B. Urbaszek, A. S. Baimuratov, I. C. Gerber, A. Högele, and I. Bilgin, *Physical Review B* **106**, 045411, (2022), DOI: 10.1103/PhysRevB.106.045411.

[128] X. Li, X. Shi, D. Marian, D. Soriano, T. Cusati, G. Iannaccone, G. Fiori, Q. Guo, W. Zhao, and Y. Wu, *Science Advances* **9**, eade5706, (2023), DOI: 10.1126/sciadv.ade5706.

[129] G. Constantinescu, A. Kuc, and T. Heine, *Physical Review Letters* **111**, 036104, (2013), DOI: 10.1103/PhysRevLett.111.036104.

[130] A. Kumar and P. K. Ahluwalia, *Modelling and Simulation in Materials Science and Engineering* **21**, 065015, (2013), DOI: 10.1088/0965-0393/21/6/065015.

[131] K. M. McCreary, M. Phillips, H.-J. Chuang, D. Wickramaratne, M. Rosenberger, C. S. Hellberg, and B. T. Jonker, *Nanoscale* **14**, 147–156, (2022), DOI: 10.1039/D1NR06119D.

[132] X. Wen, Z. Gong, and D. Li, *InfoMat* **1**, 317–337, (2019), DOI: 10.1002/inf2.12024.

[133] X. Yin, Z. Ye, D. A. Chenet, Y. Ye, K. O'Brien, J. C. Hone, and X. Zhang, *Science* **344**, 488–490, (2014), DOI: 10.1126/science.1250564.

[134] W. Zhang, Q. Wang, Y. Chen, Z. Wang, and A. T. S. Wee, *2D Materials* **3**, 022001, (2016), DOI: 10.1088/2053-1583/3/2/022001.

[135] Z. Chu, E. C. Regan, X. Ma, D. Wang, Z. Xu, M. I. B. Utama, K. Yumigeta, M. Blei, K. Watanabe, T. Taniguchi, S. Tongay, F. Wang, and K. Lai, *Physical Review Letters* **125**, 186803, (2020), DOI: 10.1103/PhysRevLett.125.186803.

[136] D. Litvinov, A. Wu, M. Barbosa, K. Vaklinova, M. Grzeszczyk, G. Baldi, M. Zhu, and M. Koperski, *Materials Science and Engineering: R: Reports* **163**, 100928, (2025), DOI: 10.1016/j.mser.2025.100928.

[137] Z. Lin, B. R. Carvalho, E. Kahn, R. Lv, R. Rao, H. Terrones, M. A. Pimenta, and M. Terrones, *2D Materials* **3**, 022002, (2016), DOI: 10.1088/2053-1583/3/2/022002.

[138] Z. Wu, Z. Luo, Y. Shen, W. Zhao, W. Wang, H. Nan, X. Guo, L. Sun, X. Wang, Y. You, and Z. Ni, *Nano Research* **9**, 3622–3631, (2016), DOI: 10.1007/s12274-016-1232-5.

[139] J. Jiang, T. Xu, J. Lu, L. Sun, and Z. Ni, *Research* **2019**, 2019/4641739, (2019), DOI: 10.34133/2019/4641739.

[140] H.-P. Komsa and A. V. Krasheninnikov, "Chapter 2 - Physics and theory of defects in 2D materials: The role of reduced dimensionality," in *Defects in Two-Dimensional Materials*, R. Addou and L. Colombo, Eds., Elsevier, (2022), pages 7–41, ISBN: 978-0-12-820292-0. DOI: 10.1016/B978-0-12-820292-0.00008-2.

[141] H.-P. Komsa and A. V. Krasheninnikov, *Physical Review B* **91**, 125304, (2015), DOI: 10.1103/PhysRevB.91.125304.

[142] S. Haldar, H. Vovusha, M. K. Yadav, O. Eriksson, and B. Sanyal, *Physical Review B* **92**, 235408, (2015), DOI: 10.1103/PhysRevB.92.235408.

[143] K. Ko, M. Jang, J. Kwon, and J. Suh, *Journal of Applied Physics* **135**, 100901, (2024), DOI: 10.1063/5.0185604.

[144] W. Zhou, X. Zou, S. Najmaei, Z. Liu, Y. Shi, J. Kong, J. Lou, P. M. Ajayan, B. I. Yakobson, and J.-C. Idrobo, *Nano Letters* **13**, 2615–2622, (2013), DOI: 10.1021/nl4007479.

[145] F. Liu and Z. Fan, *Chem. Soc. Rev.* **52**, 1723–1772, (2023), DOI: 10.1039/D2CS00931E.

[146] A. Srivastava, M. Sidler, A. V. Allain, D. S. Lembke, A. Kis, and A. Imamoğlu, *Nature Nanotechnology* **10**, 491–496, (2015), DOI: 10.1038/nnano.2015.60.

[147] S. Hou, H. Hu, M. Xu, J. Zhang, H. Xiao, Z. Liu, W. Xing, X. Liu, S. You, B. Liu, Y. Zhang, J. Yu, Z. Xie, X. He, J. Zhang, and Y. Hao, *Advanced Optical Materials* **13**, 2500693, (2025), DOI: 10.1002/adom.202500693.

[148] A. K. Singh, *2D Transition-Metal Dichalcogenides (TMDs): Fundamentals and Application* (Materials Horizons: From Nature to Nanomaterials). Springer Singapore, (2025). DOI: 10.1007/978-981-96-0247-6.

[149] X. Wang, J. Wu, Y. Zhang, Y. Sun, K. Ma, Y. Xie, W. Zheng, Z. Tian, Z. Kang, and Y. Zhang, *Advanced Materials* **35**, 2206576, (2023), DOI: 10.1002/adma.202206576.

[150] M. G. Sensoy, D. Vinichenko, W. Chen, C. M. Friend, and E. Kaxiras, *Physical Review B* **95**, 014106, (2017), DOI: 10.1103/PhysRevB.95.014106.

[151] E. Mitterreiter, B. Schuler, A. Micevic, D. Hernangómez-Pérez, K. Barthelmi, K. A. Cochrane, J. Kiemle, F. Sigger, J. Klein, E. Wong, E. S. Barnard, K. Watanabe, T. Taniguchi, M. Lorke, F. Jahnke, J. J. Finley, A. M. Schwartzberg, D. Y. Qiu, S. Refaely-Abramson, A. W. Holleitner, A. Weber-Bargioni, and C. Kastl, *Nature Communications* **12**, 3822, (2021), DOI: 10.1038/s41467-021-24102-y.

[152] M. Cavallini and D. Gentili, *ChemPlusChem* **87**, e202100562, (2022), DOI: 10.1002/cplu.202100562.

[153] M. Koperski, K. Nogajewski, A. Arora, V. Cherkez, P. Mallet, J.-Y. Veuillen, J. Marcus, P. Kossacki, and M. Potemski, *Nature Nanotechnology* **10**, 503–506, (2015), DOI: 10.1038/nnano.2015.67.

[154] K. Parto, S. I. Azzam, K. Banerjee, and G. Moody, *Nature Communications* **12**, 3585, (2021), DOI: 10.1038/s41467-021-23709-5.

[155] H. Nan, Z. Wang, W. Wang, Z. Liang, Y. Lu, Q. Chen, D. He, P. Tan, F. Miao, X. Wang, J. Wang, and Z. Ni, *ACS nano* **8**, 5738–5745, (2014), DOI: 10.1021/nn500532f.

[156] J.-Y. Tsai, J. Pan, H. Lin, A. Bansil, and Q. Yan, *Nature Communications* **13**, 492, (2022), DOI: 10.1038/s41467-022-28133-x.

[157] H.-P. Komsa, S. Kurasch, O. Lehtinen, U. Kaiser, and A. V. Krasheninnikov, *Physical Review B* **88**, 035301, (2013), DOI: 10.1103/PhysRevB.88.035301.

[158] L. Gao, Q. Liao, X. Zhang, X. Liu, L. Gu, B. Liu, J. Du, Y. Ou, J. Xiao, Z. Kang, Z. Zhang, and Y. Zhang, *Advanced Materials* **32**, 1906646, (2020), DOI: 10.1002/adma.201906646.

[159] M. Donarelli, F. Bisti, F. Perrozzi, and L. Ottaviano, *Chemical Physics Letters* **588**, 198–202, (2013), DOI: 10.1016/j.cplett.2013.10.034.

[160] I. Demeridou, I. Paradisanos, Y. Liu, N. Pliatsikas, P. Patsalas, S. Germanis, N. T. Pelekanos, W. A. Goddard, G. Kioseoglou, and E. Stratakis, *2D Materials* **6**, 015003, (2018), DOI: 10.1088/2053-1583/aae45c.

[161] E. Katsipoulaki, G. Vailakis, I. Demeridou, D. Karfaridis, P. Patsalas, K. Watanabe, T. Taniguchi, I. Paradisanos, G. Kopidakis, G. Kioseoglou, and E. Stratakis, *2D Materials* **10**, 045008, (2023), DOI: 10.1088/2053-1583/ace980.

[162] P. K. Chow, R. B. Jacobs-Gedrim, J. Gao, T.-M. Lu, B. Yu, H. Terrones, and N. Koratkar, *ACS Nano* **9**, 1520–1527, (2015), DOI: 10.1021/nn5073495.

[163] J. Jo, J. H. Kim, C. H. Kim, J. Lee, D. Choe, I. Oh, S. Lee, Z. Lee, H. Jin, and J.-W. Yoo, *Nature Communications* **13**, 2759, (2022), DOI: 10.1038/s41467-022-30414-4.

[164] S. Sovizi, S. Angizi, S. A. Ahmad Alem, R. Goodarzi, M. R. R. Taji Boyuk, H. Ghanbari, R. Szoszkiewicz, A. Simchi, and P. Kruse, *Chemical Reviews* **123**, 13869–13951, (2023), DOI: 10.1021/acs.chemrev.3c00147.

[165] H.-P. Komsa, J. Kotakoski, S. Kurasch, O. Lehtinen, U. Kaiser, and A. V. Krasheninnikov, *Phys. Rev. Lett.* **109**, 035503, (2012), DOI: 10.1103/PhysRevLett.109.035503.

[166] R. F. Egerton, *Ultramicroscopy* **127**, 100–108, (2013), DOI: 10.1016/j.ultramic.2012.07.006.

[167] R. F. Egerton, P. Li, and M. Malac, *Micron* **35**, 399–409, (2004), DOI: 10.1016/j.micron.2004.02.003.

[168] R. Egerton, *Micron* **119**, 72–87, (2019), DOI: 10.1016/j.micron.2019.01.005.

[169] L. W. Hobbs, *Scanning Microscopy* **1990**, 12, (1990).

[170] M. Hugenschmidt, K. Adrion, A. Marx, E. Müller, and D. Gerthsen, *Microscopy and Microanalysis* **29**, 219–234, (2022), DOI: 10.1093/micmic/ozac003.

[171] T. Lehnert, O. Lehtinen, G. Algara–Siller, and U. Kaiser, *Applied Physics Letters* **110**, 033106, (2017), DOI: 10.1063/1.4973809.

[172] M. Jain, S. Kretschmer, J. Meyer, and A. V. Krasheninnikov, *Physical Review Materials* **8**, 054004, (2024), DOI: 10.1103/PhysRevMaterials.8.054004.

[173] R. Egerton, *Ultramicroscopy* **229**, 113363, (2021), DOI: 10.1016/j.ultramic.2021.113363.

[174] J. Cazaux, *Ultramicroscopy* **60**, 411–425, (1995), DOI: 10.1016/0304-3991(95)00077-1.

[175] D. Nicholls, J. Lee, H. Amari, A. J. Stevens, B. L. Mehdi, and N. D. Browning, *Nanoscale* **12**, 21248–21254, (2020), DOI: 10.1039/D0NR04589F.

[176] T. Susi, J. C. Meyer, and J. Kotakoski, *Ultramicroscopy* **180**, 163–172, (2017), DOI: 10.1016/j.ultramic.2017.03.005.

[177] A. V. Krasheninnikov and K. Nordlund, *Journal of Applied Physics* **107**, 071301, (2010), DOI: 10.1063/1.3318261.

[178] J. Kotakoski, A. V. Krasheninnikov, U. Kaiser, and J. C. Meyer, *Physical Review Letters* **106**, 105505, (2011), DOI: 10.1103/PhysRevLett.106.105505.

[179] S. Kretschmer, T. Lehnert, U. Kaiser, and A. V. Krasheninnikov, *Nano Letters* **20**, 2865–2870, (2020), DOI: 10.1021/acs.nanolett.0c00670.

[180] A. Garcia, A. M. Raya, M. M. Mariscal, R. Esparza, M. Herrera, S. I. Molina, G. Scavello, P. L. Galindo, M. Jose-Yacaman, and A. Ponce, *Ultramicroscopy* **146**, 33–38, (2014), DOI: 10.1016/j.ultramic.2014.05.004.

[181] S. de Graaf and B. J. Kooi, *2D Materials* **9**, 015009, (2021), DOI: 10.1088/2053-1583/ac3377.

[182] R. Leiter, Y. Li, and U. Kaiser, *Nanotechnology* **31**, 495704, (2020), DOI: 10.1088/1361-6528/abb335.

[183] K. Li, J. Li, X. Han, W. Zhou, and X. Zhao, *Chinese Physics B* **33**, 096804, (2024), DOI: 10.1088/1674-1056/ad641f.

[184] A. B. Yankovich, B. Berkels, W. Dahmen, P. Binev, S. I. Sanchez, S. A. Bradley, A. Li, I. Szlufarska, and P. M. Voyles, *Nature Communications* **5**, 4155, (2014), DOI: 10.1038/ncomms5155.

[185] B. Berkels, P. Binev, D. A. Blom, W. Dahmen, R. C. Sharpley, and T. Vogt, *Ultramicroscopy* **138**, 46–56, (2014), DOI: 10.1016/j.ultramic.2013.11.007.

[186] L. Jones, H. Yang, T. J. Pennycook, M. S. Marshall, S. Van Aert, N. D. Browning, M. R. Castell, and P. D. Nellist, *Advanced Structural and Chemical Imaging* **1**, 8, (2015), DOI: 10.1186/s40679-015-0008-4.

[187] A. Castellanos-Gomez, M. Buscema, R. Molenaar, V. Singh, L. Janssen, H. S. J. van der Zant, and G. A. Steele, *2D Materials* **1**, 011002, (2014), DOI: 10.1088/2053-1583/1/1/011002.

[188] T. F. Schranghamer, M. Sharma, R. Singh, and S. Das, *Chemical Society Reviews* **50**, 11032–11054, (2021), DOI: 10.1039/D1CS00706H.

[189] P. Gao, A. Kumamoto, R. Ishikawa, N. Lugg, N. Shibata, and Y. Ikuhara, *Ultramicroscopy* **184**, 177–187, (2018), DOI: 10.1016/j.ultramic.2017.09.001.

[190] S. Lopatin, A. Aljarb, V. Roddatis, T. Meyer, Y. Wan, J.-H. Fu, M. Hedhili, Y. Han, L.-J. Li, and V. Tung, *Science Advances* **6**, eabb8431, (2020), DOI: 10.1126/sciadv.abb8431.

[191] E. J. Kirkland, *Ultramicroscopy* **111**, 1523–1530, (2011), DOI: 10.1016/j.ultramic.2011.09.002.

[192] A. Lubk and J. Zweck, *Physical Review A* **91**, 023805, (2015), DOI: 10.1103/PhysRevA.91.023805.

[193] S. Majert and H. Kohl, *Ultramicroscopy* **148**, 81–86, (2015), DOI: 10.1016/j.ultramic.2014.09.009.

[194] B. Shevitski, M. Mecklenburg, W. A. Hubbard, E. R. White, B. Dawson, M. S. Lodge, M. Ishigami, and B. C. Regan, *Physical Review B* **87**, 045417, (2013), DOI: 10.1103/PhysRevB.87.045417.

[195] S. H. Sung, N. Schnitzer, L. Brown, J. Park, and R. Hovden, *Physical Review Materials* **3**, 064003, (2019), DOI: 10.1103/PhysRevMaterials.3.064003.

[196] J. Chapman, I. McFadyen, and S. McVitie, *IEEE Transactions on Magnetics* **26**, 1506–1511, (1990), DOI: 10.1109/20.104427.

[197] I. Lobato and D. Van Dyck, *Acta Crystallographica Section A* **70**, 636–649, (2014), DOI: 10.1107/S205327331401643X.

[198] T. Ishida, T. Kawasaki, T. Tanji, and T. Ikuta, *Microscopy* **64**, 121–128, (2015), DOI: 10.1093/jmicro/dfu113.

[199] D. J. Chang, D. S. Kim, A. Rana, X. Tian, J. Zhou, P. Ercius, and J. Miao, *Physical Review B* **102**, 174101, (2020), DOI: 10.1103/PhysRevB.102.174101.

[200] D. Van Dyck and M. Op de Beeck, *Ultramicroscopy* **64**, 99–107, (1996), DOI: 10.1016/0304-3991(96)00008-3.

[201] S. Van Aert, P. Geuens, D. Van Dyck, C. Kisielowski, and J. Jinschek, *Ultramicroscopy* **107**, 551–558, (2007), DOI: 10.1016/j.ultramic.2006.04.031.

[202] R. Hovden, H. L. Xin, and D. A. Muller, *Physical Review B* **86**, 195415, (2012), DOI: 10.1103/PhysRevB.86.195415.

[203] K. H. W. van den Bos, A. De Backer, G. T. Martinez, N. Winckelmans, S. Bals, P. D. Nellist, and S. Van Aert, *Physical Review Letters* **116**, 246101, (2016), DOI: 10.1103/PhysRevLett.116.246101.

[204] S. Li, Y. Chang, Y. Wang, Q. Xu, and B. Ge, *Micron* **130**, 102813, (2020), DOI: 10.1016/j.micron.2019.102813.

[205] R. J. Wu, A. Mittal, M. L. Odlyzko, and K. A. Mkhoyan, *Microscopy and Microanalysis* **23**, 794–808, (2017), DOI: 10.1017/S143192761700068X.

[206] B. Cordero, V. Gómez, A. E. Platero-Prats, M. Revés, J. Echeverría, E. Cremades, F. Barragán, and S. Alvarez, *Dalton Trans.*, 2832–2838, (2008), DOI: 10.1039/B801115J.

[207] J. Cowley, J. Spence, and V. V. Smirnov, *Ultramicroscopy* **68**, 135–148, (1997), DOI: 10.1016/S0304-3991(97)00022-3.

[208] X. Yang and B. Li, *Nanophotonics* **9**, 1557–1577, (2020), DOI: 10.1515/nanoph-2019-0533.

[209] R. Thayil, S. R. Parne, and C. Ramana, *Small* **21**, 2412467, (2025), DOI: 10.1002/smll.202412467.

[210] V. Boureau, B. Sklenard, R. McLeod, D. Ovchinnikov, D. Dumcenco, A. Kis, and D. Cooper, *ACS nano* **14**, 524–530, (2019), DOI: 10.1021/acsnano.9b06716.

[211] Z. Chen, Y. Jiang, Y.-T. Shao, M. E. Holtz, M. Odstrčil, M. Guizar-Sicairos, I. Hanke, S. Ganschow, D. G. Schlom, and D. A. Muller, *Science* **372**, 826–831, (2021), DOI: 10.1126/science.abg2533.

[212] F. Allars, A. Maiden, D. J. Batey, and C. S. Allen, *Journal of Microscopy* **300**, 191–200, (2025), DOI: 10.1111/jmi.70039.

[213] A. Mahmoudi, M. Bouaziz, A. Chiout, G. Di Berardino, N. Ullberg, G. Kremer, P. Dudin, J. Avila, M. Silly, V. Derycke, D. Romanin, M. Pala, I. C. Gerber, J. Chaste, F. Oehler, and A. Ouerghi, *Physical Review B* **108**, 045417, (2023), DOI: 10.1103/PhysRevB.108.045417.

[214] Y. Wan, J.-K. Huang, C.-P. Chuu, W.-T. Hsu, C.-J. Lee, A. Aljarb, C.-W. Huang, M.-H. Chiu, H.-L. Tang, C. Lin, X. Zhang, C.-M. Wei, S. Li, W.-H. Chang, L.-J. Li, and V. Tung, *ACS Materials Letters* **3**, 442–453, (2021), DOI: 10.1021/acsmaterialslett.0c00554.

[215] J. Köster, A. Storm, T. E. Gorelik, M. J. Mohn, F. Port, M. R. Gonçalves, and U. Kaiser, *Micron* **160**, 103303, (2022), DOI: 10.1016/j.micron.2022.103303.

[216] H. Guo, X. Zhang, and G. Lu, *Science Advances* **6**, eabc5638, (2020), DOI: 10.1126/sciadv.abc5638.

[217] Y. Cao, V. Fatemi, S. Fang, K. Watanabe, T. Taniguchi, E. Kaxiras, and P. Jarillo-Herrero, *Nature* **556**, 43–50, (2018), DOI: 10.1038/nature26160.

[218] S. Brem, C. Linderälv, P. Erhart, and E. Malic, *Nano Letters* **20**, 8534–8540, (2020), DOI: 10.1021/acs.nanolett.0c03019.

[219] K. F. Mak and J. Shan, *Nature Nanotechnology* **17**, 686–695, (2022), DOI: 10.1038/s41565-022-01165-6.

[220] J. Hagel, S. Brem, and E. Malic, *Nano Letters* **24**, 14702–14708, (2024), DOI: 10.1021/acs.nanolett.4c03915.

[221] Y. Cao, V. Fatemi, A. Demir, S. Fang, S. L. Tomarken, J. Y. Luo, J. D. Sanchez-Yamagishi, K. Watanabe, T. Taniguchi, E. Kaxiras, R. C. Ashoori, and P. Jarillo-Herrero, *Nature* **556**, 80–84, (2018), DOI: 10.1038/nature26154.

[222] L. Wang, E.-M. Shih, A. Ghiotto, L. Xian, D. A. Rhodes, C. Tan, M. Claassen, D. M. Kennes, Y. Bai, B. Kim, K. Watanabe, T. Taniguchi, X. Zhu, J. Hone, A. Rubio, A. N. Pasupathy, and C. R. Dean, *Nature Materials* **19**, 861–866, (2020), DOI: 10.1038/s41563-020-0708-6.

[223] J. Zhu, Y.-Z. Chou, M. Xie, and S. Das Sarma, *Physical Review B* **111**, L060501, (2025), DOI: 10.1103/PhysRevB.111.L060501.

[224] Y. Wen, M. J. Coupin, L. Hou, and J. H. Warner, *ACS Nano* **17**, 19600–19612, (2023), DOI: 10.1021/acsnano.2c12179.

[225] T. Devakul, V. Crépel, Y. Zhang, and L. Fu, *Nature Communications* **12**, 6730, (2021), DOI: 10.1038/s41467-021-27042-9.

[226] K. P. Bera, D. Solanki, S. Mandal, R. Biswas, T. Taniguchi, K. Watanabe, V. Raghunathan, M. Jain, A. K. Sood, and A. Das, *ACS Nano* **18**, 24379–24390, (2024), DOI: 10.1021/acsnano.4c06767.

[227] A. Yoshimura, M. Lamparski, N. Kharche, and V. Meunier, *Nanoscale* **10**, 2388–2397, (2018), DOI: 10.1039/C7NR07024A.

[228] J. Lin, S. T. Pantelides, and W. Zhou, *ACS Nano* **9**, 5189–5197, (2015), DOI: 10.1021/acsnano.5b00554.

[229] P. V. Gaikwad, T. T. Hoang, S. Park, and J. Bang, *RSC Advances* **15**, 6585–6592, (2025), DOI: 10.1039/D4RA08374A.

[230] X. Zhao, K. P. Loh, and S. J. Pennycook, *Journal of Physics: Condensed Matter* **33**, 063001, (2020), DOI: 10.1088/1361-648X/abbdb9.

[231] G. T. Leuthner, T. Susi, C. Mangler, J. C. Meyer, and J. Kotakoski, *2D Materials* **8**, 035023, (2021), DOI: 10.1088/2053-1583/abf624.

[232] E. H. Åhlgren, A. Markevich, S. Scharinger, B. Fickl, G. Zagler, F. Herterich, N. McEvoy, C. Mangler, and J. Kotakoski, *Advanced Materials Interfaces* **9**, 2200987, (2022), DOI: 10.1002/admi.202200987.

[233] T. Malis, S. C. Cheng, and R. F. Egerton, *Journal of Electron Microscopy Technique* **8**, 193–200, (1988), DOI: 10.1002/jemt.1060080206.

[234] Y.-Y. Yang and R. Egerton, *Micron* **26**, 1–5, (1995), DOI: 10.1016/0968-4328(94)00039-S.

[235] W. Van den Broek, A. Rosenauer, B. Goris, G. T. Martinez, S. Bals, S. Van Aert, and D. Van Dyck, *Ultramicroscopy* **116**, 8–12, (2012), DOI: 10.1016/j.ultramic.2012.03.005.

[236] A. Mohsin, N. G. Cross, L. Liu, K. Watanabe, T. Taniguchi, G. Duscher, and G. Gu, *2D Materials* **5**, 015007, (2017), DOI: 10.1088/2053-1583/aa8d8b.

[237] J. M. LeBeau and S. Stemmer, *Ultramicroscopy* **108**, 1653–1658, (2008), DOI: 10.1016/j.ultramic.2008.07.001.

[238] A. De Backer, G. Martinez, A. Rosenauer, and S. Van Aert, *Ultramicroscopy* **134**, 23–33, (2013), DOI: 10.1016/j.ultramic.2013.05.003.

[239] P. Giannozzi, S. Baroni, N. Bonini, M. Calandra, R. Car, C. Cavazzoni, D. Ceresoli, G. L. Chiarotti, M. Cococcioni, I. Dabo, A. Dal Corso, S. de Gironcoli, S. Fabris, G. Fratesi, R. Gebauer, U. Gerstmann, C. Gougoussis, A. Kokalj, M. Lazzeri, L. Martin-Samos, N. Marzari, F. Mauri, R. Mazzarello, S. Paolini, A. Pasquarello, L. Paulatto, C. Sbraccia, S. Scandolo, G. Sclauzero, A. P. Seitsonen, A. Smogunov, P. Umari, and R. M. Wentzcovitch, *Journal of Physics: Condensed Matter* **21**, 395502, (2009), DOI: 10.1088/0953-8984/21/39/395502.

[240] P. Giannozzi, O. Andreussi, T. Brumme, O. Bunau, M. Buongiorno Nardelli, M. Calandra, R. Car, C. Cavazzoni, D. Ceresoli, M. Cococcioni, N. Colonna, I. Carnimeo, A. Dal Corso, S. de Gironcoli, P. Delugas, R. A. DiStasio, A. Ferretti, A. Floris, G. Fratesi, G. Fugallo, R. Gebauer, U. Gerstmann, F. Giustino, T. Gorni, J. Jia, M. Kawamura, H.-Y. Ko, A. Kokalj, E. Küçükbenli, M. Lazzeri, M. Marsili, N. Marzari, F. Mauri, N. L. Nguyen, H.-V. Nguyen, A. Otero-de-la-Roza, L. Paulatto, S. Poncé, D. Rocca, R. Sabatini, B. Santra, M. Schlipf, A. P. Seitsonen, A. Smogunov, I. Timrov, T. Thonhauser, P. Umari, N. Vast, X. Wu, and S. Baroni, *Journal of physics: Condensed matter* **29**, 465901, (2017), DOI: 10.1088/1361-648X/aa8f79.

[241] J. P. Perdew, K. Burke, and M. Ernzerhof, *Physical review letters* **77**, 3865, (1996), DOI: 10.1103/PhysRevLett.77.3865.

[242] U. Gerstmann, N. Vollmers, A. Lücke, M. Babilon, and W. Schmidt, *Physical Review B* **89**, 165431, (2014), DOI: 10.1103/PhysRevB.89.165431.

Declaration of Plagiarism

I hereby declare that I have authored this thesis independently, that I have not used other than the declared sources/resources, and that I have explicitly marked all material which has been quoted either literally or by content from the used sources. According to my knowledge, the content or parts of this thesis have not been presented to any other examination authority. I declare that I have only used text-generating AI tools (i. e. DeepL) as an aid for the revision of sentences in order to correct grammatical and orthographic errors, and not for entire passages of text. Furthermore, AI tools (i. e. GWDG: Gwen3) were used for the support of creating user interfaces in Matlab. I am aware that AI does not guarantee the quality of the content. Consequently, the results have been manually reviewed prior to use. The use of AI tools for the specified areas was agreed with the first examiner Prof. Jörg Lindner.

Paderborn, 03. December 2025

Maja Groll

List of Publications

Peer-reviewed Publications

- M. Groll, J. Bürger, I. Caltzidis, K. D. Jöns, W. G. Schmidt, U. Gerstmann, J. K. N. Lindner, "DFT-Assisted Investigation of the Electric Field and Charge Density Distribution of Pristine and Defective 2D WSe_2 by Differential Phase Contrast Imaging", Small 2024, 20, 2311635. DOI: 10.1002/smll.202311635

Conference contributions

(The presenting author is indicated in bold fonts)

- "Characterization of 2D WSe_2 by high-resolution STEM and Differential Phase Contrast STEM", **Maja Groll**, Julius Bürger, Ioannis Caltzidis, Marc Sartison, Klaus D. Jöns, and Jörg K.N. Lindner, DPG Spring Meeting 2022, 04–09 September 2022, Regensburg, Germany.

- "Scattergram analysis and filtering of differential phase contrast STEM images", **Julius Bürger**, Maja Groll, Thomas Riedl, Jörg K. N. Lindner, DPG Spring Meeting, 04–09 September 2022, Regensburg, Germany.

- "Investigation of atomic electric fields in 2D WSe_2 by STEM differential phase contrast", **Maja Groll**, Julius Bürger, Ioannis Caltzidis, Marc Sartison, Klaus D. Jöns, and Jörg K.N. Lindner, 14th International Conference on Physics and Advanced Materials (ICPAM), 08–14 September 2022, Dubrovnik, Croatia.

- "Characterization of 2D WSe_2 by STEM differential phase contrast", **Maja Groll**, Julius Bürger, Jörg K. N. Lindner, DGE Arbeitskreistreffen Differentieller Phasenkontrast, 25–27 September 2022, Munich, Germany.

- "Influences of DPC images captured with segmented detectors", **Julius Bürger**, Maja Groll, Thomas Riedl, Jörg K. N. Lindner DGE Arbeitskreistreffen Differentieller Phasenkontrast, 25–27 September 2022, Munich, Germany.

- "Characterization of two-dimensional WSe_2 using differential phase contrast STEM", **Maja Groll**, Julius Bürger, Jörg K.N. Lindner, Microscopy Conference 2023, 26 February – 02 March 2023, Darmstadt, Germany.

- “DPC-Toolbox, a software for post-processing and analysis of differential phase contrast STEM images”, **Julius Bürger**, Maja Groll, Jörg K.N. Lindner, Microscopy Conference 2023, 26 February – 02 March 2023, Darmstadt, Germany.

- “Electric field and charge density distribution of 2D mono- and multilayers of WSe_2 by high-resolution STEM-DPC”, **Maja Groll**, Julius Bürger, Ioannis Caltzidis, Marc Sartison, Klaus D. Jöns, and Jörg K.N. Lindner, 20th International Microscopy Congress (IMC20), 10–15 September 2023, Busan, Republic of Korea.

- “Increasing azimuthal momentum space resolution of segmented detectors for differential phase contrast STEM imaging”, **Julius Bürger**, Maja Groll, Aladin Ullrich, Manfred Albrecht, Jörg K. N. Lindner, 20th International Microscopy Congress (IMC20), 10–15 September 2023, Busan, Republic of Korea.

- “Differential Phase Contrast STEM Investigation of Interatomic Electric Fields in Pristine and Defective 2D-WSe_2 Multi- and Monolayers”, Maja Groll, Julius Bürger, Ioannis Caltzidis, Klaus D. Jöns, and **Jörg K.N. Lindner**, 15th International Conference on Physics and Advanced Materials (ICPAM), 19–26 November 2023, Sharm El Sheikh, Egypt, (invited Talk).

- “DFT-assisted Investigation of Defects in 2D WSe_2 by High-Resolution STEM and Differential Phase Contrast Imaging”, **Maja Groll**, Julius Bürger, Ioannis Caltzidis, Klaus D. Jöns, Wolf Gero Schmidt, Uwe Gerstmann, and Jörg K. N. Lindner, DPG Spring Meeting 2024, 17–22 March 2024, Berlin, Germany.

- “DFT-assisted investigations of the atomic electric field distribution of vacancy-type defects in 2D WSe_2 by STEM differential phase contrast imaging”, **Maja Groll**, J. Bürger, I. Caltzidis, K. D. Jöns, Wolf Gero Schmidt, Uwe Gerstmann, Jörg K. N. Lindner, European Materials Research Society (EMRS) Spring Meeting, 27–31 May 2024, Strasbourg, France.

- “Influence of dynamical diffraction on DPC measurements of 2D materials”, **Maja Groll**, Julius Bürger, Jörg K. N. Lindner, European Microscopy Congress, 25–30 August 2024, Copenhagen, Denmark.

- “Investigation of electric fields at sub-atomic resolution with the STEM”, Maja Groll, Julius Bürger, **Jörg K. N. Lindner**, 2nd International Conference on Laser, Plasma and Radiation Science and Technology, 16–21 June 2024, Danube Delta, Romania, (invited Talk).

- “Investigations of the atomic electric field and charge density distribution in 2D WSe_2 by high-resolution STEM Differential Phase Contrast imaging and DFT”, **Maja Groll**, Julius Bürger, Ioannis Caltzidis, Klaus D. Jöns, Wolf Gero Schmidt, Uwe Gerstmann, and Jörg K. N. Lindner, Atomic structure of nanosystems from first-principles simulations and microscopy experiments (AS-SIMEX 2024), 28–30 May 2024, Helsinki, Finland.

- “Influence of the detector rotation on STEM-DPC investigation of atomic electric fields in WSe_2 with a segmented detector”, **Maja Groll**, Julius Bürger, Jörg K. N. Lindner, Microscopy Conference 2025, 31 August – 04 September 2025, Karlsruhe, Germany.

- “Investigation of vacancy-like defects in monolayer of WSe_2 using differential phase contrast imaging in the scanning transmission electron microscope”, **Maja Groll**, Jörg K. N. Lindner, European Materials Research Society (EMRS) Fall Meeting, 15–18 September 2025, Warschau, Poland.

- “Influence of point defects on the atomic electric field distribution in 2D-WSe_2”, **Maja Groll**, Jörg K. N. Lindner, 17th International Conference on Physics and Advanced Materials (ICPAM), 16–23 November 2025, Shizuoka, Japan.